

*Bridgmanite crystal chemistry and iron
content in the Earth's lower mantle*

DISSERTATION

zur Erlangung des akademischen Grades einer Doktorin
der Naturwissenschaften (Dr. rer. nat.)
in der Bayreuther Graduiertenschule für Mathematik und Naturwissenschaften
(BayNAT)
der Universität Bayreuth

vorgelegt von

Rong Huang
aus *Hubei (China)*
Bayreuth, 2020

This doctoral thesis was prepared at the department of Bayerisches Geoinstitut at the University of Bayreuth from November 2014 until January 2020 and was supervised by Prof. Dr. Daniel Frost and Dr. Tiziana Boffa Ballaran.

This is a full reprint of the thesis submitted to obtain the academic degree of Doctor of Natural Sciences (Dr. rer. nat.) and approved by the Bayreuth Graduate School of Mathematical and Natural Sciences (BayNAT) of the University of Bayreuth.

Date of submission: 08.01.2020

Date of defence: 03.02.2020

Acting director: Prof. Dr. Markus Lippitz

Doctoral committee:

Prof. Dr.	Daniel Frost	(reviewer)
PD Dr.	Catherine McCammon	(reviewer)
Prof. Dr.	David Rubie	(chairman)
Dr.	Marcel Thielmann	

Table of contents

Abstract	1
Zusammenfassung	3
1 Introduction	7
1.1 Seismic observations of the mantle	8
1.1.1 Velocity-depth profile	8
1.1.2 Lateral heterogeneity.....	13
1.2 Chemical composition of the mantle	15
1.3 Mineralogy of pyrolite and subducted slab as a function of depth	19
1.3.1 Phase relations and phase transitions in pyrolite.....	19
1.3.2 Phase relations and phase transitions in subducted slabs	22
1.4 Bridgmanite in the lower mantle.....	26
1.4.1 Proportions of bridgmanite in different bulk compositions	27
1.4.2 Bridgmanite structure	28
1.4.3 Composition of bridgmanite	29
1.4.4 Substitution mechanisms in bridgmanite	30
1.4.5 Spin transition of bridgmanite	32
1.5 Oxygen fugacity of Earth's mantle.....	32
1.5.1 Upper mantle oxygen fugacity	35
1.5.2 Deep upper mantle and transition zone oxygen fugacity.....	38
1.5.3 Oxygen fugacity in the lower mantle	39
1.6 Aim of this study	40
2 Experimental methods	45
2.1 Starting material preparation.....	45

2.2 High pressure experiments.....	49
2.3 Sample characterization	52
2.3.1 Scanning electron microscopy	52
2.3.2 Electron probe micro-analyzer (EPMA).....	53
2.3.3 Micro-focus X-ray diffraction	54
2.4 Single crystal X-ray diffraction and structural refinements	55
2.4.1 Crystal selection	57
2.4.2 Accurate Unit-cell parameter determination	57
2.5 Mössbauer spectroscopy and electron energy loss spectroscopy (EELS).....	61
2.5.1 Mössbauer spectroscopy	61
2.5.2 Electron energy-loss spectroscopy (EELS).....	67
3 Phase assemblage and composition of recovered samples	71
3.1 Recovered phase assemblages from experiments to obtain single crystals.....	71
3.2 Recovered phase assemblages from oxygen fugacity buffered experiments	74
3.3 Composition of run products.....	77
3.4 Fe ³⁺ /ΣFe determination in bridgmanite	84
4 The crystal chemistry of Fe-Al-bearing bridgmanite.....	91
4.1 Al and Fe substitution mechanisms in bridgmanite	96
4.2 Unit-cell parameters and Molar volumes of (Fe,Al)-bearing MgSiO ₃ bridgmanite ..	96
4.3 Distortion of the perovskite-type structure of bridgmanite	102
4.4 Spontaneous strain.....	112
4.5 Compression behavior of bridgmanite	117
5 Speciation of Fe and Al in bridgmanite as a function of composition and oxygen fugacity	121
5.1 Determination of oxygen fugacity.....	121
5.2 Fe ³⁺ /ΣFe dependence on <i>f</i> _{O₂} , composition and temperature in bridgmanite.....	125

5.3 Substitution mechanisms in Bridgmanite.....	129
5.3.1 Al-bearing bridgmanite	129
5.3.2 Fe-bearing bridgmanite.....	134
5.3.3 Fe, Al-bearing bridgmanite.....	140
5.4 Composition of bridgmanite and ferropericlase as a function of oxygen fugacity in pyrolite.....	146
5.5 Metal saturation determination.....	150
5.6 Extrapolation to higher pressures	154
6 Other Mg, Fe-bearing phases coexisting with bridgmanite	161
6.1 Speciation of carbon at different oxygen fugacities.....	161
6.2 Fe partitioning between bridgmanite and melt and density of the melt	164
6.2.1 Chemical compositions of coexisting Brg and melt	164
6.2.2 Fe partitioning between Brg and melt	167
6.2.3 Composition of hydrous melt at the uppermost lower mantle.....	170
6.2.4 Density of the melt.....	171
7 Major conclusions	181
References	189
Acknowledgements.....	211

Abstract

Although the pyrolite model is widely accepted as providing the chemical composition of the Earth's fertile upper mantle, it is still not clear whether it is also representative of the lower mantle. A comparison between seismic wave velocities in the lower mantle with models for what these velocities should be if the lower mantle has a pyrolitic composition is the only way to ultimately test this assumption. This requires data on mineral elastic properties and a method for determining the proportions and compositions of minerals as a function of depth and bulk composition. The Earth's lower mantle is comprised mainly of the mineral bridgmanite (Brg), with lesser amounts of ferropericlase (Fp) and CaSiO_3 perovskite. In this study multi-anvil experiments have been performed to derive a methodology for determining the compositions of Brg and Fp as a function of bulk composition in the lower mantle. As Brg can contain significant proportions of ferric iron it is also important to predict the composition of Brg as a function of oxygen fugacity. Brg-Fp assemblages have been synthesized with different proportions of Fe and Al and at different oxygen fugacities at 25 GPa and 1973 K. Water was added to some assemblages to induce the growth of large Brg single crystals with differing amounts of Fe^{2+} , Fe^{3+} and Al. This produced hydrous partial melts that were also examined.

In the first part of the study, single crystal X-ray diffraction measurements were made on ten Brg single crystals with different compositions. Based on these measurements and some data from the literature the partial molar volumes of the main Brg components were determined assuming a linear volume-composition relationship. These volumes, which are essential for the thermodynamic description of Brg chemistry at high pressures, decrease in the order: $\text{FeFeO}_3 > \text{MgFeO}_{2.5} > \text{FeAlO}_3 > \text{MgAlO}_{2.5} > \text{AlAlO}_3 > \text{FeSiO}_3 > \text{MgSiO}_3$. All lattice parameters, B-O bond distances, octahedral tilting and polyhedral distortion as well as the spontaneous strain components, e_4 and e_{tx} , increase with charge coupled $\text{M}^{3+}\text{M}^{3+}\text{O}_3$ ($\text{M}^{3+}=\text{Al}^{3+}+\text{Fe}^{3+}$) and oxygen vacancy $\text{MgM}^{3+}\text{O}_{2.5}$ substitution, whereas the octahedral tilting and A-site distortion decrease with $\text{Fe}^{2+}\text{SiO}_3$ substitution. Calculations based on the bond strengths of individual B-O and A-O lengths suggest that the octahedral tilting of Fe,Al-bearing Brg increases with pressure and point to a more compressible octahedral site and less compressible A-site with respect to the MgSiO_3 end-member.

In the second part of this study, the Fe^{3+} content of Brg was investigated experimentally as a function of composition and oxygen fugacity (f_{O_2}). Recovered samples were analyzed using the electron microprobe and Mössbauer spectroscopy. The Brg $\text{Fe}^{3+}/\Sigma\text{Fe}$ ratio increases with Brg Al content and f_{O_2} and decreases with increasing total Fe content and with temperature. The f_{O_2} dependence was found to decrease with increasing Al content. Thermodynamic models were calibrated to describe Brg and Fp compositions in the Fe-Mg-Si-O and Fe-Al-Mg-Si-O systems as well as the inter-site partitioning of 3+ cations in Brg. These models fit the experimental data very well, particularly given the small number of adjustable terms. The models allow the mineral compositions for plausible mantle bulk compositions to be calculated as a function of f_{O_2} and can be extrapolated to higher pressures using data on the partial molar volumes of Brg components. The results show that Fe-Mg partitioning between Brg and Fp is strongly f_{O_2} dependent, which allows the results of previous contradictory studies to be brought into agreement. For a pyrolite bulk composition with an upper mantle bulk oxygen content, a lower mantle f_{O_2} of IW – 0.8 is indicated with a Brg $\text{Fe}^{3+}/\Sigma\text{Fe}$ ratio of 0.51 and a bulk rock ratio of 0.28. This requires the formation of 0.6 wt.% Fe-Ni alloy. With increasing pressure, the model predicts a gradual increase in the $\text{Fe}^{3+}/\Sigma\text{Fe}$ ratio in Brg in contrast to several previous studies. Oxygen vacancies in Brg decrease to practically zero by 40 GPa, likely influencing transport properties in the top portion of the lower mantle.

Lastly, using analyses of melts coexisting with Brg and Fp a thermodynamic model was developed to describe the Fe-Mg exchange between Brg and hydrous melt. Based on this model melt compositions were calculated at different assumed melt fractions (0.1 wt.%- 1 wt.%) for a pyrolite composition and the corresponding melt density was calculated along a mantle geotherm from 22-28 GPa. The density of a 1 wt.% hydrous partial melt is significantly lower than the surrounding lower mantle but is close to neutral buoyancy at the base of the transition zone. This raises the possibility that hydrous melts might rise out of the lower mantle but pond or freeze on entering the transition zone. If such a process occurs in regions of down-welling then melt bearing regions may be continuously dragged into the lower mantle before grain scale migration allows melts to flow upwards, potentially creating long term seismically observable low velocity layers.

Zusammenfassung

Obwohl das Pyrolit-Modell weitestgehend akzeptiert ist als das, das die chemische Zusammensetzung des oberen Erdmantels darstellt, ist es jedoch nicht klar, ob die Pyrolit-Zusammensetzung auch repräsentativ für den unteren Erdmantel ist. Ein Vergleich zwischen seismischen Wellengeschwindigkeiten als Funktion der Tiefe im unteren Erdmantel und Modellen dieser Geschwindigkeiten für eine pyrolitische Zusammensetzung des unteren Erdmantels ist die einzige Möglichkeit, diese Annahme schlussendlich zu testen. Das erfordert Daten über die elastischen Eigenschaften der Minerale sowie eine Methode zur Bestimmung der Anteile und Zusammensetzung der Minerale als Funktion der Tiefe und der Gesamtzusammensetzung. Der untere Erdmantel besteht hauptsächlich aus dem Mineral Bridgmanit (Brg), mit geringeren Anteilen von Ferroperiklas (Fp) und CaSiO_3 Perowskit. In der vorliegenden Arbeit wurden Experimente mit der Vielstempelpresse durchgeführt, um eine Methodologie zur Bestimmung der chemischen Zusammensetzung von Brg und Fp als Funktion des Gesamtchemismus im unteren Erdmantel zu abzuleiten. Da Brg signifikante Anteile von Eisen im oxidierten Zustand enthalten kann, war es außerdem auch wichtig, die Zusammensetzung von Brg als Funktion der Sauerstoffugazität vorhersagen zu können. Brg-Fp Aggregate wurden von Ausgangszusammensetzungen mit unterschiedlichen Anteilen von Fe und Al sowie bei verschiedenen Sauerstoffugazitäten bei 25 GPa und 1973 K synthetisiert. Wasser wurde bei einigen Ausgangsmaterialien hinzugegeben, um das Wachstum von großen Brg Einkristallen mit verschiedenen Anteilen von Fe^{2+} , Fe^{3+} und Al zu induzieren. Das führte außerdem zur Bildung von hydratisierten Schmelzen, die auch untersucht wurden.

Im ersten Teil der vorliegenden Arbeit wurden Röntgenbeugungsmessungen an zehn Brg Einkristallen mit verschiedenen Zusammensetzungen durchgeführt. Basierend auf diesen Messungen und Literaturdaten wurden die partiellen Molarvolumen der Brg-Hauptkomponenten unter der Annahme einer linearen Beziehung zwischen Volumen und Zusammensetzung bestimmt. Die Volumina sind essentiell für die thermodynamische Beschreibung des Brg Chemismus unter Hochdruckbedingungen und nehmen in dieser Reihenfolge ab: $\text{FeFeO}_3 > \text{MgFeO}_{2.5} > \text{FeAlO}_3 > \text{MgAlO}_{2.5} > \text{AlAlO}_3 > \text{FeSiO}_3 > \text{MgSiO}_3$. Alle Gitterparameter, B-O Bindungsabstände, Oktaederkippungen und Polyederverformungen sowie die spontanen Strainkomponenten e_4 and e_{tx} steigen mit den ladungsgekoppelten

$M^{3+}M^{3+}O_3$ ($M^{3+}=Al^{3+}+Fe^{3+}$) und an Sauerstoffleerstellen gebundenen $MgM^{3+}O_{2.5}$ Substitutionen an, während die Oktaederkippung und die Verformung des A Gitterplatzes mit der $Fe^{2+}SiO_3$ Substitution abnehmen. Auf der Bindungsstärke der individuellen B-O und A-O Bindungslängen basierende Berechnungen deuten darauf hin, dass die Oktaederkippung von Fe,Al-haltigem Brg mit Druck zunimmt und zeigen einen stärker komprimierbaren Oktaeder-Gitterplatz und einen weniger komprimierbaren A-Gitterplatz relativ zum $MgSiO_3$ -Endglied auf.

Im zweiten Teil dieser Untersuchung wurde der Fe^{3+} -Gehalt von Brg experimentell als Funktion von chemischer Zusammensetzung und Sauerstoffugazität untersucht. Aus Experimenten gewonnene Proben wurden mithilfe der Elektronenmikrosonde und der Mössbauerspektroskopie analysiert. Das Brg $Fe^{3+}/\Sigma Fe$ Verhältnis steigt mit Brg Al-Gehalt und Sauerstoffugazität (f_{O_2}) an und verringert sich mit steigendem Gesamt-Fe-Gehalt und mit steigender Temperatur. Die f_{O_2} Abhängigkeit verringert sich mit steigendem Al-Gehalt. Thermodynamische Modelle wurden kalibriert, um die Brg und Fp Zusammensetzungen in den Fe-Mg-Si-O and Fe-Al-Mg-Si-O Systemen sowie die Verteilung von 3+ Ionen zwischen Gitterplätzen in Brg zu beschreiben. Das Modell reproduziert die experimentellen Daten sehr gut, insbesondere angesichts der geringen Anzahl von anpassbaren Termen. Das Modell erlaubt es ausserdem, die Mineralzusammensetzungen für plausible Gesamtzusammensetzungen des Mantels als Funktion der Sauerstoffugazität zu berechnen und kann durch die Nutzung der Daten der partiellen Molarvolumen der Brg-Komponenten zu höheren Drücken extrapoliert werden. Die Resultate zeigen, dass die Fe-Mg Verteilung zwischen Brg und Fp stark abhängig von f_{O_2} ist, so dass die Resultate vorhergehender, sich widersprechender Studien wahrscheinlich in Einklang zu bringen sind, wenn f_{O_2} berücksichtigt wird. Für eine Pyrolit-Gesamtzusammensetzung mit einem Sauerstoffgehalt wie im oberen Erdmantel ergibt das Modell eine Mantel f_{O_2} von $IW - 0,8$, einem $Fe^{3+}/\Sigma Fe$ Verhältnis von 0,51 für Brg und 0,28 für das Gesamtgestein, was die Bildung von 0,6 Gew.% Fe-Ni Legierung bei 25 GPa erfordert. Mit ansteigendem Druck sagt das Modell einen graduellen Anstieg im $Fe^{3+}/\Sigma Fe$ Verhältnis von Brg voraus, was im Widerspruch zu einigen vorhergehenden Studien steht. Die Sauerstoff-Leerstellen-Komponente von Brg reduziert sich gegen praktisch Null bei 40 GPa, was die Transporteigenschaften im oberen Bereich des unteren Mantels stark beeinflussen würde.

Im letzten Teil der Arbeit wurde ein thermodynamisches Modell entwickelt, das, basierend auf chemischen Analysen der Schmelzen, die mit Brg und Fp koexistieren, den Fe-Mg Austausch zwischen Brg und wasserhaltigen Schmelzen bei 25 GPa und 1923 K beschreibt. Mit diesem Modell wurden Schmelzzusammensetzungen bei unterschiedlichen Aufschmelzungsgraden (0,1 - 1 Gew.%) für eine Pyrolitzusammensetzung berechnet und die korrespondierenden Schmelzdichten wurden entlang einer Mantelgeotherme von 22 bis 28 GPa ermittelt. Die Dichte einer 1 Gew.% wasserhaltigen Schmelze wäre signifikant geringer als die des umgebenden unteren Mantels, aber sie hätte einen nahezu neutralen Auftrieb an der Basis der Übergangszone des Erdmantels. Das eröffnet die Möglichkeit, dass wasserhaltige Schmelzen aus dem unteren Mantel aufsteigen, aber sich an der Übergangszone sammeln oder kristallisieren. Wenn ein solcher Prozess in Regionen von absinkendem Material vorkommt, dann würden schmelzhaltige Bereiche kontinuierlich in den unteren Mantel transportiert, bevor Migration auf der Kornebene ihnen erlauben würde wieder aufwärts zu fließen, und so potentiell zur Bildung einer seismisch detektierbaren Schicht mit niedrigen Wellengeschwindigkeiten beizutragen.

1 Introduction

The lower mantle makes up by far the largest region of the Earth and its composition is not only important for understanding how, and from what, the Earth was formed, but also for determining the style of mantle convection and the geochemical evolution of the interior. Despite the importance of the lower mantle's composition to the geophysical and geochemical state of the Earth, it remains uncertain. It is still a matter of debate, for example, whether the lower mantle is chemically different from the upper mantle. The only feasible way to ultimately constrain this composition is through the interpretation of seismic wave velocities as they travel through the lower mantle (Cottaar et al., 2014; Jackson, 1983; Stixrude and Jeanloz, 2007). In order to do this a mineral model is required that reproduces the elastic properties, and therefore the seismic velocities, of the lower mantle for a specific chosen bulk composition. Such a model principally requires data on the elastic properties of minerals at suitable pressures and temperatures. A further important aspect, however, is the necessity to determine the compositions and proportions of the mineral phases as a function of pressure, temperature and bulk composition because elastic properties are dependent on mineral chemistry (Boffa Ballaran et al., 2012; Chantel et al., 2012; Lin et al., 2013). The bulk composition of the lower mantle can then be evaluated from the extent to which the mineral physics-based model, based on a specific composition, matches the observed seismic velocity profiles. Although there may be more than one bulk composition and adiabatic profile that gives a good fit to these profiles (Bina and Helffrich, 2014), the results would nevertheless place constraints on plausible solutions and potentially exclude possible scenarios. The chemical compositions of individual minerals in the lower mantle are also important for understanding transport properties such as rheology (Holzapfel et al., 2005) and electrical and thermal conductivity (Keppler et al., 2008; Manthilake et al., 2011; Ohta et al., 2014; Okuda et al., 2019; Xu et al., 1998) and for exploring the origin of mineral inclusions in diamonds that are proposed to come from the deep mantle (Kaminsky et al., 2015; McCammon et al., 1997; McCammon et al., 2004c; Walter et al., 2011). The diamond anvil cell based experimental methods used to explore

the mineralogy of the lower mantle have intrinsic uncertainties due to small sample sizes and large thermal gradients. For this reason, it is essential to have a thermodynamic model based on a rigorous set of experiments performed at well constrained experimental conditions that can be used to assess and interpolate between high pressure data sets.

This thesis is aimed at understanding the composition of the dominant lower mantle mineral bridgmanite and determining how its composition and structure will be influenced by changes in chemistry and oxygen fugacity. Understanding the controls on the chemistry of bridgmanite is the first step in ultimately modelling the mineral physics and seismic properties throughout the lower mantle.

1.1 Seismic observations of the mantle

Seismic waves propagating through the Earth's interior provide direct information on the Earth's structure, since their propagation velocities depend on the density and elasticity of the medium they travel through. Geophysical observations are therefore essential for constraining any mineral physics model of the deep Earth.

1.1.1 Velocity-depth profile

Spherically symmetrical (1D) Earth models such as the Preliminary Reference Earth Model (PREM, Dziewonski and Anderson, 1981), iasp91 (Kennett and Engdahl, 1991) and AK135 (Kennett et al., 1995) are based on a large catalogue of body-wave travel times and normal mode observations (standing waves due to the free-oscillation of the Earth) and provide profiles of wave velocity, density, and attenuation throughout the Earth. In these models, velocities are refined to a set of polynomial functions that operate over certain depth ranges, with assumed seismic discontinuities at certain depths (Fig. 1.1). Several discontinuities in the upper mantle have been well established, the properties of which provide a link between mineral physics experiments and seismic observations as well as important constraints on models of mantle composition and dynamics. These discontinuity properties include the discontinuity depths and topography, the size of the velocity and

density increases and the sharpness of the boundaries. Discontinuities in the transition zone, for example, are considered to arise from nominally isochemical first order mineral phase transitions. The depths of these discontinuities can, therefore, be interpreted, through experimental studies, to provide information on the temperature of the mantle.

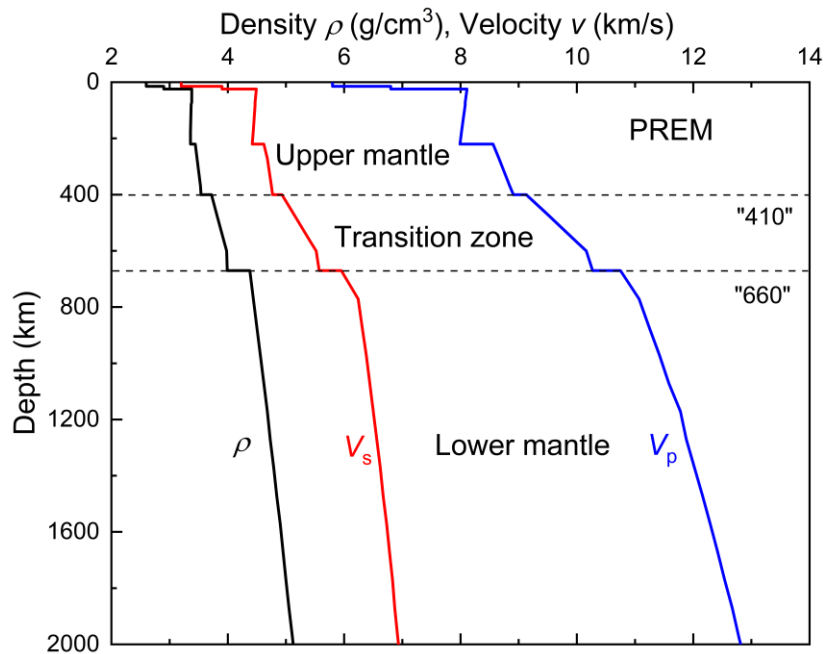


Figure 1.1 The density ρ , S wave velocity V_s and P wave velocity V_p as a function of depth according to the PREM model (Dziewonski and Anderson, 1981).

1.1.1.1 Discontinuity depth

The depths of seismic discontinuities can be obtained using a variety of approaches including analysis of seismic waves that bottom near the discontinuities (refractory seismology) or seismic waves that are either reflected or converted at the discontinuity (Shearer, 2000). The Mohorovicic discontinuity marks the base of the crust and the top of the Earth's upper mantle. Two major global seismic discontinuities of the mantle transition zone at mean depths of about 410 and 660 km (hereafter termed 410 and 660) have been well established by observations in SS (S phase with one reflection at the surface) (e.g. Heit et al., 2010 and references therein), PP (P phase with one reflection at the surface) (e.g. Deuss, 2009 and references therein), and P[']P['] (abbreviation of PKIKP, a P phase bottoming in the inner core with one reflection at the surface) precursors (e.g. Day and Deuss, 2013

and references therein), Ps (P-to-S converted wave) and Sp (S-to-P converted wave) conversions at the discontinuities (receiver functions) (e.g. Andrews and Deuss, 2008 and references therein), and ScS (S wave reflected from the core-mantle boundary) reverberations (e.g. Katzman et al., 1998 and references therein), whereas the presence of a discontinuity at about 520 km (hereafter termed 520) has been controversial (e.g. Kind and Li, 2015 and references therein). This discontinuity is clearly observed in some regions by SS precursor, PP precursor, ScS reverberation and receiver function studies but it is not visible in other regions. Therefore, the 520 does not appear to be a laterally homogeneous global discontinuity, but also it cannot be considered a local one because it has a relatively common distribution (e.g. Kind and Li, 2015 and references therein). All modern global reference Earth models (Brown and Shankland, 1981; Kennett and Engdahl, 1991; Kennett et al., 1995) include a sudden increase of the velocities of the elastic waves and densities at 410 and 660 km, while the 520 is absent in all but the mineral physics based model of Cammarano et al. (2005). The depth ranges reported for the 410, 520 and 660 are from 390 km to 430 km, from 500 km to 520 km and from 650 km to 680 km, respectively. The SS precursor observations may be the most suitable for globally averaged depth estimates due to the wide distribution of their bounce points which provides comprehensive global coverage (Shearer, 2000), resulting in mean discontinuity depths close to 410, 520 and 660 km. These average discontinuity depths to a first approximation match well with those expected for the pressure and temperature-induced phase transitions from olivine to wadsleyite, from wadsleyite to ringwoodite and from ringwoodite to bridgmanite (Brg) plus ferropericlase (Fp), respectively. If this is true, the discontinuity depth could provide relatively direct information on mantle temperatures using knowledge of the transformation boundaries of certain mineral phase changes.

1.1.1.2 Discontinuity topography

Differences among discontinuity depth estimates obtained in different studies imply that global variations in discontinuity depths, i.e. topography, exists (Shearer, 2000) that can be most likely attributed to mantle temperature variations. Discontinuity topography may be

detected using SS precursor techniques, ScS reverberations or Ps and Sp conversion techniques (Kind and Li, 2015). Precursor techniques can reach locations without local stations or earthquake sources, allowing a better global distribution of sampling points. The resolution of long period SS precursors does not allow small-scale topography of the discontinuities to be resolved because they are associated with maximum travel-time phases and can be contaminated by small scale, off-great-circle-path structure (Kind and Li, 2015; Shearer, 2000). Small-scale discontinuity topography less than a few tens of kilometers can be detected instead using Ps and Sp conversion techniques, i.e. waves reflected or converted at the discontinuities close to either the source or receiver (receiver function) (Kind and Li, 2015). The converted phases are minimum travel-time phases and allow a better resolution due to their smaller Fresnel zones but are restricted to near-station or earthquake locations (Kind and Li, 2015).

The amplitude of the global 660 topography (38-50 km) appears to be larger than the 410 topography (22-40 km) (Flanagan and Shearer, 1998; Gu et al., 2012; Shearer, 1991, 1993). Whether the 410 and 660 are globally anticorrelated is still under debate due to contradictory observations (Gu et al., 2003; Gu et al., 2012; Hu et al., 2013; Humphreys et al., 2000; Ramesh et al., 2005). Both global and high-resolution local observations show depression of the 660 of between 20 and 50 km at subduction zones on a large scale (Tibi and Wiens, 2005; Tonegawa et al., 2005; Tonegawa et al., 2006; Tono et al., 2005). Evidence of 410 uplift at subduction zones, instead, is less convincing due to locally contradicting observations (Tibi and Wiens, 2005; Tonegawa et al., 2005; Tonegawa et al., 2006; Tono et al., 2005). The transition zone structure beneath hot spots, many of which are in oceanic regions, is less clear due to the limited data set (Kind and Li, 2015). To a first approximation the discontinuity topography provides information on lateral mantle temperature variations and depends on the Clapeyron slopes of the mineral transformations giving rise to the discontinuity, although other factors such as chemistry and metastable olivine due to sluggish kinetics at low temperature may also play a role (Kirby et al., 1996). The Clapeyron slopes of mineral phase transitions can be determined by means of high pressure and high temperature experiments, but to be useful they need to be determined with high accuracy.

The local elevation of the 410 and depression of the 660 near the slabs (Fig. 1.2) are consistent with the opposite sign of the Clapeyron slopes of corresponding phase transitions (Helffrich and Bina, 1994; Shearer, 2000). If the Clapeyron slope of the 410 phase transition is higher than that of the 660 as some mineral physics studies proposed (Hirose, 2002; Irifune, 1998; Ito and Takahashi, 1989; Katsura et al., 2004; Katsura et al., 2003), the above mentioned observation would indicate larger lateral temperature variations at 660 km depth.

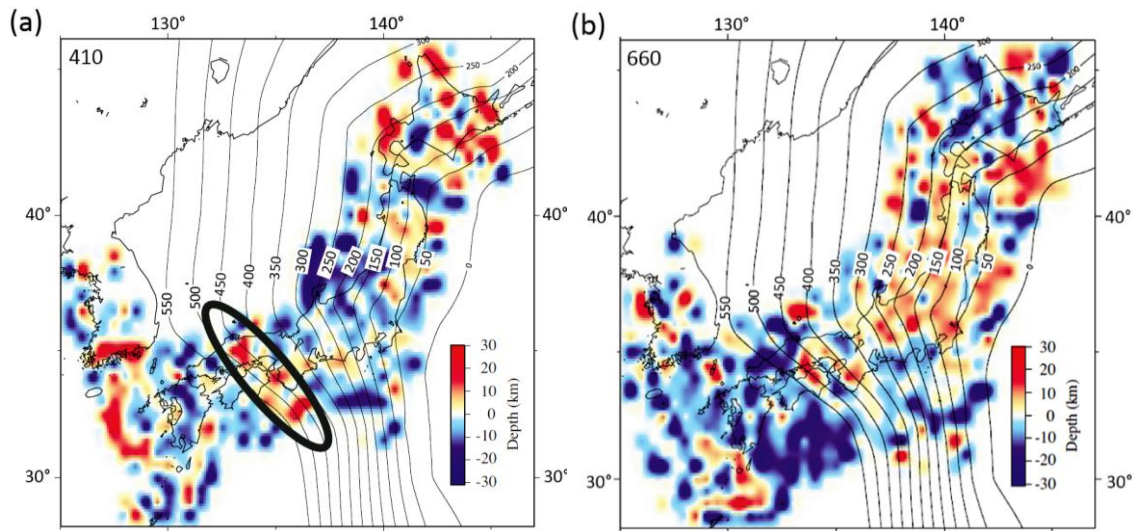


Figure 1.2 Topography of 410 and 660 km discontinuities in the region of the Japan subduction zone (modified from Tonegawa et al., 2005). (a) Depth variations of 410 km discontinuity. (b) Depth variations of 660 km discontinuity. The black curves denote the depth contours corresponding to the top surface of the Pacific Plate (PAC). Colors indicate differences from 410 km and 660 km. Red to yellow shows the elevation and pale-blue to blue shows the depression. The black ellipse indicates the uplift portion of 410 km discontinuity.

1.1.1.3 Discontinuity sharpness

The sharpness of the transition zone discontinuities, i.e. the depth interval over which a discontinuity occurs, can be determined using observations of high-frequency data such as $P^{\prime}P^{\prime}$ precursors or locally reflected and converted seismic waves because such high-frequency seismic waves can only be influenced by a high impedance contrast (equal to the product of compressional velocity and density) across a narrow discontinuity. These data are consistent with a sharp 660 (≤ 2 km thick) and a more diffuse 410 discontinuity which

can be modelled as a 7-km-wide gradual transition with a sharp jump at the end (Xu et al., 2003). The variation of the sharpness of 660 discontinuity among different areas was quite small between 2-5 km (Benz and Vidale, 1993; Tibi and Wiens, 2005; Tonegawa et al., 2005; Yamazaki and Hirahara, 1994) while the 410 may be more variable in sharpness than 660 which ranges from 2 to 35 km (Benz and Vidale, 1993; Priestley et al., 1994; Tonegawa et al., 2005; Yamazaki and Hirahara, 1994). Two exceptions were reported by Bostock (1996) and Petersen et al. (1993) who found a sharper 410 (5-7 km) than 660 (20-30 km) from Ps conversion studies. The 520 reflector was observed in long-period SS precursor studies but absent in high-frequency P'P' precursor observations, suggesting that the thickness of 520 discontinuity is between 10 and 50 km (Shearer, 2000). The sharpness of the discontinuities provides important information of the deep mantle. If the phase transition of the olivine system is responsible for the discontinuities, the pressure interval of the phase transition should be consistent with the sharpness of the discontinuity.

1.1.2 Lateral heterogeneity

The oceanic lithosphere is thought to drive convection and create chemical heterogeneity in the mantle during subduction. A subducting slab is in fact a downward continuation of the surface oceanic plate, marked seismologically by high P-wave and S-wave velocities and low P-wave and S-wave attenuations and geodynamically by low temperature, high density, and negative buoyancy relative to the surrounding mantle. The most reliable indicator of a subducting slab is the positive anomaly of seismic velocity.

Near-horizontal deflection of subducted slabs was first detected by Okino et al. (1989) from travel time analysis and later imaged by Van der Hilst et al. (1991) and Van der Hilst and Seno (1993) in the transition zone beneath Japan and by Fukao et al. (1992) in the western Pacific using P-wave travel time tomography. Fukao et al. (2001) referred to these subducted slabs with a tendency to horizontally flatten at various depth between ~ 400 and 1000 km as stagnant slabs. Fukao and Obayashi (2013) systematically imaged the subducted slabs in the circum-Pacific region revealing a progressive lateral variation of the configuration of slabs along arcs. They interpreted this systematic change as an indication

for successive stages of slab subduction and identified four distinct stages: (1) slab stagnant above the 660 discontinuity; (2) slab penetrating the 660 km discontinuity; (3) slab trapped in the uppermost lower mantle at a depth of 660-1000 km and (4) slab descending well into the deep lower mantle (Fig. 1.3, Fukao and Obayashi, 2013). Moreover, at least some slab segments appear to sink to the core-mantle boundary (Van der Hilst et al., 1997). As there is no velocity discontinuity in one-dimensional seismic models (Dziewonski and Anderson, 1981) nor known phase transition at ~ 1000 km depth, the reason for slab stagnation at this depth which may lead to the formation of chemically distinct reservoirs in Earth's deep mantle (Hofmann, 1997), is still unclear. A possible explanation of increasing viscosity in this region between 800 and 1200 km depth has been proposed (Marquardt and Miyagi, 2015; Rudolph et al., 2015), which would have to result from changes in the rheological properties of mantle minerals and rocks. A further possibility would be the attainment of neutral buoyancy between the slabs and the surrounding mantle. To evaluate either possibility requires a detailed understanding of the chemistry, defect structures and elastic properties of lower mantle minerals.

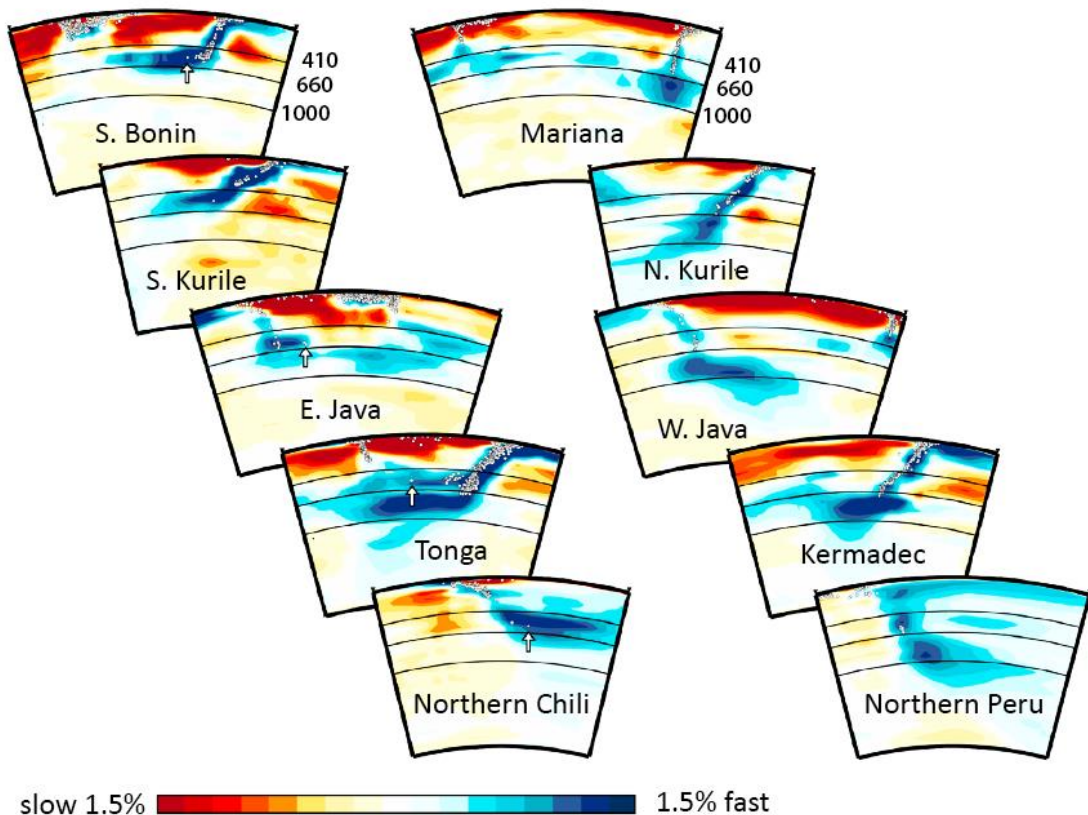


Figure 1.3 Seismic images of stagnant slabs in the transition zone (left) and of trapped slabs in the uppermost lower mantle (right) from five subduction zones. Each pair of the left and right images horizontally belongs to the same subduction zone (Modified from Fukao and Obayashi, 2013).

1.2 Chemical composition of the mantle

There are three main approaches which have been used to estimate the chemical composition of the upper mantle: (1) using analysis of primitive peridotites; (2) using mantle melt-residue relations; (3) using cosmochemical constraints.

The first approach makes use of petrological and geochemical analyses of tectonically exposed mantle rocks such as massif peridotites and ophiolite bodies, abyssal peridotites and xenoliths in kimberlites and alkali basalts. For example, Jagoutz et al. (1979) used the average composition of six seemingly fertile spinel lherzolite xenoliths (Fig. 1.4) which were believed to have experienced only very small degrees of partial melting. High pressure and high temperature experiments (Fujii and Scarfe, 1985; Hirose, 1997; Hirose and Kawamoto, 1995; Hirose and Kushiro, 1993) have shown that 10-30% partial melting of lherzolite is able to produce ordinary basaltic melts; lherzolites, therefore, represent a fertile bulk composition. By contrast, harzburgites or dunites represent the most melt-depleted refractory mantle bulk compositions (Fig. 1.4). Care must be taken to choose such primitive samples. On the one hand, most natural peridotites are depleted in incompatible elements to different extents, i.e. they have lower contents of CaO, Al₂O₃, Na₂O, etc. than the fertile mantle is expected to have (Palme and O'Neill, 2014). On the other hand, some peridotites with the highest CaO and Al₂O₃ may also not represent the pristine peridotite because they show evidence of metasomatism which may replenish incompatible elements after melt extraction (Palme and O'Neill, 2014). However, aside from a few inclusions in diamonds that may have a deeper origin, most mantle rock samples come from depths less than ~ 200 km, therefore studies on natural samples can constrain only the composition of the upper mantle. Isotope and trace element heterogeneities found in ocean island basalts (OIB), which are considered to derive from plumes rising from the Earth's lower mantle, have led geochemists to argue for an undepleted and undegassed reservoir as a result of limited

mass exchange between the lower and the upper mantle (Albarède and van der Hilst, 2002; Arevalo and McDonough, 2010; Jochum et al., 1983).

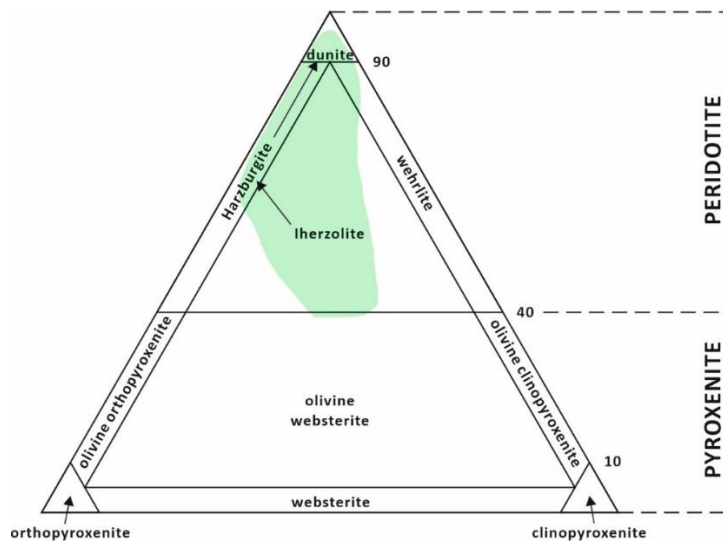


Figure 1.4 Mineralogical classification ternary diagram for peridotites and pyroxenites. Peridotite have > 40% olivine. The shaded field represents the range of values for most upper mantle peridotite samples. The arrows indicate the melting trend from Iherzolite (L) to harzburgite (H) to dunite (D) (Modified from McDonough and Rudnick, 1998).

Rather than directly using the chemical composition of natural samples, the second approach is based on melt-residue relations. Pyrolite, a theoretical model mantle composition conceived by Ringwood as the source rock for mid-oceanic ridge basalts (MORB), was constructed by mixing a mantle-derived magma (basaltic or komatiitic) with a refractory residue (harzburgite or dunite) in proportions so that the resultant model mantle would contain 3-4 wt.% CaO and Al₂O₃ and olivine of approximately Fo₈₉ composition (Ringwood, 1975; Sun, 1982). The term 'Pyrolite' refers, thus, to a model-dependent composition instead of a rock type and consists of a mineralogy dominated by olivine > pyroxene and capable of yielding basaltic magmas during partial melting. Whether this mineralogical model is also capable of describing the composition of the lower mantle is still a matter of debate. However, if the mantle convects and mixes as a single unit then the asthenospheric mantle that melts beneath ridges should have the same composition as the lower mantle.

The third approach consists of constructing compositional models based on chondritic meteorite compositions. Chondrite classification is based on bulk chemistry, oxygen isotopic composition, mineralogy, petrology and proportions of various chondritic components (Krot et al., 2014). Fourteen groups of chondrites have been recognized and thirteen of them comprise three major classes: carbonaceous (C), ordinary (O), and enstatite (E), each of which contains different groups. If we assume these chondrites to be the possible building blocks of the Earth, the mass ratio between the Earth's core and mantle as well as their chemical compositions could be calculated based on the bulk composition of these meteorites. CI carbonaceous chondrites may be the most suitable for this purpose as they are the most primitive chondritic meteorites having a composition which closely matches that of the solar photosphere (Allègre et al., 1995; Li and Fei, 2014; Lodders, 2003). Most meteorite-based Earth models assume that the refractory lithophile elements have chondritic ratios but models then differ in the way they consider major element abundances. Some models assume that the Earth has a bulk major element composition equal to that of CI carbonaceous chondrites or enstatite chondrites (Allègre et al., 1995; Javoy, 1995), whereas other models assume that the Earth is depleted in major elements (50% condensation temperature $T_c=1355-1250$ K) relative to the refractory lithophile elements ($T_c=1850-1355$ K) (McDonough and Sun, 1995; Palme and O'Neill, 2014). As Mg and Si are depleted in the upper mantle relative to refractory lithophile elements, when compared to all chondritic meteorites, the first class of models appeal either to a superchondritic Mg/Si ratio or to an additional reservoir of Si either in the core or lower mantle. Such models are, therefore, often cited as evidence that the lower mantle is chemically different from that of the upper mantle. The question of whether the lower mantle is isochemical with the upper mantle is therefore a complex issue which is still controversial. Some believe peridotitic or pyrolitic materials are dominant in the whole mantle (e.g. Ringwood, 1962), while others claim a more Fe and Si-rich lower mantle (e.g. Anderson, 1989; Hart and Zindler, 1986; Liu, 1982). Although it is difficult to unambiguously resolve such a controversy based on the current seismological observations and mineral-physics data (e.g. Bina, 2003; Mattern et al., 2005), most geophysical observations such as seismic velocities and electrical conductivity

measurements are in reasonable agreement with a pyrolitic whole mantle composition to a first approximation, although the uncertainties are currently very large. Indeed, seismic tomography supports ‘whole-mantle’ circulation with oceanic lithosphere subducted into the lower mantle and a return flow of upwelling plumes into the upper mantle (Bercovici and Karato, 2003). This evidence, however, does not exclude the possibility that the mass exchange between the upper and lower mantle has been only partial during the history of the Earth and that very deep regions of the lower mantle may have indeed a different composition (Ballmer et al., 2017; Kellogg et al., 1999).

Estimated bulk silicate Earth/upper mantle compositions from different studies using various methods are compared in Table 1.1, which show remarkable similarity to one another in major element concentrations. As mentioned above, models assuming similar bulk Earth major element concentrations with chondritic meteorites require a lower Fe and higher Si content for the lower mantle (Liu, 1982).

Table 1.1 Major element composition of pyrolite calculated by different studies.

	1	2	3	4	5	6	7	8	9	10	11 ^a	11 ^b
MgO	38.1	38.8	38.30	37.97	36.86	35.5	37.8	37.8	37.77	36.77	39.89	35.1
Al ₂ O ₃	3.3	4.4	3.97	4.30	4.11	4.75	4.06	4.45	4.09	4.49	3.30	3.8
SiO ₂	45.1	45.0	45.16	44.49	45.94	46.2	46.0	45.0	46.12	45.40	45.00	53.8
CaO	3.1	3.4	3.50	3.50	3.54	4.36	3.27	3.55	3.23	3.65	2.65	2.8
FeO	8.0	7.6	7.82	8.36	7.58	7.70		8.05	7.49	8.10	8.00	3.5
TiO ₂	0.2	0.17	0.217	0.22	0.18	0.23		0.201	0.18	0.21	0.15	0.15
Cr ₂ O ₃	0.4	0.45	0.46	0.44	0.46	0.43		0.384	0.38	0.37	0.44	0.39
NiO	0.2	0.26	0.27	0.25	0.27	0.23		0.25	0.25	0.24	0.09	0.08
MnO	0.15	0.11	0.13	0.14	0.13	0.13		0.135	0.15	0.14	0.13	0.12
Na ₂ O	0.4	0.4	0.33	0.39	0.39	0.40		0.36	0.36	0.35	0.33	0.3
K ₂ O		0.003	0.03					0.03	0.03	0.03	0.02	0.02
Total	98.95	100.59	100.12	100.06	99.46	99.93		100.21	100.05	99.75	100	100.1
Mg#	0.895	0.901	0.897	0.890	0.897	0.891		0.893	0.900	0.890	0.90	0.94

Notes: 1 Ringwood (1979); 2 Green (1979); 3 Jagoutz et al. (1979); 4 Sun (1982); 5 Wänke et al. (1984); 6 Palme and Nickel (1985); 7 Hart and Zindler (1986); 8 McDonough and Sun (1995); 9 Allègre et al. (1995); 10 Palme and O'Neill (2014); 11 Liu (1982). Mg#, molar Mg/(Mg+Fe). ^aupper mantle; ^bmore silica-rich lower mantle.

1.3 Mineralogy of pyrolite and subducted slab as a function of depth

Knowledge of the mineralogical composition of the mantle is essential for determining the velocity and density structure, which is required for the interpretation of geophysical data. Mineralogical models for the deep mantle are based on the results of high pressure and high temperature phase equilibria experiments performed as a function of pressure, temperature and bulk chemical composition. Such results can also be evaluated, supported and interpolated using thermodynamic modeling (Holland et al., 2013; Stixrude and Lithgow-Bertelloni, 2005, 2011). Moreover, it is not only important to determine the proportion of stable phases and phase transformations which dominate the structure and dynamics of the Earth. The element partitioning, which controls the chemical compositions of the individual minerals with varying pressures and temperatures, is also important in order to constrain the influence of mineral chemistry on the elastic properties of these materials.

1.3.1 Phase relations and phase transitions in pyrolite

The variation in mineral proportions of a pyrolitic bulk composition as a function of depth along the geotherm (Brown and Shankland, 1981) is shown in Fig. 1.5a. The topmost upper mantle consists of four main minerals-olivine $(\text{Mg,Fe})_2\text{SiO}_4$, orthopyroxene $(\text{Mg,Fe})_2\text{Si}_2\text{O}_6$, clinopyroxene $\text{Ca}(\text{Mg,Fe})\text{Si}_2\text{O}_6$ and an aluminous phase which varies with increasing pressure from plagioclase, to spinel or garnet (Frost, 2008). For the purpose of describing the phase transformations in pyrolite the assemblage can be divided into two parts: (1) the $(\text{Mg,Fe})_2\text{SiO}_4$ phase, which undergoes a series of phase transformations that occur over very narrow depth intervals and are each related to a seismic discontinuity; (2) the remaining Si- and Al- rich minerals, which undergo phase transformations over much boarder depth intervals.

At a depth of 410 km (~ 14 GPa), $(\text{Mg,Fe})_2\text{SiO}_4$ olivine (57 vol.%) transforms to

wadsleyite (also referred to as β -phase or modified spinel), marking the beginning of the transition zone. At ~ 17.5 GPa (520 km), wadsleyite transforms into ringwoodite (also referred to as γ -phase or silicate spinel), causing a weak seismic discontinuity observed only regionally. The discontinuity between the bottom of the transition zone and the top of the lower mantle occurs at ~ 24 GPa (660 km), where ringwoodite breaks down to an assemblage of bridgmanite $(\text{Mg,Fe})(\text{Si,Al})\text{O}_3$ and ferropericlase $(\text{Mg,Fe})\text{O}$.

Above 3 GPa the Si- and Al-rich phases are orthopyroxene (16 vol.%), clinopyroxene (14 vol.%) and garnet (13 vol.%). With increasing pressure, both orthopyroxene and clinopyroxene start to dissolve into garnet $(\text{Mg,Fe,Ca})_3\text{Al}_2\text{Si}_3\text{O}_{12}$ due to the substitution of Mg, Fe and Si onto the octahedral site initially occupied by Al. The substitution first decreases the proportion of orthopyroxene and then also that of clinopyroxene. As a result, the majoritic component, i.e. the Al-free garnet end member $(\text{Mg,Fe})_4\text{Si}_4\text{O}_{12}$, increases with pressure as more and more of the pyroxene components are incorporated into garnet. By mid-transition zone conditions, all pyroxene components are hosted by garnet with an approximate stoichiometry $(\text{Mg,Fe,Ca})_3(\text{Mg,Al,Si})_2\text{Si}_3\text{O}_{12}$ and the mineralogy of the pyrolitic mantle may be simply described by wadsleyite/ringwoodite + garnet. At pressures higher than 18 GPa, CaSiO_3 starts to exsolve from garnet, forming an additional calcium silicate perovskite phase. At depths greater than 660 km, garnets also undergo a phase transition into bridgmanite over a wider pressure range than that expected for the transformation of ringwoodite into bridgmanite and ferropericlase. The transformation of garnet gives rise to a gradual increase of the Al content of bridgmanite within the top 50 km of the lower mantle.

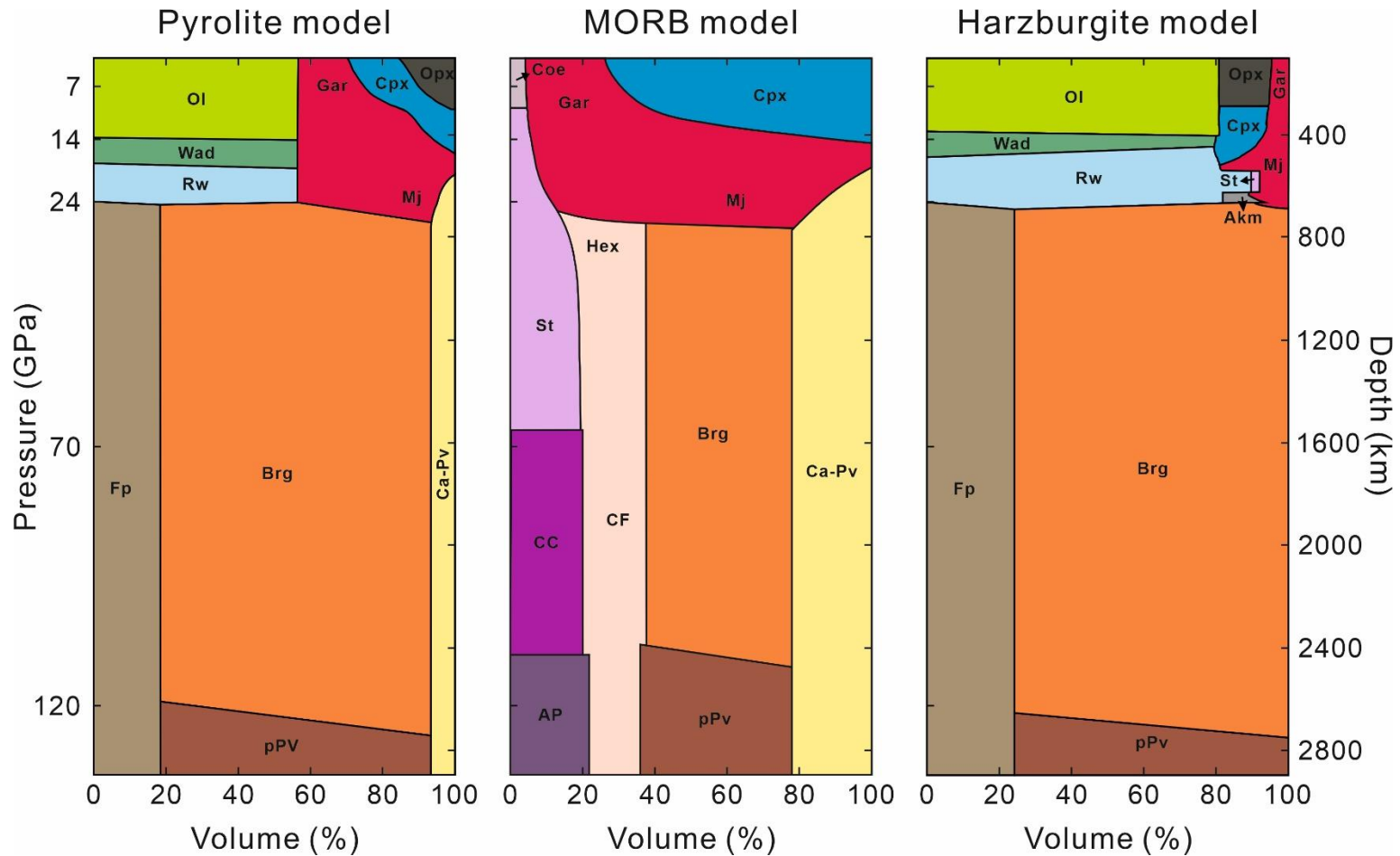


Figure 1.5 Mineral proportion changes in (a) Pyrolite, (b) MORB, and (c) harzburgite as a function of depths. Data modified from Akaogi (2007); Frost (2008); Hirose et al. (1999, 2005); Hunter et al. (2013); Irifune and Ringwood (1987a); Ono et al. (2001); Trønnes (2010) and Irifune and Tsuchiya (2015). Ol, olivine; Wad, wadsleyite; Rw, ringwoodite; Gar, garnet; Mj, majorite garnet; Cpx, clinopyroxene; Opx, orthopyroxene; Fp, ferropericlase; Brg, bridgmanite; Ca-Pv, calcium perovskite; pPv, post-perovskite; Coe, coesite; St, stishovite; Hex, hexagonal Al phase; Akm, akimotoite; CF, calcium-ferrite phase; CT, calcium-titanite phase; CC, CaCl₂ phase; AP, α -PbO₂ phase.

At depths of approximately 750 km a pyrolite composition assemblage comprises bridgmanite (75 vol.%), ferropericlase (18 vol.%) and calcium silicate perovskite (7 vol.%) (Irifune et al., 2010). This assemblage is stable throughout most of the lower mantle. Only at pressures corresponding to that of the top of the so-called D'' layer, does bridgmanite transform to a post-perovskite phase with the CaIrO_3 structure (Murakami et al., 2004). Moreover, a spin crossover of Fp was proposed to occur between 1700 km and 2700 km depth (Lin et al., 2013; Mao et al., 2011) and a high-spin to low-spin transition of Fe^{3+} on the B site of Brg was proposed to occur at approximately 15-50 GPa (see Lin et al., 2013 for a review), which may yield an additional density increase and affect the partitioning of iron between bridgmanite and ferropericlase.

1.3.2 Phase relations and phase transitions in subducted slabs

Subducting oceanic lithosphere shows marked vertical stratification and can be generalized as having a top thin layer (~ 1 km) of terrigenous and pelagic sediments, covering layers of basaltic-gabbroic oceanic crust of about 6 km thick overlying thicker layers (~ 50-100 km) of melt depleted harzburgite (5-20 km) and followed by more fertile lherzolite (Fig. 1.6). During subduction a significant section of the sedimentary layer may be scraped off the slab to form a fore-arc accretionary wedge. A thermal and rheological boundary layer must also form most likely within the less depleted lherzolite material to decouple the asthenospheric mantle from the subducting lithosphere. A slab approaching the 660 km seismic discontinuity can be reasonably simplified as comprising a basaltic crust (MORB) and underlying harzburgite rocks (Irifune and Tsuchiya, 2015). The compositions of harzburgite and MORB are different from pyrolite (Table 1.2), leading as a result to different mineralogies at high pressure and high temperature conditions corresponding to the Earth's mantle.

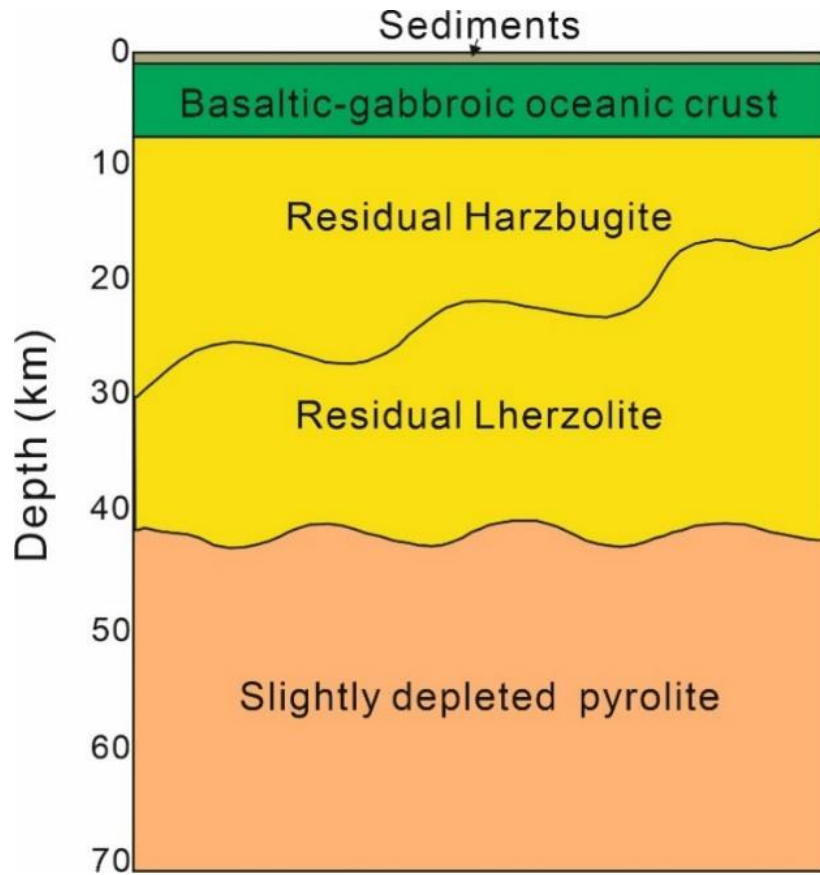


Figure 1.6 Schematic sections of the subducting oceanic lithosphere (modified from Ringwood, 1991).

Table 1.2 Representative chemical compositions of pyrolite, MORB and Harzburgite.

	Pyrolite	Harzburgite	MORB
SiO ₂	44.5	43.6	50.4
TiO ₂	0.2	-	0.6
Al ₂ O ₃	4.3	0.7	16.1
Cr ₂ O ₃	0.4	0.5	-
FeO	8.6	7.8	7.7
MgO	38.0	46.4	10.5
CaO	3.5	0.5	13.1
Na ₂ O	0.4	-	1.9
K ₂ O	0.1	-	0.1

Notes: Pyrolite, Sun (1982); Harzburgite, Michael and Bonatti (1985); MORB, Green (1979).

1.3.2.1 Harzburgite

Harzburgite, which represents the melt residue of lherzolite, is depleted in Al and Ca and enriched in Mg and thus it has a lower Fe/Mg ratio compared with pyrolite. As a result, harzburgite has a higher proportion of olivine with high magnesium number, Mg# ($=\text{Mg}/(\text{Mg}+\text{Fe})\times 100$) = ~ 92 and a smaller proportion of garnet and clinopyroxene. At the topmost part of the mantle, harzburgite consists of ~ 80 vol.% olivine, ~ 15 vol.% orthopyroxene and ~ 5 vol.% garnet. Thus, the mineralogy of harzburgite is dominated by the phase transformations in olivine described in section 1.3.1 and orthopyroxene. Orthopyroxene transforms to clinopyroxene at ~ 10 GPa and then into garnet at transition zone conditions. At ~ 19 - 22 GPa, ringwoodite (~ 89 vol.%) coexists with garnet (~ 8 vol.%) and a minor amount of stishovite (~ 3 vol.%). Due to the low Al content, the (Mg,Fe)SiO₃ pyroxene component is not able to be totally incorporated into garnet at high pressures, and an additional phase, akimotoite ((Mg,Fe)SiO₃ with an ilmenite-type structure) (~ 6 - 10 vol.%) coexists with ringwoodite (~ 82 vol.%) and majoritic garnet (~ 7 - 12 vol.%) at pressure above 22 GPa (~ 600 km) (Irifune and Ringwood, 1987a; Ringwood, 1991). This assemblage transforms to bridgmanite (~ 75 vol.%) plus ferropericlase (~ 25 vol.%) near the 660 km discontinuity (Irifune and Ringwood, 1987a; Ringwood, 1991). Because the transformation of akimotoite to bridgmanite occurs at lower pressures compared with ringwoodite, the bridgmanite stability field will be shifted to shallower depth compared to a pyrolitic composition (Irifune and Ringwood, 1987a). Although no experimental data is available at pressures higher than 26 GPa, the phase relations in harzburgite at lower mantle conditions can be inferred based on changes in the two constituent phases—bridgmanite and ferropericlase which have been extensively studied in other bulk compositions (Irifune and Tsuchiya, 2015). The mineral assemblages of harzburgite as a function of depth are shown in Figure 1.5c.

1.3.2.2 Mid-ocean ridge basalt (MORB)

Phase transitions in basaltic compositions as illustrated in Figure 1.5b are quite different from those expected in pyrolitic and harzburgitic compositions due to the higher Al, Ca and

Na and lower Mg contents. At the uppermost mantle conditions, MORB is comprised of clinopyroxene, garnet and an additional Si phase, i.e. coesite (~ 10 vol.%) (Irifune and Ringwood, 1987b, 1993). At pressures between 4-10 GPa, the relative proportions of garnet and pyroxene only change a little (<10 vol.%). Above 10 GPa, coesite transforms to stishovite (St) and Ca-rich clinopyroxene progressively dissolves into garnet (Irifune and Ringwood, 1987b, 1993). At transition zone conditions (14-15 GPa), Ca-rich clinopyroxene is entirely dissolved into garnet, forming a garnetite assemblage (majorite garnet+small amount of St) (Irifune and Ringwood, 1987b, 1993). CaSiO₃ perovskite (Ca-Pv) begins to exsolve from majorite (Mj) at ~ 20 GPa (Akaogi, 2007; Irifune and Ringwood, 1987b) and a mineral assemblage of Mj (~ 74 vol.%) +St (~ 10 vol.%) +Ca-Pv (~ 16 vol.%) is observed at 24 GPa (Hirose et al., 1999; Irifune and Ringwood, 1993). The assemblage progressively changes to an assemblage of bridgmanite (~ 40 vol.%), CaSiO₃ perovskite (~ 22 vol.%), stishovite (~ 20 vol.%) and an Al-rich phase (hexagonal or calcium-ferrite (CF)/ calcium-titanite (CT) structures, ~ 18 vol.%) over a wide pressure range from ~ 24 to 27 GPa (Akaogi, 2007; Hirose et al., 1999; Irifune and Ringwood, 1993; Irifune and Tsuchiya, 2015; Ono et al., 2001; Trønnes, 2010). Because only garnet is involved in the transformation to bridgmanite, the stability field of bridgmanite is shifted to greater depth compared with pyrolitic compositions. This assemblage of Brg+Ca-Pv+St+Al-phase is stable in the upper part of the lower mantle. Stishovite transforms to a CaCl₂-type structure at 62 GPa (~ 1500 km) (Hirose et al., 2005; Ono et al., 2002) which further transforms to α -PbO₂-type structure at ~ 120 GPa (~ 2600 km) (Hirose et al., 2005; Murakami et al., 2003). The most abundant mineral, bridgmanite, then undergoes the phase transition to the CaIrO₃-type post-perovskite phase above 110 GPa at 2500 K (Hirose et al., 2005).

When the oceanic lithosphere subducts into the mantle, a density contrast between MORB and the surrounding pyrolite, due to their different mineralogy, is expected. At transition zone conditions, the garnetite facies of MORB consisting of majorite, stishovite and CaSiO₃ perovskite, are denser than the mineral assemblage of the surrounding pyrolite mantle. However, a density crossover is expected to occur at 660-720 km depth due to the slow garnet to bridgmanite phase transition. Therefore, the oceanic crust may be

gravitationally trapped at this depth. Nevertheless, MORB will be denser than pyrolite at depths greater than ~ 720 km and throughout almost the entire region of the lower mantle once bridgmanite and Ca perovskite are formed. As a result, if slabs accumulate to a sufficient thickness at the top of the lower mantle, they may have the chance to sink into the deeper lower mantle (Akaogi, 2007; Hirose et al., 1999).

Due to the slow solid-state homogenization processes in the mantle, equilibration between cold subducted slabs and the surrounding mantle is only expected to occur at lengths scales of the order of meters (Holzapfel et al., 2005). Therefore, the mantle may be a disequilibrium mechanical mixture of different rock types with varying length scales. In fact, geophysical observations have confirmed the existence of small-scale heterogeneities in the mantle that scatter seismic waves, which may be attributed to recycled oceanic crust based on the size of the scatter (Frost, 2008; Kaneshima and Helffrich, 1999, 2003; Vinnik et al., 2001). Moreover, the cold subducting slabs are also far from being in thermal equilibrium with the surrounding mantle although the temperature difference may decrease with depth. The unique chemical compositions and temperature of the subducted oceanic lithosphere would give rise to distinct seismic velocities and transport properties compared to the surrounding pyrolite mantle, which may have considerable geodynamic significance.

1.4 Bridgmanite in the lower mantle

Although the composition of Earth's lower mantle is still poorly constrained, bridgmanite $(\text{Mg,Fe})(\text{Si,Al})\text{O}_3$, formed from both the primary pyrolite mineral ringwoodite and the secondary mineral majorite garnet in the transition zone, is widely thought to be the dominant phase of this region. Bridgmanite dominated by the MgSiO_3 component is stable over a wide range of depths from 660 km to several hundred kilometers above the core-mantle boundary (~ 2700 km) and as such its physical properties are primarily responsible for the seismic and transport properties of this region.

1.4.1 Proportions of bridgmanite in different bulk compositions

As described in section 1.3.1 and 1.3.2, the proportions of bridgmanite and other lower mantle minerals depend on the assumed composition of the mantle. For a most exhaustive comparison, average compositions reported in the literature for different chondritic meteorites (Wasson and Kallemeyn, 1988) have been used to derive mineral proportions at conditions of the lower mantle. To this end, only the major elements of the chondritic compositions have been considered and the following assumptions have been used to calculate the oxides wt.% reported in Table 1.3 following a minimization procedure: (1) highly volatile elements like C, H, N as well as the moderately volatile S were neglected; (2) The core was assumed to consist exclusively of Fe and Ni, with the total amount of Ni partitioning completely into the core; (3) The Fe content of the mantle has been fixed at 6.2 atomic wt.% according to the value accepted for the upper mantle of the Earth. This resulted in a value of 7.98 wt.% of FeO for all chondritic compositions; (4) the oxygen content was calculated in order to obtain a final mantle composition expressed in oxide wt.% (Table 1.3) close to 100%. From these compositions it was then possible to calculate the mineral proportions; partitioning all elements between bridgmanite and ferropericlase according to the experimental compositions reported by Irifune et al. (2010) at 36.4 GPa and 1973 K, and assuming both CaSiO_3 perovskite and stishovite SiO_2 to be pure end-members (Table 1.3). Although these calculations are only a crude approximation, the trend obtained for different chondrite compositions shows that bridgmanite is always the most abundant phase in the lower mantle, that CaSiO_3 perovskite amount is pretty constant among all chondritic compositions. Only Carbonaceous chondrites would form ferriopericlase in the lower mantle whereas enstatite chondrites produce a lower mantle containing an excess SiO_2 phase. A number of studies have proposed such meteorite based mantle models for the bulk silicate Earth (Fitoussi et al., 2016; Javoy et al., 2010). If suitable mineral models and elasticity data were available, the extent to which these different mantle compositions fit lower mantle seismic velocities could be evaluated.

Table 1.3 Calculated mantle compositions, lower mantle mineral proportions for different chondrite compositions. The lower mantle mineral proportion calculated from pyrolite composition from McDonough and Sun (1995) is also shown for comparison.

	Pyrolite	Carbonaceous chondrite				Ordinary chondrite			Enstatite chondrite	
		CI	CM	CO	CV	H	L	LL	EH	EL
Mantle compositions (wt.%)										
SiO ₂	45.00	48.37	48.36	48.44	47.30	50.96	51.61	51.69	56.48	53.56
TiO ₂	0.20	0.16	0.17	0.19	0.23	0.14	0.14	0.13	0.12	0.13
Cr ₂ O ₃	0.38	0.82	0.78	0.74	0.75	0.75	0.74	0.70	0.73	0.60
Al ₂ O ₃	4.45	3.45	3.91	3.85	4.69	3.01	3.01	2.87	2.42	2.67
FeO	8.05	7.98	7.98	7.98	7.98	7.98	7.98	7.98	7.98	7.98
MgO	37.80	33.97	34.00	34.24	34.08	32.72	32.22	32.44	27.79	31.47
CaO	3.55	2.75	3.11	3.15	3.77	2.46	2.39	2.33	1.88	1.90
Na ₂ O	0.36	1.46	0.97	0.79	0.63	1.22	1.23	1.21	1.45	1.05
MnO	0.14	0.53	0.38	0.30	0.27	0.42	0.43	0.43	0.45	0.28
P ₂ O ₅	0.02	0.53	0.36	0.34	0.32	0.35	0.28	0.25	0.72	0.36
Total	99.95	100.02	100.01	100.00	100.01	100.01	100.03	100.02	100.01	100.02
Lower mantle mineral proportions (%)										
Brg	80	89	88	88	85	96	96	96	87	93
Fp	13	6	7	6	9					
Ca-Pv	6	5	5	5	7	4	4	4	3	3
SiO ₂									10	4

1.4.2 Bridgmanite structure

MgSiO₃ bridgmanite has a perovskite-type structure with an orthorhombic distortion and space group *Pbnm* (Horiuchi et al., 1987). It consists of a three-dimensional framework of tilted corner-linked SiO₆ octahedra (B site) forming cavities in the shape of bicapped trigonal prisms (A site) occupied by Mg. This orthorhombic structure derives from an ideal cubic structure (Space group *Pm $\bar{3}$ m*) through in-phase and out-of-phase tilting of the SiO₆ octahedra in addition to cation displacements at the A site due to the relatively small Mg²⁺ ion (e.g. Glazer, 1972; Howard and Stokes, 1998, 2005) (see Fig. 1.7). Compared with the aristotype structure, four of the Mg-O bonds are lengthened and the remaining eight are

shortened (Fiquet et al., 2000; Ross and Hazen, 1990). This distortion increases with pressure and eventually leads to a phase transition into “post-perovskite” above 120 GPa (Murakami et al., 2004).

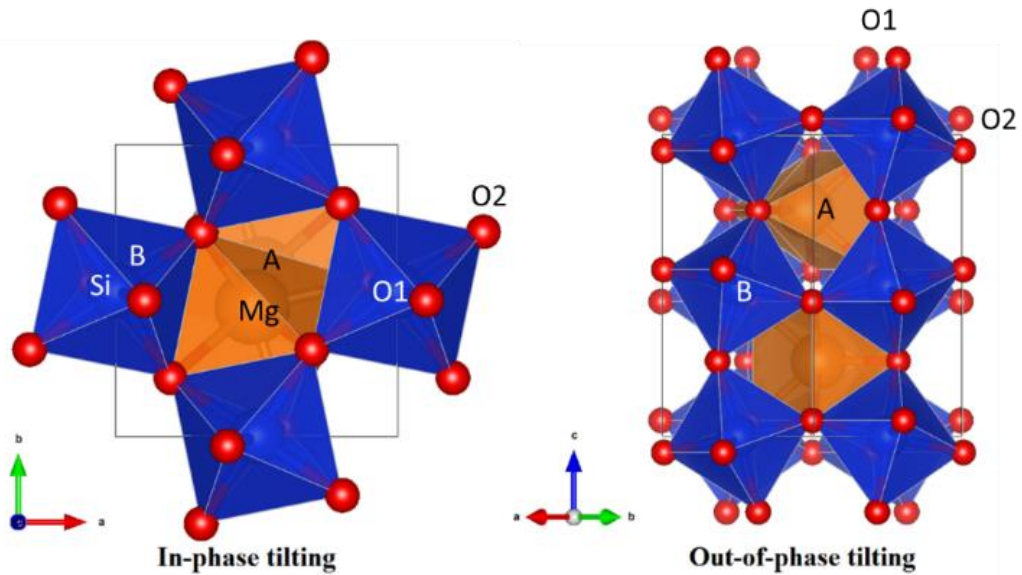


Figure 1.7 Structural model of MgSiO₃ bridgmanite consisting of two cation sites. The A site is occupied by Mg (orange) and the octahedral B site is occupied by Si (blue). The orthorhombic distortion of the perovskite-like structure is due to the in-phase and out-of-phase tilting of the octahedral framework.

1.4.3 Composition of bridgmanite

High-pressure and high-temperature experiments indicate that bridgmanite can accommodate a substantial amount of Fe and Al (Frost and Langenhorst, 2002; Lauterbach et al., 2000). For a pyrolitic mantle composition, bridgmanite incorporates most of the Al and much of the Fe (Irifune, 1994; Irifune et al., 2010), with a nominal FeO content of ~ 6-7 wt.% and Al₂O₃ content of ~ 4-5 wt.% at the top lower mantle. The Al₂O₃ content increases gradually from 1 wt.% to 4-5 wt.% over the first 50 km of the lower mantle due to the transformation of majoritic garnet, the main host for Al in the upper mantle and transition zone. The Fe content will also vary as a result of the effect of pressure on the partitioning of Fe between bridgmanite and coexisting ferropericlase, which may be further influenced by an electronic spin transition of FeO in ferropericlase at pressures between 70-125 GPa (Lin

et al., 2013; Mao et al., 2011). Harzburgite has a lower Al content than pyrolite, due to melt extraction beneath ridges, thus bridgmanite in harzburgitic compositions has an Al_2O_3 content of only 1-2 wt.%; on the contrary, MORB is enriched in Al while depleted in Mg, thus bridgmanite in a MORB composition has an extremely high Al_2O_3 and Fe_2O_3 content of ~ 16 wt.% and ~ 23 wt.%, respectively (Hirose et al., 1999; Hirose et al., 2005; Irifune and Ringwood, 1987b). Therefore, although bridgmanite in Earth's lower mantle has a nominal Al and Fe content of ~ 0.1 atoms per formula unit (pfu), such content may vary between 0 to 0.40 atoms pfu due to the presence of chemical heterogeneities that may arise either from the subduction of oceanic lithosphere or the presence of primordial material (Kellogg et al., 1999). Cation substitutions in bridgmanite may strongly influence the behavior of MgSiO_3 bridgmanite such as density and elastic properties in Earth's lower mantle.

1.4.4 Substitution mechanisms in bridgmanite

Although iron exists predominantly as Fe^{2+} in the upper mantle and transition zone, significant amounts of Fe^{3+} have been identified in bridgmanite ($\text{Fe}^{3+}/\Sigma\text{Fe} = \sim 16\%$ without Al and $\sim 50-75\%$ with Al), even when in equilibrium with Fe metal (Frost et al., 2004; Lauterbach et al., 2000; McCammon, 1997). The abundance of Fe^{3+} appears to depend on the Al content of bridgmanite and arises from the unusual crystal chemistry of silicate perovskite (McCammon, 2005). The higher Fe^{3+} content seemingly required in the lower mantle relative to the upper mantle could be explained in an isochemical mantle if the disproportionation of Fe^{2+} ($2\text{Fe}^{2+} \rightarrow \text{Fe}^{3+} + \text{Fe}^0$) occurs. This expansion in the stabilization of Fe^{3+} is induced by the coupled substitution in bridgmanite of $\text{Fe}^{3+} + \text{Al}^{3+}$ replacing $\text{Mg} + \text{Si}$. This results in a rather complex crystal chemistry of lower mantle bridgmanite as a result of the different possible substitution mechanisms.

Ferrous iron, Fe^{2+} , incorporates into the bridgmanite structure through the substitution of Mg^{2+} on the A site creating compositions along the $\text{MgSiO}_3\text{-FeSiO}_3$ join (Andrault et al., 1998; Lauterbach et al., 2000; McCammon et al., 1992). For the incorporation of trivalent cations M^{3+} ($\text{M}^{3+} = \text{Fe}^{3+}$ or Al^{3+}) into bridgmanite at least two mechanisms need to be taken into account. One is a charge-coupled substitution (CCS) forming compositions along the

MgSiO₃-M₂O₃ join:



where two trivalent cations substitute for Mg at the A site and Si at the B site, maintaining electrical neutrality without the formation of vacancies (here the superscripts \cdot and \prime represent a positive or negative net charge on the site, respectively and X indicates no charge). This reaction is analogous to the substitution of aluminum for tetrahedral silicon and octahedral magnesium along the diopside-Ca-Tschermak's pyroxene join, CaMgSi₂O₆-CaAlAlSiO₆, therefore it also is referred to as stoichiometric or Tschermakitic substitution (Navrotsky et al., 2003). Although Fe³⁺ and Al may occupy both cation sites in bridgmanite, there is some evidence that in the presence of Al, Fe³⁺ preferentially occupy the A site (McCammon et al., 2013).

The other mechanism is oxygen vacancy substitution (OVS) along the MgSiO₃-MgMO_{2.5} join



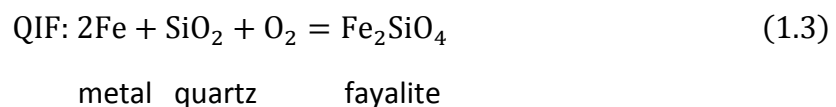
where trivalent cations only replace Si⁴⁺ at the B site and oxygen vacancies are required for charge balance ($\text{V}_{\text{O}}^{\cdot\cdot}$ is an oxygen vacancy). This mechanism is analogous to the formation of defect perovskites along the CaTiO₃ perovskite-CaFeO_{2.5} brownmillerite join (Becerro et al., 1999), thus it also is referred to as nonstoichiometric, defect, or brownmilleritic substitution. Most low-pressure ceramic perovskites incorporate trivalent cations according to this second mechanism (Navrotsky, 1999) and this also may be an important mechanism in the Earth's lower mantle, which contains ferropericlase coexisting with bridgmanite and thus buffers low SiO₂ activity favouring Mg/Si > 1. The oxygen vacancies created by this substitution mechanism are of particular interest since they may provide a way of incorporating water into the dense structure of bridgmanite (Murakami et al., 2002; Navrotsky et al., 2003) and may affect the diffusivity, conductivity, compressibility and creep rate of the mantle.

1.4.5 Spin transition of bridgmanite

Fe^{2+} and Fe^{3+} in bridgmanite exist in the high-spin state under ambient conditions (e.g. McCammon, 2006). For Fe^{2+} , it is still under debate whether the abnormal increase in quadrupole splitting of Fe^{2+} at the A site of bridgmanite at high pressures is related to a high-spin (HS) to intermediate-spin (IS) transition or enhanced lattice distortion of the A site (Hsu et al., 2010; Lin et al., 2012; Lin et al., 2013; McCammon et al., 2008). On the other hand, there is general consensus that Fe^{3+} at the A site remains in the high-spin state to at least 100 GPa (Catalli et al., 2011; 2010; Fujino et al., 2012; Glazyrin et al., 2014; Kupenko et al., 2014; Lin et al., 2012; Potapkin et al., 2013) and only Fe^{3+} at the B site undergoes a spin crossover from high-spin to low-spin at about 30 to 60 GPa (Catalli et al., 2011; 2010; Fujino et al., 2012; Kupenko et al., 2015; Lin et al., 2012; Liu et al., 2018a; Mao et al., 2015). The spin transition pressure of Fe^{3+} is positively related to the Fe^{3+} content. Knowledge of the Fe^{3+} distribution among the two structural sites of the bridgmanite structure is therefore important in order to assess whether its spin state may influence the elastic properties of bridgmanite or whether it may be invisible to seismic observations.

1.5 Oxygen fugacity of Earth's mantle

Oxygen fugacity (f_{O_2}) is the effective partial pressure of oxygen in a particular environment and was first used in petrology by Eugster (1957) when developing oxygen buffers to control the oxidation potential in experimental runs. In this method, oxygen fugacity is imposed upon the system by redox reactions in the surrounding oxygen buffers, i.e. oxygen controlling equilibria. The well-known end-member reactions extensively used in petrology to define planes of increasing f_{O_2} in oxygen fugacity-pressure-temperature (P - T - f_{O_2}) space (Fig. 1.8) are (Frost, 1991; Wood et al., 1990):

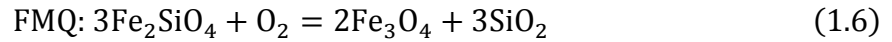




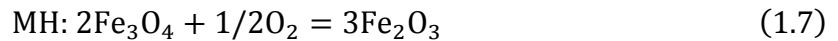
metal wustite



wustite magnetite



fayalite magnetite quartz



magnetite hematite

For pure end-member phases, the stability field of the three oxidation states of iron (Fe^0 , Fe^{2+} , and Fe^{3+}) are well-defined in the P - T - f_{O_2} space by these reaction curves (Fig. 1.8). For example, in the Fe-O-SiO₂ system, the stability field of Fe^{2+} -bearing assemblages are limited by the reactions FMQ and QIF. Therefore, oxygen fugacity is a variable that determines the valence state of iron in a particular phase for a given set of conditions. In the mantle, however, although Fe^{2+} is dominant in the peridotitic upper mantle, it does not constrain f_{O_2} closely because the stability of Fe^{2+} in the f_{O_2} space is largely expanded due to the solution of Mg into iron silicates.

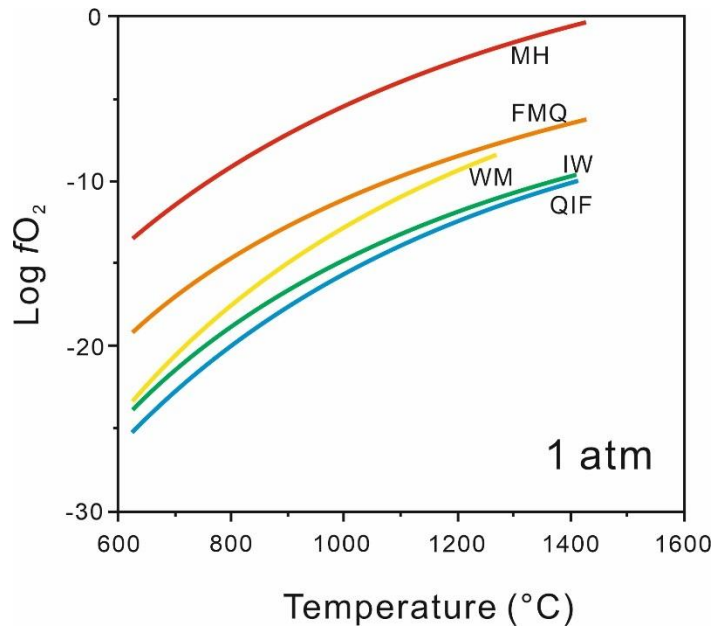


Figure 1.8 Log oxygen fugacity corresponding to the buffer equilibria (Eq. 1.3-1.7) plotted against the temperature at 1 bar. The acronyms are the same as explained in the text (modified from Wood et al., 1990).

In natural systems, oxygen fugacity, rather than a fixed parameter imposed upon a rock by the environment, is controlled by multicomponent equilibria reactions that happen during rock formation process and varies to accommodate the change of mineral compositions (Frost, 1991). The oxygen fugacities recorded by natural assemblages can be determined using conditions of equilibrium based on equilibria (1.3) -(1.7) given above. For example, the oxygen fugacity of a mineral assemblage could be calculated by equilibrium (1.6) according to:

$$\log f_{O_2} = \frac{\Delta G_{(1.6)}^0}{\ln(10)RT} + 2\log a_{Fe_3O_4} + 3\log a_{SiO_2} - 3\log a_{Fe_2SiO_4} \quad (1.8)$$

where $\Delta G_{(1.6)}^0$ is the standard state (pure end-members at the pressure and temperature of interest) Gibbs free energy change of equilibrium (1.6), R is the gas constant, a_i is the activity of component i in the corresponding phase j . In the case of pure end-member phases, the activity is 1 for each phase while in the case of solid solution, the activity could be expressed by

$$a_i^j = x_i^j \times \gamma_i^j \quad (1.9)$$

where x_i^j is the mole fraction of component i in phase j and γ_i^j is the activity coefficient which is 1 in the case of ideal mixing between sites and in the case of a symmetrical regular solution, γ_i^j maybe obtained from:

$$RT \ln \gamma_i^j = (1 - x_i^j)^2 W_G \quad (1.10)$$

where W_G is the interchange energy or interaction parameter called Margules parameter representing the interchange energy between cations (Wood and Fraser, 1977).

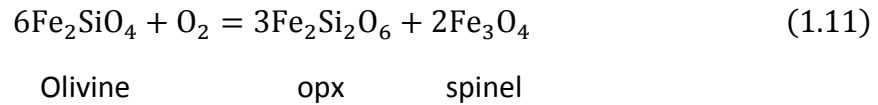
As shown in Fig. 1.8, the oxygen fugacity of all buffers changes dramatically with temperature, therefore the oxygen fugacities are usually normalized to a given buffer to remove the effect of temperature from the buffer curves. For natural assemblages in the mantle, FMQ is commonly used and the oxygen fugacity compared with FMQ buffer is denoted by Δ FMQ. For the current study, IW buffer was used for the normalization.

1.5.1 Upper mantle oxygen fugacity

The upper mantle oxygen fugacity has been evaluated by studying the distribution of $Fe^{3+}/\Sigma Fe$ ratio in peridotites, and in MORB and OIB. In particular, MORB and OIB show a narrow range of $Fe^{3+}/\Sigma Fe$ between 8%-15% with an average value of 12%, giving an oxygen fugacity (f_{O_2}) of 0.4 log units below the FMQ buffer at ambient conditions and \sim FMQ at its mantle source region. Abyssal peridotites, considered to be the MORB mantle residues, display a more reduced value between FMQ and FMQ-2.5. Comparison of V/Sc ratio of peridotites and basalts between samples from the Archean and those from present days indicates that the oxygen fugacity almost did not change over the last 3.5 billion years (Gyrs).

Spinel peridotite xenoliths, that formed at depths between 30 and 60 km, contain 0.1-0.3 wt.% Fe_2O_3 in the whole rock which corresponds to a $Fe^{3+}/\Sigma Fe$ ratio of between 1% and 3% (Canil and O'Neill, 1996; Woodland et al., 2006). Spinel itself has the highest $Fe^{3+}/\Sigma Fe$ ratio which ranges between 15 wt.% and 34 wt.%; in contrast, the dominant mineral olivine

contains negligible Fe_2O_3 (Canil and O'Neill, 1996). The oxygen fugacity in spinel peridotites can be calculated using the equilibrium



The measured oxygen fugacity for the spinel peridotite facies from different localities and settings vary significantly between -3 and +2 log units with respect to the FMQ buffer as shown in Fig. 1.9, reflecting some degree of heterogeneity of the mantle as a result of different processes such as partial melting and metasomatism. Abyssal peridotites and some massif peridotites record the lowest f_{O_2} , with a mean value 1 log unit below MORB at its source while other massif peridotites and xenoliths are more oxidized which may be attributed to metasomatism processes. The most oxidized samples are xenoliths from subduction zones where the mantle reacts with hydrous fluids (Frost and McCammon, 2008).

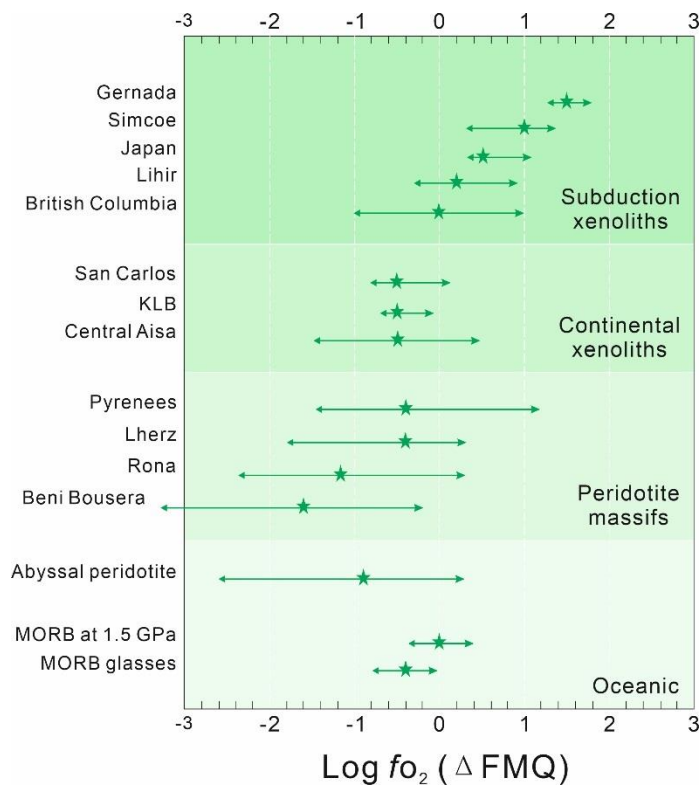
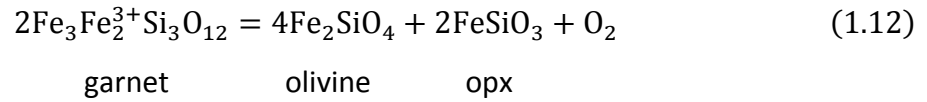


Figure 1.9 Calculated Oxygen fugacity ranges for spinel peridotites from different geological settings. The stars represent the mean values (modified from Frost and McCammon, 2008).

The redox state of the mantle at depths greater than 60 km is recorded by garnet peridotite xenoliths from kimberlite magmas (Luth et al., 1990). Garnet peridotites show similar whole rock Fe₂O₃ contents as spinel peridotites and the Fe³⁺/ΣFe in garnet varies between 2% and 14% (Canil and O'Neill, 1996). The Fe³⁺/ΣFe in garnet increases with depth due to the preferred partitioning of Fe³⁺ into garnet compared with pyroxene with increasing temperature, while the Fe₂O₃ content of the whole rock remains generally constant (Canil and O'Neill, 1996; Woodland and Koch, 2003). The oxygen fugacity recorded by garnet peridotites can be calculated using the equilibrium (Gudmundsson and Wood, 1995),



according to the equation,

$$\log f_{\text{O}_2} = \frac{-\Delta G_r^0}{\ln(10) RT} + 2 \log a_{\text{Fe}_3\text{Fe}_2\text{Si}_3\text{O}_{12}}^{\text{Gar}} - 2 \log a_{\text{FeSiO}_3}^{\text{opx}} - 4 \log a_{\text{Fe}_2\text{SiO}_4}^{\text{olivine}} \quad (1.13)$$

The calculated oxygen fugacity relative to FMQ for garnet peridotite rocks from Kaapvall cratonic lithosphere are plotted in Fig. 1.10 as a function of pressure, showing a general trend of decreasing f_{O_2} with depth from +5 log units at ~ 2 GPa to +0.5 log units at ~ 7 GPa relative to IW (Frost and McCammon, 2008; Luth et al., 1990; McCammon et al., 2001; Woodland and Koch, 2003). In fact, this decrease of f_{O_2} with pressure is not related to composition. Instead, it can be totally attributed to the positive volume change of Eq. (1.12) which means that increasing pressure stabilizes the Fe₃Fe₂³⁺Si₃O₁₂ skiaegitic garnet component (Gudmundsson and Wood, 1995).

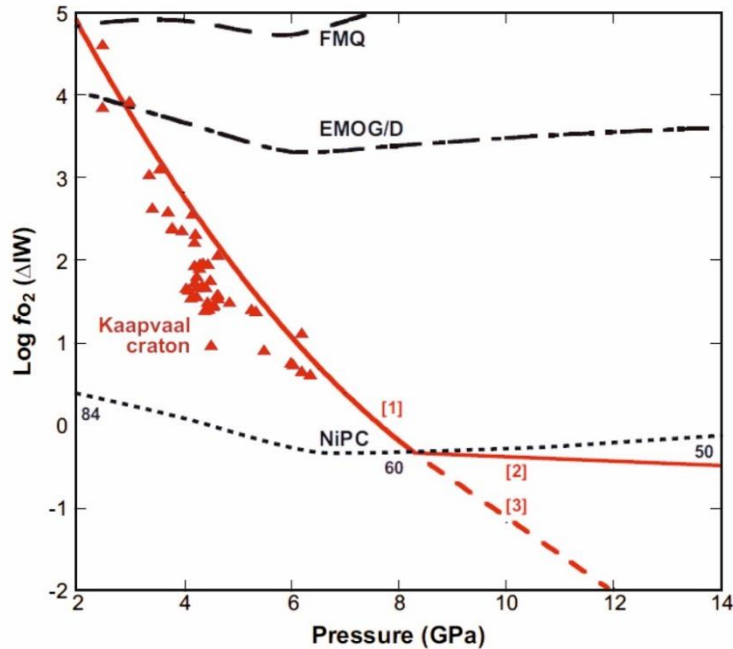


Figure 1.10 Oxygen fugacity in the upper mantle calculated for a four-phases garnet peridotite assemblage assuming a value of $\text{Fe}^{3+}/\Sigma\text{Fe}=2\%$ along a cratonic geotherm relative to the IW buffer. The solid triangles are xenoliths from Kaapvaal craton lithosphere. The blue dashed line is the calculated Ni precipitation curve (NiPC) for a peridotite assemblage with values indicating the Ni content (mol%) in the precipitating metal. Line 1 and line 2 are the f_{O_2} calculated for garnet peridotite before and after crossing the NiPC respectively. Line 3 is the metastable extrapolation assuming no metal precipitation. The figure has been modified from Frost and McCammon (2008) in which the details for the calculation were described.

1.5.2 Deep upper mantle and transition zone oxygen fugacity

Due to the lack of natural samples from depths below 200 km (6 GPa), a model of the mantle oxygen fugacity as a function of depth was estimated by Frost and McCammon (2008) for a bulk silicate Earth (BSE, McDonough and Sun, 1995) composition assuming a constant bulk O/Fe ratio. The model was calculated along a continental geotherm and shows a general trend of decreasing f_{O_2} with pressure, which agrees generally with value calculated from natural garnet peridotite xenoliths (Fig. 1.10). This decrease is induced by the positive volume change of Eq. (1.12) as discussed above as well as by the dilution of the $\text{Fe}_3\text{Fe}_2^{3+}\text{Si}_3\text{O}_{12}$ skiaigite component in garnet due to the increase of the $\text{Mg}_4\text{Si}_4\text{O}_{12}$ majoritic component arising from the pyroxene-garnet transition. The oxygen fugacity is about 5 log

units above the iron-wüstite (IW) buffer at ~ 2 GPa but decreases continuously, and is projected to meet the Ni precipitation curve (NiPC, O'Neill and Wall, 1987) at about 8 GPa and 250 km depth, which is slightly below the IW buffer. As Ni-Fe metal precipitates, the oxygen fugacity deviates from that calculated assuming no metal precipitation and continues to decrease only slightly with depth, reaching a value of \sim IW-0.3 at the bottom of the upper mantle (~ 14 GPa) where about 0.1-0.2 wt.% metal would form (Fig. 1.10, Frost and McCammon, 2008).

In the transition zone, olivine transforms to wadsleyite and ringwoodite which can have a $\text{Fe}^{3+}/\Sigma\text{Fe}$ content $\sim 2\%$ when in equilibrium with Fe metal. Since majorite garnet with $\text{Fe}/(\text{Fe}+\text{Mg})=0.15$ can contain $\sim 7\%$ $\text{Fe}^{3+}/\Sigma\text{Fe}$ when in equilibrium with Fe metal at transition zone conditions (O'Neill et al., 1993a; O'Neill et al., 1993b), the minimum bulk $\text{Fe}^{3+}/\Sigma\text{Fe}$ ratio is $\sim 3\%$ for transition zone pyrolite, which is larger than the 2% expected for the pristine mantle; requiring precipitation of ~ 0.1 wt.% Fe-Ni metal therefore a similar f_{O_2} as the base of the upper mantle (IW-0.3) (Frost and McCammon, 2008).

1.5.3 Oxygen fugacity in the lower mantle

The dominant mineral of the lower mantle, bridgmanite, has a strong preference for Fe_2O_3 , which can be incorporated into its structure in large proportions ($\text{Fe}^{3+}/\Sigma\text{Fe}$ ratio as high as 0.6) (Frost and Langenhorst, 2002; Lauterbach et al., 2000; McCammon et al., 2004b) at typical mantle Al_2O_3 contents even at very reducing conditions. If the lower mantle has the same bulk O/Fe ratio as that of the upper mantle, Fe^{2+} likely disproportionates to produce the high Fe_2O_3 content present in bridgmanite. For example, Frost et al. (2004) have shown that ~ 1 wt.% metal with a composition approximately 88 wt.% Fe, 10 wt.% Ni and 1 wt.% S would be produced by disproportionation in a BSE lower mantle composition. The oxygen fugacity in the lower mantle would be well buffered by the metal and was calculated to be between IW and IW-1.5 based on the composition of coexisting metal and ferropericlasite (Frost and McCammon, 2008).

The oxygen fugacity in the Earth's interior is a key parameter controlling the reactions and dynamic processes within the mantle and between the mantle and the surface. For example, the oxidation state of the mantle governs the speciation of the C-H-O volatiles present (Frost and McCammon, 2008; Wood et al., 1990), the form of which would in turn influence the mantle solidus and the composition of liquids, playing an important role in magma genesis, metasomatism and mantle degassing processes (Rohrbach and Schmidt, 2011; Stagno et al., 2013). In addition, the valence and electronic states of Fe, Earth's most abundant transition metal, also depend on the redox state of the mantle which may have important effects on mantle seismic velocities, rheology, transport properties and chemical reactions. If a significant proportion of the iron in bridgmanite is Fe³⁺ then this may also influence the elastic properties and the velocities of seismic waves in the lower mantle (Boffa Ballaran et al., 2012; Mao et al., 2015).

1.6 Aim of this study

The Earth's lower mantle consists mainly of bridgmanite with lesser amounts of ferropericlase and CaSiO₃ perovskite. Although the pyrolite model for the composition of the mantle is widely accepted for Earth's upper mantle, it is still not clear whether it is also representative for the lower mantle (Xu et al., 2008). The conclusions from previous studies based on comparisons between sound velocity measurements for lower-mantle minerals under high pressure and high temperature conditions and seismological observations are contradictory (Kurnosov et al., 2017; Murakami et al., 2012). The elasticity and seismic velocities of both bridgmanite and ferropericlase are strongly dependent on the chemical composition of the phases, especially the Fe content and its valence state (Fan et al., 2019; Mao et al., 2017). Therefore, to make a reliable comparison, it is important to know the compositions of each phase under lower mantle conditions. While ferric iron appears to partition favorably into bridgmanite, ferrous iron is more strongly partitioned into ferropericlase (Frost and Langenhorst, 2002; Lauterbach et al., 2000; McCammon et al., 2004b; McCammon et al., 1998; Nakajima et al., 2012). As a result, knowledge of the

oxidation state of iron in Brg is necessary in order to constrain how Fe partitions between Brg and Fp. The valence state and structural position of iron in Brg will also have an effect on whether a spin transition of iron would occur under lower mantle pressure and temperature conditions (Hsu et al., 2011; Kuppenko et al., 2014; 2012; Lin et al., 2013; Mao et al., 2015; McCammon et al., 2010) and may also influence lower mantle elasticity, rheology and transport properties (Boffa Ballaran et al., 2012; Holzapfel et al., 2005; Reichmann et al., 2000; Xu et al., 1998). In spite of the importance mentioned above, the $\text{Fe}^{3+}/\Sigma\text{Fe}$ in Brg at lower mantle conditions is poorly constrained. As can be seen in Fig. 1.11, results on $\text{Fe}^{3+}/\Sigma\text{Fe}$ in Brg and Fe partitioning between Brg and Fp as a function of pressure obtained by different diamond anvil cell (DAC) studies show hardly any agreement (Piet et al., 2016; Prescher et al., 2014; Shim et al., 2017; Sinmyo et al., 2011). Experiments on Brg at deep lower mantle conditions are extremely challenging considering the large thermal gradients, the difficulty in precise pressure calibration and control of oxygen fugacity within laser-heated DAC experiments. However, even in multi-anvil studies at uppermost lower mantle conditions, the $\text{Fe}^{3+}/\Sigma\text{Fe}$ ratios reported vary over a wide range between 30% and 80% (Fig. 1.11a) (Frost et al., 2004; Irifune et al., 2010; Lauterbach et al., 2000; McCammon, 1997; Stagno et al., 2011). These variations between studies likely arise due to poor control of the oxygen fugacity in addition to possible experimental error. By varying the oxygen fugacity however good constraints on the thermodynamic properties of ferric iron bearing bridgmanite components can be potentially gained. This could be used to construct a model that describes the composition of bridgmanite for a given bulk composition, temperature and oxygen fugacity. If the volumes of these bridgmanite components could also be determined an understanding of how the composition of bridgmanite may change at higher pressures in the lower mantle could be obtained. This could then be used to evaluate the results of DAC studies performed at higher pressure conditions.

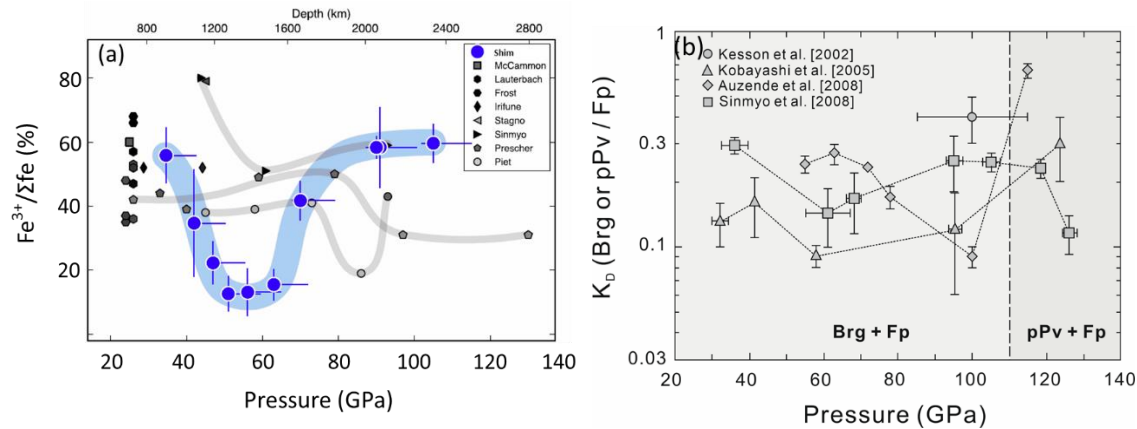


Figure 1.11 (a) Ferric iron content in Al-bearing bridgmanite as a function of pressure from different previous studies (modified from Shim et al., 2017). (b) Fe^{2+} -Mg distribution coefficient ($K_D = (x_{\text{Fe}^{2+}}^{\text{Brg or pPv}} / x_{\text{Mg}}^{\text{Brg}}) / ((x_{\text{Fe}^{2+}}^{\text{Fp}} / x_{\text{Mg}}^{\text{Fp}}))$) between bridgmanite or post-perovskite and coexisting ferropericlase as a function of pressure from previous studies (modified from Sinmyo et al., 2008).

There are three main aims of this study.

1) To examine the compositions of Brg and Fp at 25 GPa and 1973 K using starting materials with different bulk Fe and Al compositions and under different oxygen fugacities and to derive a thermodynamic model to describe these results. The factors that influence the speciation of Fe and Al in Brg were explored and thermodynamic models describing this speciation are constructed in Al-bearing, Fe-bearing and Fe + Al-bearing systems. Based on these models, the compositions of phases in the lower mantle and the amount of metal that may need to be formed through Fe^{2+} disproportionation were calculated. The oxygen fugacity in the lower mantle can be determined for varying scenarios from these models. This has important implications for the speciation of volatiles, the conditions at which diamonds may be formed in the lower mantle and the redox state of the mantle as a whole during core formation.

2) In order to extrapolate thermodynamic calculations for the speciation of Fe and Al components in Brg to higher pressures, single crystal X-ray diffraction measurements were performed on synthesized large Brg single crystals principally to determine the partial molar volumes of these components. The influence of Al and Fe on the structure and compressibility of Brg were investigated. Since the phase transition of Brg to post-perovskite

can be related to the degree of octahedral tilting (Martin and Parise, 2008; Tateno et al., 2010), the effect of Al and Fe substitution on the pressure dependence of distortion are also discussed for a possible explanation of the higher phase transition pressure in Fe, Al-bearing Brg reported in some previous studies (see Hirose et al., 2017 for a review).

3) To determine the partitioning of Fe between Brg, Fp and hydrous melt at lower mantle conditions. A low-velocity anomaly has been observed at the top of the lower mantle (Liu et al., 2016, 2018b; Schmandt et al., 2014) which was proposed to be explained by the presence of buoyant hydrous partial melt. The iron content of the melt at these conditions will exert one of the major influences on the melt density but this is poorly constrained by existing studies. Although numerous melting studies have been conducted in anhydrous peridotite systems (Herzberg and Zhang, 1996; Ito and Takahashi, 1987; Trønnes et al., 1992; Trønnes and Frost, 2002; Zhang and Herzberg, 1994), the temperatures of these experiments are much higher than the current mantle geotherm. Only two previous studies in hydrous peridotite systems have been performed at uppermost lower mantle conditions (Kawamoto, 2004; Nakajima et al., 2019), however, the composition of the partial melts are significantly different between these studies. In order to resolve this discrepancy, experiments were performed under hydrous conditions at ~ 25 GPa and 1923 ± 50 K. A thermodynamic model was constructed to describe Fe partitioning between Brg and melt at these conditions and the composition of the melt in a hydrous peridotite system was calculated based on mass balance calculations performed for a range of melt fractions. The density of the melt was calculated along the current mantle geotherm (Brown and Shankland, 1981) between 22 and 28 GPa and compared with previous studies.

2 Experimental methods

2.1 Starting material preparation

Six pyroxene compositions (A)-(F) with different Fe and Al contents as shown in Table 2.1 were prepared from dried oxide mixtures of reagent grade MgO, SiO₂, Al₂O₃ and Fe₂O₃. To ensure chemical homogeneity, the oxides were first made into glass by grinding the weighed oxide powders together under ethanol, then, after drying, fusing them at 1650 °C followed by rapidly quenching into cold water. The obtained glass (Table 2.1) was then powdered and cold pressed into pellets and fired in a CO₂-CO gas-mixing furnace at 1250 °C at an oxygen fugacity of 2 log units below the fayalite-magnetite-quartz buffer for 48 hours. To make sure that the Fe³⁺ of the whole sample was reduced homogeneously, the rapidly quenched pellets were re-ground and re-fired at identical conditions. The recovered samples consisted of pyroxene containing only Fe²⁺ as confirmed by means of Mössbauer spectroscopy. Glass (F) was not reduced and thus contains only some Fe²⁺ as a result of the glass making process in air. These pyroxenes (A-E) and glass (F) were then mixed with different materials to produce the starting compositions for multi-anvil experiments.

Table 2.1 Composition of pyroxenes and glass starting materials.

		MgO	SiO ₂	Al ₂ O ₃	Fe ₂ O ₃	Tot.	Mg	Si	Al	Fe	ΣCat
(A)	F11	34.7	57.2	-	8.0 ¹	100	0.89	1.00	-	0.11	2.0
(B)	A5F5	37.6	56.0	2.5	3.9	100	0.95	0.95	0.05	0.05	2.0
(C)	A7F7	36.6	54.5	3.5	5.5	100	0.93	0.93	0.07	0.07	2.0
(D)	A7F11	35.3	52.7	3.4	8.6 ²	100	0.91	0.91	0.07	0.11	2.0
(E)	A12F12	34.0	50.8	5.9	9.3 ²	100	0.88	0.88	0.12	0.12	2.0
(F)	A25F11	31.8	47.4	12.3	8.5 ¹	100	0.82	0.82	0.25	0.11	2.0

Notes: Oxides are reported in wt.%. Cations are reported normalized to two cations. (A)-(E) crystallized to pyroxene during the reducing procedure and (F) was still glass since it was not reduced. ¹Enriched with 20% ⁵⁷Fe. ²Enriched with 100% ⁵⁷Fe.

In order to study the influence of Fe and Al substitution on the crystal chemistry of bridgmanite, large high-quality single crystals with various compositions are needed. To this end several strategies were followed (see Table 2.2 for details). In most experiments, $(\text{Mg}_{0.9}\text{Fe}_{0.1})\text{O}$ (reduced to have only Fe^{2+}) was added to produce an MgO saturated environment in order to maximize the oxygen vacancy substitution mechanism (Litasov et al., 2003; Navrotsky, 1999). In other experiments, Fe metal (6-9 μm grain size powder) or hematite were added to achieve relatively reducing or oxidizing conditions respectively. In order to synthesize crystals large enough for single crystal X-ray diffraction (XRD), water was added either directly using a syringe or as hydroxides in order to favor growth of the bridgmanite crystals. For one synthesis experiment (S6631), the starting material consisted of a ground mixture of MgO, $\text{Mg}(\text{OH})_2$, $\text{Al}(\text{OH})_3$, SiO_2 and Fe_2O_3 designed to produce a $(\text{Mg}_{0.8}\text{Fe}_{0.2})(\text{Si}_{0.8}\text{Al}_{0.2})\text{O}_3 + 10 \text{ wt.}\% \text{ H}_2\text{O}$ bulk composition. The final starting compositions (Table 2.2) were loaded into gold foil capsules of 1.8 mm length and 0.8 mm diameter, which were then put into a platinum tube 2 mm long with a 1.0-0.8 mm diameter that was welded closed. The amount of free water added using a syringe could be only roughly estimated due to the small volumes involved.

Table 2.2 Starting compositions and run conditions used for the syntheses of large bridgmanite single crystals. Pt capsule was employed for sample S6631 and Pt-Au double capsule were employed for all other syntheses. All experiments were conducted at 25 GPa and the temperatures were estimated from the power-temperature relationship.

Run No.	Start composition (wt.%)	Temperature (°C)	Run duration (h)
S6631	13.5% MgO, 19.5% Mg(OH) ₂ , 13.5% Fe ₂ O ₃ , 40.4% SiO ₂ , 13.1% Al(OH) ₃	1300	2.5
S6689	100% (B), 0.1 μl H ₂ O	1400	2
S6732	85% (B), 10%Fe, 5%(Mg _{0.9} Fe _{0.1})O, 0.2 μl H ₂ O	1400	8
S6805	75% (C), 15%Fe, 10%(Mg _{0.9} Fe _{0.1})O, 3 Fe foil (φ=0.65mm, Thickness=0.025 mm), 0.2 μl H ₂ O	1600	12
S6813	80% (C), 15%Fe, 5%(Mg _{0.9} Fe _{0.1})O, 0.2 μl H ₂ O	1700	12
S6833	75% (C), 15%Fe, 5% Ir, 5%(Mg _{0.9} Fe _{0.1})O, 0.4 μl H ₂ O	1700	12
S6840	75% (C), 15%Fe, 5% Ir, 5%(Mg _{0.9} Fe _{0.1})O, 0.4 μl H ₂ O	1600	12
S6843	75% (C), 15%Fe, 5% Ir, 5%(Mg _{0.9} Fe _{0.1})O, 0.2 μl H ₂ O	1600	12
S6848	63.8% (C), 15% Fe, 5% Ir, 16.2% Mg(OH) ₂	1600	12
S6838	75% (C), 20%Fe ₂ O ₃ , 5%(Mg _{0.9} Fe _{0.1})O, 0.5 μl H ₂ O	1700	12
H4615	90% (E), 5%Ir, 5%(Mg _{0.9} Fe _{0.1})O, 0.1 μl H ₂ O	1700	12
S7241	83.8% (F), 16.2% Mg(OH) ₂	1600	12

To study the effect of composition and oxygen fugacity on the $\text{Fe}^{3+}/\Sigma\text{Fe}$ ratio in bridgmanite, the starting materials (Table 2.1) were mixed with different oxygen buffering assemblages (Table 2.3). Depending on the redox conditions needed, either Fe metal, ReO_2 , Fe_2O_3 , Ru- RuO_2 (molar ratio 1:10), or PtO_2 were used. In some experiments, buffers were not used and iridium metal (5 wt.%) was added to act as a sliding redox sensor which alloys with some of the Fe present in the starting material during the experiment. The Fe content of the Ir-Fe alloy depends on the f_{O_2} at the experimental conditions, from which the f_{O_2} can be determined using chemical analyses performed after the experiment is recovered. In addition, reduced $(\text{Mg}_{0.9}\text{Fe}_{0.1})\text{O}$ ferropericlase (5-10 wt.%) was added to all experiments to ensure an MgO saturated bulk composition as in the lower mantle. In most experiments, the starting compositions were loaded into folded Au foil capsules that were enclosed in welded Pt tubes to avoid the loss of Fe through the formation of Pt-Fe alloy. In experiments where the Ru- RuO_2 buffer was added, the mixtures were directly sealed into platinum capsules in order to avoid the possible reaction of Ru with the Au capsule. In experiments where PtO_2 was added, a Pt capsule was used to buffer the oxygen fugacity of the experiment through the Pt- PtO_2 buffer. For experiments where ReO_2 was added or for which a high temperature of ~ 2100 °C was employed, folded Re foil capsules were adopted (Table 2.3). The capsules were 1 mm in diameter and 1.5 mm in length. In experiments S7132 and S7138, two capsules with 1 mm length were placed in the same assemblage on either side of the thermocouple. The measured oxygen fugacities of the experiments are reported in Table 3.2 and the methods of calculation are described in detail in Chapter 5.1.

Table 2.3 Starting materials, buffers, capsule materials and run conditions for the experiments for which the oxygen fugacity was controlled. All experiments were conducted at 25 GPa.

Run No.	Starting materials	buffer	Capsule	Temp. (°C)	Duration (h)
S7122	(A)	Fe	Pt-Au	1700	20
S7251	(A)	ReO ₂	Re	1700	12
S7262	(A)	ReO ₂	Re	1700	12
S7113-2	(A)	Ru-RuO ₂	Pt	1700*	4
S7138-1	(A)	Ru-RuO ₂	Pt	1700*	12
S7120	(A)	Pt-PtO ₂	Pt	1700	12
H4737	(C)	Fe	Pt-Au	1700	24
S7132-2	(C)	Fe	Pt-Au	1700	24
S7021	(C)	Ir	Pt-Au	1700	12
S7028	(C)	Ru-RuO ₂	Pt	1700	12
H4755	(D)	Fe	Pt-Au	1700	24
S7132-1	(D)	Fe	Pt-Au	1700	24
S7046	(D)	Ru-RuO ₂	Pt	1700	12
S7138-2	(D)	Ru-RuO ₂	Pt	1700*	12
H4746	(E)	Fe	Pt-Au	1700	24
S7209	(E)	Fe	Re	2100*	2
S6920	(E)	Fe+Ir	Pt-Au	1700	12
S6907	(E)	Ir	Pt-Au	1700*	12
S6921	(E)	Fe ₂ O ₃	Pt-Au	1700	12
S6950-1	(E)	Fe ₂ O ₃	Pt-Au	1700	12
S6950-2	(E)	Fe ₂ O ₃	Pt-Au	1700	12
S6952	(E)	Ru-RuO ₂	Pt	1700	12
S7214	(F)	Ru-RuO ₂	Pt	1700	12

Notes: *Temperature estimated from the power curve due to failure of the thermocouple.

2.2 High pressure experiments

The bridgmanite syntheses were carried out at high pressure and high temperature conditions using the 1000-tonne (Hymag) or 1200-tonne (Sumitomo) kawai-type multi-anvil apparatus at the Bayerisches Geoinstitut (BGI). This split-sphere multi-anvil design was introduced by Kawai et al. (1970), which featured a steel sphere split into 6 wedge-shaped anvils also referred to as first stage anvils forming cubic space in which a set of eight corner-

truncated tungsten carbide cubes (second stage anvils) is placed. High pressures are achieved using these two stages of anvils to direct a uniaxial force of up to 1200 tonnes generated by a hydraulic press onto a small sample volume occupied by a ceramic high-pressure octahedral assembly. The sample is contained inside the octahedral pressure medium and pyrophyllite gaskets are placed between the anvils. Both pressure medium and gaskets flow under pressure, creating a quasi-hydrostatic pressure on the sample (Figure 2.1). By varying the force exerted by the hydraulic press, the truncation edge length (TEL) of the second stage anvils and the octahedral edge length (OEL) of the pressure medium, different pressures can be achieved.

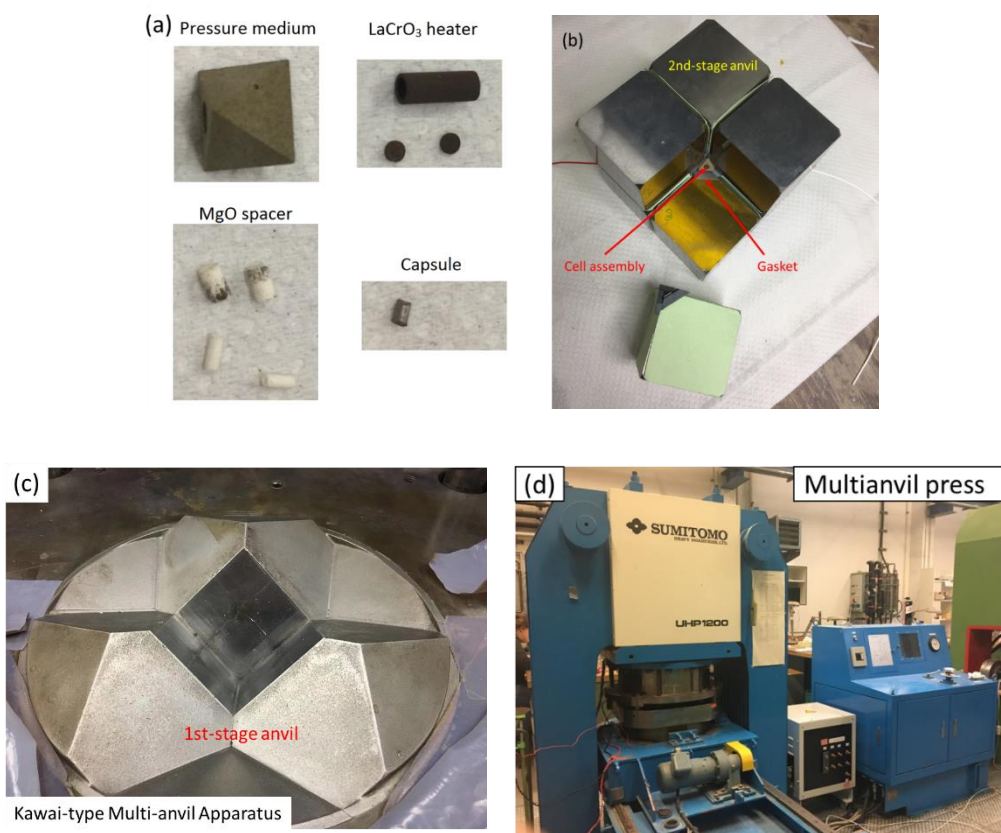


Figure 2.1 The setup for a multi-anvil press experiment. (a) Assembly parts used; (b) The octahedral cell assembly placed in the eight corner-truncated tungsten carbide anvils; (c) Kawai-type split-sphere first stage anvils; (d) 1200-tonne Sumitomo multi-anvil press.

In this study, all experiments were conducted at 25 GPa and temperatures ranging between 1300 and 2000 °C in a multi-anvil press (Table 2.2 and 2.3), corresponding to pressures in

the upper part of the Earth's lower mantle. Tungsten carbide cubes of 32 mm edge length and 3 mm truncation edge length were employed with standard 7 mm edge length Cr₂O₃-doped (5 wt.%) MgO octahedron as pressure medium (referred to as 7/3 assembly). The capsule was surrounded by an insulating MgO sleeve and placed in the central portion of a cylindrical lanthanum chromite (LaCrO₃) furnace. MgO spacers filled the space at the top and bottom of the capsule and LaCrO₃ lids were located at the top and bottom of the heater to ensure good electrical contact with the anvils (Figure 2.2).

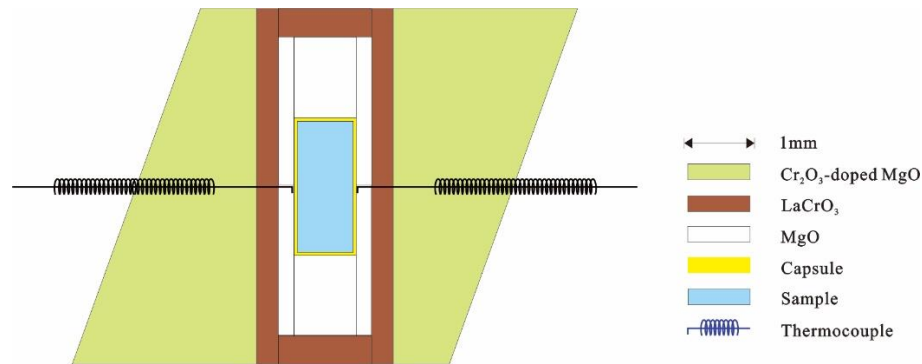


Figure 2.2 Schematic cross-section of 7/3 pressure assembly for multi-anvil experiments.

The pressure calibrations as a function of oil pressure employed in this study were those routinely used at BGI based on the phase transitions of quartz to coesite, CaGeO₃ garnet to perovskite and coesite to stishovite (Keppler and Frost, 2005). For large bridgmanite single crystal syntheses experiments, temperatures were estimated from the power-temperature relationship. In experiments performed to study the effect of oxygen fugacity on ferric Fe in bridgmanite, temperature was monitored with a W97Re3-W75Re25 (Type D) thermocouple wire (0.08 or 0.13 mm thick) inserted longitudinally through the wall of the furnace, with the hot junction at the midpoint of the heater. Coils made of the same thermocouple wire were used to protect the thermocouple as they pass through the gaskets. For those experiments in which the thermocouple failed, temperature was estimated from the electrical power-temperature relationship (Table 2.3).

The experiments were first pressurized up to approximately 25 GPa and then heated to the target temperature between 1300-2100 °C by a rate of ~ 100 °C/min. The desired

temperature was kept for 2-24 hours after which the runs were rapidly quenched by shutting off the electric power to the heater and the pressure was released slowly over 20 hours. The experimental conditions are summarized in Table 2.2 and 2.3. Two bridgmanite samples, H3004 and S4253, synthesized from a previous study (Boffa Ballaran et al., 2012), having respectively a MgSiO_3 end-member composition and a very Fe,Al-rich composition were also used in this study. All run products are described in detail in section 3.1 and 3.2.

2.3 Sample characterization

The recovered samples were mounted in epoxy resin, sectioned and polished for analysis with scanning electron microscope (SEM), energy-dispersive spectroscopy (EDS), X-ray diffraction (XRD), and electron probe microanalysis (EPMA). Before the SEM and EPMA measurements, the charges were coated with an 8 nm thick carbon layer to avoid electrical charging of the surface under electron beams.

2.3.1 Scanning electron microscopy

Textural observations, preliminary phase identification and semi-quantitative composition determination of the recovered run products were performed using a scanning electron microscope (ZEISS Gemini 1530) operating at 15 kV equipped with a field emission gun and energy-dispersive X-ray spectrometer (EDS). A working distance of 13-14 mm was normally applied.

In this technique, a focused electron beam generated from an electron gun, is scanned across a polished specimen. Depending on the interaction between the electron beam and the sample, different signals such as secondary electrons, back-scattered electrons and auger electrons can be generated. The secondary electrons with low energy are emitted from the near-surface regions of the sample due to inelastic interactions between the primary electron beam and the sample, which can be used for inspection of the topography of the sample's surface. On the other hand, backscattered electrons (BSE), produced by elastic collisions of electrons with atoms originate from a wide region within the interaction

volume. Heavy atoms are stronger scatterers of electrons compared with light atoms, therefore the intensity of the BSE is proportional to the average atomic number of the target sample, providing imaging with information on the sample's composition and helping to distinguish between different phases. Moreover, when the electron beam collides with the sample, electrons from the inner shells are ejected and the resulting vacancies are filled later by outer shell electrons, emitting characteristic X-rays, which depend only on the type of elements and thus can be used for rapid qualitative chemical analysis of minerals.

2.3.2 Electron probe micro-analyzer (EPMA)

Precise quantitative analysis of major and minor element concentrations of coexisting phases were obtained using a JEOL JXA-8200 electron microprobe equipped with five wavelength-dispersive spectrometers.

The physical principles of electron microprobe are fundamentally the same as the ones of the SEM. When the sample is bombarded by an accelerated and focused electron beam produced by a tungsten filament, the electron-sample interactions yield both derivative electrons and X-rays. The secondary and back-scattered electrons, as discussed before, are useful for imaging a surface or obtaining an average composition of the material; while accurate quantitative elemental analyses are mainly based on measurement of characteristic X-rays. Electrons penetrate a volume of the sample whereby an inner-shell electron is ejected from its orbit by inelastic collisions of the incident electrons, leaving a vacancy. And electrons from the outer shell fall back to fill this vacancy and shed some energy as X-rays (Reed, 2005).

These X-rays are characteristic of the element and can be analyzed either by an energy dispersive spectrometer or by crystal spectrometers (wavelength dispersive mode). For precise quantitative analysis wavelength-dispersive spectroscopy (WDS) was employed. The electron microprobe is equipped with different crystal spectrometers (e.g. synthetic LiF, PET or TAP crystals) each with a specific d spacing, and the characteristic X-rays from the samples are selected based on their wavelength using the Bragg reflections from the

crystals. The position and intensity of each spectral line are then compared with those emitted by standards with known composition, allowing precise chemical composition determination after matrix corrections have been made. In EPMA analysis, matrix corrections are applied in order to obtain 'true' concentrations including atomic number, absorption and fluorescence corrections represented by the acronym 'ZAF' (Reed, 2005). There are mainly four actual types of models used for matrix corrections in EPMA: (1) Empirical, the simplest, it is based on known binary experimental data; (2) ZAF: 1st generalized algebraic procedure, it assumes a linear relation between concentration and x-ray intensity; (3) Phi-rho-Z, it is based upon depth profile (tracer) experiments; (4) Monte Carlo, it is based upon statistical probabilities of electron-sample interactions and it is used particularly for unusual specimen geometries (Heinrich and Newbury, 2013).

In this study, an accelerating voltage of 15 kV and a beam current of 5 nA were employed. Counting times per element were 10 s on the peak and 5 s on the background with a defocused beam of 30 μm for melt and 3 μm for Brg grains larger than 5 μm . For smaller Brg grains and other mineral phases, focused beam was used. Enstatite for Mg and Si, Fe metal for Fe, corundum for Al, Ir metal for Ir, Pt metal for Pt, and Ru metal for Ru were used as standards. The composition of pure MgSiO_3 akimotoite single crystals also was determined using the same settings as a benchmark analysis before each period of measurement to ensure that an accurate Mg/Si ratio was measured for these high-pressure phases. Only once the Mg/Si ratio obtained both for the enstatite and akimotoite standards was equal to 1.00 (1) the analyses of the samples were performed. The purpose of using low beam current, short counting time and defocused beam was to minimize the amorphization and damage of Brg induced by the electron beam. The Phi-rho-Z correction routine was applied for all analyses of this work. More than 20 points for each sample were measured in order to check the homogeneity of the synthesized bridgmanite crystals. The average compositions of the Brg crystals synthesized in this study are reported in Table 3.3 and 3.4.

2.3.3 Micro-focus X-ray diffraction

Micro-focus X-ray diffractions was performed for phase identification of the recovered samples. A micro-focused X-ray diffractometer (Bruker, D8 DISCOVER) equipped with a two-dimensional solid-state detector (VÅNTEC500) and micro-focus Co- $K\alpha$ radiation source ($1\mu\text{S}$) operated at 40 kV and 500 μA was used (Figure 2.3). The X-ray beam was collimated to a minimum of 50 μm spot in diameter using an IFG polycapillary X-ray mini-lens. The unique 2-dimensional large-area detector enables the coverage of a larger reciprocal space and achievement of high diffraction angles. The patterns were collected for 2400 - 6000 s in the 2θ range between 25° and 85° .

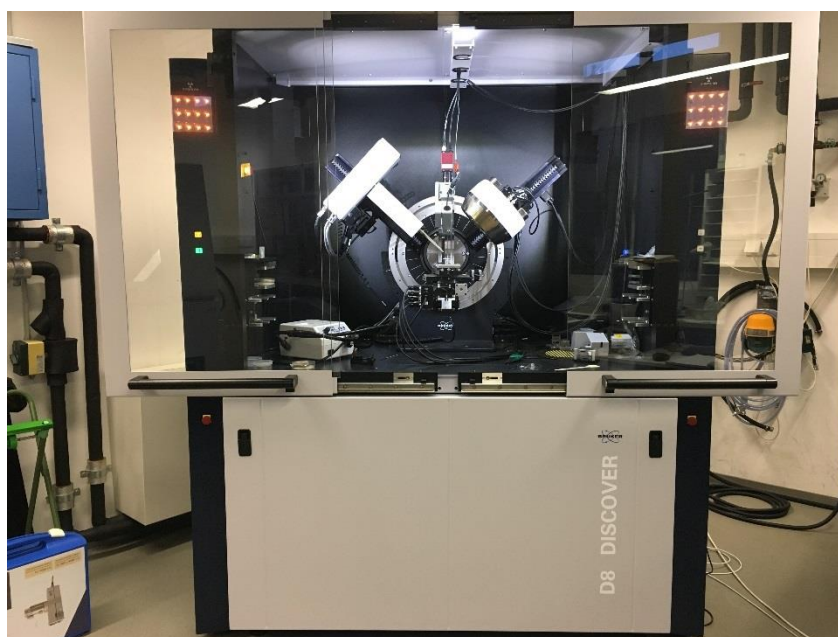


Fig 2.3 D8 DISCOVER diffractometer equipped with a micro-focus Co- $K\alpha$ radiation source ($1\mu\text{S}$) and two-dimensional solid-state detector (VÅNTEC500).

2.4 Single crystal X-ray diffraction and structural refinements

Single-crystal X-ray diffraction experiments provide direct measurements of intensity data which can be used to determine both unit-cell parameters and the atomic structure of a material. Ten single crystals with a wide range of Fe and Al contents varying from 0 to 0.40 atoms pfu were selected for single crystal X-ray diffraction study using the Xcalibur single crystal diffractometer and the Huber 4-circle diffractometer. The Huber 4-circle Eulerian

cradle diffractometer (Fig. 2.4) is equipped with Mo- $K\alpha$ radiation operating at 50 kV and 40 mA and a point detector. Point detectors offer advantages over area detectors in terms of signal-to-noise ratio and accuracy of the determined lattice parameters (Angel et al., 2000). Intensity data were collected at ambient conditions using an Oxford Diffraction Xcalibur 2 diffractometer (kappa geometry) with Mo- $K\alpha$ radiation ($\lambda=0.71073 \text{ \AA}$) operated at 50 kV and 40 mA, equipped with a Sapphire 2 CCD detector and a graphite monochromator (Figure 2.5).

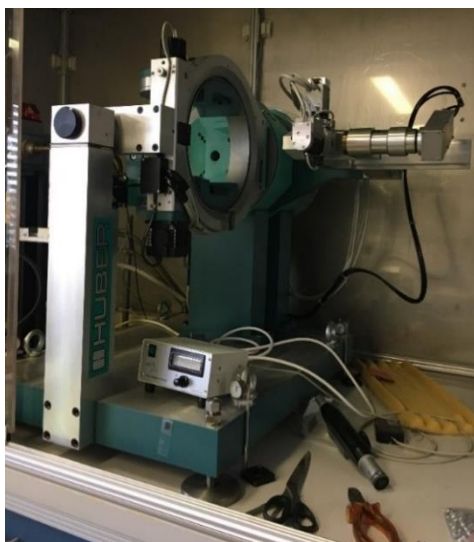


Figure 2.4 Four-circle Huber diffractometer (Mo- $K\alpha$ radiation) equipped with a conventional tube and a point detector.



Figure 2.5 Oxford Diffraction Xcalibur 2 diffractometer (kappa geometry) with Mo- $K\alpha$ radiation equipped with a Sapphire 2 CCD detector and a graphite monochromator.

2.4.1 Crystal selection

Bridgmanite crystals larger than 70 μm in size and optically free of defects with homogeneous extinction under crossed polarizers were carefully selected from the run products reported in Table 3.1 under an optical microscope and mounted on the tip of glass fibers for single crystal diffraction.

After determination of the orientation matrix using the Xcalibur diffractometer, the crystal quality was assessed by scanning ω profiles of individual reflections on a Huber 4-circle Eulerian cradle diffractometer. The widths of ω profiles of individual reflections reflect the degree of defects of a crystal. Broader ω profile of a given reflection indicate higher misorientations of domains in the crystal. Therefore, only crystals with full width at half maximum (FWHM) of ω scans below 0.1° were used for further analysis.

2.4.2 Accurate Unit-cell parameter determination

The unit-cell lattice parameters of single crystals were accurately and precisely determined using the Huber diffractometer. Each crystal was first aligned to the center of rotation, then, based on the preliminary lattice parameters and orientation matrices extracted from two-dimensional diffraction pattern obtained by CCD area detector on Xcalibur diffractometer, individual reflections were centered following a 8-position centering procedure according to King and Finger (1979) and Angel et al. (2000). The setting angles of a single reflection always deviate from the “true” angles as a result of a number of experimental aberrations (Angel et al., 2000) such as offsets of the crystal from the center of the goniometer, absorption by the crystal and a number of diffractometer aberrations like an incorrect zero position. By applying the eight-position centering method, small misalignments of the crystal and of the diffractometer can be taken into account (Miletich et al., 2005).

The centering procedure and vector least square refinement of the lattice parameters were performed using the SINGLE software (Angel and Finger, 2011). The procedure consists of centering a single reflection at the 8 equivalent positions on the diffractometer. This involves measurements of well resolved profiles of a Bragg reflection in various

directions in the reciprocal space through a sequence of ω , $\omega/2\theta$, and χ scans. More than 30 reflections were centered for each crystal. The total integrated intensity, the positions and FWHM of individual reflections were refined based on the refit reflection positions, providing lattice parameters and unit cell volumes with uncertainties smaller than 0.001 Å and 0.05 Å³ respectively. Unit cell parameters were refined assuming orthorhombic symmetry with space group *Pbnm* and are reported in Table 4.4.

2.4.3 Intensity data collection and structure refinement

Intensity data were collected at ambient conditions using an Oxford Diffraction Xcalibur 2 diffractometer (kappa geometry). Omega scans were chosen to obtain the coverage of the full reciprocal sphere up to $2\vartheta_{\max}=80^\circ$, with an exposure time of 20 s/frame and step size of 0.5° at a crystal-detector distance of 45.1 mm.

Lorentz and polarization factors together with an analytical absorption correction based on the crystal shape were performed for the correction of the reflection intensities using the CrysAlis package (Oxford Diffraction 2006). The measured reflections were consistent with the orthorhombic space group *Pbnm* and resulted in a total of 472-723 unique reflections with a discrepancy factor

$$R_{\text{int}} = \frac{\sum |F_{\text{obs}}^2 - F_{\text{obs}}^2(\text{mean})|}{\sum |F_{\text{obs}}^2|} \quad (2.1)$$

between 0.022 and 0.051 (Table 2.4) where F_{obs} is the observed structure-factor amplitude of individual symmetry-equivalent reflections contributing to the same unique reflection and $F_{\text{obs}}(\text{mean})$ is the mean structure-factor amplitude value of these symmetry equivalent contributors.

Symmetrically equivalent reflections were merged and structure refinements were performed based on F^2 using the SHELX97 program package (Sheldrick, 2008) implemented in the WinGx System (Farrugia, 1999). The structure refinements were carried out in space group *Pbnm* using the atomic coordinates reported by Horiuchi et al. (1987) as starting

parameters. Neutral scattering factors for Mg, Si, Al, Fe, and O were used (Allen et al., 1992; Wilson and Prince, 1992) and all atoms were refined anisotropically.

In order to model the cation distribution of Al and Fe between the A- and B- site we have taken the following steps: 1) the occupancies of Fe and Mg were refined at the A site with their sum constrained to be equal to 1; 2) the B site has been refined only using the Si scattering factor with the occupancy of Si free to vary; 3) oxygen occupancies have been fixed to the value of 1, given that the amount of vacancies resulting from the EPMA analyses is smaller than 0.02 atoms pfu (Table 4.1) , concentration well below the sensitivity of the structural refinements. In this way we obtained mean atomic numbers (m.a.n., number of electrons) representing the electronic charge of the cations at the A- and B- sites which can be compared with the cation distribution calculated from the EPMA analysis (Table 4.1). Details of data collections and refinement parameters are reported in Table 2.4 and the refinement results are listed in Table 4.2.

Table 2.4 Details of the structural refinements performed for the Brg single crystals in this study.

Sample	H3004	S6689	S6732	H4615	S6848	S6805	S6838	S6631	S4253	S7241
Measured reflections	3423	3424	3642	3977	3400	3584	3491	6199	4413	3608
Unique reflections	474	472	476	552	476	476	477	493	723	482
$F_o > 4\sigma(F_o)$	454	432	462	527	450	453	456	485	673	468
R_{int}	0.0299	0.0509	0.0222	0.0318	0.0399	0.0265	0.0388	0.0236	0.0286	0.0368
$R_1 (F)$ for $F_o > 4\sigma(F_o)$	0.0295	0.0391	0.0247	0.0306	0.0349	0.0272	0.0360	0.0173	0.0253	0.0295
$R_1 (F)$ for all	0.0323	0.0450	0.0258	0.0330	0.0399	0.0288	0.0390	0.0179	0.0285	0.0301
$wR_2 (F^2)$	0.0712	0.0936	0.0591	0.0671	0.0727	0.0675	0.0843	0.0446	0.0562	0.0772
Goof	1.194	1.176	1.132	1.207	1.21	1.101	1.251	1.152	1.107	1.153
No. parameters	28	30	30	30	30	30	30	30	30	30

Notes: $R_1 = \frac{\sum ||F_{\text{obs}}| - |F_{\text{calc}}||}{\sum |F_{\text{obs}}|}$; $wR_2 (F^2) = \left\{ \frac{\sum [w(F_{\text{obs}}^2 - F_{\text{calc}}^2)^2]}{\sum [w(F_{\text{obs}}^2)^2]} \right\}^{0.5}$; $w = \frac{1}{\sigma^2(F_{\text{obs}}^2) + (a \times P)^2 + b \times P}$; $P = \frac{\text{Max}(F_{\text{obs}}^2, 0) + 2F_{\text{calc}}^2}{3}$; $\text{Goof} = \left(\frac{\sum [w(F_{\text{obs}}^2 - F_{\text{calc}}^2)^2]}{(n-p)} \right)^{0.5}$ where n

is the number of reflections and p is the total number of parameters refined.

2.5 Mössbauer spectroscopy and electron energy loss spectroscopy (EELS)

The $\text{Fe}^{3+}/\Sigma\text{Fe}$ ratios in the Brg samples synthesized in this study were determined using either Mössbauer spectroscopy or electron energy loss spectroscopy (EELS) with a transmission electron microscope (TEM).

2.5.1 Mössbauer spectroscopy

Mössbauer spectroscopy is based on the emission and absorption of gamma rays which are related to transitions between different states of the atomic nucleus, therefore could be used to study the local atomic environment around the nuclei of the atoms of interest. During the emission and absorption of a γ quantum by an atomic nucleus in a gas or liquid, the γ quantum would lose some of its energy to the recoil of the nuclei; as a result, recoilless emission as well as resonant absorption of γ radiation are not possible. However, when the emitting nucleus is incorporated into a solid crystal, the emitting or absorbing atoms hardly move and this recoil-free emission and resonant absorption of γ radiation is called the Mössbauer effect.

The principle set-up of the Mössbauer experiment used in this study is shown in Figure 2.6 and can be divided into three parts—the source, the absorber and the detector. Radioactive nuclides serve as a convenient source of gamma rays. Upon decay of a nuclide, the newly formed nucleus is initially in an excited state which decays to the ground state by emission of gamma rays. ^{57}Fe is the most frequently used Mössbauer isotope, which is produced by the decay of $^{57}\text{Co}/\text{Rh}$ with a half-life of 270 days. The transition of the Fe nucleus from the first excited state with a spin 3/2 to the ground state with a spin 1/2 provides γ radiation with an energy of 14.413 KeV (Figure 2.6a). This monochromatic energy can be changed using the Doppler effect by moving the source relative to the absorber. The gamma rays interact with the sample (absorber) as they pass through. A detector is placed behind the sample that records the count rate as a function of frequency (or source velocity

(mm/s)). Only gamma rays that do not interact with the absorber are recorded while those that are absorbed are not recorded by the detector because they will be re-emitted in a different direction (Fig. 2.6b). Usually, the absorption frequency of the sample is not equal to the emission frequency of the source due to the hyperfine interactions between the nuclear moments and surrounding electric and/or magnetic fields which perturb the nuclear energy levels (as discussed in detail below). The resulting Mössbauer spectrum shows dips instead of peaks (Fig. 2.6b) and two important spectral parameters, the isomer-shift, δ_0 , (or chemical shift) and the quadrupole splitting, ΔE_Q , can be extracted to provide information on the hyperfine interactions between the nucleus and the atomic electrons.

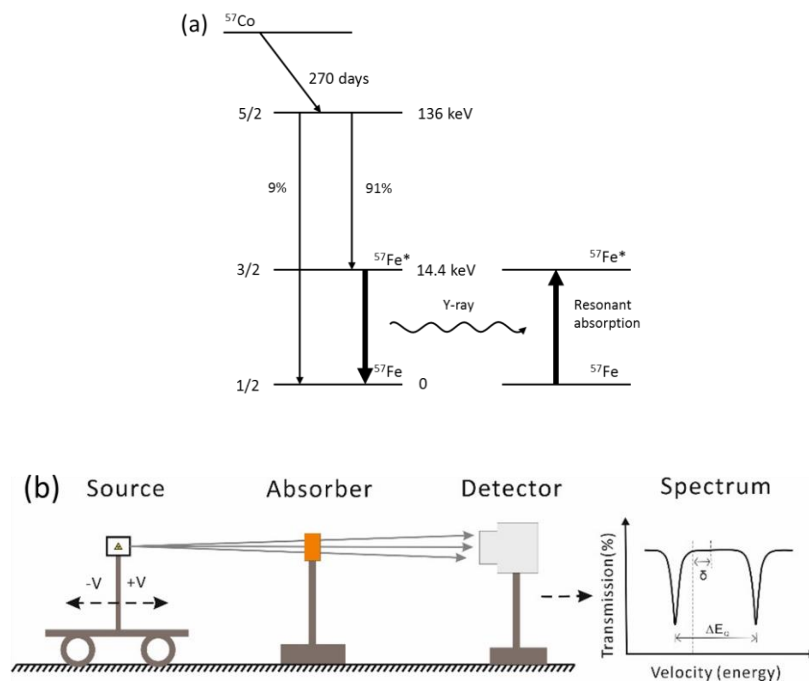


Figure 2.6 (a) Energy levels for Mössbauer spectroscopy. (b) Schematic view of a Mössbauer spectrometer modified from McCammon (2004).

The electric monopole interaction is an electrostatic interaction between the positively charged nucleus and the negatively charged electrons and causes a shift of the nuclear energy levels which is called the isomer shift or chemical shift (δ_0) (Fig. 2.7a). Upon transition from the ground state to the excited state, the radius of the atom changes slightly. The isomer shift δ_0 relative to a standard source (Fig. 2.7b) depends on this radius

difference as well as the difference in the electronic charge density especially the s electron density at the absorber nuclei and the source nuclei. The former is a constant for a particular Mössbauer isotope while the latter depends on the coordination, valence state and spin state of the Mössbauer atoms.

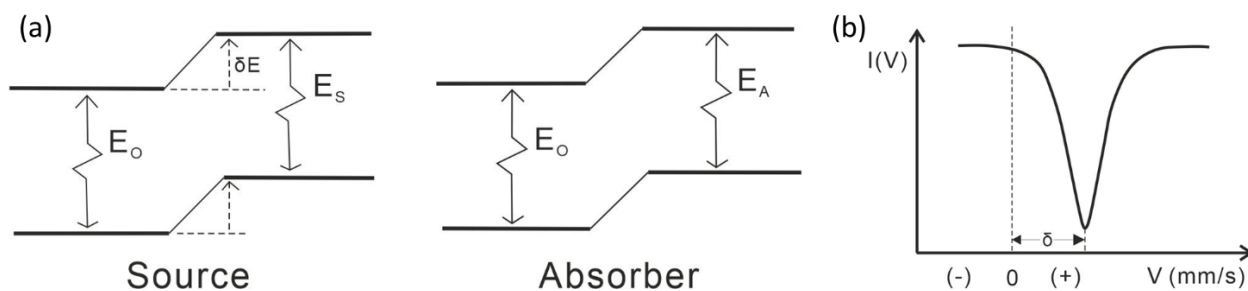


Figure 2.7 Nuclear energy level diagram and the corresponding Mössbauer spectrum. (a) The electric monopole interaction shifts the nuclear energy levels of the source and the absorber differently. (b) In the corresponding Mössbauer spectrum, the difference between the centroid of the line and the zero-velocity point corresponds to the isomer shift δ_0 (modified from Gütlich et al., 1978).

Quadrupole splitting (QS or ΔE_Q) is often regarded as a measure of the degree of site distortion. Electric quadrupole interaction takes place between the nuclear quadrupole moment Q and an electric field gradient (EFG) q , causing the splitting of degenerate nuclear energy levels. When the nuclear spin quantum number I is larger than $1/2$, the nuclear charge distribution deviates from spherical symmetry and the nucleus has a quadrupole moment. If the charge distribution around the nucleus (valence electrons and lattice ions) deviates from cubic symmetry, the EFG would be non-zero. This deviation arises from two contributions: (1) the valence term which reflects the asymmetry of the charge distribution arising from the valence electrons; (2) the lattice term which results from non-cubic charge distribution of the surrounding atoms. In the case of ^{57}Fe the quadrupole interaction splits the first excited level ($I=3/2$) of ^{57}Fe nucleus in two sublevels. Since the ground state with spin $1/2$ has no quadrupole moment, two nuclear transitions from the ground state to the split excited state would occur. This results in two resonant absorption lines in the Mössbauer spectrum separated by the quadrupole splitting ΔE_Q which describes the energy

difference between the two excited states (Fig. 2.8). The magnitude of quadrupole splitting ΔE_Q depends on both Q and EFG. The quadrupole moment Q is constant for a certain Mössbauer isotope therefore the difference in quadrupole splitting mainly arises from changes of the EFG. The quadrupole splitting depends on the valence, spin state, coordination of the absorber atoms as well as the degree of distortion of the crystallographic site at which the atom resides.

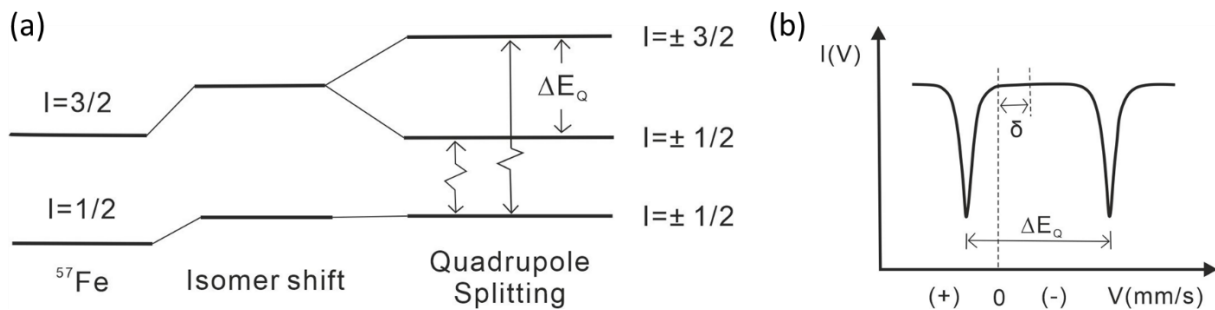


Figure 2.8 (a) The quadrupole splitting in a $1/2 \rightarrow 3/2$ transition of ^{57}Fe . The ground state of the nucleus with spin $1/2$ does not split whereas the first excited state with spin $3/2$ split into two sublevels. As a result, two transitions from the ground state to both excited sublevels are possible. (b) In the corresponding Mössbauer spectrum, two lines are observed (quadrupole doublet) and the distance between them is the quadrupole splitting ΔE_Q (mm/s). The distance between the centroid of both lines and the zero-velocity point corresponds to the isomer shift δ_0 (modified from Gütlich et al., 1978).

A nucleus with a spin quantum number I larger than 1 has a non-zero magnetic dipole moment. The magnetic hyperfine splitting ΔE_M arises from the interaction of this nuclear magnetic dipole moment μ and a magnetic field H (internal or external) at the nucleus, i.e. Zeeman effect. In the case of ^{57}Fe , the magnetic dipole interaction splits the first excited state ($I=3/2$) into 4 sublevels and the ground state ($I=1/2$) into 2 sublevels. Considering the selection rules for magnetic dipole transitions, six transitions are allowed, resulting in a sextet peak in the Mössbauer spectrum (Fig. 2.9).

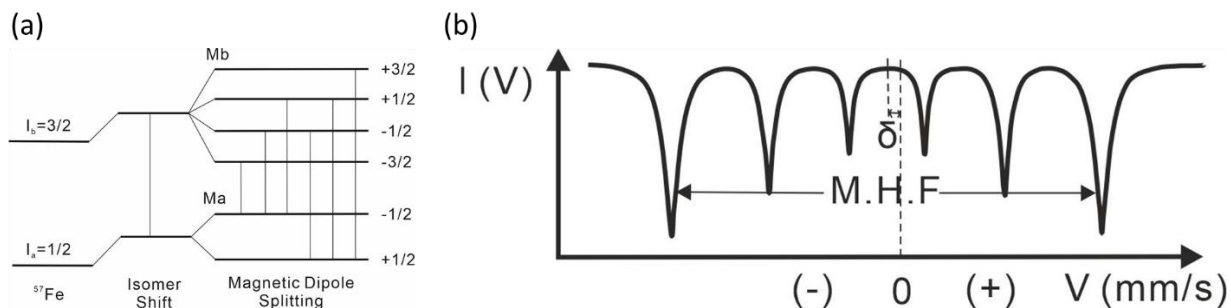


Figure 2.9 (a) A schematic view of the magnetic dipole splitting in ^{57}Fe . (b) In the corresponding Mössbauer spectrum, six peaks are observed (sextet). The distance between the centroid of the six lines and the zero-velocity point corresponds to the isomer shift δ_0 (modified from Gütlich et al., 1978).

For a particular Mössbauer isotope, the isomer shift δ_0 relative to a standard source can be simply expressed as $\delta_0 = \alpha(|\psi(0)|_A^2 - |\psi(0)|_S^2)$ where α is the isomer shift calibration constant, $|\psi(0)|_A^2$ is the s -electron density at the absorber nuclei and $|\psi(0)|_S^2$ is the s -electron density at the source nuclei. $\alpha = 2/5\pi Ze^2(R_e - R_g)/(R_e + R_g)$ (Ze is the nuclear charge, R_e and R_g are the radius of the nucleus of the excited state and ground state respectively) is positive when $R_e > R_g$ and negative when $R_e < R_g$ (Amthauer et al., 2004). In the case of Fe, the radius of the nucleus in the excited state (R_e) is smaller than the ground state (R_g) therefore α is negative (Amthauer et al., 2004) and the isomer shift δ_0 decreases with increasing s -electron density at the ^{57}Fe nucleus. Ferrous iron Fe^{2+} with an electronic configuration of $[\text{Ar}]3d^6$ has a smaller s electron density at the nucleus compared to Fe^{3+} with an electronic configuration of $[\text{Ar}]3d^5$ due to the shielding effect of the extra $3d$ electron on $3s$ electrons of Fe^{2+} . Therefore Fe^{2+} would have a larger isomer shift in comparison with Fe^{3+} if the coordination polyhedron remains unchanged. Moreover, for Fe species with the same electron configuration, δ_0 decreases with decreasing coordination number of iron because the smaller average cation-anion distance causes strong orbital overlap therefore increases s -electron density at the Fe-nucleus (Fig. 2.10a). In general, a quadrupole doublet assigned to high spin Fe^{2+} exhibits a large quadrupole splitting whereas that assigned to Fe^{3+} often exhibits a smaller quadrupole splitting (Fig. 2.10b). The high value of quadrupole splitting of high spin Fe^{2+} mainly arises from the strong asymmetry of the Fe^{2+} electron distribution around the nucleus with a configuration $[\text{Ar}]3d^5_3d^1_\uparrow$. In contrast, the five valence electrons

of high spin Fe^{3+} each occupies one $3d$ orbitals with the same spin direction ($[\text{Ar}]3d_1^5$) is almost spherically symmetric, therefore leading to a small quadrupole splitting.

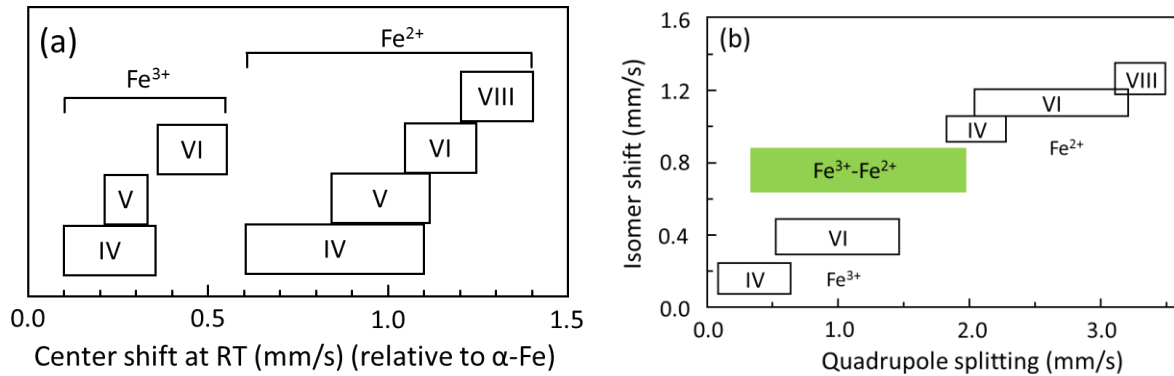


Figure 2.10 (a) Room temperature center shift ranges for high-spin Fe^{2+} and Fe^{3+} minerals with different coordination, modified from McCammon (2004). (b) Room temperature isomer shift versus quadrupole splitting data for common rock-forming minerals, modified from Dyar et al. (2006). The highlighted region with a center shift in the range 0.5 - 0.9 mm/s between the ranges for Fe^{2+} and Fe^{3+} is poorly constrained and usually assigned to $\text{Fe}^{2.5+}$, representing the delocalization of electrons between adjacent Fe^{2+} and Fe^{3+} .

In this study, samples were prepared as stacked single crystals or thin sections for Mössbauer measurements. For single crystal synthesis experiments, the recovered samples for Mössbauer spectroscopy were carefully prepared in order to exclude large areas of melt. In some measurements, Brg single crystals were used. In other experiments the bulk assemblages were used but because the melt concentrates in the higher temperature part, i.e. middle part of the capsule (Fig. 3.1), the bulk assemblage on the side consisting mainly of Brg were cut and areas for γ -ray to pass through were carefully chosen in a way that large melt areas were not observed from both ends of the sample. In this way only bridgmanite and ferropericlasite were measured in the recovered assemblage from the single crystal synthesis experiments. For all oxygen fugacity buffered experiments, thin sections of bulk assemblages were used. The thicknesses of the different samples varied between 30-500 μm , depending on the Fe content and ^{57}Fe enrichment of Brg (Table 2.1), to produce an absorber thickness of $\sim 5 \text{ mg Fe/cm}^2$ to avoid saturation effects. Mössbauer spectra were recorded in transmission mode over 1 to 7 days at room temperature (298 K) on a constant

acceleration Mössbauer spectrometer with a nominal 370 MBq ^{57}Co point source in a 12 μm Rh matrix. The active dimensions of the point source were 500 x 500 μm^2 . The velocity scale was calibrated relative to a 25 μm $\alpha\text{-Fe}$ foil. Spectra were collected using a velocity range of -5 to +5 mm/s for normal samples and -7 to +7 mm/s for samples containing magnetically ordered Fe metal phase. Spectra were then folded and fitted to multiple doublets and sextets with pseudo-Voigt line shape using the MossA program. The full transmission integral was used for thick samples (Prescher et al., 2012). The resulting Mössbauer parameters are discussed in Section 3.4.

2.5.2 Electron energy-loss spectroscopy (EELS)

Transmission Electron microscopy (TEM) is a microscopy technique in which a beam of electrons is transmitted through a specimen and the interaction between the specimen and electrons can be used to observe the internal fine structure (the microstructure or ultrastructure) and chemistry in minerals. When the high-energy incident electron beam of the TEM passes through the sample, it interacts with the constituent atoms in a number of ways. Some transmitted electrons suffer inelastic scattering and lose part of their energy (traveling speed becomes slower) through interactions with electrons and with the crystal lattice of the specimen. The electron energy-loss spectroscopy (EELS) method records the energy spectra of these inelastically scattered electrons to perform qualitative and quantitative analysis of elements and electronic structure analysis from micro- or nano-scale areas. Measurement of the transmitted electron-energy distribution is achieved by dispersing the electrons according to their kinetic energy (and hence energy loss during passage through the sample) using an electron spectrometer that employs a magnetic field that is normal to the electron beam. The high energy region (more than about 50 eV) of an EELS spectrum is called the "core-loss spectrum". The energy-loss near-edge structure (ELNES) describes the fine structure in an energy region of about 30 eV above the absorption-edge energy in the EELS core-loss spectrum, which arises due to transitions of electrons from the inner-shell state to the conduction band (unoccupied state).

In this study, EELS was carried out at the Fe $L_{2,3}$ edges to study the valence state of iron in some of the recovered Brg samples (Table 4.1), which were not suitable for Mössbauer measurement due to peak overlap with coexisting ferropicriase. The ELNES of the Fe $L_{2,3}$ edges are characterized by two white-lines features arising from dipole-allowed transitions to vacant d orbitals. The excitation of a $2p$ core electron changes the atomic state from the ground state $2p^63d^n$ to the $2p^53d^{n+1}$ state ($n=5$ for Fe^{3+} and $n=6$ for Fe^{2+}). The spin quantum number (s) can couple to the orbital angular momentum (l) either positively or negatively, leading to spin-orbit splitting of the Fe $2p$ core hole with an energy difference of about 13 eV (Van Aken and Liebscher, 2002). As a result, two signals with similar shape successively appear in the EELS spectrum: the L_3 line corresponds to transitions from the $2p_{3/2}$ to the $3d_{3/2}3d_{5/2}$ orbital and the L_2 line corresponds to transitions from the $2p_{1/2}$ to the $3d_{3/2}$ orbital. The subscripts refer to the total spin angular momentum number (j) of the electron that equals to the orbital angular momentum (l) plus the spin quantum number (s) (Garvie and Craven, 1994). Their intensities are related to the unoccupied $3d$ states (Garvie and Craven, 1994; Van Aken and Liebscher, 2002). $L_{2,3}$ edges are sensitive to the valence state of Fe, for example, the L_3 edges for the divalent and trivalent Fe are at ca. 707.8 eV, and ca. 709.5 eV, respectively. In this project, $\text{Fe}^{3+}/\Sigma\text{Fe}$ ratios were determined following the procedure of Van Aken and Liebscher (2002) using the modified integral intensity ratio $I(L_3)/I(L_2)_{\text{mod}}$ which employs two 2-ev-wide integration windows from 708.5 to 710.5 eV centered at the Fe L_3 maximum for Fe^{3+} and from 719.7 to 721.7 eV centered at the Fe L_2 maximum for Fe^{2+} (e.g. Figure 2.11).

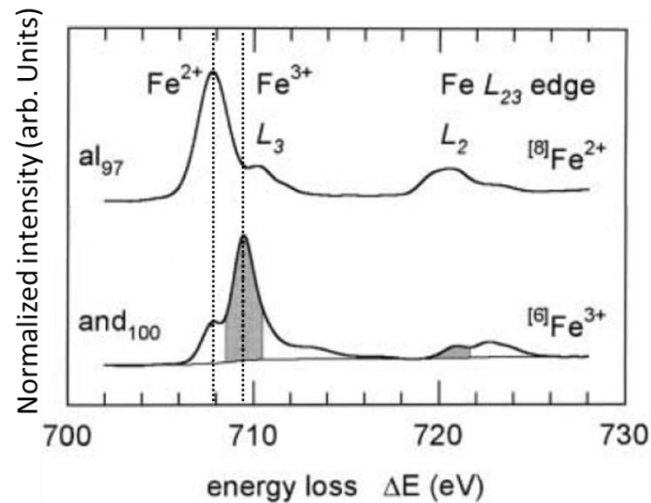


Figure 2.11 Fe $L_{2,3}$ edges from almandine and andradite, modified from Van Aken and Liebscher (2002). The dotted lines represent the position of the Fe L_3 white-line maxima located at 707.8 and 709.5 eV for Fe^{2+} and Fe^{3+} , respectively. The grey shaded areas represent the 2-eV-wide integration windows used for the $\text{Fe}^{3+}/\Sigma\text{Fe}$ quantification by applying the universal curve.

TEM thin foils were prepared using either a conventional Ar-milling or a focused ion beam (FIB) instrument. Ar-milling is a physical etching technique whereby the ions of an inert gas (typically Ar) are accelerated from a wide beam ion source into the surface of a substrate (or coated substrate) in vacuum in order to remove material to some desired depth or underlayer. FIB-SEM is a highly versatile tool in the field of materials research. It consists of a fully equipped scanning electron microscope incorporating a scanning ion beam column. The latter one allows imaging of the surface of the samples by ion induced secondary electrons as well as by secondary ions. Depending on the selected beam parameters, the focused ion beam is used to remove material from the sample. This, in conjunction with electron beam imaging enables structuring of the samples surface with an accuracy in the range of 10 nm. The combination of ion beam-cutting and electron imaging facilitates the highly localized metallographic sectioning of all materials accessible by scanning electron microscopy. Sequential sectioning and imaging are the fundament of the “slice and view” technique delivering three-dimensional microstructure information. Furthermore, thin lamellae for TEM investigations can be produced from relevant regions of devices or

materials by controlled thinning. Removal is done by means of an integrated micro manipulator with a Platinum needle.

ELNES spectra were collected using both a Philips *CM20FEG* equipped with a parallel electron energy-loss spectrometer, PEELS Gatan 666, and a FEI Titan G2 80-200 S/TEM equipped with an energy filter system, Gatan Quantum SE, operating at 200 kV. The TEM experiments were performed at -170 °C using a liquid-nitrogen-cooling holder. *Fe-L_{2,3}* edge ELNES spectra were collected in diffraction modes at the thinnest part of the ion-thinned sample. Quantification of the *Fe-L_{2,3}* edge ELNES was performed following the procedure described by Van Aken and Liebscher (2002), using an empirically calibrated universal curve. The EELSA program (<https://github.com/CPrescher/EELSA>), was used to evaluate the $Fe^{3+}/\Sigma Fe$ ratios reported in Table 4.1. The time-series analyses of the spectra showed that the measured ratios did not change remarkably with increasing electron irradiation time up to 80 secs of acquisition.

3 Phase assemblage and composition of recovered samples

3.1 Recovered phase assemblages from experiments to obtain single crystals

In the run products recovered from the synthesis experiments aimed at obtaining large single crystals (Table 3.1), melt coexisted with Brg due to the presence of water in the starting materials (Fig. 3.1). Runs S6631 and S7241 each contained an additional hydrous phase, which was identified by single crystal XRD to be phase D and superhydrous phase B (shy B), respectively (Table 3.1; Figure 3.1b, e). These hydrous phases were not observed in other runs. Phase D has the nominal composition $\text{MgSi}_2\text{O}_4(\text{OH})_2$ with approximately 10 wt.% H_2O , which has a stability field up to ~ 50 GPa (Frost, 1999; Frost and Fei, 1998) relatively high among the dense hydrous magnesium silicates (DHMS). Previous studies on the $\text{Mg}_2\text{SiO}_4\text{-H}_2\text{O}$ system have shown the stability limit of phase D of 1200-1400 °C at 24 GPa (Frost and Fei, 1998; Ohtani et al., 2000). A more recent study has shown that the addition of Al_2O_3 increases the stability temperature of phase D to 1600 °C in the Fe-free, Al-bearing bulk composition; while addition of FeO has an opposite effect, leading to the thermal stability of phase D in the $\text{FeO-MgO-Al}_2\text{O}_3\text{-SiO}_2\text{-H}_2\text{O}$ (FMASH) composition similar to those in the $\text{MgO-SiO}_2\text{-H}_2\text{O}$ (MSH) system between 1350 and 1400 °C at 24 GPa (Ghosh and Schmidt, 2014). All the starting materials for the purpose of synthesizing large Brg single crystals (Table 2.1 and 2.2) in this study contain both Fe and Al, therefore phase D in such bulk compositions should only be stable up to near 1350- 1400 °C at 25 GPa, this may explain why phase D only appears in run S6631 conducted at 1300 °C but not in other experiments conducted at higher temperatures (> 1400 °C) (Table 2.2). The water content of Phase D in S6631 with $(\text{Mg}+\text{Fe})/\text{Si}$ of 0.69 is about 14 wt.% as inferred from the total mass of EPMA analysis (Table 3.3) and single crystal XRD by Xcalibur diffractometer

confirmed the crystal structure with the $P31m$ symmetry (Boffa Ballaran et al., 2010). Shy B has a nominal composition of $Mg_{10}Si_3O_{14}(OH)_4$ containing approximately 6 wt.% H_2O (Gasparik, 1993). Although studies in the $MgO-SiO_2-H_2O$ system have shown that the stability temperature of shy B at 24-25 GPa is between 1200-1500 °C (Frost, 1999; Frost and Fei, 1998; Gasparik, 1993; Ohtani et al., 2003; Ohtani et al., 2001), the most recent study in the Al-bearing system indicated that the incorporation of Al would increase the stability field of shy B. Shy B can accommodate a significant amount of Al_2O_3 , up to 32 wt.%, and shy B with an Al content of 3.91 atoms pfu is still stable at 24 GPa and 2000 °C (Kakizawa et al., 2018). Moreover, the maximum water content appears to increase to 11.1 wt.% when Al=3 atoms pfu in Al-bearing shy B, which is 1.9 times higher than the content in the end-member $Mg_{10}Si_3O_{14}(OH)_4$ shy B (Kakizawa et al., 2018). The starting material of S7241 contained a large amount of Al_2O_3 (12.3 wt.%, Table 2.1, 2.2), resulting in the formation of Brg with Al_2O_3 as high as 9.3 wt.% (Table 3.3) and an additional Al-rich phase shy B containing 21.1 wt.% Al_2O_3 (or 2.8 pfu of Al normalized to 13 cations) with the presence of water at 25 GPa and 1600 °C. Considering the high Al content, the experimental conditions were well within the stability field of shy B. The water content is estimated to be 11.4 wt.%, inferred from the total mass of the EPMA analyses, and single crystal XRD using the Xcalibur diffractometer confirmed the shy B structure with the space group $Pn\bar{m}n$ (Pacalo and Parise, 1992). The Al_2O_3 content of the starting materials in other experiments were lower (<6 wt.%, Table 2.1, 2.2), therefore all of the Al could be incorporated into Brg and melt, and likely due to the resulting contraction in the stability field, shy B did not form.

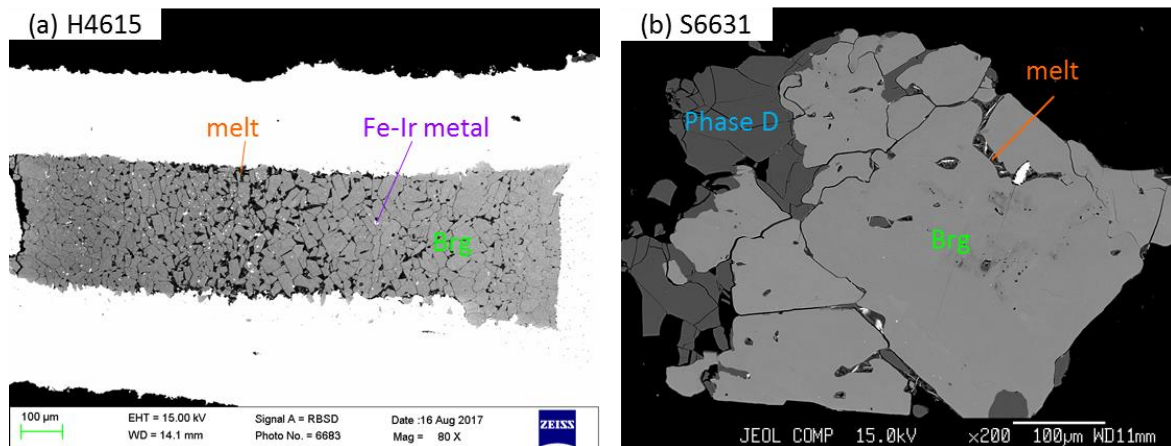
The other phases present in the run products from single crystal synthesis experiments include, melt, which crystallized to a fine-grained assemblage on quenching (e.g. Fig. 3.1c, d), ferropericlase (Fig. 3.1c), stishovite (Fig. 3.1d), and Fe metal (Fig. 3.1a). High quality bridgmanite crystals from 8 of the 12 synthesis experiments (Table 3.1 marked with superscripts ^a) were chosen for the single crystal XRD study described in detail in section 2.4. The remaining four experiments (Table 3.1 marked with superscripts ^b) provided unsuitable crystals and were only used to study the Fe-Mg partitioning between bridgmanite and melt, as discussed in detail in Chapter 6 (Table 3.3). These experiments contained Fp coexisting

with Brg and melt and the fraction of melt was sufficiently large enough to enable accurate compositions to be obtained by EPMA (Table 3.1, Figure 3.1c).

Table 3.1 Recovered phase assemblage in single crystal synthesis experiment conducted at 25 GPa.

Run No.	Recovered assemblages	Run No.	Recovered assemblages
S6631 ^a	Brg+Phase D+melt	S6813 ^b	Brg+Fp+melt
S6689 ^a	Brg+melt	S6833 ^b	Brg+Fp+Fe-Ir+melt
S6732 ^a	Brg+Phase D+Fp+melt	S6840 ^b	Brg+Fp+melt
S6805 ^a	Brg+Fp+St+melt	S6843 ^b	Brg+Fp+Fe-Ir+melt
S6848 ^{a, b}	Brg+Fp+Fe-Ir+melt		
S6838 ^a	Brg+St+melt		
H4615 ^a	Brg+Fe-Ir+melt		
S7241 ^a	Brg+shy B +melt		

Notes: ^aSamples chosen for single crystal X-ray diffraction measurements. ^bSamples used for Fe partitioning study. Brg=bridgmanite; Fp=ferropericlaese; St=stishovite; shy B=superhydrous Phase B; Fe-Ir=Fe-Ir metal alloys.



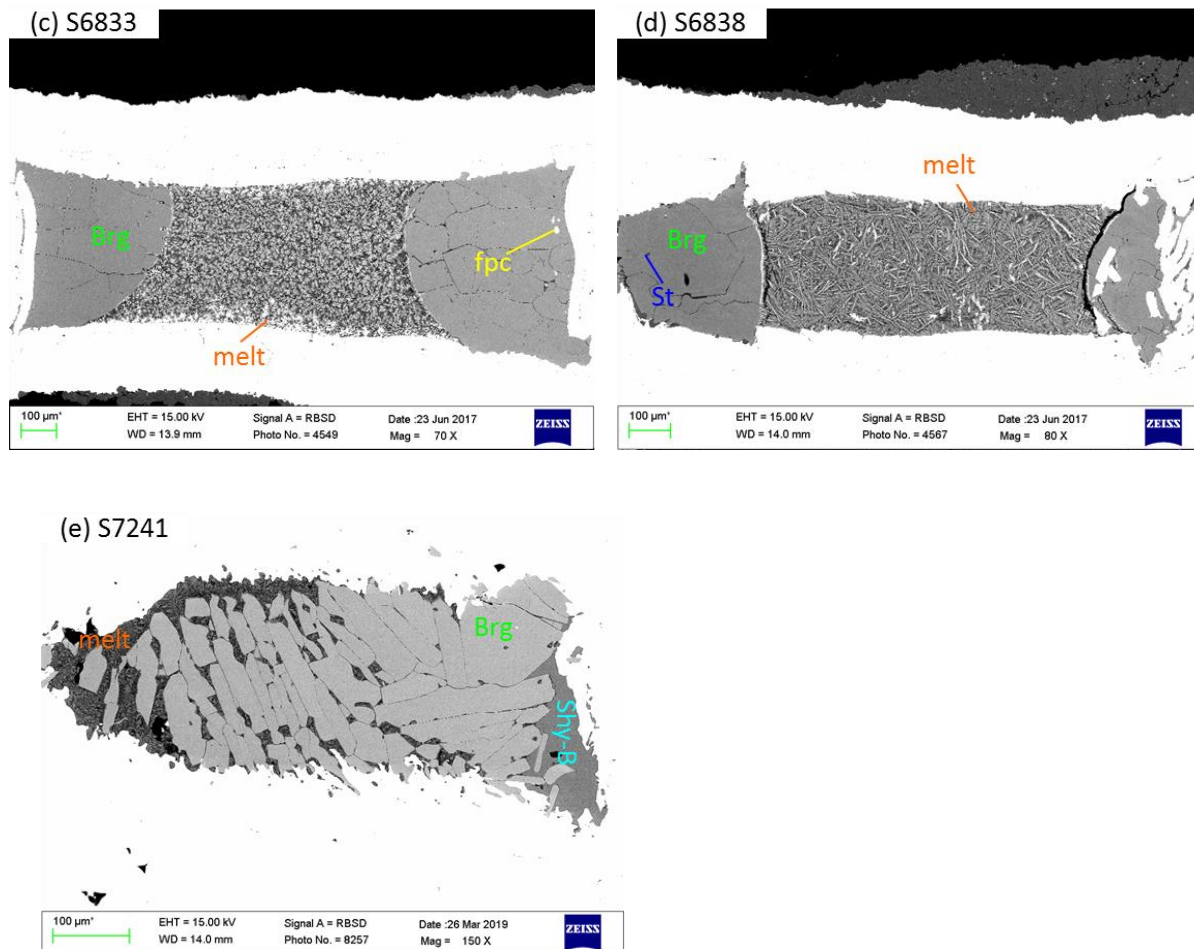


Figure 3.1 Selected back scattered images of recovered assemblage of Brg single crystal synthesis experiments: (a) Run H4615, Brg crystals (grey) coexist with Fe-Ir metal (bright) and minor amount of melt (dark). (b) Run S6631, large Brg crystals (bright) coexist with Phase D (dark) and minor amount of melt. (c) Run S6833, large Brg crystals (grey) coexist with minor amount of Fp (bright) and large amount of melt. (d) Run S6838, large Brg crystals (bright) coexist with minor amount of St (dark) and huge amount of melt. (e) Run S7241, Brg crystals (bright) coexist with Phase superhydrous phase B (dark) and melt. Abbreviations are the same with Table 3.1.

3.2 Recovered phase assemblages from oxygen fugacity buffered experiments

In all experiments where the oxygen fugacity was controlled or monitored, coexisting Brg and Fp were successfully recovered together with the buffering phases which were disperse throughout the charge (Table 3.2; Fig. 3.2). In the synthesis experiments performed with

Re+ReO₂ or Ru+RuO₂ oxygen buffers, both phases were present. For experiments in which 20 wt.% Fe₂O₃ was added as the buffer material, however, no hematite was observed in the run products and a (Mg,Fe)₂Fe₂O₅ phase belonging to the Mg₂Fe₂O₅-Fe₄O₅ join was present instead (Fig. 3.2b). A trace amount of carbon was observed in a few experimental charges indicating the presence of carbon in the starting material (Table 3.2), the carbon may come from the absorption of atmospheric CO₂ by the oxygen buffering materials and/or dust from the air during sample preparation. Carbon appeared as carbide Fe₃C in metal saturated experiments and as carbonate in higher oxygen fugacity experiments, which is discussed in detail in section 6.1 (Table 3.2). In the low Al and high Fe bearing experiments where the Ru/RuO₂ buffer was added (S7113, S7138-1, S7138-2, S7046), an extra phase, (Mg,Fe)(Fe,Ru,Si)₂O₄, was present which had the CaMn₂O₄ or CaTi₂O₄ structure (personal communication from Nobuyoshi Nakajima who performed electron diffraction using the TEM). A minor amount of majorite garnet with composition Mg_{2.8}Fe_{0.5}Al_{1.4}Si_{3.3}O₁₂ (H4746) and Mg_{2.7}Fe_{0.8}Al_{1.4}Si_{3.1}O₁₂ (S6920) was observed in experiments at reduced conditions when employing starting materials with Al₂O₃ contents higher than 5.9 wt.%. The Al content of the majorite phase was more than three times that of coexisting Brg, note that garnet was not present in experiments with similar starting compositions run at higher oxygen fugacities, implying that the formation of ferric iron expanded the Brg stability field. In experiment S7214 which had a starting composition containing 12.3 wt.% Al₂O₃, an Al-rich phase Mg_{1.37}Si_{0.42}Fe_{0.09}Al_{1.05}Ru_{0.07}O₄ with the CaFe₂O₄ structure was found to coexist with Brg and Fp. The run conditions and recovered phase assemblages are reported in Table 3.2.

Table 3.2 Recovered assemblages for experiments where the oxygen fugacities were controlled.

Run No.	buffer	Mineral assemblage ^a	log f_{O_2} (ΔIW)
S7122	Fe	Brg, Fp, Fe, Fe ₃ C	-0.71 (25)
S7251	ReO ₂	Brg, Fp, Re, ReO ₂	4.05 (52)
S7262	ReO ₂	Brg, Fp, Re, ReO ₂	4.05 (52)
S7113-2	Ru-RuO ₂	Brg, Fp, Ru, RuO ₂ , Mst, CT/CM	7.65 (31)
S7138-1	Ru-RuO ₂	Brg, Fp, Ru, RuO ₂ , Mst, CT/CM	7.65 (31)
S7120	PtO ₂	Brg, Fp, Pt, Mst	8.75 (87)
H4737	Fe	Brg, Fp, Fe, Fe ₃ C	-0.93 (13)
S7132-2	Fe	Brg, Fp, Fe, Fe ₃ C	-0.82 (14)
S7021	Ir	Brg, Fp, Fe-Ir alloy	2.30 (82)
S7028	Ru-RuO ₂	Brg, Fp, Ru, RuO ₂ , Mst	7.65 (31)
H4755	Fe	Brg, Fp, Fe, Fe ₃ C	-0.64 (5)
S7132-1	Fe	Brg, Fp, Fe, Fe ₃ C	-0.67 (6)
S7046	Ru-RuO ₂	Brg, Fp, Ru, RuO ₂ , Mst, CT/CM	7.65 (31)
S7138-2	Ru-RuO ₂	Brg, Fp, Ru, RuO ₂ , Mst, CT/CM	7.65 (31)
H4746	Fe	Brg, Fp, Fe, Fe ₃ C, Mj	-0.60 (5)
S7209	Fe	Brg, Fp, Fe	-0.89 (5)
S6920	Fe+Ir	Brg, Fp, Fe-Ir alloy, Fe ₃ C, Mj	-0.14 (11)
S6907	Ir	Brg, Fp, Mst, Fe-Ir alloy	2.70 (73)
S6921	Fe ₂ O ₃	Brg, Fp, (Mg,Fe) ₄ O ₅ , Mst	4.90 (66)
S6950-1	Fe ₂ O ₃	Brg, Fp, (Mg,Fe) ₄ O ₅ , Mst, Fe-Ir alloy	3.95 (34)
S6950-2	Fe ₂ O ₃	Brg, Fp, (Mg,Fe) ₄ O ₅ , Mst, Fe-Pt alloy	3.61 (30)
S6952	Ru-RuO ₂	Brg, Fp, Ru, RuO ₂ , Mst	7.65 (30)
S7214	Ru-RuO ₂	Brg, Fp, Mst, CF, Ru, RuO ₂	7.65 (31)

Notes: Brg: bridgmanite; Fp: ferroperricite; Mst: magnesite; Mj: majorite garnet; CF: (Mg,Fe)₂SiO₄-(Mg,Fe)Al₂O₄ solid solution with the CaFe₂O₄ structure; CT/CM: (Mg,Fe)(Fe,Ru,Si)O₄ phase with CaTi₂O₄ or CaMn₂O₄ structure.

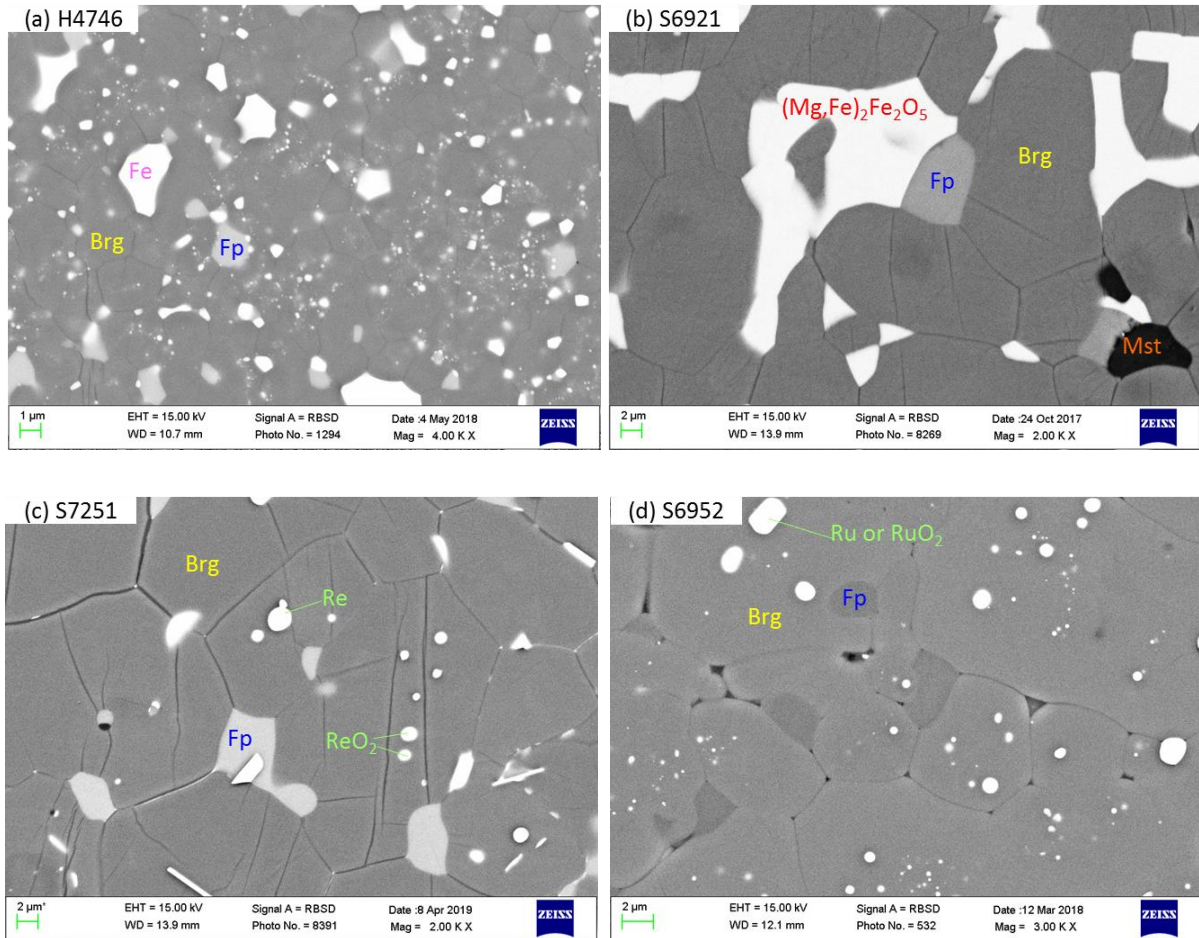


Fig. 3.2 Back-scattered electron images of experimental run products obtained at different oxygen fugacities: (a) Run H4746: low oxygen fugacity buffered by Fe metal. (b) Run S6921: Hematite was added and reduced to $(\text{Mg,Fe})_2\text{Fe}_2\text{O}_5$ phase, carbon exists as magnesite. (c) Run S7251: Middle oxygen fugacity buffered by the coexisting of Re and ReO_2 . (d) Run S6952: High oxygen fugacity achieved by the coexistence of Ru-RuO₂ buffer. In all of the experiments, the buffer materials were well mixed with the starting material and dispersed throughout the sample to minimize the diffusion pathways. Abbreviations: Brg, bridgmanite; Fp, ferropericlae; Mst, magnesite.

3.3 Composition of run products

The compositions, measured by EPMA, of each phase in the recovered assemblages are summarized in Table 3.3 and Table 3.4. The details of the measurements can be found in chapter 2.3.2. Table 3.3 shows the results from experiments aiming at synthesizing large bridgmanite single crystals. In general, more than 20 points were measured for each phase in the experiment and the 1 sigma standard deviations of these analyses are shown. For

some phases, only a few points could be measured due to only minor amounts of suitably sized crystals being present. Quenched crystals from melts were measured with a 30- μm diameter defocused beam in order to get an average composition. When melt was present only in small amounts, a smaller beam size of 10- μm was used. Table 3.4 shows results from experiments studying the effect of composition and oxygen fugacity on the $\text{Fe}^{3+}/\Sigma\text{Fe}$ ratio in bridgmanite.

Table 3.3 Phase compositions in wt.% measured by EPMA and cation proportions normalized by number of cations per formula unit. All Fe (Σ Fe) is treated as FeO. No. represents the number of points measured for each phase and the number in parenthesis are 1 standard deviation of the analysis. Abbreviations are the same as in Table 3.1.

Run #	Phases	No.	MgO	SiO ₂	FeO	Al ₂ O ₃	Total	Mg	Si	Fe	Al	Σ Cation
S6631	Brg	25	28.3(4)	44.4(3)	17.2(6)	9.2(2)	99.2(6)	0.753(7)	0.794(6)	0.258(8)	0.194(4)	2.00
	Phase D	22	19.0(3)	48.8(5)	6.2(3)	12.1(4)	86.0(5)	0.882(8)	1.516(16)	0.160(7)	0.441(15)	3.00
S6689	Brg	26	37.7(3)	56.0(4)	3.6(2)	2.7(2)	100.0(4)	0.948(5)	0.947(5)	0.050(3)	0.055(3)	2.00
S6732	Brg	41	34.7(4)	54.9(6)	8.3(5)	2.3(2)	100.2(7)	0.890(8)	0.944(8)	0.119(7)	0.047(4)	2.00
	Fp	25	34.0(6)	0.05(3)	67.7(9)	0.03(3)	101.7(10)	0.472(6)	0.0005(2)	0.528(6)	0.0003(3)	1.00
	Phase D	2	21.3(1)	57.4(3)	3.4(1)	4.52(1)	86.6(1)	0.978(6)	1.769(9)	0.088(3)	0.1642(2)	3.00
	Melt (10 μ m)	10	23.2(5)	56.0(5)	3.59(2)	4.5(3)	87.1(8)	0.350(4)	0.567(4)	0.030(2)	0.054(4)	1.00
S6805	Brg	31	31.9(4)	53.4(4)	11.0(5)	3.49(2)	99.7(7)	0.834(7)	0.936(7)	0.161(6)	0.070(4)	2.00
	Fp	14	28.1(3)	0.05(3)	71.7(6)	0.10(3)	100.0(5)	0.411(4)	0.0005(3)	0.588(4)	0.0011(3)	1.00
	St	10	0.03(4)	98.8(6)	1.1(4)	1.3(2)	101.2(7)	0.0004(6)	0.975(5)	0.009(3)	0.015(2)	1.00
S6813	Brg	41	32.8(5)	52.7(5)	11.0(5)	3.4(2)	99.9(7)	0.852(8)	0.919(9)	0.160(6)	0.069(3)	2.00
	Fp	23	33.7(7)	0.13(7)	66.7(8)	0.13(4)	100.6(9)	0.472(6)	0.0015(6)	0.525(6)	0.0012(4)	1.00
	Melt (30 μ m)	14	26.0(11)	23.3(20)	28.1(23)	1.5(4)	78.9(37)	0.445(26)	0.266(15)	0.269(17)	0.020(5)	1.00
S6833	Brg	61	33.0(3)	53.2(3)	10.6(4)	3.3(2)	100.2(7)	0.854(5)	0.924(6)	0.155(6)	0.067(3)	2.00
	Fp	7	35.8(3)	0.14(4)	65.0(11)	0.12(2)	101.0(13)	0.494(3)	0.0013(4)	0.503(4)	0.0013(2)	2.00
	Melt (30 μ m)	99	27.4(13)	22.9(20)	28.9(20)	1.6(4)	80.7(31)	0.455(18)	0.255(19)	0.269(15)	0.021(5)	2.00

(continued on next page)

Table 3.3 (Continued)

Run #	Phases	No.	MgO	SiO ₂	FeO	Al ₂ O ₃	Total	Mg	Si	Fe	Al	ΣCation
S6840	Brg	25	33.1(2)	52.2(4)	10.5(4)	3.2(2)	99.0(6)	0.866(4)	0.914(8)	0.154(6)	0.067(4)	2.00
	Fp	4	33.7(4)	0.08(2)	67.0(9)	0.10(2)	100.9(8)	0.472(5)	0.0008(2)	0.527(5)	0.0011(2)	1.00
	Melt (30 μm)	28	28.6(13)	21.7(14)	27.5(24)	1.6(1)	79.4(18)	0.478(23)	0.243(15)	0.257(22)	0.022(2)	1.00
S6843	Brg	32	33.1(4)	53.1(4)	10.5(5)	3.3(2)	99.9(8)	0.858(6)	0.923(6)	0.152(6)	0.067(4)	2.00
	Fp	18	31.3(3)	0.05(3)	69.0(9)	0.09(3)	100.4(9)	0.446(4)	0.0005(3)	0.552(4)	0.0010(4)	1.00
	Melt (30 μm)	6	28.3(11)	22.4(25)	27.2(40)	1.9(2)	79.2(22)	0.471(19)	0.250(28)	0.254(37)	0.026(2)	1.00
S6848	Brg	22	33.3(4)	54.0(4)	10.1(5)	3.3(2)	100.7(6)	0.857(8)	0.931(6)	0.145(7)	0.067(5)	2.00
	Fp	17	40.9(3)	0.06(3)	59.6(8)	0.10(3)	100.7(9)	0.549(4)	0.0005(3)	0.449(4)	0.0011(3)	1.00
	melt	5	31.8(11)	21.2(16)	27.7(31)	1.5(8)	82.3(35)	0.506(17)	0.227(17)	0.248(27)	0.019(11)	1.00
S6838	Brg	33	32.4(5)	49.6(5)	13.2(7)	3.8(1)	99.1(7)	0.850(9)	0.875(5)	0.195(11)	0.080(3)	2.00
	St	9	0.02(1)	98.5(7)	0.3(1)	0.55(5)	99.4(7)	0.0003(2)	0.990(1)	0.003(1)	0.006(1)	1.00
	Melt (30 μm)	97	29.3(15)	19.0(14)	28.2(24)	0.6(1)	77.0(15)	0.503(23)	0.218(17)	0.271(23)	0.008(1)	1.00
H4615	Brg	25	34.2(3)	51.7(3)	8.1(4)	5.7(2)	99.7(7)	0.879(5)	0.889(6)	0.117(5)	0.115(4)	2.00
S7241	Brg	37	33.9(3)	48.8(4)	7.8(4)	9.3(3)	99.9(5)	0.865(6)	0.835(7)	0.112(5)	0.188(6)	2.00
	shy B	17	47.2(3)	18.2(2)	2.0(2)	21.1(2)	88.6(5)	7.948(35)	2.056(23)	0.191(23)	2.804(27)	13.00
	Melt (10 μm)	13	45.5(14)	15.3(8)	1.9(3)	7.8(4)	70.5(17)	0.722(11)	0.163(7)	0.017(3)	0.097(5)	1.00

Table 3.4 Composition of bridgmanite, ferropericlase, magnesite and oxides of run products in wt.% and cation proportions normalized by number of cations per formula unit obtained from oxygen fugacity buffered experiments. No. represents the number of points measured for each phase and the number in parenthesis are 1 standard deviation of the analysis. The abbreviations are the same as in Table 3.2.

Run #	Phase	No.	MgO	SiO ₂	FeO	Al ₂ O ₃	RuO ₂	Total	Mg	Si	Fe	Al	Ru	ΣCat
S7122	Brg	27	35.3(4)	56.8(4)	6.7(4)	-	-	98.8(5)	0.915(8)	0.988(8)	0.098(5)	-	-	2.00
	Fp	19	57.8(106)	0.2(1)	41.2(104)	-	-	99.1(7)	0.708(88)	0.001(1)	0.290(89)	-	-	1.00
S7251	Brg	29	36.7(4)	57.0(5)	6.3(5)	-	-	100.0(7)	0.935(7)	0.975(7)	0.091(7)	-	-	2.00
	Fp	16	64.5(12)	0.2(3)	35.9(12)	-	-	100.7(7)	0.760(9)	0.002(2)	0.238(9)	-	-	1.00
S7262	Brg	59	36.7(4)	57.7(5)	6.2(5)	-	-	100.6(6)	0.931(6)	0.981(7)	0.088(8)	-	-	2.00
	Fp	34	58.3(12)	0.1(1)	42.1(11)	-	-	100.05(6)	0.711(10)	0.001(1)	0.288(9)	-	-	1.00
S7113-2	Brg	36	38.1(4)	57.7(5)	4.0(5)	-	-	99.9(6)	0.964(9)	0.979(7)	0.057(7)	-	-	2.00
	Fp	18	90.9(7)	0.2(1)	8.5(4)	-	-	99.5(6)	0.949(2)	0.001(1)	0.050(2)	-	-	1.00
	Mst	4	46.4(6)	1.2(6)	1.0(1)	-	-	48.6(7)	0.971(10)	0.017(9)	0.012(1)	-	-	1.00
	CT/CM	6	15.7(5)	1.1(2)	45.2(12)	-	34.0(35)	96.0(24)	0.921(17)	0.040(6)	1.484(19)	-	0.555(13)	3.00
S7138-1	Brg	41	38.3(4)	58.1(5)	4.0(4)	-	-	100.4(7)	0.963(8)	0.980(8)	0.056(5)	-	-	2.00
	Fp	24	91.7(4)	0.1(2)	7.8(3)	-	-	99.6(5)	0.954(2)	0.001(1)	0.045(2)	-	-	1.00
	Mst	2	46.87(4)	0.05(3)	0.85(4)	-	-	47.77(5)	0.989(0)	0.001(0)	0.010(0)	-	-	1.00
	CT/CM	8	14.5(5)	1.0(6)	46.3(7)	-	32.5(7)	94.2(10)	0.853(25)	0.038(23)	1.530(34)	-	0.579(11)	2.42
S7120	Brg	37	36.8(3)	54.9(5)	7.3(5)	-	-	99.0(5)	0.946(6)	0.949(8)	0.105(8)	-	-	2.00
	Fp	5	86.2(2)	0.1(0)	12.2(2)	-	-	98.5(1)	0.926(1)	0.001(0)	0.074(1)	-	-	1.00
	Mst	30	47.3(4)	0.1(4)	0.7(1)	-	-	48.2(5)	0.991(2)	0.001(1)	0.008(2)	-	-	1.00
H4737	Brg	18	37.0(5)	55.6(5)	4.9(3)	3.8(4)	-	101.3(6)	0.925(11)	0.932(7)	0.069(5)	0.074(8)	-	2.00
	Fp	16	70.1(4)	0.2(2)	30.5(6)	0.3(1)	-	101.1(5)	0.800(4)	0.002(2)	0.195(4)	0.003(0)	-	1.00
S7132-2	Brg	19	36.8(4)	55.8(5)	4.9(2)	3.7(4)	-	101.2(5)	0.921(7)	0.937(9)	0.068(2)	0.073(8)	-	2.00
	Fp	22	64.3(58)	0.3(4)	36.2(57)	0.4(1)	-	101.2(7)	0.754(44)	0.002(3)	0.240(44)	0.004(1)	-	1.00

(continued on next page)

Table 3.4 (Continued)

Run #	Phase	No.	MgO	SiO ₂	FeO	Al ₂ O ₃	RuO ₂	Total	Mg	Si	Fe	Al	Ru	ΣCat
S7021	Brg	23	36.9(6)	56.8(6)	4.2(3)	3.5(6)	-	101.4(4)	0.921(13)	0.951(10)	0.059(4)	0.069(11)	-	2.00
	Fp	12	81.8(9)	0.3(4)	18.8(8)	0.2(1)	-	101.1(6)	0.882(5)	0.002(3)	0.113(5)	0.002(1)	-	1.00
S7028	Brg	17	36.8(2)	55.3(6)	5.4(4)	3.3(2)	-	100.9(6)	0.925(6)	0.932(7)	0.076(5)	0.066(4)	-	2.00
	Fp	16	92.5(5)	0.3(4)	6.4(2)	0.1(0)	-	99.3(6)	0.961(1)	0.001(1)	0.037(1)	0.001(0)	-	1.00
	Mst	14	47.6(5)	0.3(4)	0.6(1)	0.0(0)	-	48.5(6)	0.990(3)	0.003(3)	0.007(2)	0.000(0)	-	1.00
H4755	Brg	15	35.7(4)	54.893	7.0(5)	3.7(4)	-	101.2(4)	0.900(7)	0.928(4)	0.099(7)	0.074(8)	-	2.00
	Fp	17	54.2(8)	0.2(2)	46.5(8)	0.5(1)	-	101.3(4)	0.671(7)	0.001(2)	0.323(7)	0.005(1)	-	1.00
S7132-1	Brg	37	35.0(7)	55.3(5)	7.0(6)	3.9(4)	-	101.2(6)	0.886(14)	0.938(9)	0.099(8)	0.077(8)	-	2.00
	Fp	27	55.8(26)	0.1(1)	45.0(26)	0.3(0)	-	101.3(7)	0.685(22)	0.001(1)	0.311(22)	0.003(0)	-	1.00
S7046	Brg	27	36.0(3)	53.0(4)	6.9(3)	3.4(1)	-	99.2(6)	0.922(6)	0.911(6)	0.099(4)	0.069(2)	-	2.00
	Fp	29	88.9(5)	0.1(1)	9.7(4)	0.1(0)	-	98.8(5)	0.941(3)	0.001(0)	0.057(3)	0.001(0)	-	1.00
	Mst	29	46.9(4)	0.2(2)	1.1(2)	0.0(0)	-	48.2(5)	0.985(5)	0.000(1)	0.013(2)	0.002(3)	-	1.00
S7138-2	Brg	37	35.9(3)	53.7(4)	6.7(4)	3.3(1)	-	99.6(5)	0.918(5)	0.920(6)	0.096(5)	0.067(2)	-	2.00
	Fp	27	90.5(5)	0.1(1)	8.7(3)	0.0(0)	0.8(4)	100.1(7)	0.946(2)	0.000(1)	0.051(2)	0.000(0)	0.003(1)	1.00
	Mst	23	47.7(5)	0.0(1)	0.8(1)	-	-	48.6(5)	0.989(2)	0.001(1)	0.010(1)	-	-	1.00
	CT/CM	23	15.0(3)	0.8(2)	48.0(12)	-	30.2(6)	94.0(10)	0.874(17)	0.030(7)	1.565(24)	-	0.531(13)	3.00
H4746	Brg	23	34.2(6)	52.8(8)	8.2(7)	5.5(5)	-	100.6(8)	0.870(10)	0.902(12)	0.118(10)	0.110(9)	-	2.00
	Fp	23	51.4(19)	0.2(2)	49.1(19)	0.3(0)	-	100.9(6)	0.648(17)	0.001(2)	0.347(17)	0.003(0)	-	1.00
	Mj	18	26.8(5)	46.9(7)	9.1(6)	17.2(9)	-	100.0(7)	2.790(47)	3.273(42)	0.528(39)	1.409(67)	-	8.00
S7209	Brg	38	33.3(4)	52.4(4)	8.3(7)	5.8(2)	-	99.8(7)	0.856(7)	0.904(8)	0.120(10)	0.119(3)	-	2.00
	Fp	24	62.6(10)	0.2(1)	35.8(12)	1.6(1)	-	100.3(6)	0.744(8)	0.002(1)	0.239(9)	0.015(1)	-	1.00
S6920	Brg	15	33.7(5)	53.1(4)	8.4(5)	6.1(4)	-	101.3(5)	0.855(10)	0.903(8)	0.119(7)	0.123(8)	-	2.00
	Fp	17	41.0(4)	0.1(1)	58.3(9)	0.5(1)	-	100.0(10)	0.552(5)	0.001(1)	0.441(5)	0.006(1)	-	1.00

(continued on next page)

Table 3.4 (Continued)

Run #	Phase	No.	MgO	SiO ₂	FeO	Al ₂ O ₃	RuO ₂	Total	Mg	Si	Fe	Al	Ru	ΣCat
	Mj	1	25.7	45.09	12.91	17.55	-	101.2	2.668	3.140	0.752	1.440	-	8.00
S6907	Brg	21	34.4(4)	52.2(4)	7.5(4)	5.6(2)	-	99.6(7)	0.882(6)	0.897(7)	0.108(6)	0.113(3)	-	2.00
	Fp	15	81.8(5)	0.12(8)	18.3(5)	0.25(5)	-	100.4(9)	0.886(2)	0.001(1)	0.111(2)	0.002(0)	-	1.00
	Mst	3	46.9(2)	0.6(2)	1.94(2)	-	-	49.4(4)	0.969(3)	0.008(3)	0.023(0)	-	-	1.00
S6921	Brg	34	31.7(5)	49.8(4)	14.8(6)	5.1(1)	-	101.4(4)	0.818(9)	0.863(6)	0.214(9)	0.105(3)	-	2.00
	Fp	12	71.1(4)	0.5(1)	29.5(4)	0.3(0)	-	101.4(5)	0.806(3)	0.004(1)	0.188(3)	0.003(0)	-	1.00
	(Mg,Fe) ₄ O ₅	19	22.0(3)	1.7(1)	69.2(8)	1.5(1)	-	94.3(8)	1.394(14)	0.073(4)	2.460(14)	0.073(4)	-	4.00
	Mst	17	46.0(4)	0.1(1)	3.7(6)	0.03(2)	-	49.8(7)	0.955(6)	0.000(0)	0.043(7)	0.002(2)	-	1.00
S6950-1	Brg	16	31.1(4)	49.3(3)	14.5(6)	5.3(1)	-	100.1(9)	0.813(4)	0.865(7)	0.212(7)	0.109(3)	-	2.00
	Fp	11	32.2(4)	0.34(6)	67.7(9)	0.15(4)	-	100.3(11)	0.457(4)	0.003(1)	0.538(4)	0.002(0)	-	1.00
	(Mg,Fe) ₄ O ₅	13	9.5(3)	1.6(2)	81.3(7)	1.3(1)	-	93.6(7)	0.664(19)	0.073(8)	3.194(22)	0.069(4)	-	4.00
	Mst	7	45.3(4)	0.3(2)	5.1(3)	0.03(2)	-	50.7(5)	0.936(4)	0.004(3)	0.059(3)	0.001(0)	-	1.00
S6950-2	Brg	18	28.8(5)	50.0(4)	16.6(5)	5.2(1)	-	100.6(9)	0.759(9)	0.886(7)	0.247(8)	0.108(3)	-	2.00
	Fp	7	22.5(3)	0.6(3)	75.7(6)	0.16(4)	-	99.1(5)	0.343(3)	0.007(3)	0.648(6)	0.002(0)	-	1.00
	(Mg,Fe) ₄ O ₅	9	8.4(2)	1.9(3)	81.3(11)	1.0(1)	-	92.6(12)	0.599(15)	0.092(15)	3.252(23)	0.057(6)	-	4.00
	Mst	12	43.0(4)	0.1(2)	8.1(4)	0.10(4)	-	51.3(4)	0.902(6)	0.002(3)	0.095(4)	0.002(1)	-	1.00
S6952	Brg	37	34.7(4)	50.9(4)	8.6(3)	5.6(2)	-	99.8(7)	0.889(5)	0.875(5)	0.124(4)	0.113(3)	-	2.00
	Fp	22	91.7(6)	0.2(2)	7.1(3)	0.3(0)	-	99.3(7)	0.955(2)	0.001(1)	0.041(2)	0.002(2)	-	1.00
	Mst	17	46.1(4)	0.2(2)	0.9(2)	0(0)	-	47.3(5)	0.986(4)	0.003(3)	0.011(2)	0.001(1)	-	1.00
S7214	Brg	42	32.3(3)	46.2(4)	8.0(4)	11.2(4)	1.1(2)	98.8(6)	0.840(6)	0.804(7)	0.116(6)	0.231(7)	0.009(2)	2.00
	Fp	35	89.7(7)	0.2(3)	3.8(3)	1.9(1)	4.5(2)	100.2(7)	0.945(3)	0.002(2)	0.023(1)	0.016(1)	0.014(1)	1.00
	CF	19	36.3(4)	16.7(2)	4.4(3)	35.2(3)	6.5(3)	99.1(6)	1.367(7)	0.421(5)	0.092(5)	1.046(8)	0.074(3)	3.00
	Mst	11	46.3(9)	0.5(4)	0.6(2)	0.4(1)	0.4(6)	48.1(9)	0.977(9)	0.006(5)	0.007(2)	0.007(2)	0.003(4)	1.00

3.4 Fe³⁺/ΣFe determination in bridgmanite

As mentioned in section 2.5.1, either single Brg crystals or thin sections comprise mainly of Brg and Fp were used for Mössbauer measurement for single crystal synthesis experiments. All Mössbauer spectra present two main quadrupole doublets corresponding to high-spin (HS) Fe²⁺ (chemical shift (CS)=1.01-1.15 mm/s, quadrupole splitting (QS)=1.69-1.99 mm/s) and HS Fe³⁺ (CS=0.45 mm/s, QS=0.87-0.90 mm/s) which are consistent with these cations occupying the A site of Brg. These hyperfine parameters are in excellent agreement with values reported for bridgmanite in previous studies (see for example McCammon et al., 2013). These are the only features present in the spectra collected for samples S6689, S6631, and H4615 and S7241 (Fig. 3.3a). For sample S6848 an additional doublet with CS=0.965 mm/s and QS=0.962 mm/s is visible (Fig. 3.3b) and can be assigned to Fe²⁺ in ferropericlase. Finally the Mössbauer spectrum of sample S6838 presents two additional doublets (Fig. 3.3c), one with relatively low CS=0.183 mm/s and QS=0.590 mm/s which may be attributed to Fe³⁺ at the B site of Brg (Kupenko et al., 2015) in agreement with the EPMA analysis and the other with relatively larger CS=1.089 mm/s and QS=2.350 mm/s which may also be assigned to Fe²⁺ in the A site in Brg. It has been reported that the signal of Fe²⁺ present at the A site of bridgmanite may be very broad due to the slightly different coordination environment around the Fe²⁺ atoms and therefore it may be better described using 2 doublets instead of only one (McCammon et al., 2013). The Fe³⁺/ΣFe ratios of the bridgmanite samples used in this study were determined from the relative areas of their Fe³⁺ and Fe²⁺ Mössbauer components and are reported in Table 4.1.

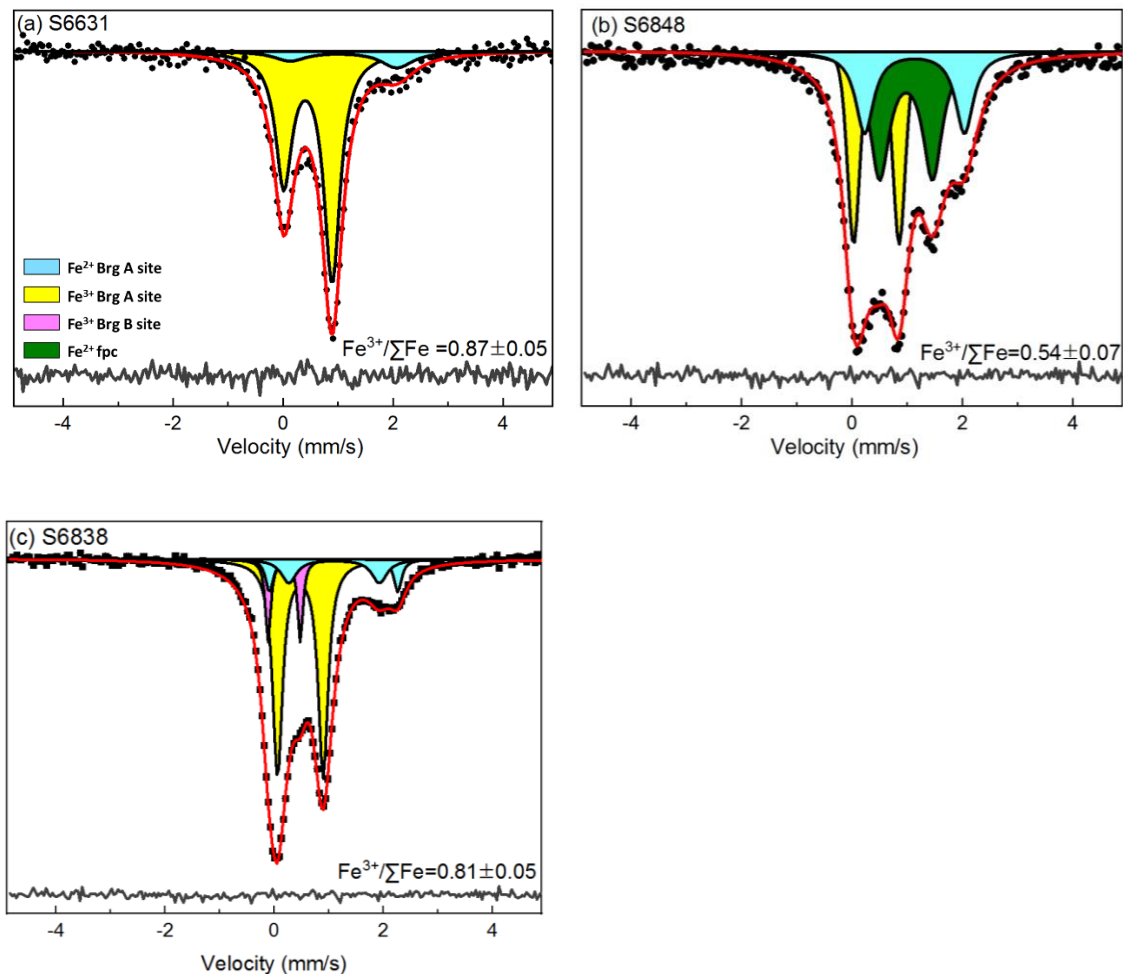


Figure 3.3 Selected Mössbauer spectra of Fe, Al-bearing Brg at Room temperature: (a) S6631; (b) S6648; (c) S6638. Experimental data are indicated by solid circles while the fitted curve is shown by the red thick solid line. Components are shaded as indicated and the fitting residual is shown beneath each spectrum. For S6631, single crystal of Brg was used for the measurement thus the doublet is asymmetric and the ratio between the two peaks of the doublet of Fe³⁺ and Fe²⁺ in Brg was constrained to be equal. For S6848 and S6838, the bulk sample assemblages in the capsule were used, therefore, other Fe component of coexisting phases like the Fp was also detected and shown in the spectrum.

Selected Mössbauer spectra collected at room temperature for the samples synthesized in oxygen fugacity controlling experiments are shown in Fig. 3.4. Because the bulk assemblages were measured, peaks from all iron-containing phases are present. Mössbauer spectra were deconvoluted using the minimum number of components (quadrupole doublets and magnetic sextets) required to achieve statistically acceptable fits to the data. The full transmission integral was used and conventional constraints for quadrupole

doublets (i.e. components constrained to equal width and area) were applied. In many cases, three doublets were used to fit the spectra: one corresponding to Fe³⁺ in Brg and two to Fe²⁺ in Brg and Fp respectively. In a few spectra, some hyperfine parameters had to be constrained due to peak overlap or weak peak intensity (Table 3.5). Derived hyperfine parameters are listed in Table 3.5 and compared with data for Brg in the literature (reviewed by McCammon et al., 2013) in Fig. 3.4d. In the Brg samples measured in this study, the hyperfine parameters for Fe²⁺ (center shift (CS)= ~ 1.1 mm/s, quadrupole splitting (QS)=1.60-2.30 mm/s) and Fe³⁺ (CS=0.33-0.51 mm/s, QS=0.29-0.96 mm/s) are in good agreement with previous studies. While the hyperfine parameters allow Fe²⁺ to be assigned unambiguously to the A site (8-12 coordinated), the location of Fe³⁺ in the perovskite-type structure is difficult to resolve from QS values alone because high-spin Fe³⁺ in both the A and B sites have low values of QS (Lin et al., 2012; McCammon, 1998). The Fe³⁺/ΣFe ratios in Brg then determined from the relative areas of Fe²⁺ and Fe³⁺ Brg components are reported in Table 3.5. Uncertainties were estimated based on fit statistics and from the uncertainties in the fitting model itself.

No peaks from carbonate were observed in the spectra, most likely because the Fe contents measured for the carbonates in the experiments were always less than 2 mol% (Table 3.4). Samples saturated with Fe metal show additional peaks indicating magnetically ordered phases (Fig. 3.4a), which were fitted to one or two magnetic sextets. The phase with the larger hyperfine magnetic field of $H = \sim 33$ T could be assigned to Fe metal and the other phase with a smaller hyperfine magnetic field of $H = \sim 20$ T could be assigned to Fe⁰ in carbides. In certain spectra, the Fe bearing phase (Mg,Fe)(Fe, Ru, Si)₂O₄ (S7113-2, S7138-1) or (Mg,Fe)₂(Fe, Al, Si)₂O₅ (S6921, S6950-1, S6950-2) also exist. However, the hyperfine parameters of these phases are not well constrained and couldn't be separated from the current spectra, therefore we assume all the peaks of these samples are from Brg and Fp in the fitting process.

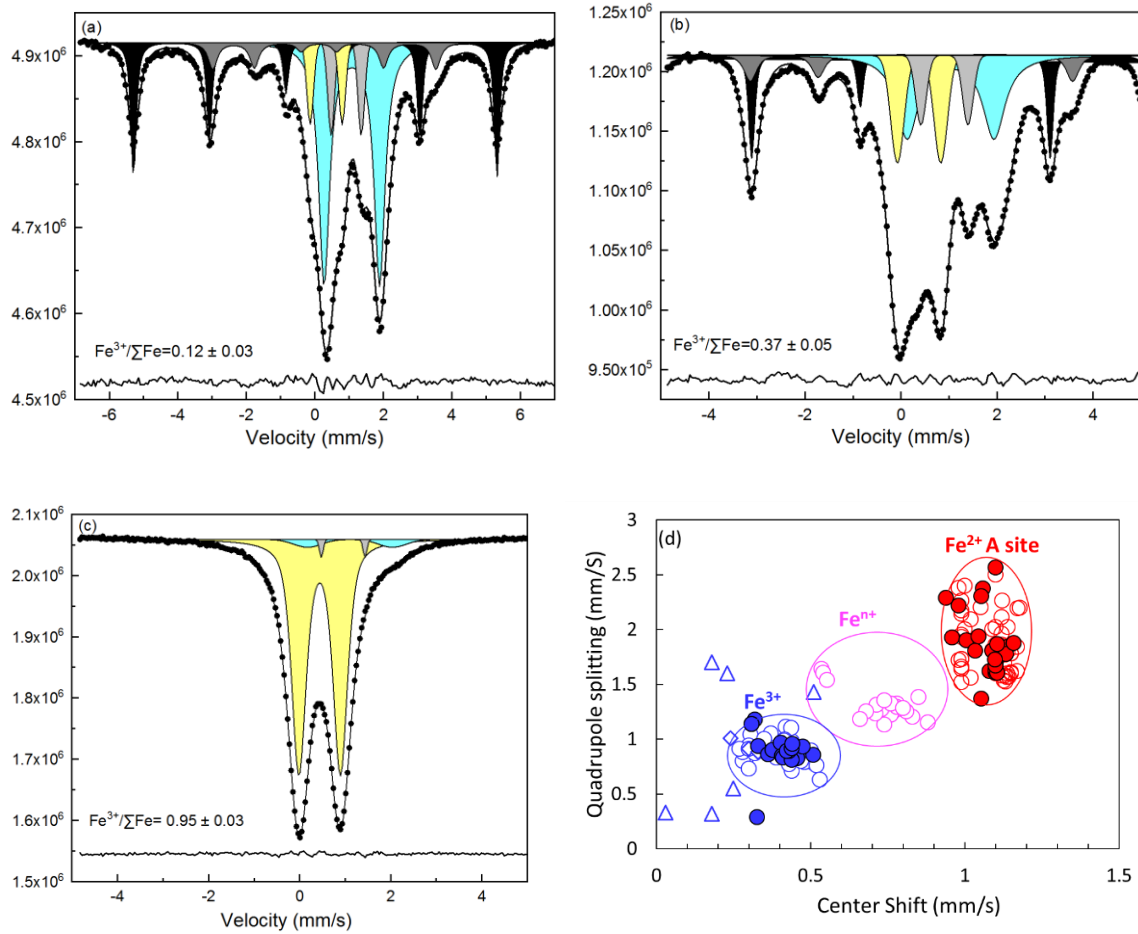


Figure 3.4 Representative room temperature Mössbauer spectra of run products: (a) S7122 (Brg+Fp+Fe+carbide) (b) H4755 (Brg+Fp+Fe+carbide) (c) S6952 (Brg+Fp) (d) Hyperfine parameters of Brg from Mössbauer spectra collected at ambient conditions. Solid red and blue circle indicate the parameters of Fe^{2+} on the A site and Fe^{3+} in Brg obtained from this study respectively. Open red, pink and blue circles indicate the Brg Fe_A^{2+} , Fe^{n+} , and Fe^{3+} parameters from previous studies of Fei et al. (1994); Jackson et al. (2005); Lauterbach et al. (2000); Li et al. (2006); McCammon (1997, 1998); McCammon et al. (1992, 2004b) and Narygina et al. (2010). The blue triangle and diamond represent the parameters of Fe^{3+} on the A site and B site in Brg proposed by Hummer and Fei (2012).

Table 3.5 Hyperfine parameters derived from fitting to Mössbauer spectra.

Run No.	CS (mm/s)	FWHM (mm/s)	QS or ϵ (mm/s)	BHF (T)	χ^2	Site assignment	Fe ³⁺ / Σ Fe Brg	in
S7122	0.00(1)	0.19(5)	0.02(1)	32.89(3)	2.8	Fe ⁰ alloy	0.12(3)	
	0.20(2)	0.31(17)	0.16(5)	20.19(18)		Fe ⁰ carbide		
	0.33(2)	0.23(6)	0.93(3)	N/A		Fe ³⁺ Brg		
	1.08(1)	0.38(3)	1.62(1)	N/A		Fe ²⁺ Brg		
	0.92(1)	0.23(6)	0.88(3)	N/A		Fe ²⁺ Fp		
S7251	0.41(2)	0.40(5)	0.95(2)	N/A	1.5	Fe ³⁺ Brg	0.32(5)	
	1.10(1)	0.51(3)	1.71(2)	N/A		Fe ²⁺ Brg		
	0.94(3)	0.41(8)	0.85(4)	N/A		Fe ²⁺ Fp		
S7262	0.41(2)	0.33(6)	0.90(3)	N/A	1.6	Fe ³⁺ Brg	0.27(7)	
	1.10(1)	0.49(3)	1.67(2)	N/A		Fe ²⁺ Brg		
	0.94(3)	0.46(7)	0.86(6)	N/A		Fe ²⁺ Fp		
S7113-2	0.44(1)	0.42(1)	0.67(1)	N/A	5.9	Fe ³⁺ Brg	0.66(5)	
	0.82(1)	0.38(3)	2.18(2)	N/A		Fe ²⁺ Brg		
	0.86(1)	0.32(2)	0.91(2)	N/A		Fe ²⁺ Fp		
S7138-1	0.43(1)	0.44(2)	0.64(1)	N/A	1.4	Fe ³⁺ Brg	0.69(6)	
	0.83(1)	0.32(6)	2.21(3)	N/A		Fe ²⁺ Brg		
	0.85(2)	0.34(6)	0.99(4)	N/A		Fe ²⁺ Fp		
S7120	0.42(1)	0.47(3)	0.91(2)	N/A	2.6	Fe ³⁺ Brg	0.92(4)	
	0.33(1)	0.16(8)	0.29(2)	N/A		Fe ³⁺ Brg		
	1.10	0.60	1.81(12)	N/A		Fe ²⁺ Brg		
H4737	0.00(1)	0.17(9)	0.00	33.13(4)	1.4	Fe ⁰ alloy	0.53(6)	
	0.21	0.35	0.35(12)	20.28(47)		Fe ⁰ carbide		
	0.39(4)	0.29(21)	0.87(7)	N/A		Fe ³⁺ Brg		
	1.05	0.51	2.11(19)	N/A		Fe ²⁺ Brg		
	0.89(4)	0.34(14)	1.00	N/A		Fe ²⁺ Fp		
S7132-2	0.00(1)	0.12(17)	0.00	32.85(4)	1.0	Fe ⁰ alloy	0.53(7)	
	0.21	0.35	0.12(12)	20.08(40)		Fe ⁰ carbide		
	0.36(3)	0.35(9)	0.86(5)	N/A		Fe ³⁺ Brg		
	1.00	0.60	1.94(21)	N/A		Fe ²⁺ Brg		

(continued on next page)

Table 3.5 (Continued)

Run No.	CS (mm/s)	FWHM (mm/s)	QS or (mm/s)	ϵ	BHF (T)	χ^2	Site assignment	Fe ³⁺ / Σ Fe Brg	in
S7021	0.85(4)	0.36(12)	1.08(9)		N/A		Fe ²⁺ Fp		
	0.44(2)	0.37(10)	0.83(5)		N/A	1.1	Fe ³⁺ Brg	0.70(6)	
	1.00	0.51	2.13(19)		N/A		Fe ²⁺ Brg		
S7028	0.90	0.48(20)	0.85(11)		N/A		Fe ²⁺ Fp		
	0.45(1)	0.26(7)	0.88(2)		N/A	1.1	Fe ³⁺ Brg	0.94(5)	
	1.10	0.40(36)	1.94(29)		N/A		Fe ²⁺ Brg		
H4755	0.90	0.50(54)	0.90		N/A		Fe ²⁺ Fp		
	0.00(1)	0.14(8)	0.00		33.23(7)	6.2	Fe ⁰ alloy	0.37(5)	
	0.22(1)	0.27(8)	-0.02(3)		20.91(11)		Fe ⁰ carbide		
S7132-1	0.37(1)	0.32(2)	0.91(1)		N/A		Fe ³⁺ Brg		
	1.03(1)	0.51	1.81(3)		N/A		Fe ²⁺ Brg		
	0.91(1)	0.27(4)	0.98(2)		N/A		Fe ²⁺ Fp		
S7132-1	0.00(1)	0.21(6)	0.00		33.27(7)	1.7	Fe ⁰ alloy	0.37(7)	
	0.23(5)	0.25(44)	0.23(10)		20.06(33)		Fe ⁰ carbide		
	0.41(2)	0.36(8)	0.96(2)		N/A		Fe ³⁺ Brg		
S7046	1.10	0.60	1.85(6)		N/A		Fe ²⁺ Brg		
	0.91(4)	0.28(26)	1.02(5)		N/A		Fe ²⁺ Fp		
	0.44(1)	0.53(1)	0.86(1)		N/A	1.2	Fe ³⁺ Brg	0.88(3)	
S7138-2	1.13(2)	0.79(7)	1.77(4)		N/A		Fe ²⁺ Brg		
	0.44(1)	0.44(1)	0.86(1)		N/A	1.2	Fe ³⁺ Brg	0.89(3)	
	1.04(2)	0.73(6)	1.94(7)		N/A		Fe ²⁺ Brg		
H4746	0.90(1)	0.30(7)	0.94(2)		N/A		Fe ²⁺ Fp		
	0.00(1)	0.16(7)	0.00		32.96(3)	2.2	Fe ⁰ alloy	0.50(7)	
	0.20(2)	0.37(12)	0.12(4)		20.58(13)		Fe ⁰ carbide		
S7209	0.38(1)	0.34(5)	0.88(2)		N/A		Fe ³⁺ Brg		
	1.05	0.51	2.22(7)		N/A		Fe ²⁺ Brg		
	0.89(2)	0.55(8)	1.12(4)		N/A		Fe ²⁺ Fp		
S7209	0.46(1)	0.29(1)	0.82(1)		N/A	2.4	Fe ³⁺ Brg	0.28(6)	
	1.06(1)	0.46(3)	2.37(5)		N/A		Fe ²⁺ Brg		
	1.11(1)	0.27(3)	1.60(3)		N/A		Fe ²⁺ Brg		

(continued on next page)

Table 3.5 (Continued)

Run No.	CS (mm/s)	FWHM (mm/s)	QS or ϵ (mm/s)	BHF (T)	χ^2	Site assignment	Fe ³⁺ / Σ Fe Brg	in
S6920	0.99(3)	0.54(3)	0.90(2)	N/A	8.0	Fe ²⁺ Fp	0.55(7)	
	0.19(1)	0.32(6)	0.00(2)	20.23(7)		Fe ⁰ carbide		
	0.35(1)	0.33(2)	0.85(2)	N/A		Fe ³⁺ Brg		
	1.05	0.51	2.06(7)	N/A		Fe ²⁺ Brg		
S6907	0.89(1)	0.53(4)	1.10(2)	N/A	5.1	Fe ²⁺ Fp	0.76(13)	
	0.43(1)	0.36(3)	0.90(1)	N/A		Fe ³⁺ Brg		
	1.00	0.51	2.27(4)	N/A		Fe ²⁺ Brg		
	0.90	0.59(8)	0.91(4)	N/A		Fe ²⁺ Fp		
S6921	0.48(1)	0.52(1)	0.71(1)	N/A	2.6	Fe ³⁺ Brg	0.67(10)	
	0.89(1)	0.42(9)	2.03(6)	N/A		Fe ²⁺ Brg		
	0.89(1)	0.36(7)	2.88(5)	N/A		Fe ²⁺ Brg		
	0.98(2)	0.28(6)	0.91(3)	N/A		Fe ²⁺ Fp		
S6950-1	0.43(1)	0.34(3)	0.86(2)	N/A	2.1	Fe ³⁺ Brg	0.69(8)	
	1.19(2)	0.39(4)	1.95(2)	N/A		Fe ²⁺ Brg		
	0.97(1)	0.59(4)	0.98(3)	N/A		Fe ²⁺ Fp		
S6950-2	0.42(1)	0.30(3)	0.89(1)	N/A	1.6	Fe ³⁺ Brg	0.51(5)	
	1.16(1)	0.42(3)	1.88(1)	N/A		Fe ²⁺ Brg		
	0.94(1)	0.59(3)	0.99(2)	N/A		Fe ²⁺ Fp		
S6952	0.44(1)	0.38(1)	0.91(1)	N/A	1.6	Fe ³⁺ Brg	0.95(3)	
	1.11(3)	0.71(12)	1.87(11)	N/A		Fe ²⁺ Brg		
	0.95(2)	0.10(18)	0.96(3)	N/A		Fe ²⁺ Fp		
S7214	0.44(1)	0.44(1)	0.96(1)	N/A	1.8	Fe ³⁺ Brg	0.98(2)	
	1.10	0.7	2.33 (18)	N/A		Fe ²⁺ Brg		

Notes: CS=Center shift relative to α -Fe; FWHM=Full width at half maximum; QS=Quadrupole splitting (non-magnetic spectra); ϵ =Quadrupole shift (magnetic spectra); BHF=Hyperfine magnetic field. Uncertainties of the last digit are shown in brackets. Values without uncertainties were fixed during the fitting process.

4 The crystal chemistry of Fe-Al-bearing bridgmanite

The Brg samples investigated in this study cover a wide range of Fe and Al contents up to 0.40 Fe and 0.36 Al pfu and have variable $\text{Fe}^{3+}/\Sigma\text{Fe}$ ratios (Table 4.1). Based on cation radii ($^{\text{VIII}}\text{Mg}^{2+}_{\text{A}}=1.03 \text{ \AA}$, $^{\text{VIII}}\text{Fe}^{2+}_{\text{A, HS}}=1.06 \text{ \AA}$, $^{\text{VIII}}\text{Fe}^{3+}_{\text{A, HS}}=0.92 \text{ \AA}$, $^{\text{VI}}\text{Si}^{4+}_{\text{B}}=0.54 \text{ \AA}$, $^{\text{VI}}\text{Al}^{3+}_{\text{B}}=0.675 \text{ \AA}$, $^{\text{VI}}\text{Fe}^{2+}_{\text{B, HS}}=0.92 \text{ \AA}$, $^{\text{VI}}\text{Fe}^{3+}_{\text{B, HS}}=0.785 \text{ \AA}$) it would seem logical that Fe^{3+} partitions more favorably into the Brg A site and Al^{3+} into the B site (Shannon, 1976). As the Mössbauer spectroscopy results are inconclusive in determining the Fe^{3+} site assignment (Lin et al., 2013; McCammon, 1998) we can only estimate the site occupancies by assuming that the cations partition between the two sites in according to their radii. Moreover, although Fe^{3+} and Al may occupy both cation sites in bridgmanite, there is some evidence that in the presence of Al, Fe^{3+} preferentially occupy the A site (McCammon et al., 2013). A simple procedure can, therefore, be followed to estimate the site occupancies whereby the B site is first filled with the Al cations and the A site with Fe^{3+} and if either cations remain after the site occupancy reaches unity then they are placed on the other site. The trivalent cations on the A and B site are considered to form CCS first. If charge balance is not maintained, then OVS is assumed to occur. The resulting cation distribution between A and B site and the amount of different substitutions are listed in Table 4.1. In line with Fig. 4.1, this procedure never results in an excess of 3+ cations on the A site, which would require an A site cation vacancy to achieve charge balance.

The fractional occupancies, atomic coordinates and anisotropic displacement parameters from the single crystal XRD refinement are reported in Table 4.2. The m.a.n. (mean atomic numbers) for each Brg site determined by means of single-crystal structural refinements are in good agreement with the cation assignments resulting from the EPMA analysis (Table 4.3), confirming the preference of Fe^{3+} in the A site and Al in the B site when

coexisting. The small difference may suggest the presence of slightly larger disorder between Al and Fe³⁺ than assumed.

Table 4.1 Brg compositions measured by EPMA, cation proportions normalized to two cations per formula unit and derived end-member components for the Brg single crystals investigated in this study.

Sample	S6689	S6732	H4615	S6848	S6805	S6838	S6631	S7241
Chemical compositions of bridgmanite by EPMA (wt.%)								
MgO	37.7(3)	34.7(4)	34.4(2)	33.3(4)	32.0(4)	31.9(4)	28.3(3)	34.0(2)
SiO ₂	56.0(4)	54.8(6)	51.6(3)	54.0(4)	53.4(3)	50.1(5)	44.4(3)	48.9(5)
Al ₂ O ₃	2.7(2)	2.3(2)	5.7(2)	3.3(2)	3.4(2)	3.8(1)	9.2(2)	9.3(4)
FeO	3.6(2)	8.2(5)	8.3(4)	10.1(5)	11.2(4)	13.3(7)	17.4(4)	7.9(3)
total	100.0(4)	100.0(7)	100.0(3)	100.1(3)	100.0(3)	99.1(6)	99.4(4)	100.0(2)
Fe ³⁺ /ΣFe	0.85(5) ^a	0.30(5) ^b	0.83(8) ^a	0.54(7) ^a	0.30(5) ^b	0.81(5) ^a	0.87(5) ^a	0.95(2) ^a
Cation proportions normalized to a total of two cations								
A site								
Mg	0.949(5)	0.891 (8)	0.880(5)	0.857 (8)	0.833 (8)	0.840(7)	0.753 (7)	0.865(5)
Fe ²⁺	0.008(5)	0.083 (8)	0.020(6)	0.067(10)	0.115 (9)	0.038(8)	0.034(13)	0.006(4)
Fe _A ³⁺	0.043(6)	0.026(11)	0.099(8)	0.076(11)	0.049(10)	0.122(9)	0.213(15)	0.107(7)
Al _A	-	-	-	-	0.003 (5)	-	-	0.022(10)
B site								
Si	0.946(5)	0.944(9)	0.886(6)	0.932 (6)	0.933(7)	0.882 (9)	0.794 (5)	0.835(7)
Al	0.054(3)	0.047(4)	0.114(5)	0.067 (5)	0.067(5)	0.079 (2)	0.194 (4)	0.165(7)
Fe _B ³⁺	-	0.009(9)	-	0.002(11)	-	0.039(10)	0.012(15)	-
O	2.994	2.985	2.992	3.001	2.993	3.002	3.003	2.982
End-member components								
MgSiO ₃	0.938	0.861	0.859	0.857	0.818	0.840	0.753	0.829
Fe ²⁺ SiO ₃	0.008	0.083	0.020	0.067	0.115	0.038	0.034	0.006
Mg(M ³⁺)O _{2.5}	0.011	0.030	0.015	-	0.015	-	-	0.036
M ³⁺ M ³⁺ O ₃	0.043	0.026	0.099	0.076	0.052	0.122	0.206	0.129

^a Determined by means of Mössbauer spectroscopy; ^b determined by means of EELS. Mg(M³⁺)O_{2.5} = oxygen vacancy component; M³⁺ M³⁺O₃=couple substitution component. Note: Sample S4253 (Boffa Ballaran et al. 2012) with composition: ^A(Mg_{0.60}Fe²⁺_{0.03}Fe³⁺_{0.37})^B(Si_{0.63}Al_{0.36}Fe³⁺_{0.01})O₃ has the following end-member components: MgSiO₃=0.600, Fe²⁺SiO₃=0.030, M³⁺ M³⁺O₃=0.370

Table 4.2 Refined fractional occupancies, fractional atomic coordinates and anisotropic displacement parameters of bridgmanite single crystals.

Sample	H3004	S6689	S6732	H4615	S6848	S6805	S6838	S6631	S4253	S7241
Mg, Fe (A-site)										
X_{Mg}	1	0.943(8)	0.888(5)	0.908(5)	0.885(5)	0.840(5)	0.843(7)	0.766(4)	0.625(5)	0.890(6)
X_{Fe}	-	0.057(8)	0.112(5)	0.092(5)	0.115(5)	0.160(5)	0.157(6)	0.234(4)	0.375(5)	0.110(6)
x	0.5139(1)	0.5141(1)	0.5123(1)	0.5145(1)	0.5125(1)	0.5118(1)	0.5139(1)	0.5149(1)	0.5160(1)	0.5151(1)
y	0.5556(1)	0.5566(2)	0.5543(1)	0.5577(1)	0.5546(1)	0.5540(1)	0.5571(1)	0.5584(1)	0.5599(1)	0.5588(1)
z	0.25	0.25	0.25	0.25	0.25	0.25	0.25	0.25	0.25	0.25
U_{11}	0.0066(2)	0.0085(4)	0.0079(2)	0.0066(2)	0.0073(3)	0.0086(2)	0.0076(3)	0.0068(1)	0.0071(1)	0.0075(2)
U_{22}	0.0070(2)	0.0082(4)	0.0085(2)	0.0063(2)	0.0074(3)	0.0093(2)	0.0085(3)	0.0066(1)	0.0064(1)	0.0074(3)
U_{33}	0.0082(2)	0.0106(4)	0.0095(2)	0.0079(2)	0.0091(3)	0.0101(2)	0.0101(3)	0.0087(1)	0.0092(1)	0.0115(3)
U_{eq}	0.0073(1)	0.0091(3)	0.0086(2)	0.0069(2)	0.0079(2)	0.0093(2)	0.0087(2)	0.0074(1)	0.0076(1)	0.0088(2)
Si, Al, Fe ³⁺ (B-site)										
X_{Si}	1	1.001(8)	1.003(5)	0.976(5)	0.990(6)	1.003(5)	1.018(7)	0.994(4)	0.985(4)	0.997(6)
x	0.5	0.5	0.5	0.5	0.5	0.5	0.5	0.5	0.5	0.5
y	0	0	0	0	0	0	0	0	0	0
z	0.5	0.5	0.5	0.5	0.5	0.5	0.5	0.5	0.5	0.5
U_{11}	0.0044(2)	0.0065(3)	0.0053(2)	0.0049(2)	0.0052(2)	0.0063(2)	0.0057(2)	0.0052(1)	0.0058(1)	0.0062(2)
U_{22}	0.0052(2)	0.0057(3)	0.0055(2)	0.0048(2)	0.0047(3)	0.0058(2)	0.0064(3)	0.0049(1)	0.0052(1)	0.0062(2)

(continued on next page)

Table 4.2 (Continued)

Sample	H3004	S6689	S6732	H4615	S6848	S6805	S6838	S6631	S4253	S7241
U_{33}	0.0049(2)	0.0064(3)	0.0059(2)	0.0046(2)	0.0054(3)	0.0064(2)	0.0062(3)	0.0054(1)	0.0058(1)	0.0066(2)
U_{eq}	0.0048(1)	0.0062(2)	0.0056(1)	0.0048(1)	0.0051(2)	0.0062(1)	0.0061(2)	0.0052(1)	0.0056(1)	0.0063(2)
O1										
x	0.1023(2)	0.1039(3)	0.1022(2)	0.1056(2)	0.1030(3)	0.1026(2)	0.1057(3)	0.1082(1)	0.1134(2)	0.1079(2)
y	0.4666(2)	0.4656(3)	0.4655(2)	0.4631(2)	0.4647(3)	0.4647(2)	0.4628(3)	0.4610(1)	0.4565(2)	0.4618(2)
z	0.25	0.25	0.25	0.25	0.25	0.25	0.25	0.25	0.25	0.25
U_{11}	0.0058(4)	0.0078(6)	0.0071(3)	0.0067(4)	0.0081(6)	0.0077(4)	0.0078(5)	0.0072(3)	0.0079(3)	0.0078(4)
U_{22}	0.0077(4)	0.0088(6)	0.0076(3)	0.0075(4)	0.0073(6)	0.0083(3)	0.0087(5)	0.0068(2)	0.0071(3)	0.0083(3)
U_{33}	0.0049(4)	0.0071(6)	0.0065(3)	0.0066(4)	0.0073(5)	0.0071(3)	0.0091(5)	0.0072(2)	0.0088(3)	0.0078(4)
U_{eq}	0.0061(2)	0.0079(3)	0.0070(2)	0.0070(2)	0.0076(3)	0.0077(2)	0.0085(3)	0.0071(1)	0.0079(1)	0.0080(2)
O2										
x	0.1963(1)	0.1955(2)	0.1956(1)	0.1950(2)	0.1953(2)	0.1951(1)	0.1945(2)	0.1941(1)	0.1924(1)	0.1943(1)
y	0.2014(1)	0.2009(2)	0.2007(1)	0.2000(1)	0.2004(2)	0.2003(1)	0.1998(2)	0.1990(1)	0.1975(1)	0.1993(1)
z	0.5529(1)	0.5537(2)	0.5527(1)	0.5545(1)	0.5534(1)	0.5531(1)	0.5546(1)	0.5559(1)	0.5586(1)	0.5556(1)
U_{11}	0.0055(3)	0.0080(4)	0.0067(2)	0.0072(3)	0.0077(4)	0.0080(3)	0.0078(4)	0.0075(2)	0.0088(2)	0.0074(3)
U_{22}	0.0065(3)	0.0070(4)	0.0069(2)	0.0071(3)	0.0071(4)	0.0077(2)	0.0094(4)	0.0074(2)	0.0086(2)	0.0084(2)
U_{33}	0.0070(3)	0.0095(5)	0.0083(2)	0.0076(3)	0.0085(4)	0.0087(2)	0.0092(4)	0.0079(2)	0.0093(2)	0.0090(3)
U_{eq}	0.0063(1)	0.0082(3)	0.0073(1)	0.0073(2)	0.0078(2)	0.0081(2)	0.0088(2)	0.0076(1)	0.0089(1)	0.0083(2)

Table 4.3 Comparison between mean atomic numbers (m.a.n.) obtained for the A and B sites from single crystal X-ray diffraction and those calculated from the cation distribution derived from the chemical analyses reported in Table 3.3.

	m.a.n. A site		m.a.n. B site	
	XRD	EPMA	XRD	EPMA
S6689	12.770	12.714	14.028	13.946
S6732	13.582	13.526	14.042	14.061
H4615	13.302	13.680	13.720	13.886
S6848	13.862	13.988	13.888	13.957
S6805	14.254	14.299	14.042	13.933
S6838	14.212	14.240	14.280	14.389
S6631	15.332	15.458	13.916	13.950
S4253	17.376	17.600	13.790	13.760
S7241	13.526	13.591	13.972	13.835

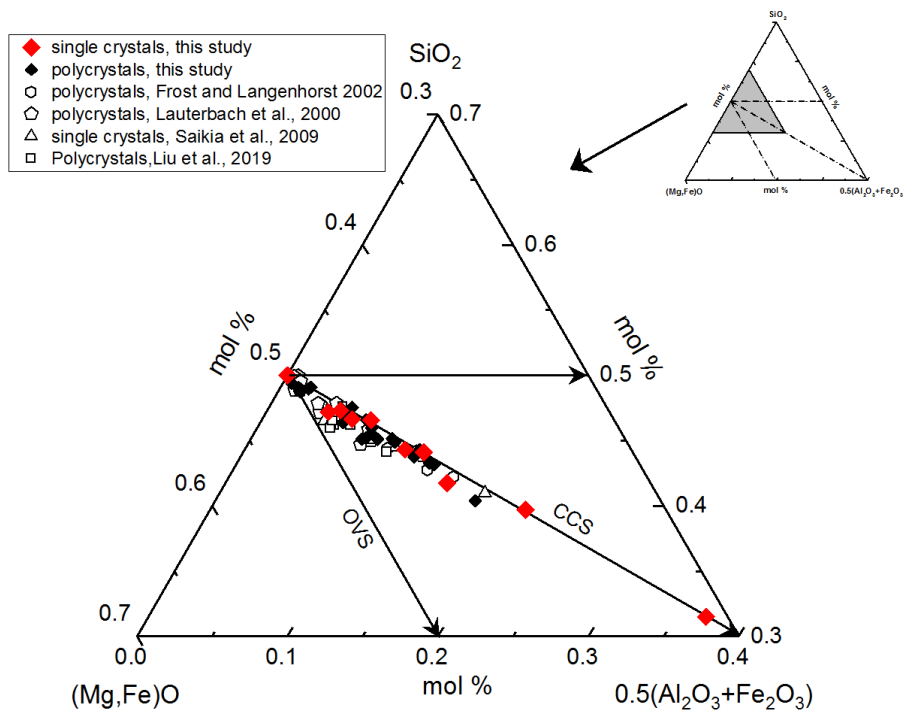


Figure 4.1 Ternary concentration diagram of the system $(\text{Mg,Fe}^{2+})\text{O}-0.5(\text{Al}_2\text{O}_3 + \text{Fe}_2\text{O}_3)\text{-SiO}_2$ showing the compositions of $(\text{Mg,Fe})(\text{Si,Al})\text{O}_3$ bridgmanite synthesized in the current study and those from Frost and Langenhorst (2002); Lauterbach et al. (2000) and Saikia et al. (2009). The two vectors correspond to the charge coupled substitution and oxygen vacancy substitution, respectively.

4.1 Al and Fe substitution mechanisms in bridgmanite

The Brg compositions investigated in this study are plotted in a ternary diagram with respect to the (Mg,Fe)O - SiO₂ - (Al,Fe)₂O₃ components (Fig. 4.1). Data from Frost and Langenhorst (2002), Lauterbach et al. (2000), Saikia et al. (2009) and Liu et al. (2019a) are also shown for comparison. The solid lines in Figure 4.1 indicate the substitution trends expected along the MgSiO₃-M₂O₃ join, i.e. the charge coupled substitution mechanism, CCS, (where M=Fe³⁺ or Al³⁺) and the MgSiO₃-MgMO_{2.5} join, i.e. the oxygen vacancy substitution mechanism, OVS. At low M³⁺ concentrations (<0.1 pfu), our data fall between the two trend lines, indicating both substitution mechanisms are important. At higher M³⁺ concentrations (>0.1 pfu), our samples follow the CCS trend line confirming that the CCS (mainly FeAlO₃) is the predominant substitution mechanism for trivalent cations. Some sample deviate slightly from the trend indicating MgM³⁺O_{2.5} OVS is also included even at high trivalent cation concentrations. The MgM³⁺O_{2.5} component is mainly MgAlO_{2.5} and do not exceed 0.04 pfu for the investigated single crystals.

4.2 Unit-cell parameters and Molar volumes of (Fe,Al)-bearing MgSiO₃ bridgmanite

The molar volumes (V_m) of the samples investigated in this study (Table 4.4) are plotted as a function of their composition expressed as the sum of the end-member contents and compared with published data in Figure 4.2. The trend defining the Fe²⁺SiO₃ substitution is well constrained by the data along the MgSiO₃-FeSiO₃ join reported by McCammon et al. (1992), Jephcoat et al. (1999) and Tange et al. (2009) whose samples were synthesized using starting materials mixed with Fe metal and loaded into Fe capsules, ensuring in this way relatively reducing conditions during the synthesis experiments. The molar volume of the Fe²⁺SiO₃ end-member assuming ideal mixing i.e. a linear relation between the end member volumes, is 25.339 cm³/mol, calculated using a linear fit through these data. The trend defining the variation of the Brg molar volume along the MgSiO₃-Fe³⁺AlO₃ join has been

constrained using the Brg volumes reported by Mao et al. (2017), and those of samples S6631 and S4253 in which the composition and $\text{Fe}^{3+}/\Sigma\text{Fe}$ were measured, containing no OVS and only a small amount of FeSiO_3 substitution (<0.03 pfu). The volume was linearly corrected for the contribution due to the presence of a small amount of Fe^{2+} (i.e. $V_m = X_{\text{MgSiO}_3} * V_{\text{MgSiO}_3} + X_{\text{FeSiO}_3} * V_{\text{FeSiO}_3} + X_{\text{FeAlO}_3} * V_{\text{FeAlO}_3}$). The resulting molar volume of $\text{Fe}^{3+}\text{AlO}_3$ is $27.081 \text{ cm}^3/\text{mol}$. Most samples investigated in this study lie between these two linear trends suggesting that FeAlO_3 CCS and FeSiO_3 are the two main substitution mechanisms in our single crystal samples. The molar volume of each Brg sample investigated in this study has been expressed in terms of the summation of partial molar volumes of the four end-member components (Table 4.1) in order to constrain the molar volume of the $\text{MgM}^{3+}\text{O}_{2.5}$ end-member. This procedure resulted in a molar volume for $\text{MgM}^{3+}\text{O}_{2.5}$ of $26.565 \text{ cm}^3/\text{mol}$, i.e. practically identical to the molar volume of $\text{MgAlO}_{2.5}$ of $26.64 \text{ cm}^3/\text{mol}$ reported by Liu et al. (2019a). This suggests that the creation of oxygen vacancies has a similar effect on the structure of bridgmanite independently of whether this substitution occurs in an Fe + Al-bearing or in an Al-bearing system. In the Fe + Al-bearing system, however, Al^{3+} very likely dominates as the M^{3+} cation at the B site. The molar volume of $25.79 \text{ cm}^3/\text{mol}$ for AlAlO_3 end member reported by Liu et al. (2019a) is smaller than $\text{MgAlO}_{2.5}$ end member (Fig. 4.2). Sample S6838 plot above the $\text{Fe}^{3+}\text{AlO}_3$ trend seems to mainly result from Fe^{3+} substituting into the Brg octahedral B site. It has an Fe^{3+} content that is significantly greater than Al where at least 0.04 Fe^{3+} atoms pfu must substitute into the B site to provide charge balance (Table 4.1), this could of course be more if some Al partitioning into the A site. Measurements from Catalli et al. (2011) and Hummer and Fei (2012) were proposed to be from samples that contain only an Fe_2O_3 substitution and indeed indicate that this end member must have the largest molar volume, which can be estimated from these previous studies to be $29.474 \text{ cm}^3/\text{mol}$, if a linear volume relation is assumed. For completeness it is also of interest to consider the volume of the $\text{MgFe}^{3+}\text{O}_{2.5}$ end member, which is an important component under certain conditions, as will be discussed in section 5.3.2. A rough estimate of the molar volume of this end member can be made using the results of Hummer and Fei (2012) and corresponds to $27.5 \text{ cm}^3/\text{mol}$ which is larger than the molar

volume of the $\text{Fe}^{3+}\text{AlO}_3$ end-member, but smaller than the $\text{Fe}^{3+}\text{Fe}^{3+}\text{O}_3$ end-member. It appears therefore that the OV substitution mechanism in Fe^{3+} - and Fe^{3+}/Al -bearing system gives rise to a smaller increase in molar volume than the CC substitution mechanism. This is clearly an opposite effect than that observed for Al-bearing Brg (Liu et al., 2019a). The molar volume trend for different end members in Brg are plotted in Fig. 4.2 which clearly shows a sequence of $\text{FeFeO}_3 > \text{MgFeO}_{2.5} > \text{FeAlO}_3 > \text{MgAlO}_{2.5} > \text{AlAlO}_3 > \text{FeSiO}_3 > \text{MgSiO}_3$.

Table 4.4 Unit-cell lattice parameters of the bridgmanite single-crystals investigated in this study.

Sample	a (Å)	b (Å)	c (Å)	V (Å ³)	Molar volume (cm ³ /mol)
H3004	4.7767(5)	4.9294(5)	6.8964(5)	162.38(3)	24.447(5)
S6689	4.7819(9)	4.9402(9)	6.9150(8)	163.36 (4)	24.594(6)
S6732	4.7907(5)	4.9392(6)	6.9170(6)	163.67(3)	24.641(5)
H4615	4.78811(13)	4.95280(15)	6.93762(14)	164.522(7)	24.769(1)
S6848	4.7938(3)	4.9452(3)	6.9257(3)	164.18(2)	24.718(3)
S6805	4.7969(5)	4.9452(5)	6.9267(5)	164.31(2)	24.737(3)
S6838	4.7982(4)	4.9624(4)	6.9517(4)	165.52(2)	24.920(3)
S6631	4.8003(2)	4.9742(2)	6.9714(2)	166.46(1)	25.061(2)
S4253	4.8107(4)	4.99964(14)	7.02636(17)	169.00(1)	25.444(2)
S7241	4.7883(9)	4.9606(9)	6.9563(9)	165.23(5)	24.876(8)

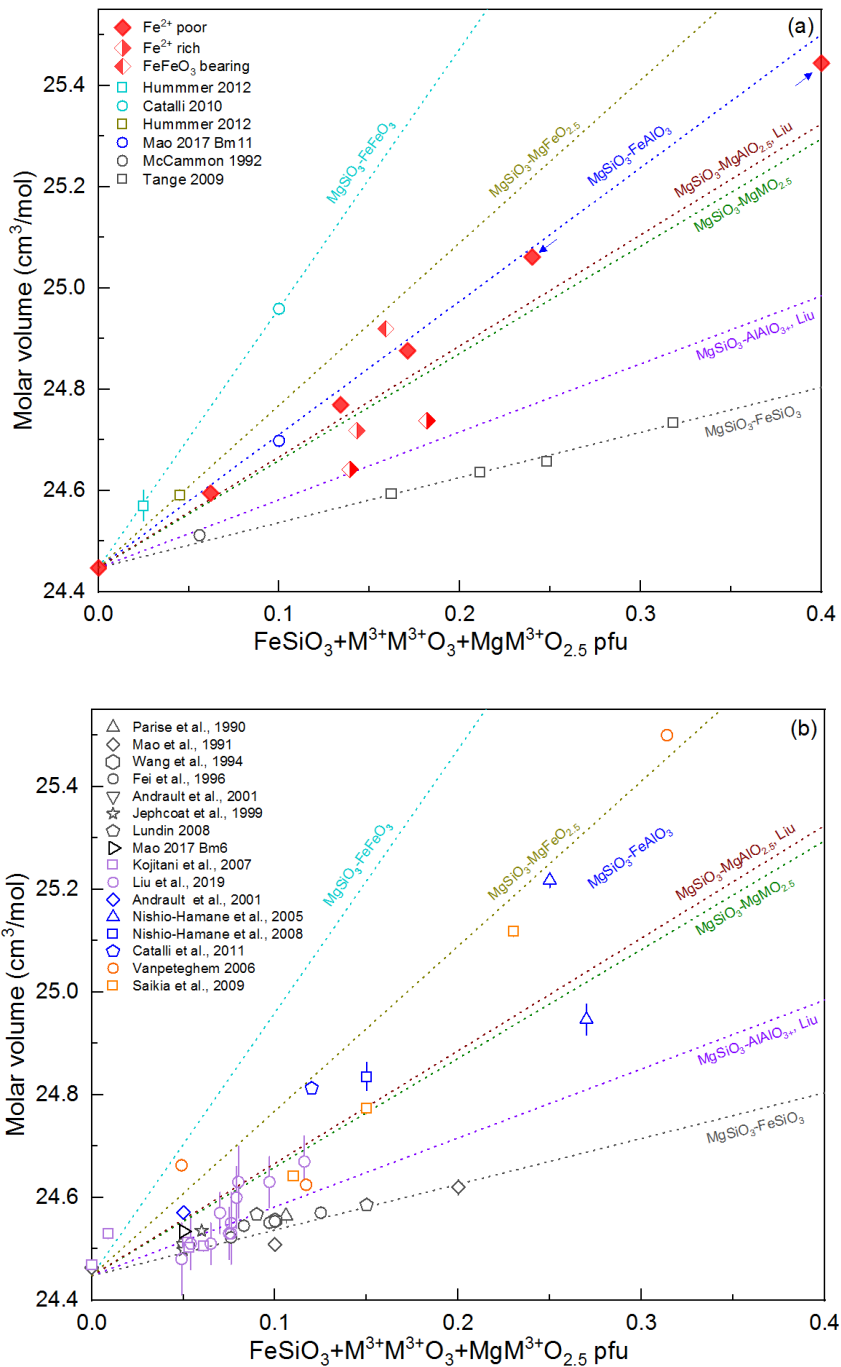


Fig. 4.2 Variation of the molar volumes of Brg as a function of the sum of end-member components. The seven dashed lines indicate molar volumes along the MgSiO₃-FeSiO₃ join, MgSiO₃-AlAlO₃ join (Liu et al., 2019a), MgSiO₃-MgMO_{2.5} join, MgSiO₃-MgAlO_{2.5} join (Liu et al., 2019a), MgSiO₃-FeAlO₃ join, MgSiO₃-MgFeO_{2.5} join and MgSiO₃-FeFeO₃ join respectively. (a) Current study and previous studies used for fitting. Fe²⁺ rich indicates the three samples (S6805, S6732, S6848) containing 0.07-0.12 pfu FeSiO₃; FeFeO₃ bearing indicates S6838 which contains 0.04 pfu FeFeO₃ and Fe²⁺ poor represents other samples which have <0.03 pfu FeSiO₃. (b) Comparison with other studies not used for fitting. The uncertainties not shown are within the symbols.

Results from previous studies not used for fitting due to unconstraint of accurate composition or contamination are also plotted for comparison in Fig. 4.2b. Studies on (Mg,Fe)SiO₃ Brg, which either report nominal compositions (Andrault et al., 2001; Lundin et al., 2008; Mao et al., 1991; Parise et al., 1990) or report small amounts of Fe³⁺ in the investigated samples (Mao et al., 2017 Bm6) give Brg molar volumes which lie close to the calculated Fe²⁺SiO₃ trend (Fig. 4.2b). Some of the diamond anvil cell experiments claiming only FeAlO₃ substitution based on the starting composition fall exactly on our FeAlO₃ trend (Andrault et al., 2001; Nishio-Hamane et al., 2008) while others deviate from the trend (Catalli et al., 2011; Nishio-Hamane et al., 2005). The larger volume than expected along the MgSiO₃-FeAlO₃ join may indicate some of the Fe³⁺ on the B site and the smaller volume compared with the MgSiO₃-FeAlO₃ trend may indicate some FeSiO₃ substitution or iron loss during laser heating. Sample S3602 studied by Saikia et al. (2009) (Table 1 in the mentioned study) containing 0.05 FeSiO₃ + 0.18 FeAlO₃ substitution also has a larger molar volume than the MgSiO₃-FeAlO₃ trend line, likely requires Fe³⁺ to enter the B site. Note that the sample of Saikia et al. (2009) appears to follow the MgSiO₃ - Fe³⁺AlO₃ molar volume trend in the plot reported by those authors (Fig. 5 in the mentioned study) because they calculated the Fe³⁺AlO₃ trend using the data point reported in Nishio-Hamane et al. (2005). We have preferred to ignore this point because the two data points in the paper are inconsistent with each other and also incompatible with Nishio-Hamane et al. (2005). The large deviation of the Fe, Al-rich samples reported by Vanpeteghem et al. (2006) instead may be due to the presence of 0.017 Na atoms pfu at the A site in one of them and of 0.030 Ti atoms pfu in the octahedral site in the other (Figure 4.2b).

All unit-cell lattice parameters (Table 4.4) increase with increasing M³⁺M³⁺O₃ substitution due to the substitution of mainly Al into the octahedral site, the largest increase being that of the *c*-axis and the smallest that of the *a*-axis (Fig. 4.3). This can be in part attributed to the changes in the individual B-O bond distances, since the B-O1 distance, which lies mainly along the *c*-axis, has the largest variation, whereas the intermediate B-O2 distance which lies mainly along the *a*-axis shows the smallest variation (Fig. 1.7, 4.4). Interestingly the FeSiO₃ substitution affects only slightly the *c*- and *b*-axes but significantly

increases the a -axis. The samples synthesized by Tange et al. (2009) have in fact c - and b -axes lengths that are very similar to those of the MgSiO_3 end-member (Figure 4 in the mentioned study), whereas their a -axes values follow the same trend as that defined by the a -axis of the sample investigated in this study. This effect can also be seen in the intermediate B-O2 distance in which the Fe^{2+} -rich samples deviate from the trend having larger distances. Although the shortest A-O1 bonds and the fourth longest A-O1 bonds mainly along the a -axis of Fe^{2+} -rich samples seem do not deviate from the trend to a larger distance (Fig. 4.5), the displacement of Mg atom may decouple the length of a -axis from individual A-O bond distances. The $\text{Fe}^{2+}\text{SiO}_3$ substitution would decrease the displacement of Mg atom along both a - and b -axes (Fig. 4.6) as will be discussed in detail in section 4.3. The data from Vanpeteghem et al. (2006) are also plotted for comparison, the impurities of Na^+ and Ti^{4+} largely increase the lattice parameters as expected (Fig. 4.3).

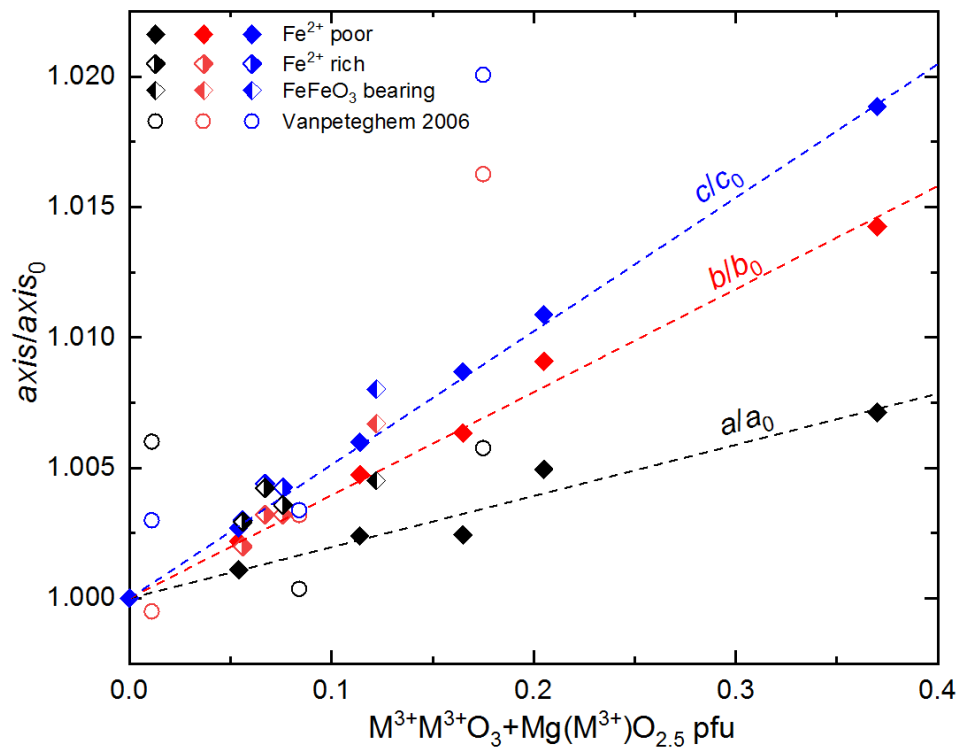


Fig. 4.3 Variation with couple and vacancy substitution of the unit-cell lattice parameters normalized with respect to those of end-member MgSiO_3 bridgmanite. Diamonds with left half-filled indicate sample S6838 which contains 0.04 pfu FeFeO_3 ; Diamonds with right half-filled indicate three Fe^{2+} -rich samples (S6805, S6732, S6848) containing 0.07-0.12 pfu FeSiO_3 and solid diamonds represent other samples which have <0.03 pfu FeSiO_3 . Errors are within the symbols.

4.3 Distortion of the perovskite-type structure of bridgmanite

The increase of molar volume in Brg with increasing Fe and Al content is mainly due to the changes occurring in the octahedral framework, in terms of B-O bond distances, octahedral tilting and distortion. The $M^{3+}M^{3+}O_3$ and $MgM^{3+}O_{2.5}$ substitution gives rise to an increase of all individual octahedral B-O bond distances (Table 4.4; Fig. 4.4) due mainly to the substitution of Al at the octahedral site. In particular the B-O1 bond distance, which involve the apical oxygen and therefore lies mainly along the *c*-axis (Fig. 1.7) increases more rapidly (Figure 4.4), giving rise to an elongated octahedron for Fe³⁺-Al-rich Brg. The bond lengths can be seen to provide a very sensitive indication of the substitution processes because sample S6838 that has Fe³⁺ substitution into the B site shows a small but clearly resolvable deviation from the Fe + Al trend (diamonds with left half-filled in Fig. 4.4). The samples analyzed by Vanpeteghem et al. (2006) are in broad agreement with the results presented in this study, except for the Fe + Al-richest sample which however contains 0.03 Ti atoms pfu at the octahedral site and therefore has much longer B-O bond distances (Fig. 4.4). There is, instead, no clear effect of Fe²⁺SiO₃ substitution on the octahedral bond lengths, as indicated from the three most Fe²⁺-rich samples (S6732, S6848, S6805) containing 0.07-0.12 pfu FeSiO₃ component which only slightly deviate from the trend (right half-filled diamonds in Fig. 4.4), since Fe²⁺ occupies only the A site. The Fe³⁺ + Al substitution also has a large effect on the coordination of the A-site (Table 4.5; Figure 4.5). In fact, the four shorter individual A-O bond distances (Figure 4.5a) all decrease, whereas all other longer distances (Figure 4.5 b,c) increase with increasing Fe³⁺+ Al content giving rise to a larger distortion of the A site. The three Brg samples (S6732, S6848 and S6805) containing a larger amount of Fe²⁺ plot off these trends (Figures 4.5) suggesting that Fe²⁺ decreases the distortion of the A site. The individual A-O bond lengths of Brg from Vanpeteghem et al. (2006) also agree with our experiments; the small deviations from our trend can likely be ascribed to the impurity contents of the samples investigated by Vanpeteghem et al. (2006).

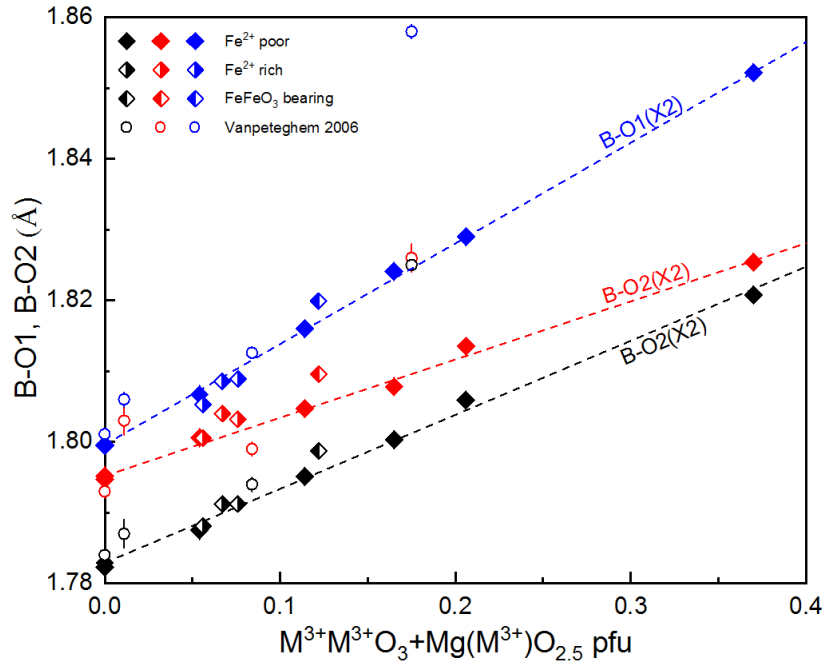
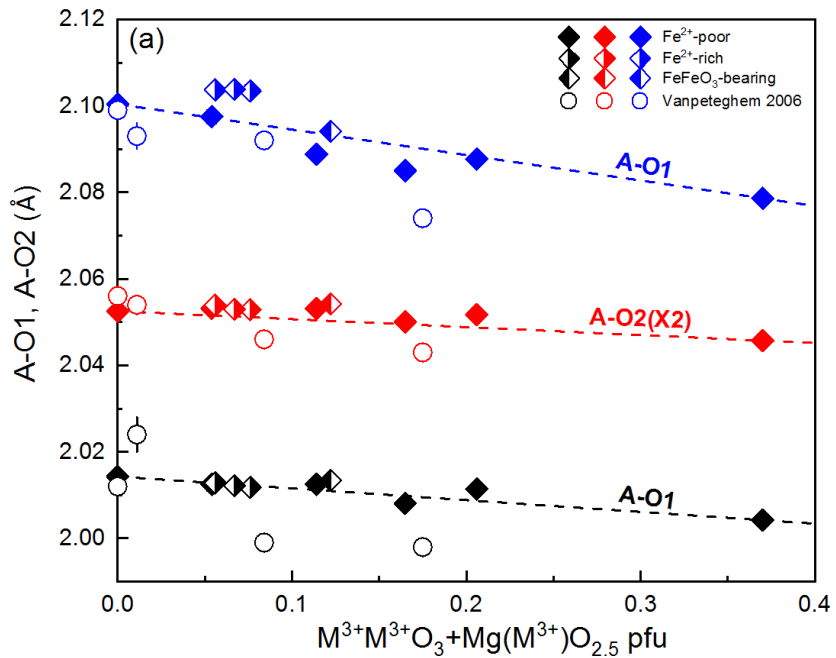


Fig. 4.4 Variation of individual B-O bond lengths of Brg as a function of the sum of $M^{3+}M^{3+}O_3$ and $MgM^{3+}O_{2.5}$ components. Symbols are the same as in Fig. 4.3. Vanpeteghem et al. (2006) indicated by open circles are also shown for comparison. The errors are within the symbols.



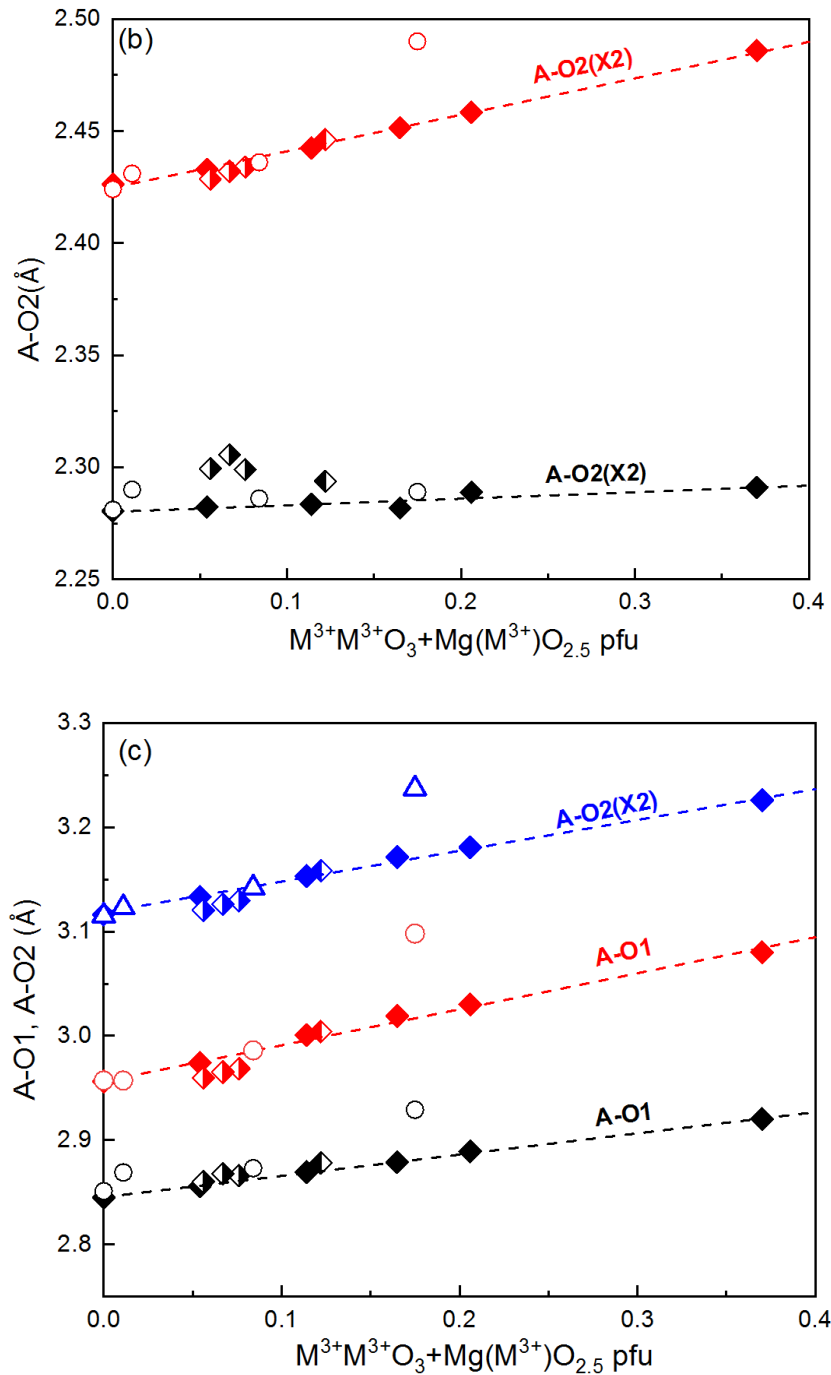


Fig. 4.5 Variation of individual A-O bond distances as a function of the coupled substitution and oxygen vacancy substitution end-members. (a) Shortest A-O bonds; (b) Intermediate A-O bonds. (c) Longest A-O bonds. Symbols are the same as in Fig. 4.3. The errors are within the symbols if not indicated.

Table 4.5 B-O bond lengths (Å) resulting from the structure refinements of the bridgmanite single crystals. <A-O>8 is the average bond lengths of the eight shortest A-O bonds and <A-O>12 is the average bond lengths of all the 12 A-O bonds. <B-O> is the average B-O bond lengths.

Sample	H3004	S6689	S6732	H4615	S6848	S6805	S6838	S6631	S4253	S7241
A-O1	2.0144(11)	2.0126(17)	2.0128(9)	2.0131(12)	2.0127(15)	2.0121(9)	2.0137(14)	2.0115(7)	2.0044(8)	2.0085(10)
A-O2(X2)	2.0526(8)	2.0528(12)	2.0539(7)	2.0533(8)	2.0524(11)	2.0533(7)	2.0547(10)	2.0519(5)	2.0456(6)	2.0504(7)
A-O1	2.1003(12)	2.0979(18)	2.1036(10)	2.0885(12)	2.1021(16)	2.1038(10)	2.0933(15)	2.0877(7)	2.0784(9)	2.0844(10)
A-O2(X2)	2.2801(8)	2.2818(12)	2.2993(7)	2.2834(8)	2.2989(11)	2.3050(7)	2.2933(10)	2.2887(5)	2.2909(6)	2.2817(7)
A-O2(X2)	2.4263(7)	2.4336(12)	2.4287(6)	2.4424(7)	2.4344(10)	2.4323(6)	2.4461(9)	2.4584(5)	2.4859(6)	2.4514(7)
<A-O> 8	2.2041(9)	2.2059(13)	2.2100(7)	2.2075(9)	2.2108(12)	2.2121(7)	2.2119(11)	2.2122(6)	2.2160(7)	2.2075(8)
A-O1	2.8448(11)	2.8558(18)	2.8601(9)	2.8688(12)	2.8655(16)	2.8680(9)	2.8781(14)	2.8891(7)	2.9202(8)	2.8786(11)
A-O1	2.9562(12)	2.9733(19)	2.9595(10)	3.0007(12)	2.9693(16)	2.9655(10)	3.0047(15)	3.0301(7)	3.0802(9)	3.0192(11)
A-O2(X2)	3.1164(9)	3.1332(13)	3.1204(7)	3.1530(8)	3.1297(11)	3.1261(7)	3.1584(10)	3.1807(5)	3.2262(6)	3.1713(8)
<A-O> 12	2.4722(9)	2.4785(14)	2.4784(8)	2.4863(9)	2.4817(12)	2.4819(8)	2.4912(11)	2.4982(6)	2.5150(7)	2.4917(8)
B-O2(X2)	1.7829(7)	1.7872(11)	1.7880(6)	1.7952(7)	1.7913(10)	1.7909(6)	1.7982(6)	1.8058(4)	1.8206(6)	1.8002(6)
B-O2(X2)	1.7952(7)	1.8009(11)	1.8006(6)	1.8046(7)	1.8033(10)	1.8042(6)	1.8100(9)	1.8136(5)	1.8257(6)	1.8079(6)
B-O1(X2)	1.7996(3)	1.8067(5)	1.8053(3)	1.8159(3)	1.8089(4)	1.8087(3)	1.8199(4)	1.8290(2)	1.8522(2)	1.8240(3)
<B-O>	1.7926(6)	1.7983(9)	1.7980(5)	1.8052(6)	1.8012(8)	1.8013(5)	1.8094(6)	1.8161(4)	1.8328(5)	1.8107(5)

The orthorhombic distortion of the Brg structure with respect to the ideal cubic $Pm\bar{3}m$ aristotype is due to the tilting of the octahedral units and has been described first by Glazer (1972) in terms of tilt components around “pseudo-cubic” axes, i.e. around the axes of the cubic aristotype structure.

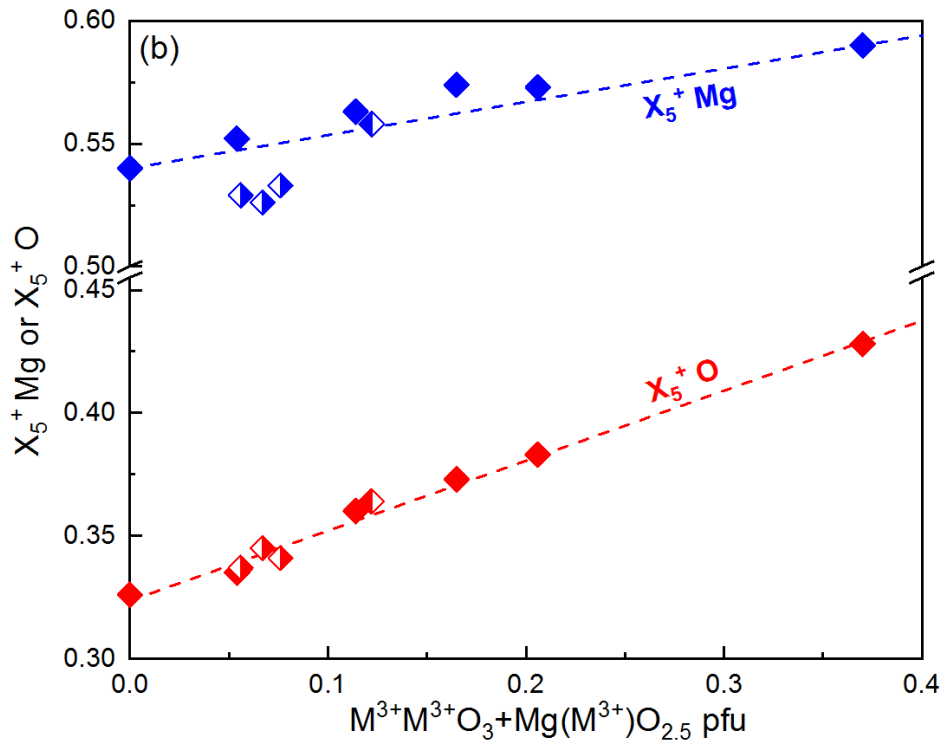
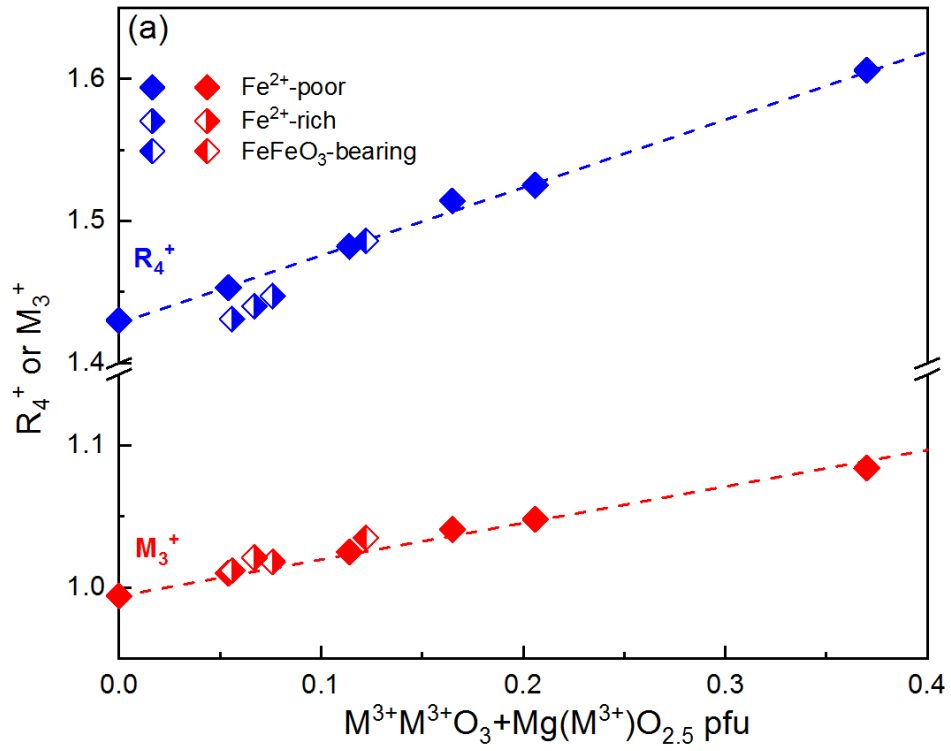
Several methods for calculating the tilting angles have been described in the literature, the simplest of them being that of using the unit-cell lattice parameters. This is based on the assumption that the octahedral framework is rigid and regular; however, the octahedral site in Brg is slightly distorted and its distortion increases with increasing Fe and Al content (Fig. 4.4). More realistic tilt angles can be calculated using the atomic coordinates of the oxygen atoms (Kennedy et al., 1999; Zhao et al., 1993a, b) whose displacements from the atomic positions in the cubic aristotype result not only from tilting but also from the distortion of the octahedral sites. A clear and unambiguous way to separate the effects of distortion and tilting of the perovskite structures is instead provided by analysis of the irreducible representations (Irreps) describing the displacive modes of the A cation and oxygens from the atomic positions of the cubic aristotype structure (Howard and Stokes, 1998; Perez-Mato et al., 2010). The program ISODISTORT (Campbell et al., 2006b) has been used to decompose the Brg structures refined in this study into different symmetry-adapted modes with respect to parent cubic structures having identical volumes to that of our samples (Table 4.6). The information needed to put into the software are the atomic positions and unit-cell parameters of both the undistorted parent phase and the distorted Brg samples as well as the relationships between the orthorhombic and the cubic space group. For the cubic parent phase, the atomic positions Mg (0.5, 0.5, 0.5), Si (0, 0, 0), O (0.5, 0, 0) were used and the lattice parameters $a=b=c$ were calculated by $a_{\text{cubic}}=V_{\text{cubic}}^{1/3}=(V_{\text{Brg}}/Z)^{1/3}$, where $Z=4$ is the number of molecules in the unit cell of Brg. The structure information of the distorted Brg are obtained from the refinement of single crystal XRD. A summary of the basis distortion modes of different symmetry frozen in the structure and corresponding distortion amplitudes of our Brg samples is shown in Table 4.6. Five mode displacements associated with the k -points X (0, 0, $\frac{1}{2}$) M ($\frac{1}{2}$, $\frac{1}{2}$, 0) and R ($\frac{1}{2}$, $\frac{1}{2}$, $\frac{1}{2}$) are allowed for the space

group $Pbnm$ [the notation is taken by Miller and Love (1967)]. We can clearly see that two of them, namely R_4^+ and M_3^+ , have much larger amplitudes, A_s , than the others. R_4^+ and M_3^+ are therefore the two dominant primary distortion modes in Brg (Table 4.6). These two modes represent oxygen displacements with R_4^+ mode correlated to the out-of-phase tilting along the $[110]$ direction where tilting occurs in the opposite sense for successive octahedral layers (through movements of both O1 and O2) and M_3^+ mode corresponds to in-phase octahedral tilting along $[001]$ where tilting occurs in the same sense for successive octahedral layers (through movement of O2). The secondary mode X_5^+ , involving both O and Mg displacements, has a significant non-zero amplitude suggesting that the cation substitution in Brg causes not only an increase of the octahedral tilting, but also a large degree of distortion of both B and A sites. In detail, the X_5 mode characterizes both the Mg displacement from the center of the aristotype unit cell along the b -axis and the O1 displacement along the b -axis. The two remaining secondary distortion modes are very weak. The M_2^+ mode which describe the distortion of the basal plane of the octahedral site is zero within experimental resolution, the R_5^+ mode describing the oxygen displacement is also zero, whereas the R_5^+ mode describing the displacement of the Mg atoms along the orthorhombic a -axis is not negligible, albeit very small. The displacement amplitudes of the R_4^+ , M_3^+ , X_5^+ and R_5^+ modes are shown in Figures 4.6 a-c as a function of the sum of $MgM^{3+}O_{2.5}$ and $M^{3+}M^{3+}O_3$ components. The X_5^+ oxygen displacement and the M_3^+ tilting mode appear to depend only on the $M^{3+}M^{3+}O_3$ and $MgM^{3+}O_{2.5}$ substitution as all samples, even those having a large Fe^{2+} content, plot on the same positive linear trends. The $Fe^{2+}SiO_3$ substitution affects instead the R_4^+ tilting and the X_5^+ and R_5^+ displacements of the A cations, giving rise to smaller oxygen and A-cation displacements for Fe^{2+} -rich samples due to the larger cation size of Fe^{2+} .

Table 4.6 Amplitudes of the symmetry-adapted modes describing the distortion of *Pbnm* bridgmanite, A and B polyhedral volumes and their ratio calculated both from the diffraction data and from the symmetry-adapted modes amplitudes.

	H3004	S6689	S6732	H4615	S6848	S6805	S6838	S6631	S6452	S7241
R_4^+	1.430	1.453	1.431	1.482	1.447	1.440	1.486	1.525	1.606	1.514
$d'_{O,R4+}$	0.1040	0.1055	0.1038	0.1074	0.1049	0.1043	0.1074	0.1100	0.1153	0.1095
R_5^+ (Mg)	-0.135	-0.137	-0.119	-0.142	-0.122	-0.115	-0.136	-0.146	-0.157	-0.148
R_5^+ (O)	0.023	0.022	0.022	0.023	0.024	0.025	0.023	0.025	0.026	0.022
$d'_{O,R5+}$	0.0017	0.0016	0.0016	0.0017	0.0018	0.0018	0.0016	0.0018	0.0019	0.0016
M_3^+	0.994	1.010	1.012	1.025	1.018	1.021	1.035	1.048	1.084	1.041
$d'_{O,M3+}$	0.1023	0.1037	0.1038	0.1050	0.1043	0.1046	0.1058	0.1069	0.1101	0.1064
M_2^+	0.049	0.052	0.049	0.049	0.049	0.050	0.051	0.049	0.049	0.048
$d'_{O,M2+}$	0.0051	0.0052	0.0051	0.0050	0.0051	0.0051	0.0052	0.0050	0.0049	0.0049
X_5^+ (Mg)	0.540	0.552	0.529	0.563	0.533	0.526	0.558	0.573	0.590	0.574
X_5^+ (O)	0.326	0.335	0.337	0.360	0.341	0.345	0.364	0.383	0.428	0.373
$d'_{O,X5+}$	0.0335	0.0344	0.0345	0.0369	0.0350	0.0353	0.0372	0.0390	0.0434	0.0382
V_A X-ray	34.338	34.537	34.625	34.774	34.724	34.761	34.990	35.165	35.658	34.908
V_B X-ray	7.675	7.748	7.744	7.837	7.784	7.786	7.891	7.978	8.197	7.908
V_A/V_B X-ray	4.474	4.457	4.471	4.437	4.461	4.464	4.434	4.407	4.350	4.414
V_A/V_B *	4.289	4.271	4.284	4.248	4.273	4.276	4.244	4.216	4.154	4.223

Notes: * V_A/V_B calculated from the symmetry adapted modes amplitudes according to Eq. (4.2).



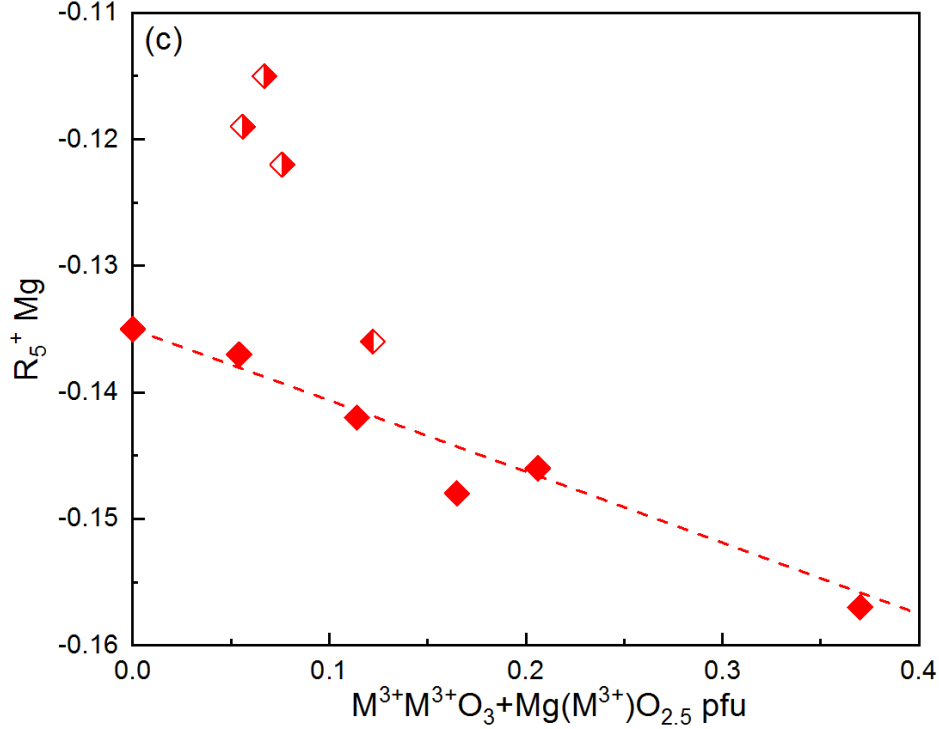


Fig. 4.6 The amplitudes of the main distortion mode in Brg structure as a function of the summation of couple and vacancy substitutions. R_4^+ and M_3^+ are related to the octahedral tilting and $X_5^+ \text{ Mg}$, $X_5^+ \text{ O}$ and $R_5^+ \text{ Mg}$ corresponding to the displacements of Mg and O ions from the aristotype cubic position. Symbols are the same as in Fig. 4.3.

The normalized mode amplitudes, A_s , obtained from ISODISTORT have been subsequently converted in mode amplitudes measured in Å, d' (Table 4.6), using the equation (Wang and Angel, 2011):

$$d' = A_s \times \text{normfactor} \times F \quad (4.1)$$

where the individual values of A_s and normfactor were produced by ISODISTORT and the F factors were calculated by transforming the displacive mode direction vectors back into the parent cell. This factor is 1 for R_4^+ , R_5^+ and X_5^+ modes and 2 for M_2^+ and M_3^+ modes as described in detail in the working example reported by Wang and Angel (2011). In this way we can calculate the A-site / B-site volume ratio in terms of the amplitudes of the symmetry adapted modes according to the expression (Wang and Angel, 2011):

$$\frac{V_A}{V_B} = \frac{6}{1 - 4d'_{O,M_2^+}{}^2 + 4d'_{O,M_3^+}{}^2 + 8d'_{O,R_4^+}{}^2 - 8d'_{O,R_5^+}{}^2 + 16d'_{O,X_5^+}(d'_{O,M_2^+} + d'_{O,M_3^+})(d'_{O,R_4^+} + d'_{O,R_5^+})} - 1 \quad (4.2)$$

where the subscripts of d' refer to the oxygen atom, O, and to the symmetry-adapted mode involved. The V_A/V_B ratio calculated using Eq. (4.2) is about 4% smaller than the V_A/V_B ratio obtained from the polyhedral A- and B-site volumes calculated using the program Vesta (Momma and Izumi, 2011) (Figure 4.7). This large difference may be due to the fact that the calculation of the A site volume in Vesta may be affected by a large error due to the large coordination of the A cations which can be described as a bi-capped prism. This polyhedron is not easily separated into well distinct tetrahedra for the volume calculation in Vesta and may results in part of its volume being counted twice in different tetrahedral, giving rise to a V_A/V_B overestimated. The behavior of this quantity is however the same independent of the calculation method and it decreases with increasing $M^{3+}M^{3+}O_3$ and $MgM^{3+}O_{2.5}$ substitution, as expected given that this component increases the distortion of bridgmanite. $Fe^{2+}SiO_3$, in the other end, plot above this trend confirming the observation that this cation enters the A site and decreases the octahedral tilting due to its slightly larger size than Mg.

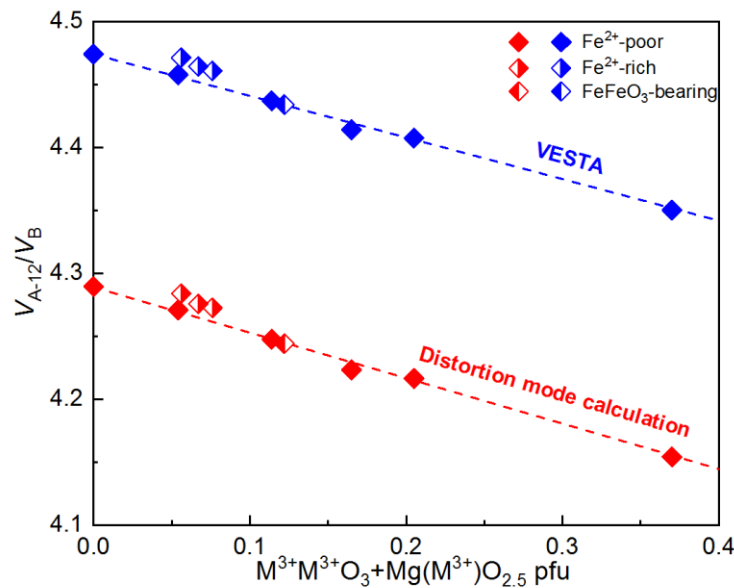


Figure 4.7 Variation of the ratio between the volume of the A site and that of the B site of the Brg investigated in this study as a function of the sum of the $M^{3+}M^{3+}O_3$ and $MgM^{3+}O_{2.5}$ end-member. Symbols are the same as in Fig. 4.3. The V_A/V_B ratio calculated using Eq. (4.2) is about 4% smaller than the V_A/V_B ratio obtained from the polyhedral A- and B-sites volumes calculated using the program Vesta.

4.4 Spontaneous strain

The symmetry-adapted modes can be used to link the microscopic geometrical description of the tilting transitions in perovskite-type structures to the macroscopic approach based on symmetry-breaking order parameters and spontaneous strains. Specifically the order parameter components giving rise to the orthorhombic symmetry of Brg are associated with the M_3^+ and R_4^+ modes and can be expressed in terms of 3 components, i.e. q_2 (relative to the M_3^+ displacement mode), q_4 and q_6 , with $q_4=q_6$ (relative to the R_4^+ displacement mode) (Carpenter et al., 2001; Stokes and Hatch, 1988). Note that the symmetry analysis is done in the conventional space group $Pnma$ and therefore the transformation of the unit-cell axes and atomic coordinates from $Pbnm$ to $Pnma$ has been applied. For the $Pnma$ perovskite-type structure, the octahedral tilting transition can be described using the Landau free energy (G) expansion at room pressure (Carpenter et al., 2001; 2006):

$$\begin{aligned}
 G = & \frac{1}{2}a_1(T - T_{c1})q_2^2 + \frac{1}{2}a_2(T - T_{c2})2q_4^2 + \frac{1}{4}(b_1 + b_1')q_2^4 + \frac{1}{2}(2b_2 + b_2')q_4^4 + \\
 & \frac{1}{6}(c_1 + c_1'')q_2^6 + \frac{2}{3}(c_2 + c_2'')q_4^6 + 2\lambda_q q_2^2 q_4^2 + e_a(\lambda_1 q_2^2 + 2\lambda_2 q_4^2) + 2\left(\frac{1}{\sqrt{3}}(2e_1 - e_2 - \right. \\
 & \left. e_3)\right)(\lambda_3 q_2^2 - \lambda_4 q_4^2) + \lambda_5 e_4 q_4^2 + (\lambda_6 + \lambda_7)e_4^2 q_2^2 + \frac{1}{4}(C_{11}^0 - C_{12}^0)(e_o^2 + e_t^2) + \frac{1}{6}(C_{11}^0 + \\
 & 2C_{12}^0)e_a^2 + \frac{1}{2}C_{44}^0(e_4^2 + e_5^2 + e_6^2)
 \end{aligned} \tag{4.3}$$

where q_2 , q_4 , and q_6 are order parameter components; a_1 , a_2 , b_1 are normal Landau coefficients; T_{c1} , T_{c2} are critical temperatures; λ_1 , λ_q , etc., are coupling coefficients between the spontaneous strain components or a linear combination of them and the order parameters; C_{11}^0 , C_{12}^0 and C_{44}^0 are bare elastic constants; e_4 , e_5 , e_6 are shear strain components; e_a , e_o and e_t are symmetry-adapted strains which are combinations of the linear strain components e_1 , e_2 and e_3 according to:

$$e_a = e_1 + e_2 + e_3 \tag{4.4}$$

$$e_o = e_1 - e_2 \tag{4.5}$$

$$e_{tx} = \frac{1}{\sqrt{3}}(2e_1 - e_2 - e_3) \quad (4.6)$$

Here e_{tx} is a tetragonal shear strain with the tetragonal axis parallel to the b -axis of the $Pnma$ bridgmanite structure. The individual spontaneous strain components can be derived from the variation of the unit-cell lattice parameters of the orthorhombic bridgmanite structures obtained in this study according to the expressions (Carpenter et al., 2001):

$$e_1 = \frac{\frac{b}{2} - a_0}{a_0} \quad (4.7)$$

$$e_2 + e_3 = \frac{\frac{a}{\sqrt{2}} - a_0}{a_0} + \frac{\frac{c}{\sqrt{2}} - a_0}{a_0} \quad (4.8)$$

$$|e_4| = \left| \frac{\frac{a}{\sqrt{2}} - a_0}{a_0} - \frac{\frac{c}{\sqrt{2}} - a_0}{a_0} \right| \quad (4.9)$$

reported by Carpenter et al. (2001) and Carpenter et al. (2006) where a , b and c are lattice parameters of our samples with the $Pnma$ structure and a_0 represents the cubic perovskite structures having the same unit-cell volumes as those of our samples. The sign of e_4 will be positive for $a > c$ and negative for $a < c$ and in our case be positive. Under equilibrium conditions, the crystal must be stress-free, implying $\partial G / \partial e_a = \partial G / \partial e_o = \partial G / \partial e_t = 0$, etc., and hence requires coupling between the order parameters and three strain components e_4 , e_t and e_a expressed as (Carpenter et al., 2001):

$$e_4 = -\frac{\lambda_5 q_4^2}{C_{44}^0} \quad (4.10)$$

$$e_a = -\frac{(\lambda_1 q_2^2 + 2\lambda_2 q_4^2)}{\frac{1}{3}(C_{11}^0 + 2C_{12}^0)} \quad (4.11)$$

$$e_{tx} = -\frac{2(\lambda_3 q_2^2 - \lambda_4 q_4^2)}{\frac{1}{2}(C_{11}^0 - C_{12}^0)} \quad (4.12)$$

The e_a strain component is very small for all compositions whereas both e_{tx} and e_4 strain components have significant values which increase with increasing $M^{3+}M^{3+}O_3$ and $MgM^{3+}O_{2.5}$ substitution and decrease with increasing $FeSiO_3$ substitution (Fig. 4.8) once again confirming that the orthorhombic distortion of the perovskite-type structure increases with increasing $M^{3+}M^{3+}O_3$ and $MgM^{3+}O_{2.5}$ component and decreases with increasing Fe^{2+} substitution. Whilst the e_{tx} strain component couples with a combination of the squares of the order parameters q_2 and q_4 , the shear strain e_4 couples either only with q_2^2 or with q_4^2 (Carpenter et al., 2001). There should be, therefore, a linear correlation between e_4 and the square of the order parameters, if our calculations are self-consistent. The square of the amplitude of the R_4^+ and M_3^+ modes which are directly correlated with the q_4 and q_2 order parameter components are plotted versus the values of e_4 obtained for our samples in Figure 4.9. The $M^{3+}M^{3+}O_3 + MgM^{3+}O_{2.5}$ substitution and $Fe^{2+}SiO_3$ substitution define two distinct linear trends suggesting that the coupling coefficient between order parameter and strain is strongly compositional dependent.

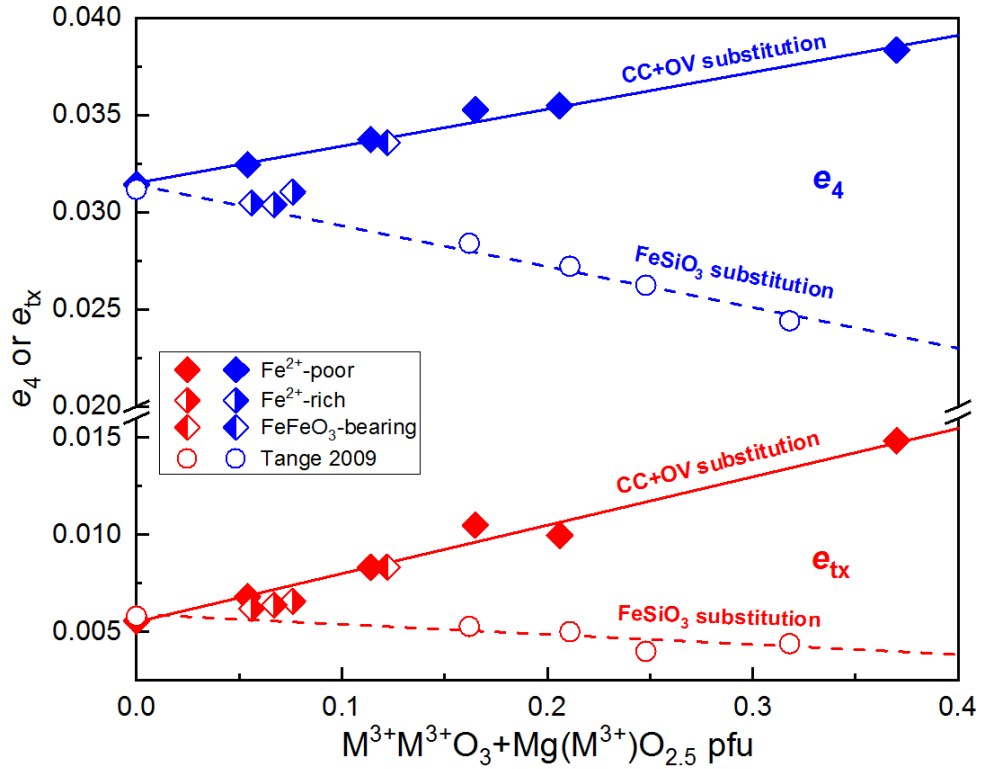


Fig. 4.8 The change of e_4 and e_{tx} strain with the increase of CC and OV substitution. Blue symbols show the e_4 strain and red symbols show the e_{tx} strain. Both strains increase with CC and OV substitution (diamonds and solid trend line) and decrease with FeSiO₃ substitution (circles and dashed trend line). Symbols are the same as in Fig. 4.3. Our samples Fe²⁺-rich samples (diamonds with right half filled) fall between these two trends, almost showing a flat trend by the opposite effect of MMO₃ substitution and FeSiO₃ substitution.

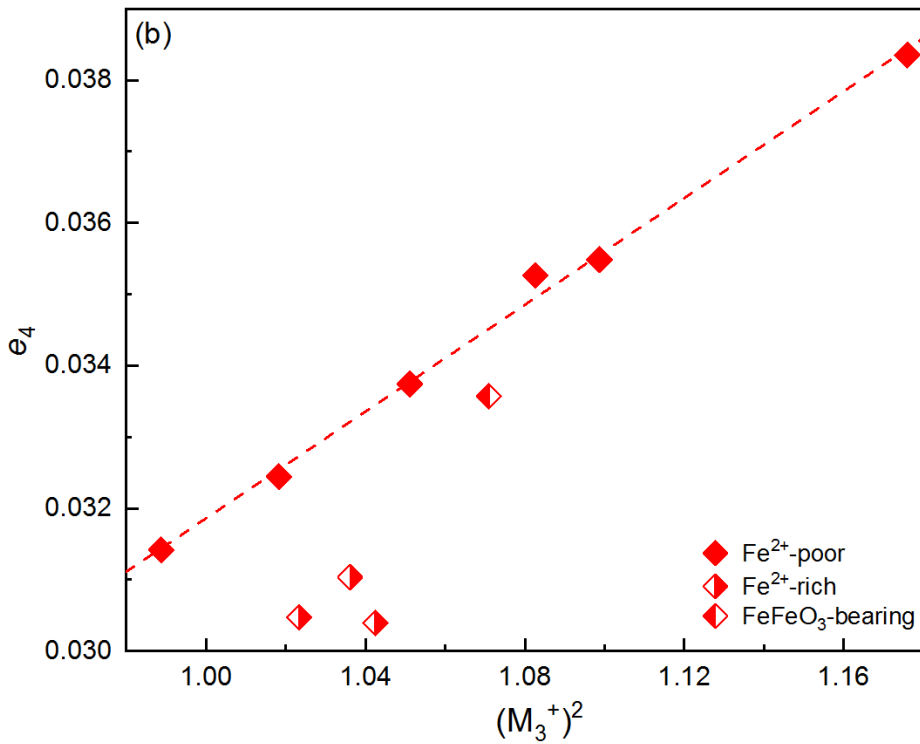
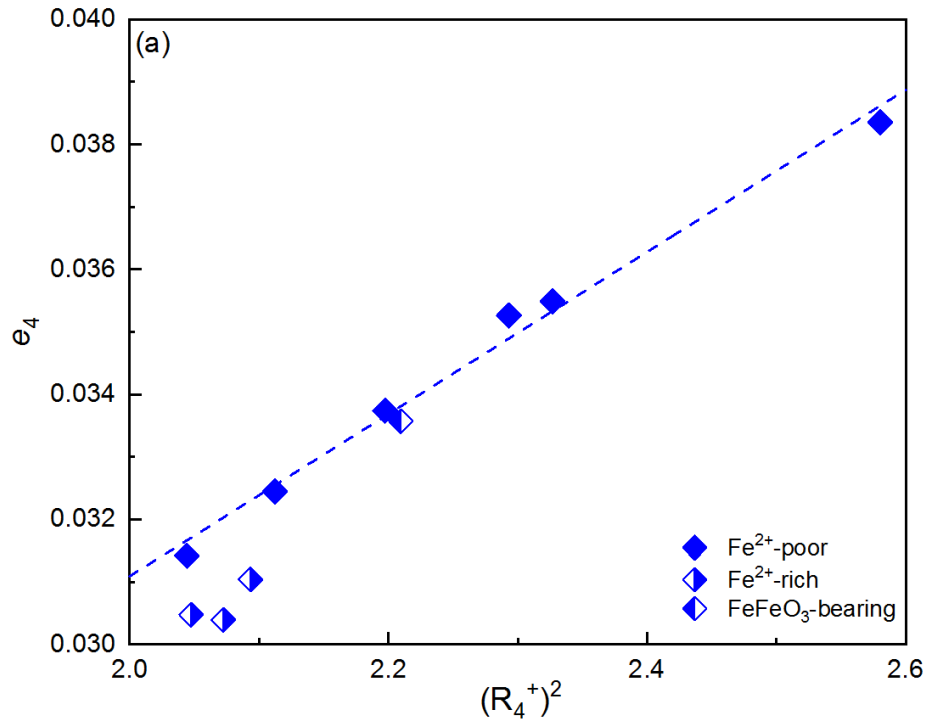


Fig. 4.9 The e_4 strain versus (a) the square of R_4^+ octahedral tilting (b) the square of M_3^+ octahedral tilting shows a linear relationship. Symbols are the same as in Fig. 4.3. The Fe²⁺-poor and Fe²⁺-rich samples show two different trends.

4.5 Compression behavior of bridgmanite

We can expect that the changes in tilting and distortion that occur in the perovskite-type structure of bridgmanite due to different cation substitutions play a role in the compression behavior of this mineral and in its transformation to the post-perovskite structure. The compressibilities of the AO_{12} and BO_6 Brg sites i.e. β_A and β_B , depend on the strengths of the individual bonds that the A- and B- cations have with the oxygens. Cation substitution will affect the bond strength and hence the compressibility behavior of the two sites determining ultimately whether the perovskite-type structure would become more or less distorted with increasing pressure and/or temperature. It has been shown how the relative compressibilities β_B/β_A can be directly deduced from the basic bond-valence parameters (Brown and Altermatt, 1985) and the bond lengths measured at room pressure (Angel et al., 2005; Zhao et al., 2004), i.e. $\beta_B:\beta_A=M_A:M_B$. M_A and M_B represent the site parameters defined as $M_i = \sum_{j=1}^{N_i} \frac{R_{ij}}{B} \exp\left(\frac{R_0 - R_{ij}}{B}\right)$ where R_0 is the bond-valence parameter that depends only upon the particular cation-anion pair, B is a universal constant equal to 0.37 Å (Bresle and O'keeffe, 1991; Brown and Altermatt, 1985) and R_{ij} and N_i are the average bond length and coordination number of the cation site at ambient conditions, respectively. Since the bridgmanites investigated in this study do not have an end-member composition, we have used individual bond lengths and we have calculated R_0 as a linear combination of the bond-valence parameters of the different proportions of cations occupying the bridgmanite A and B sites, rather than using simply the average bond distances. The resulting M_A/M_B ratio (Figure 4.10) are all smaller than 1 implying that the octahedral tilts will increase with pressure because the AO_{12} site is more compressible than the octahedral site (Angel et al., 2005). This ratio increases with increasing $\text{M}^{3+}\text{M}^{3+}\text{O}_3$ and $\text{MgM}^{3+}\text{O}_{2.5}$ substitution suggesting either an increase in B-site compressibility or a decrease of the A-site compressibility as a function of $\text{M}^{3+}\text{M}^{3+}\text{O}_3$ and $\text{MgM}^{3+}\text{O}_{2.5}$ substitution, given the inverse proportionality between the B-site/A-site compressibility ratio and the M_A/M_B ratio. This implies that substitution of mainly Al into the octahedral site increases its compressibility, whereas the

substitution of mainly Fe^{3+} at the A site decreases its compressibility likely due to the decrease of the shortest A-O distances (Fig. 4.5a).

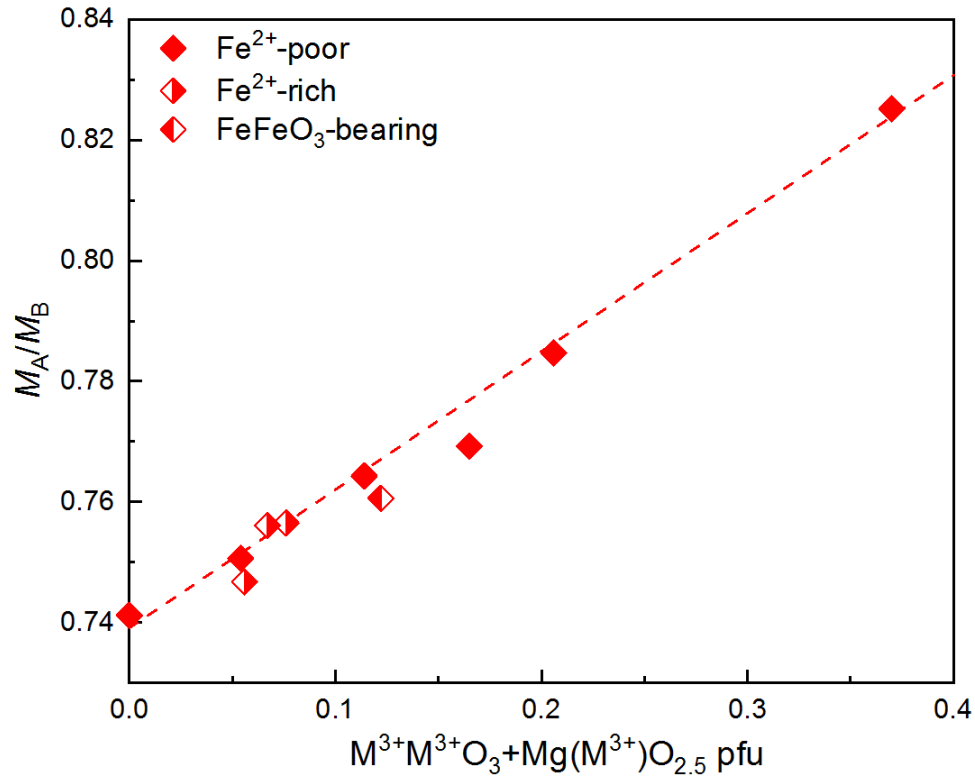


Fig. 4.10 The relative compressibility of the B site over A site ($M_A/M_B = \beta_B/\beta_A$) versus the sum of CCS and OVS. Symbols are the same as in Fig. 4.3.

It is been suggested that as octahedral tilting of a perovskite-type structure increases which decreases the polyhedral volume ratio V_A/V_B , the repulsion between inter-octahedral anions increases and may destabilize the perovskite relative to the post-perovskite structure when the distance of intra-octahedral anions (l) reaches the average separation distance of the intra-octahedral anions (i.e. the average length of the octahedra edges, $\langle X-X \rangle_l$) (Martin et al., 2006; Martin and Parise, 2008). This critical point ($l: \langle X-X \rangle_l = 1$) is empirically found to occur at $V_A/V_B = 4.038$ (Martin and Parise, 2008) (Fig. 4.11). The effect of Fe and Al substitution on the perovskite to post-perovskite phase transition in bridgmanite is still a matter of debate, however there is some experimental and theoretical evidence that points to Al and Fe stabilizing the perovskite-type structure (see Hirose et al., 2017 for a review). Although the octahedral tilting increases with $M^{3+}M^{3+}O_3$ and $MgM^{3+}O_{2.5}$

substitution at room pressure resulting in a smaller V_A/V_B ratio at ambient conditions (Fig. 4.7, 4.11), a more compressible octahedral site in Fe+Al-bearing bridgmanite would imply a less steep increase in the tilting angle or decrease in V_A/V_B ratio with pressure and therefore we may expect a larger pressure at which repulsion between oxygens will occur driving the phase transformation with respect to the $MgSiO_3$ end-member.

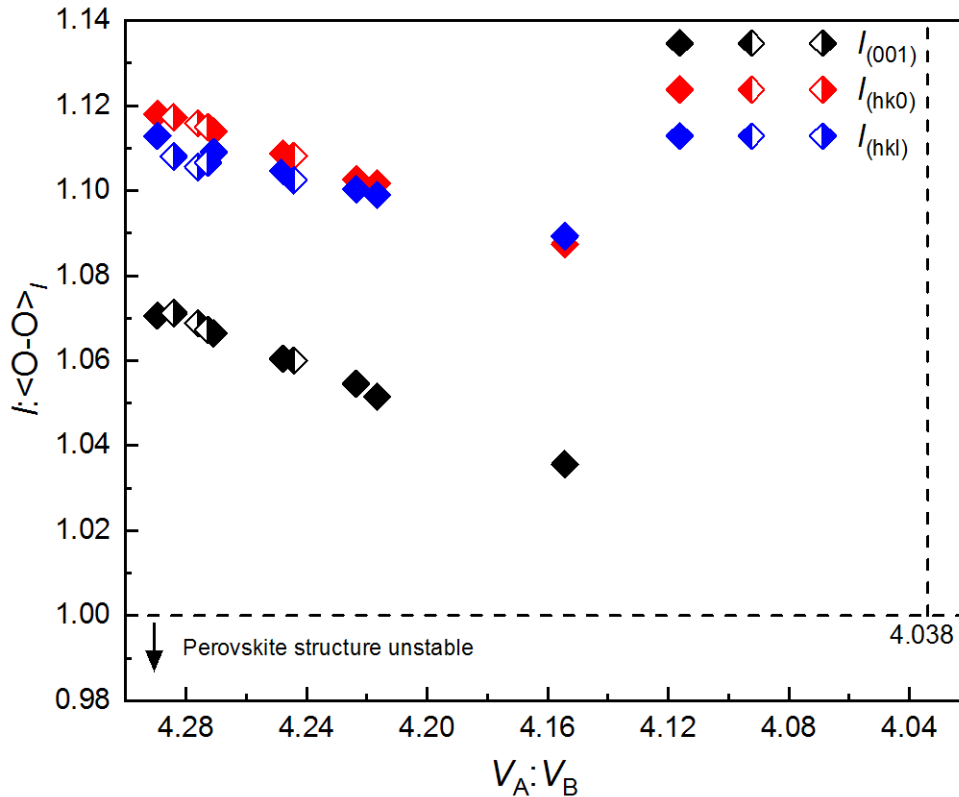


Fig. 4.11 The O2-O2 (Wyckoff position 8d) distance along the [001] direction $l_{(001)}$, the O1-O1 (Wyckoff position 4c) distance along the $[hk0]$ direction $l_{(hk0)}$ and the O2-O2 (Wyckoff position 8d) distance in a general direction $l_{(hkl)}$ normalized to the average octahedron edge length $\langle O-O \rangle_l$ and plotted with the V_A/V_B ratio in single Brg crystals from the current study. $l: \langle X-X \rangle_l = 1$ and empirical value of $V_A/V_B = 4.038$ are thought to be the critical point where perovskite structure is not stable anymore. Symbols are the same as in Fig. 4.3.

5 Speciation of Fe and Al in bridgmanite as a function of composition and oxygen fugacity

As explained in section 1.6, in order to determine the compositions of Brg and Fp in the lower mantle it is essential to understand how iron is accommodated in Brg. The Brg Fe^{3+} content, for example, is known to be strongly influenced by the presence of Al but must also be a function of the oxygen fugacity. The speciation of Fe and Al in Brg will not only affect the interphase Fe-Mg partitioning with Fp but will also influence the possible formation of metallic iron alloy and the elastic and transport properties in the lower mantle (Frost and Langenhorst, 2002; Frost et al., 2004; McCammon, 1997; Nakajima et al., 2012). Given the difficulty in performing experiments on Brg at conditions that correspond to the entire lower mantle it is essential that a clear understanding of the influences on Brg site occupancies are at least obtained at lower pressures where the conditions can be relatively well constrained.

In this study experiments have been performed to examine the compositions of Brg and Fp at 25 GPa and 1973 K within bulk compositions with varying Fe and Al contents and over a range of oxygen fugacities. The factors affecting the speciation of Fe^{3+} and Al in Brg are examined and thermodynamic models are developed to describe this speciation in the Fe-Mg-Si-O, Al-Mg-Si-O and Fe-Al-Mg-Si-O systems.

5.1 Determination of oxygen fugacity

Oxygen fugacities in the experiments were either imposed by buffering assemblages, which were assumed to have reached equilibrium, or were measured using sliding redox sensors.

For experiments conducted at Fe metal saturation, the oxygen fugacity was measured with the equilibrium,



using the expression,

$$\log(f_{\text{O}_2}) = \frac{\Delta G_{P,T}^0(5.1)}{\ln(10)RT} + 2 \log(a_{\text{FeO}}^{\text{Fp}}) - 2 \log(a_{\text{Fe}}^{\text{metal}}) \quad (5.2)$$

where $\Delta G_{P,T}^0(5.1)$ is the standard state Gibbs free energy of equilibrium (5.1), determined using the data in Table 5.1, and a_i^j is the activity of component i in phase j and is equal to $x_i^j \times \gamma_i^j$, where x_i^j and γ_i^j are the mole fraction and activity coefficient of component i in phase j , respectively. The activity coefficient of FeO in Fp ($\gamma_{\text{FeO}}^{\text{Fp}}$) was determined from,

$$RT \ln \gamma_{\text{FeO}}^{\text{Fp}} = W_{\text{MgFe}}^{\text{Fp}} (1 - x_{\text{FeO}}^{\text{Fp}})^2 \quad (5.3)$$

using the Margules interaction parameter ($W_{\text{MgFe}}^{\text{Fp}}$) from Frost (2003). In experiments where pure Fe was employed $a_{\text{Fe}}^{\text{metal}} = 1$. In experiments where Ir metal was added the activity coefficient of Fe in the resulting Fe-Ir alloy ($\gamma_{\text{Fe}}^{\text{metal}}$) was determined from,

$$RT \ln \gamma_{\text{Fe}}^{\text{metal}} = (1 - x_{\text{Fe}}^{\text{metal}})^2 \times (-51814 + 0.0736P - 21964x_{\text{Fe}}^{\text{metal}}) \quad (5.4)$$

where P is pressure in bars (Stagno and Frost, 2010). In one experiment (S7120) the oxygen fugacity was determined from a Pt-Fe alloy using the Margules expression for $\gamma_{\text{Fe}}^{\text{metal}}$ from Kessel et al. (2001).

In experiments where hematite was added to the starting material and a $(\text{Mg,Fe})_2\text{Fe}_2^{3+}\text{O}_5$ phase was formed in the resulting assemblage, the f_{O_2} was estimated using the equilibrium,



Table 5.1 End-member thermodynamic data used for calculating oxygen fugacity

	T_r (K)	$\Delta_f H_{298}^0$ (J/mol)	$H_{Tr}-H_{298}$ (J/mol)	S_{Tr} (J·K ⁻¹ ·mol ⁻¹)	Heat Capacity (C_p) terms				Source
					a	b	c	d	
Fe (FCC)	1200	0	35543	76.91	23.991	8.360E-03			1
FeO	298	-2.65E+05		58.00	42.638	8.971E-03	-2.608E+05	196.6	3
Fe ₄ O ₅	298	-1.34E+06		230.00	306.9	1.075E-03	-3.140E+06	-1470.5	3
Ru	298.15	0		28.50	13.054	1.005E-02	-3.457E+05	205.2	4
RuO ₂ (cubic)	298.15	-3.00E+05		41.94	121.951	6.260E-04	-1.058E+05	-1074.6	5
O ₂	298.15	0		205.15	47.255	-4.550E-04	4.402E+05	-393.5	4
	T_r (K)	$V_{0, Tr}$ (J/bar)	$K_{0, Tr}$ (GPa)	K'	$\partial K/\partial T$ (bar·K ⁻¹)	α_0	α_1	ϑ (K)	Source
Fe (FCC)	1273	0.738	110.8	5.3	-0.0281	4.50E-05	1.81E-08		2
FeO	298	1.224	152	4.9		3.22E-05			3
Fe ₄ O ₅	298	5.38	185.7	4		2.38E-05			3
Ru	298.15	0.8176	301		-0.05	2.15E-05	7.80E-09		5
RuO ₂ (cubic)	298.15	1.736	237			2.32E-05		512	5

Notes: 1. O'Neill (1987); 2. Tsujino et al. (2013); 3. Myhill et al. (2016); 4. O'Neill and Nell (1997); 5. Armstrong (2018). $C_p=a+bT+cT^{-2}+dT^{0.5}$ (J·K⁻¹·mol⁻¹), $\alpha=\alpha_0+\alpha_1T$. T_r is reference temperature.

and the relation

$$\log(f_{O_2}) = \frac{\Delta G_{P,T}^0(5.5)}{\ln(10)RT} + 2 \log(a_{Fe_4O_5}^{oxide}) - 8 \log(a_{FeO}^{Fp}) \quad (5.6)$$

Ideal mixing of Fe^{2+} and Mg were assumed such that $a_{Fe_4O_5}^{oxides} = (x_{Fe^{2+}}^{oxides})^2$, where $x_{Fe^{2+}}^{oxides} = Fe^{2+}/(Fe^{2+} + Mg)$. $\Delta G_{P,T}^0(5.5)$ was calculated using the data of Myhill et al. (2016) given in Table 5.1.

Oxygen fugacities for the equilibria,



and



were calculated from,

$$\log(f_{O_2}) = \frac{\Delta G_{P,T}^0(5.7,5.8)}{\ln(10)RT} \quad (5.9)$$

using the expression of Armstrong (2018) for $\Delta G_{P,T}^0(5.7)$. For Re-ReO₂ the 1 bar expression of Pownceby and O'Neill (1994) was used to calculate $\Delta G_{T,1bar}^0(5.8)$ i.e,

$$451020 + 297.595 \times T - 14.6585 \times T \times \ln T \quad (5.10)$$

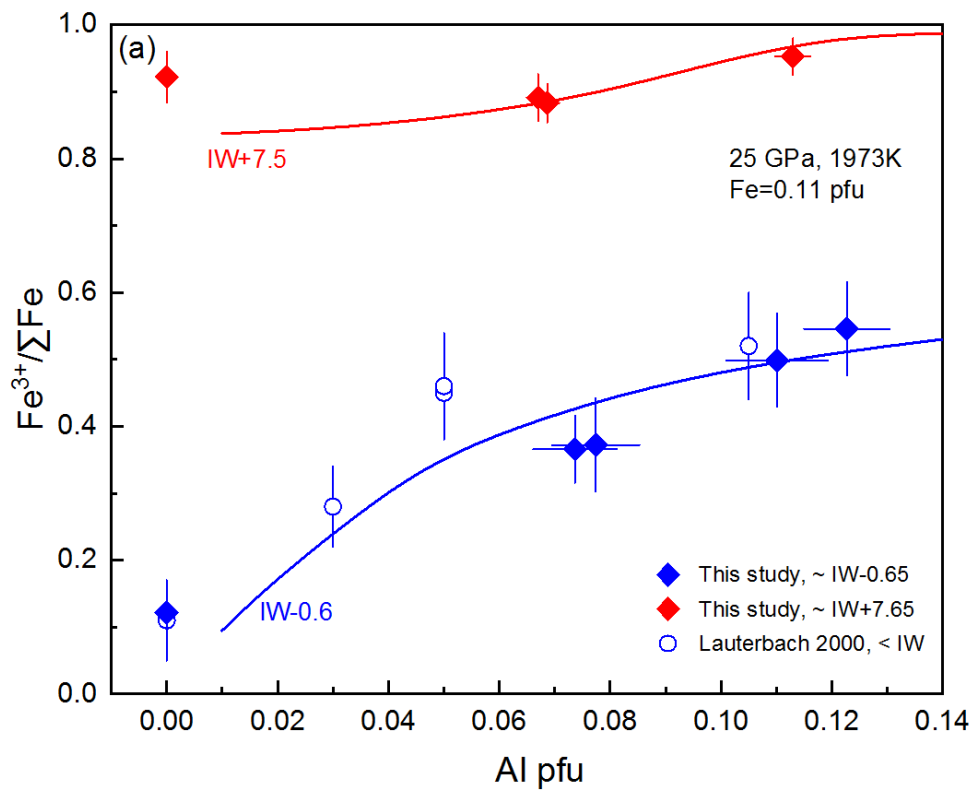
and the volume change of the equilibrium (ΔV_{RRO}) was obtain from the data of Campbell et al. (2006a) by fitting the expression,

$$\Delta V_{RRO} = A \times P + B * (T - 293) + C \quad (5.11)$$

where $A=-0.07 \text{ cm}^3/\text{GPa}$, $B=0.0002 \text{ cm}^3/\text{K}$ and $C=9.944 \text{ cm}^3$. Uncertainties in oxygen fugacities were propagated from the chemical analyses of the various oxide and metal phases involved in the determinations.

5.2 Fe³⁺/ΣFe dependence on f_{O_2} , composition and temperature in bridgmanite

Previous studies have shown that in Al free Brg, Fe³⁺/ΣFe apparently increases with increasing total iron abundance and oxygen fugacity while in Al-containing Brg, the Al concentration has been viewed as having the most important influence on the Fe³⁺/ΣFe ratio, which has been proposed to be less strongly correlated with oxygen fugacity (Frost et al., 2004; McCammon et al., 2004b; Nakajima et al., 2012). In the past this conclusion was based on the fact that the Brg Fe³⁺/ΣFe ratio is correlated with Al content regardless of whether experiments were conducted in Fe or Re capsules. In this study, however, the Brg Fe³⁺/ΣFe ratio at a fixed pressure and temperature is found to be a function of f_{O_2} in both Al-free and Al bearing samples but it is also a function of Brg Al content and total Fe content (Fig. 5.1, 5.7).



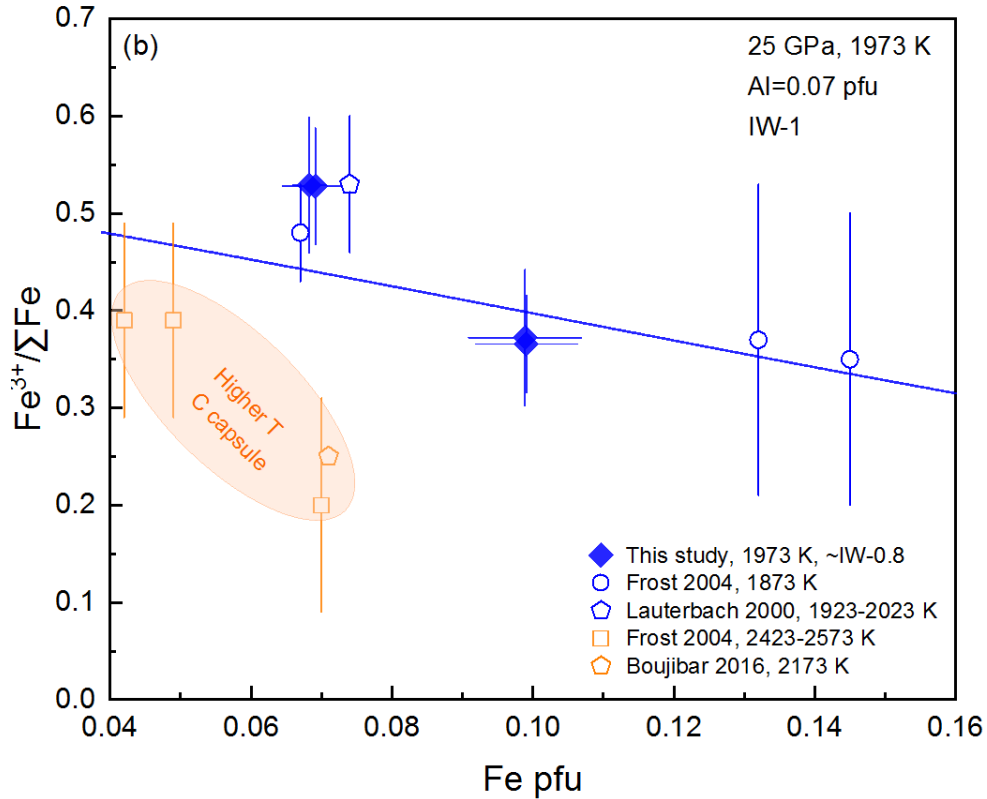


Fig. 5.1 (a) $\text{Fe}^{3+}/\Sigma\text{Fe}$ ratio as a function of Al content in Brg at fixed Fe content of 0.10-0.12 atoms pfu and oxygen fugacities of IW-0.6 and IW+7.5 at 25 GPa and 1973 K. Open circles show results from Lauterbach et al. (2000) with $\text{Fe}=0.08\text{-}0.11$ atoms pfu in Brg saturated with Fe metal at 26 GPa and 1923-2023 K. The solid line shows the calculation using the thermodynamic model constructed in the current study at 25 GPa and 1973 K with Fe fixed at 0.11 pfu and constant f_{O_2} at IW-0.6 and IW+7.5, respectively. (b) $\text{Fe}^{3+}/\Sigma\text{Fe}$ ratio versus total iron concentration (in cations per formula unit) at 25 GPa and fixed Al content of 0.07 atoms pfu. The solid diamonds indicate experiments of the current study conducted at 1973 K and $f_{\text{O}_2} \sim \text{IW}-0.8$. Open blue symbols indicate experiments from Frost et al. (2004) and Lauterbach et al. (2000) conducted at 24-26 GPa, 1873-2023 K and Fe metal saturated conditions. The open orange symbols show the results from Frost et al. (2004) and Boujibar et al. (2016) performed at 24-25 GPa and higher temperatures of 2173-2573 K in C capsules. The solid line shows the results based on the thermodynamic model from the current study calculated at an oxygen fugacity of IW-1, Al=0.07 atoms pfu, $P=25$ GPa and $T=1973$ K.

Four sets of experiments were performed at 1973 K and 25 GPa and at oxygen fugacities ranging between -1 and +9 log units relative to the iron-wüstite buffer (ΔIW). In the first three sets the total iron content of Brg was kept constant at ~ 0.11 atoms pfu but for each set the Brg Al concentration was either 0, 0.07 or 0.11 atoms pfu. In a final set of

Table 5.2 Cation proportions and site assignment in Brg normalized to two cations per formula unit.

	Run	A site				B site			Fe ³⁺ /ΣFe	log <i>f</i> _{O₂} (ΔIW)
		Mg	Fe ²⁺ _A	Fe ³⁺ _A	Al _A	Si	Al _B	Fe ³⁺ _B		
Fe _{0.10}	S7122	0.915(8)	0.086(6)	-	-	0.988(8)	-	0.012(8)	0.12(3)	-0.71(25)
	S7251	0.935(7)	0.061(6)	0.004(9)	-	0.975(7)	-	0.025(7)	0.32(5)	4.05(52)
	S7262	0.931(6)	0.064(8)	0.005(9)	-	0.981(7)	-	0.019(7)	0.27(7)	4.05(52)
	S7113-2*	0.964(9)	0.019(4)	0.017(9)	-	0.979(7)	-	0.021(7)	0.66(5)	7.65(31)
	S7138-1*	0.963(8)	0.017(5)	0.019(10)	-	0.980(8)	-	0.020(8)	0.69(9)	7.65(31)
	S7120	0.946(6)	0.008(4)	0.046(12)	-	0.949(8)	-	0.051(8)	0.92(4)	8.75(87)
Al _{0.07} Fe _{0.10}	H4755	0.900(7)	0.063(7)	0.036(6)	0.001(9)	0.928(4)	0.072(4)	-	0.37(5)	-0.64(5)
	S7132-1	0.886(14)	0.062(9)	0.037(8)	0.015(12)	0.938(9)	0.062(9)	-	0.37(7)	-0.67(6)
	S7046	0.922(6)	0.012(3)	0.067(8)	-	0.911(6)	0.069(2)	0.021(6)	0.88(3)	7.65(31)
	S7138-2	0.918(5)	0.010(3)	0.072(8)	-	0.920(6)	0.067(2)	0.013(6)	0.89(3)	7.65(31)
Al _{0.12} Fe _{0.12}	H4746	0.870(10)	0.059(10)	0.059(10)	0.012(15)	0.902(12)	0.098(12)	-	0.50(7)	-0.60(5)
	S6920	0.855(10)	0.054(9)	0.065(9)	0.025(11)	0.903(8)	0.097(8)	-	0.55(7)	-0.14(11)
	S6907	0.882(6)	0.026(14)	0.082(15)	0.010(7)	0.897(7)	0.103(7)	-	0.76(13)	2.70(73)
	S6952	0.889(5)	0.006(3)	0.105(7)	-	0.875(5)	0.113(3)	0.012(6)	0.95(3)	7.65(30)
Al _{0.07} Fe _{0.07}	H4737	0.925(11)	0.033(5)	0.036(5)	0.006(11)	0.932(7)	0.068(7)	-	0.53(6)	-0.93(13)
	S7132-2	0.921(7)	0.032(5)	0.036(5)	0.011(12)	0.937(9)	0.063(9)	-	0.53(7)	-0.82(14)
	S7021	0.921(13)	0.018(4)	0.041(5)	0.021(15)	0.951(10)	0.049(10)	-	0.70(6)	2.30(82)
	S7028	0.925(6)	0.004(4)	0.070(10)	-	0.932(7)	0.066(4)	0.002(8)	0.94(5)	7.65(31)

Notes: * Brg samples with low Fe content of 0.06 pfu.

experiments the Brg Al content was 0.07 and the Fe content was lowered to 0.07. The site assignment of Al and Fe (Table 5.2) was performed according to the procedure described in Chapter 4 with the B site first filled with the Al cations and the A site with Fe^{3+} assuming therefore cation ordering between the two sites and then allowing the excess of Al to occupy the A site or the excess of Fe^{3+} to occupy the B site only if their site occupancy had not reached unity. As can be seen in Fig. 5.1a and Fig. 5.7 the $\text{Fe}^{3+}/\Sigma\text{Fe}$ ratio of Brg increases with the Al content but is also strongly dependent on f_{O_2} . The nature of this relationship, however, apparently changes with Al content. For Al free samples, the $\text{Fe}^{3+}/\Sigma\text{Fe}$ ratio increases from 0.12(3) to 0.92(4) upon an f_{O_2} increase from IW-0.7 to IW+8.8 (Fig. 5.4). For Al-bearing samples, $\text{Fe}^{3+}/\Sigma\text{Fe}$ also increases with f_{O_2} but the slope is obviously less steep (Fig. 5.7).

The effect of Al content on the $\text{Fe}^{3+}/\Sigma\text{Fe}$ ratio in Brg is shown in Fig. 5.1a at a bulk Fe content of 0.11 atoms pfu and at oxygen fugacities determined both by the presence of metallic iron (\sim IW-0.6) and Ru-RuO₂ (IW+7.5). The $\text{Fe}^{3+}/\Sigma\text{Fe}$ ratio in Brg increases with Al content, consistent with previous work (Frost and McCammon, 2008; Lauterbach et al., 2000; McCammon et al., 2004b) but the gradient of this dependence changes with f_{O_2} content. At reducing conditions there is an initial strong dependence on Al that becomes weaker at higher Al contents, whereas at high f_{O_2} the Al content dependence is also much weaker, essentially because the $\text{Fe}^{3+}/\Sigma\text{Fe}$ ratio is near 100 % even at low Al contents.

The effect of varying the bulk Fe content at a constant Al content (0.07) and f_{O_2} (\sim IW-0.8) can be evaluated by also considering data from previous studies (Frost et al., 2004; Lauterbach et al., 2000). At 1873-2023 K, Al=0.07 atoms pfu and f_{O_2} =IW-0.8 (i.e. Fe metal saturated) the Brg $\text{Fe}^{3+}/\Sigma\text{Fe}$ ratio decreases with increasing total Fe content (Fig. 5.1b). The influence of total Fe content at other conditions, such as higher oxygen fugacities, is not well constrained by the currently available data set. For a similar f_{O_2} and Al content the $\text{Fe}^{3+}/\Sigma\text{Fe}$ ratio also appears to decrease (by \sim 0.2) with increasing temperature as shown by the orange open symbols in Fig. 5.1b. Although these higher temperature experiments were

conducted in graphite capsules, (which transformed to diamond during the synthesis), the presence of Fe metal was identified in the recovered samples implying an oxygen fugacity close to IW-0.8. A decrease in Brg $\text{Fe}^{3+}/\Sigma\text{Fe}$ ratio is also supported by experiments performed with Al=0.11 atoms pfu shown in Fig. 5.7. At oxygen fugacity of IW-0.8 the $\text{Fe}^{3+}/\Sigma\text{Fe}$ ratio drops from 0.46 at 1973 K to 0.28 at 2373 K (shown by the black diamond).

In summary, the $\text{Fe}^{3+}/\Sigma\text{Fe}$ ratio in Brg increases with both Al content and oxygen fugacity with the $\log f_{\text{O}_2}$ dependence being seemingly stronger for the Al-free samples. At $\Delta\text{IW} < 1$ the $\text{Fe}^{3+}/\Sigma\text{Fe}$ ratio is strongly dependent on Al content but this dependence weakens with increasing f_{O_2} becoming seemingly independent of Al content at high oxygen fugacity. On the other hand, the Brg $\text{Fe}^{3+}/\Sigma\text{Fe}$ ratio decreases with total Fe content and temperature.

5.3 Substitution mechanisms in Bridgmanite

5.3.1 Al-bearing bridgmanite

In order to understand the distribution of cations in Brg in the Fe + Al bearing system it is useful to first examine the speciation in the individual Al and Fe bearing subsystems. For the Al-Mg-Si-O system this is possible using previously published data (Kojitani et al., 2007; Liu et al., 2019a; 2019b; Liu et al., 2017; Navrotsky et al., 2003). In Fig. 5.2a, the Si content of Fe-free Al-bearing Brg is plotted against the Al content. Two solid lines indicate the expected trends for the charge coupled substitution mechanism along the $\text{MgSiO}_3\text{-AlAlO}_3$ join and the oxygen vacancy substitution mechanism along the $\text{MgSiO}_3\text{-MgAlO}_{2.5}$ join, respectively. Bulk compositions along the $\text{MgSiO}_3\text{-AlAlO}_3$ join (green circles) produce Brg samples that fall along the CCS trend line. Bulk compositions with $\text{Mg} > \text{Si}$, on the other hand, result in Brg compositions (orange circles) that fall between the CCS and OVS trend lines. The proportions of the two substitution mechanisms change with the Al content in bridgmanite, from $\text{MgAlO}_{2.5}$ OVS dominating at low Al content (< 0.10 pfu) to equal abundance of OVS and CCS with Al between 0.1-0.15 atoms pfu and finally to AlAlO_3 dominance at high Al content > 0.15 atoms pfu. The variation in the two substitution

mechanisms for Brg with a bulk starting composition of $Mg > Si$ can be seen more clearly in Fig. 5.2b, where the proportions of the two components are determined from the equation $Mg_xAl_zSi_yO_{x+1.5z+2y} = yMgSiO_3 + (x-y)MgAlO_{2.5} + 0.5(z-x+y)AlAlO_3$ ($x+y+z=2$, Liu et al., 2017). The CCS $AlAlO_3$ component increases monotonically with increasing Al content while the $MgAlO_{2.5}$ OVS component initially increases to a maximum at $Al = \sim 0.1$ atoms pfu and then decreases upon a further increase in Al.

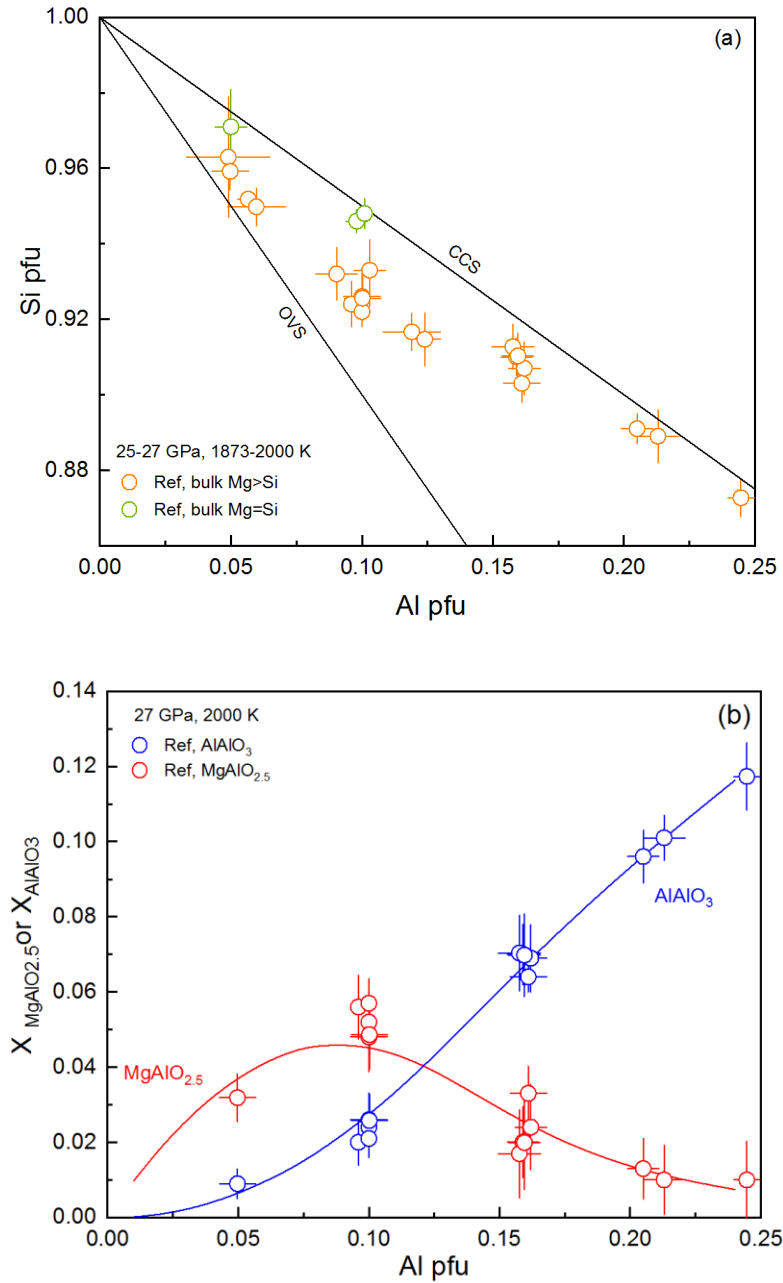
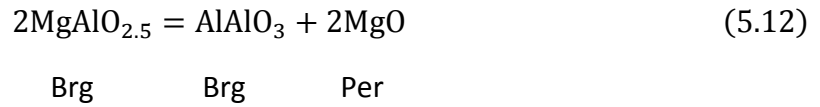


Fig. 5.2 (a) The variation of the Si content of Brg with Al content at 25-27 GPa and 1873-2000 K. The two solid lines are expected trend lines for CCS along the MgSiO₃-AlAlO₃ join and the OVS along the MgSiO₃-MgAlO_{2.5} join respectively. The orange symbols indicate Brg with starting bulk composition Mg>Si and the green symbols represent Brg with starting bulk composition Mg=Si. Data are taken from Kojitani et al. (2007); Liu et al. (2017, 2019a, b) and Navrotsky et al. (2003). (b) The mole fraction of AlAlO₃ and MgAlO_{2.5} component in Brg as a function of Al content at 27 GPa and 2000 K. Open circles represent data from Liu et al. (2019a, b) with a bulk composition Mg > Si in the system. Solid lines are the calculated values based on the thermodynamics models derived at 27 GPa and 2000 K.

The exchange of the AlAlO₃ and MgAlO_{2.5} components in Brg can be described by the equilibrium:



The equilibrium coefficient K for this reaction is defined as:

$$K = \frac{a_{\text{AlAlO}_3}^{\text{Brg}}}{(a_{\text{MgAlO}_{2.5}}^{\text{Brg}})^2} \quad (5.13)$$

where $a_{\text{AlAlO}_3}^{\text{Brg}}$ and $a_{\text{MgAlO}_{2.5}}^{\text{Brg}}$ are the activities of the AlAlO₃ and MgAlO_{2.5} components in Brg respectively. At equilibrium, the standard state Gibbs free-energy change can be expressed by

$$\Delta G_{(5.12)}^0 = -RT \ln \frac{a_{\text{AlAlO}_3}^{\text{Brg}}}{(a_{\text{MgAlO}_{2.5}}^{\text{Brg}})^2} \quad (5.14)$$

taking the standard state to be the pure end-members at the pressure and temperature of interest. The activities of the Brg component are defined as:

$$a_{\text{AlAlO}_3}^{\text{Brg}} = x_{\text{AlAlO}_3}^{\text{Brg}} \times \gamma_{\text{AlAlO}_3}^{\text{Brg}} \quad (5.15a)$$

$$a_{\text{MgAlO}_{2.5}}^{\text{Brg}} = x_{\text{MgAlO}_{2.5}}^{\text{Brg}} \times \gamma_{\text{MgAlO}_{2.5}}^{\text{Brg}} \quad (5.15b)$$

where γ is the activity coefficient. Substituting these equations into equation (5.14) yields:

$$\begin{aligned}\Delta G_{(5.12)}^0 &= -RT \ln \frac{x_{\text{AlAlO}_3}^{\text{Brg}} \times \gamma_{\text{AlAlO}_3}^{\text{Brg}}}{\left(x_{\text{MgAlO}_{2.5}}^{\text{Brg}} \times \gamma_{\text{MgAlO}_{2.5}}^{\text{Brg}}\right)^2} = -RT \ln \frac{x_{\text{AlAlO}_3}^{\text{Brg}}}{\left(x_{\text{MgAlO}_{2.5}}^{\text{Brg}}\right)^2} - RT \ln \frac{\gamma_{\text{AlAlO}_3}^{\text{Brg}}}{\left(\gamma_{\text{MgAlO}_{2.5}}^{\text{Brg}}\right)^2} \\ &= -RT \ln K_D - RT \ln \gamma_{\text{AlAlO}_3}^{\text{Brg}} + 2RT \ln \gamma_{\text{MgAlO}_{2.5}}^{\text{Brg}}\end{aligned}\quad (5.16)$$

which should yield a constant value for a given pressure and temperature regardless of the composition. MgSiO₃ bridgmanite has two oxygen sites, O1 with a multiplicity of 1 and O2 with a site multiplicity of 2. If we consider that oxygen vacancies occur on one half of the available O1 sites, then the mole fraction of the MgAlO_{2.5}V_{0.5} component can be written as,

$$x_{\text{MgAlO}_{2.5}\text{V}_{0.5}}^{\text{Brg}} = 2x_{\text{Mg,A}}x_{\text{Al,B}}(x_{\text{V,O1}})^{0.5}(x_{\text{O,O1}})^{0.5}\quad (5.17)$$

where $x_{\text{Mg,A}}$ and $x_{\text{Al,B}}$ are the mole fractions of Mg on the A site and Al on the B site respectively, and $x_{\text{V,O1}}$ and $x_{\text{O,O1}}$ are the mole fractions of vacancies and oxygen on the O1 site where $x_{\text{V,O1}} = 0.5(x_{\text{Al,B}} - x_{\text{Al,A}})$. The integer 2 in equation (5.17) is required such that the activity of the end-member MgAlO_{2.5}V_{0.5} is equal to unity. For the coupled substitution of Al, it is assumed that charge balance results in local ordering of Al on each site, such that the mole fraction of the AlAlO₃ component is:

$$x_{\text{AlAlO}_3}^{\text{Brg}} = x_{\text{Al,A}} = x_{\text{Al,B}}\quad (5.18)$$

Using a symmetric mixing model, the deviation from ideal mixing can be described by:

$$RT \ln \gamma_{\text{AlAlO}_3}^{\text{Brg}} = W_{\text{MgAl,A}}^{\text{Brg}}(1 - x_{\text{Al,A}})^2 + W_{\text{AlSi,B}}^{\text{Brg}}(1 - x_{\text{Al,B}})^2 + W_{\text{OV,O1}}^{\text{Brg}}(1 - x_{\text{O,0.5O1}})^2\quad (5.19a)$$

$$RT \ln \gamma_{\text{MgAlO}_{2.5}}^{\text{Brg}} = W_{\text{MgAl,A}}^{\text{Brg}}(1 - x_{\text{Mg,A}})^2 + W_{\text{AlSi,B}}^{\text{Brg}}(1 - x_{\text{Al,B}})^2 + W_{\text{OV,O1}}^{\text{Brg}}(1 - x_{\text{OV,0.5O1}})^2\quad (5.19b)$$

where W is a Margules interaction parameter that describes the interaction energy between Mg²⁺-Al³⁺ on the A site, Si⁴⁺-Al³⁺ on the B site and the O-vacancy on the O1 site. By using three symmetric interaction parameters, equation (5.16) becomes:

$$\begin{aligned}
\Delta G_{(5.12)}^0 = & -RT \ln K_D \\
& - \left[W_{\text{MgAl,A}}^{\text{Brg}} (1 - x_{\text{Al,A}})^2 + W_{\text{AlSi,B}}^{\text{Brg}} (1 - x_{\text{Al,B}})^2 + W_{\text{OV,O1}}^{\text{Brg}} (1 - x_{\text{O,0.5O1}})^2 \right] \\
& + 2 \\
& \times \left[W_{\text{MgAl,A}}^{\text{Brg}} (1 - x_{\text{Mg,A}})^2 + W_{\text{AlSi,B}}^{\text{Brg}} (1 - x_{\text{Al,B}})^2 \right. \\
& \left. + W_{\text{OV,O1}}^{\text{Brg}} (1 - x_{\text{OV,0.5O1}})^2 \right] \quad (5.20)
\end{aligned}$$

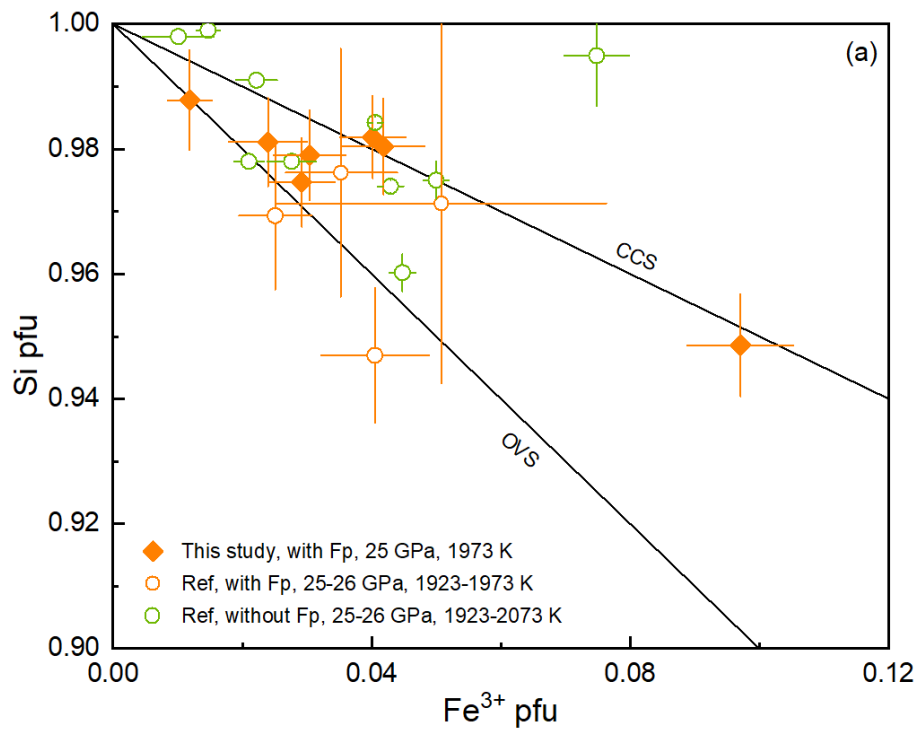
By using the mole fractions of different ions on A, B and O1 sites in Brg obtained from the experiments, the equation can be fitted using a non-linear least-squares algorithm to determine the three interaction parameters and $\Delta G_{(5.12)}^0$. However, values for the three interaction parameters are highly correlated, and a range of values will provide a satisfactory fit. Refining all three interaction parameters at the same time gives unreasonable solutions, but always gives $W_{\text{AlSi,B}}^{\text{Brg}} = 0$ kJ/mol, therefore $W_{\text{AlSi,B}}^{\text{Brg}}$ was fixed at 0 kJ/mol, $W_{\text{OV,O1}}^{\text{Brg}}$ was adjusted manually and then only $W_{\text{MgAl,A}}^{\text{Brg}}$ was refined. A reasonable solution was obtained at $W_{\text{OV,O1}}^{\text{Brg}} = 70$ kJ/mol, giving the value of $W_{\text{MgAl,A}}^{\text{Brg}} = 152.6$ kJ/mol and $\Delta G_{(5.12)}^0 = -85(4)$ kJ/mol at 27 GPa and 2000 K. The mole fraction of AlAlO_3 and $\text{MgAlO}_{2.5}$ in bridgmanite as a function of Al content calculated using the above derived interaction parameters are shown in Fig. 5.2b and they agree very well with the experimental data.

The very large interaction parameters required to fit the Al distribution in Fe-free Brg imply significant non ideality in the mixing of oxygen vacancies and between Mg and Al mixing on the A site. The magnitude of the interaction parameters is far greater than those normally observed for cation mixing among mantle silicates and is also much greater than the values required to fit AlAlO_3 mixing between Brg and corundum in the MgSiO_3 - AlAlO_3 system (Panero et al., 2006). This seems to be inevitable, however, because the concentration of the $\text{MgAlO}_{2.5}$ component goes through a maximum over a relatively small change in Al content. As the excess enthalpy contribution to the free energy is a function of concentration (Eq. 5.19 a, b), large coefficients i.e. interaction parameters, are required in order for the small change in total Al content to have a large effect on the speciation.

5.3.2 Fe-bearing bridgmanite

Experiments performed in the Fe-Mg-Si-O system coexisting with ferropericlase are plotted in Fig. 5.3a, with the trends expected for the OVS (Mg,Fe)FeO_{2.5} and the CCS FeFeO₃ substitution shown. As for the periclase saturated Al-Mg-Si-O system, the data fall very close to the OVS mechanism when Fe³⁺ is less than 0.03 atoms pfu although uncertainties here are high due to the relatively low concentrations. At higher Brg bulk Fe³⁺ concentrations, i.e. higher oxygen fugacity, the data move closer to CCS substitution. This indicates that the substitution mechanism is changing with Fe³⁺ concentration: MgFeO_{2.5} OVS appears to dominate at low Fe³⁺ abundance (<0.03 atoms pfu) and FeFeO₃ CCS dominates at higher Fe³⁺ concentration (≥ 0.04 atoms pfu). The change between these two substitution mechanisms, as for the Al-bearing system, appears to occur rapidly over within a narrow Fe³⁺ range of ~ 0.02 atoms pfu. Data from Frost and Langenhorst (2002) and McCammon et al. (2004b) saturated with MgO and Lauterbach et al. (2000) and Hummer and Fei (2012) where MgO is undersaturated are also shown for comparison. Compared with data from Lauterbach et al. (2000) and Hummer and Fei (2012) conducted at MgO undersaturated conditions, there seems to be no obvious effect of whether starting compositions are Fp-saturated or SiO₂-saturated on the substitution mechanism (Fig. 5.3). However, the EPMA composition measurement in these studies were performed using a high beam current of 15 nA and 30 nA respectively, which may have resulted in an incorrect Mg/Si ratio since Brg is metastable under electron beams especially for samples with low Fe content. Note, moreover, that the errors of the chemical compositions were not given in Lauterbach et al. (2000). The point at Fe³⁺=0.074 atoms pfu from Hummer and Fei (2012) is far above the region constrained by the CCS and OVS mechanism, indicating more Fe³⁺ on the A site than on the B site which requires the formation of Mg²⁺ vacancies on the A site for charge balance. However, the Fe³⁺/ΣFe ratio in this sample was not measured and the sample may in fact contain some ferrous iron. Moreover, the experiment may be not in equilibrium since, as mentioned in their study, in the run products Brg coexisted with small amounts of unreacted MgO and SiO₂ (Hummer and Fei, 2012).

In Fig. 5.3b, the mole fractions of FeFeO_3 CCS and $\text{MgFeO}_{2.5}$ OVS are plotted as a function of the oxygen fugacity (thus total Fe^{3+} content). As in Al-bearing Brg, the CCS component increases with increasing ferric Fe content and the OVS first increases and then decreases with increasing Fe^{3+} content. However, the OVS component appears to reach a maximum at much lower trivalent cation concentrations (~ 0.03 atoms pfu Fe^{3+}) compared with Al-bearing samples (~ 0.1 atoms pfu Al) and the proportion of the OVS component is also smaller being at most 2 mol% in the Fe-bearing system compared to ~ 5 mol% in the Al-bearing system (Liu et al., 2017).



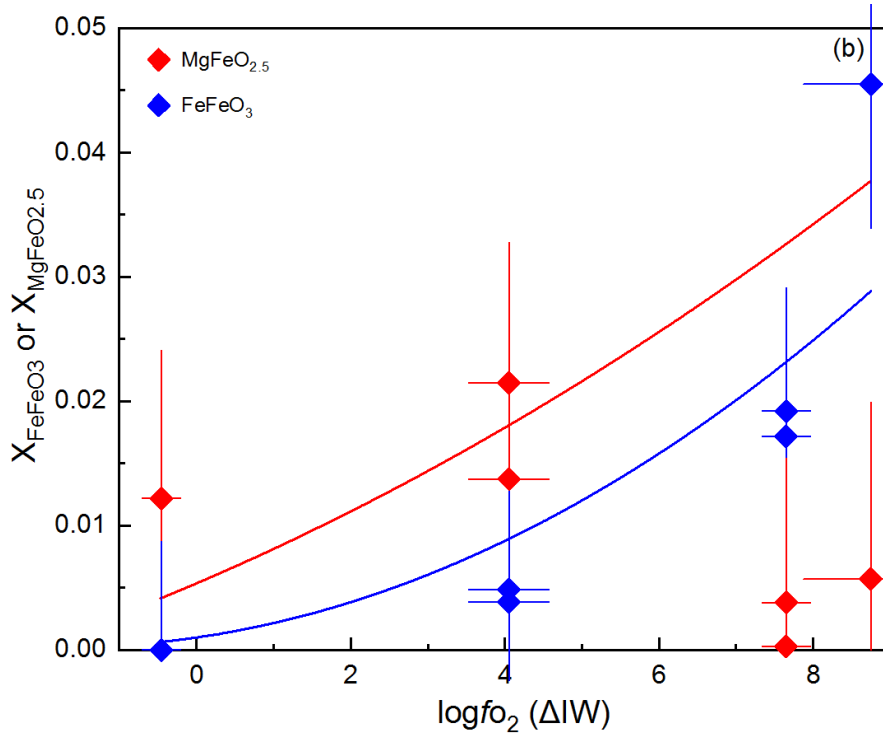
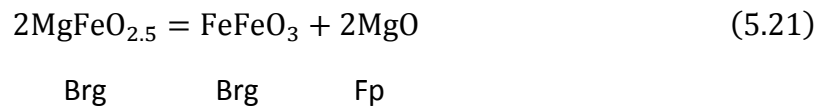


Fig. 5.3 (a) The variation of the Si content of Brg with the Fe³⁺ content at 25-26 GPa and 1923-2073 K. The two solid lines are expected trend lines for CCS along the MgSiO₃-Fe³⁺Fe³⁺O₃ join and the OVS along the MgSiO₃-MgFe³⁺O_{2.5} join respectively. The solid orange diamonds and the open orange circles represent the current study and data from Frost and Langenhorst (2002) and McCammon et al. (2004b) respectively where Brg coexisting with Fp. The open green circles are data from Lauterbach et al. (2000) and Hummer and Fei (2012) where Brg is not in equilibrium with Fp. (b) The mole fraction of FeFeO₃ and MgFeO_{2.5} component in Brg as a function of oxygen fugacity at 25 GPa and 1973 K. Solid lines are the calculated values based on the thermodynamics models derived at 25 GPa and 1973 K.

A similar equilibrium to that in the Al-bearing system can be written to describe the distribution of Fe³⁺ between cation sites in Brg i.e.,



The equilibrium coefficient K for this reaction is:

$$K = \frac{a_{\text{FeFeO}_3}^{\text{Brg}} a_{\text{MgO}}^{\text{Fp}}}{(a_{\text{MgFeO}_{2.5}}^{\text{Brg}})^2} \quad (5.22)$$

where $a_{\text{FeFeO}_3}^{\text{Brg}}$ and $a_{\text{MgFeO}_{2.5}}^{\text{Brg}}$ are the activities of the FeFeO₃ and MgFeO_{2.5} components in Brg, respectively. At equilibrium, the standard state Gibbs free-energy change can be expressed by

$$\Delta G_{(5.21)}^0 = -RT \ln \frac{a_{\text{FeFeO}_3}^{\text{Brg}} a_{\text{MgO}}^{\text{Fp}}}{\left(a_{\text{MgFeO}_{2.5}}^{\text{Brg}}\right)^2} \quad (5.23)$$

As will be seen later the Brg components are assumed to mix ideally so that

$$a_{\text{MgFeO}_{2.5}\text{V}_{0.5}}^{\text{Brg}} = 2x_{\text{Mg,A}}x_{\text{Fe,B}}(x_{\text{V},01})^{0.5}(x_{\text{O},01})^{0.5} \quad (5.24)$$

and

$$a_{\text{FeFeO}_3}^{\text{Brg}} = x_{\text{Fe,A}}x_{\text{Fe,B}} \quad (5.25)$$

For MgO in ferropericlase however,

$$a_{\text{MgO}}^{\text{Fp}} = x_{\text{MgO}}^{\text{Fp}} \gamma_{\text{MgO}}^{\text{Fp}} \quad (5.26)$$

where $x_{\text{MgO}}^{\text{Fp}}$ is the mole fraction of MgO in ferropericlase and the activity coefficient, $\gamma_{\text{MgO}}^{\text{Fp}}$, is determined from the interaction parameters given by Frost (2003).

Because the proportions of Fe³⁺ and Fe²⁺ in Brg depend on the f_{O_2} a further equilibrium is required to define their concentration, such as,

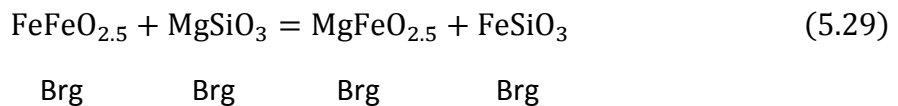


for which the condition of equilibrium is,

$$\Delta G_{(5.27)}^0 = -RT \ln \frac{a_{\text{FeFeO}_3}^{\text{Brg}}}{\left(a_{\text{FeO}}^{\text{Fp}}\right)^2 (f_{\text{O}_2})^{0.5}} \quad (5.28)$$

The activity of FeO in ferropericlase is defined as in equation (5.26) and calculated using the same activity composition data. For each experimental data point obtained in this study standard state Gibbs free energy terms can be calculated from equations (5.23) and (5.28).

Two constant values of $\Delta G_{(5.21)}^0$ and $\Delta G_{(5.27)}^0$ should then be obtained for all data, which in theory would also require activity composition relations to be considered. Brg site assignments estimated from EPMA data and Mössbauer $\text{Fe}^{3+}/\Sigma\text{Fe}$ ratios have large uncertainties, however, relative to the small concentrations of Fe^{3+} involved. One way to fit the relationship between the Fe^{3+} content and f_{O_2} is to allow the site occupancies of Fe^{3+} on the A and B Brg sites to vary under the constraint of mass balance and to find the Fe^{3+} site occupancies where constant values of the two ΔG^0 terms are found for each experiment. In fact this method leads to a range of solutions with the best result judged by the degree of agreement with the experimental f_{O_2} - Fe^{3+} relationship, shown in Fig 5.4a, and with the proportions of the two components, shown in Fig 5.3b. This result is achieved with $\Delta G_{(5.21)}^0 = -27.886$ kJ/mol and $\Delta G_{(5.27)}^0 = 172.236$ kJ/mol. Note that in Fig 5.4a the data that appear to be in poor agreement with the model at $\Delta\text{IW} +7.7$ have a Brg bulk Fe content of only 0.05 atoms pfu, whereas the other data points as well as the model have ~ 0.1 atoms pfu of Fe. In fact all data fit the model reasonably well once the different total Fe content is accounted for (Fig. 5.4b). It was not possible to find a solution that fitted both the total Fe^{3+} and the Fe^{3+} speciation perfectly, slightly better solutions could be found that assumed very little of the CCS component, but this was deemed to be in poor agreement with the experimentally determined site occupancies. Activity composition models similar to those described in equations (5.19a, b) were found to provide very little improvement in the fitting even when Margules terms of the order of mega Joules per mole were employed. Similarly, an activity model that accounts for the Brg reciprocal solution:



provided very little overall improvement of the fit. As a result, it was considered that the resulting model, which has only 2 fitting terms, provides the best fit within the uncertainties.

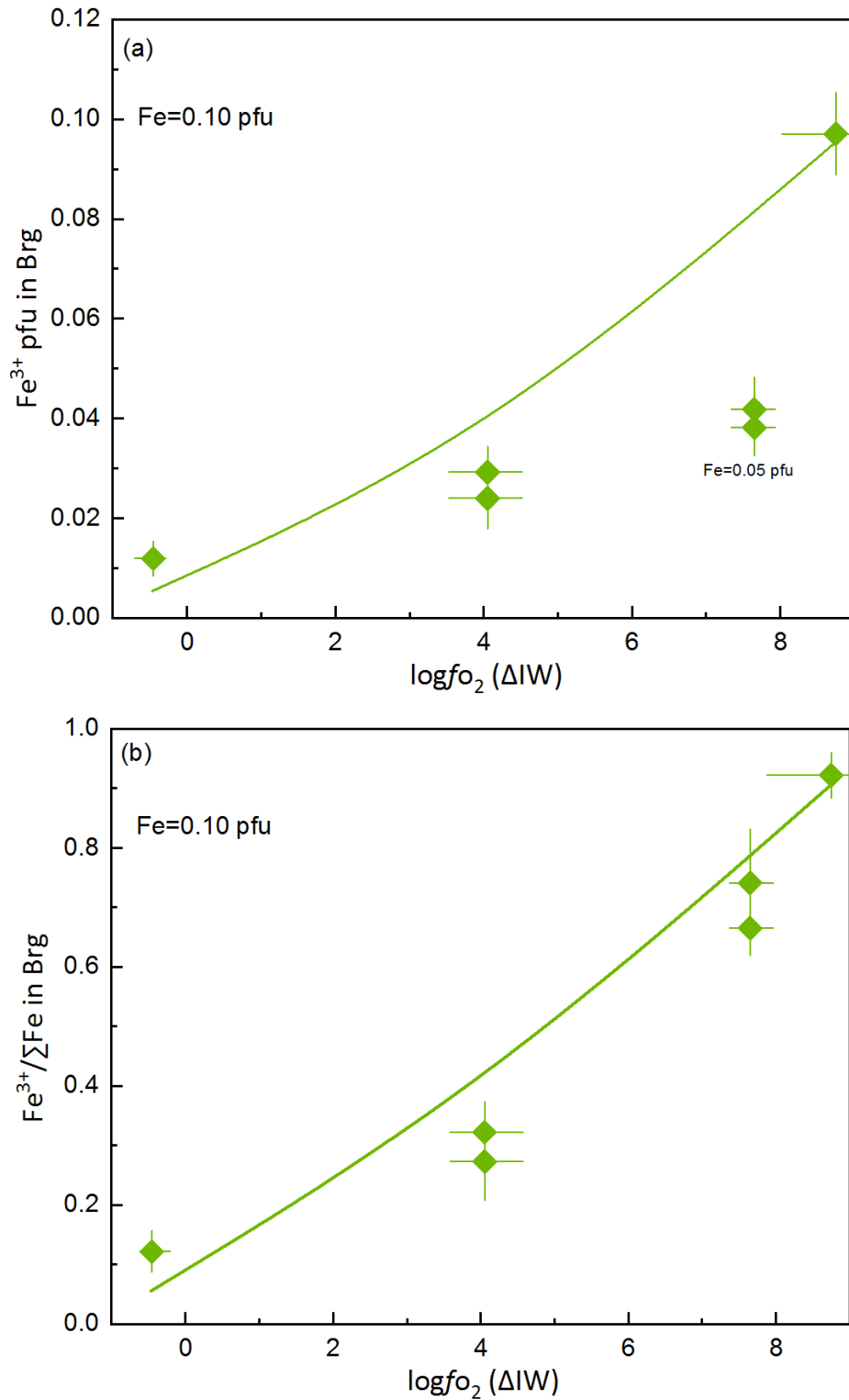


Fig. 5.4 (a) The ferric iron content in Brg and (b) the ferric iron over total iron ratio in Al-free Brg as a function of oxygen fugacity at $P=25$ GPa, $T=1973$ K and fixed Fe content of 0.10 atoms pfu (except for the data points indicated) in Brg. The solid lines are calculated model curves.

5.3.3 Fe, Al-bearing bridgmanite

The substitution mechanisms in Fe and Al bearing Brg from both f_{O_2} buffered experiments and single crystal synthesis experiments are examined using the results of EMPA and Mössbauer spectroscopy analysis in Fig. 5.5. Data from Frost and Langenhorst (2002); Frost et al. (2004); Lauterbach et al. (2000) and McCammon et al. (2004b) are also shown for comparison. At Fp saturated conditions (red symbols in Fig. 5.5), both OVS and CCS substitution mechanisms are important at low M^{3+} ($M^{3+}=Al^{3+}+Fe^{3+}$) concentrations (<0.1 atoms pfu). The CCS mechanism appears to be the most favorable substitution mechanism at high M^{3+} concentrations (> 0.1 atoms pfu) but it is possible that some OVS is present even at high M^{3+} concentrations of 0.34 atoms pfu. Based on the samples analyzed in this study, OVS accounts for up to ~4 mol% of the Brg components. This maximum OVS component value was achieved in the sample where the Al content (0.23 atoms pfu) is significantly higher than the Fe^{3+} content (0.11 atoms pfu) in Brg (S7214). Experiments performed at Fp undersaturated conditions in this study fall almost along the CCS trend line, indicating that only CCS is present as in Al-bearing samples with bulk Mg=Si. In contrast, Lauterbach et al. (2000) conducted at Fp undersaturated conditions have some $MgM^{3+}O_{2.5}$ OVS component comparable with those at Fp saturated conditions. As mentioned in section 5.3.2, it is not clear whether this may be due to errors in the EPMA composition measurements. Because Brg is easy to become amorphous under electron beams, the Mg/Si ratio may be incorrect at high electron beam current of 15 nA as that used in the mentioned study. This phenomenon is more serious at low Brg Fe concentrations. Moreover, the errors of the chemical composition were not provided by Lauterbach et al. (2000) and the errors shown in the figure all come from the $Fe^{3+}/\Sigma Fe$ ratio measurement of Brg.

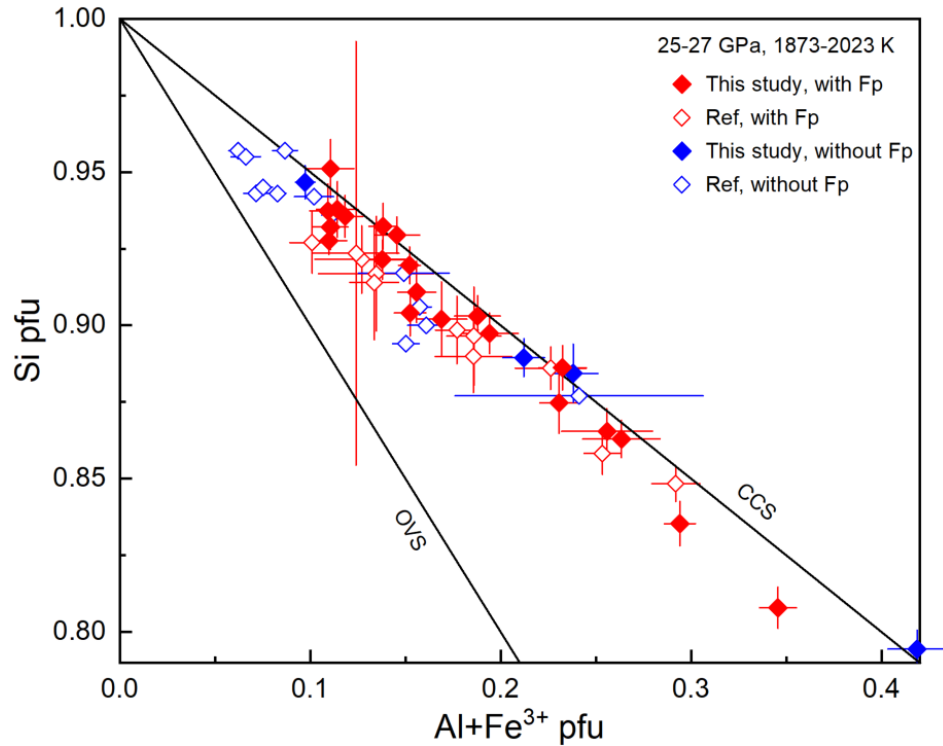


Fig. 5.5 The variation of the Si content of Brg with the total trivalent cation content (i.e. $M^{3+} = Al^{3+} + Fe^{3+}$) for Fe and Al-bearing Brg at 25-27 GPa and 1873-2023 K. Two solid lines indicate the expected trend for the charge coupled substitution (CCS) and oxygen vacancy substitution (OVS) mechanisms. Solid red diamonds and open red diamonds indicate Brg from Fp saturated experiments from this study and from Frost and Langenhorst (2002); Frost et al. (2004) and McCammon et al. (2004b) respectively. Solid blue diamonds and open blue diamonds indicate Brg at Fp undersaturated conditions from this study and from Lauterbach et al. (2000) respectively.

In line with Fig. 5.5, the cation distribution procedure (Table 5.2) never results in an excess of 3+ cations on the A site, which would require an A site cation vacancy to achieve charge balance. Whether Fe^{3+} occupies the A or B site then simply depends on the relative proportions of Fe^{3+} and Al. When $Fe^{3+} \leq Al$ (i.e. $\Delta(Fe^{3+}-Al) \leq 0$) as indicated in Fig. 5.6a, the content of Fe^{3+} determined for the B site is zero, within error. However, when Fe^{3+} becomes larger than Al, i.e. $\Delta(Fe^{3+}-Al) > 0$, Fe^{3+} also occupy the B site. In Fig. 5.6b, the two trend lines for $MgFeO_{2.5}$ OVS and $FeFeO_3$ CCS are also shown. When $\Delta(Fe^{3+}-Al)$ is small, the different substitution mechanisms are impossible to distinguish but when $\Delta(Fe^{3+}-Al)$ gets larger, the data fall on the $FeFeO_3$ CCS trend line.

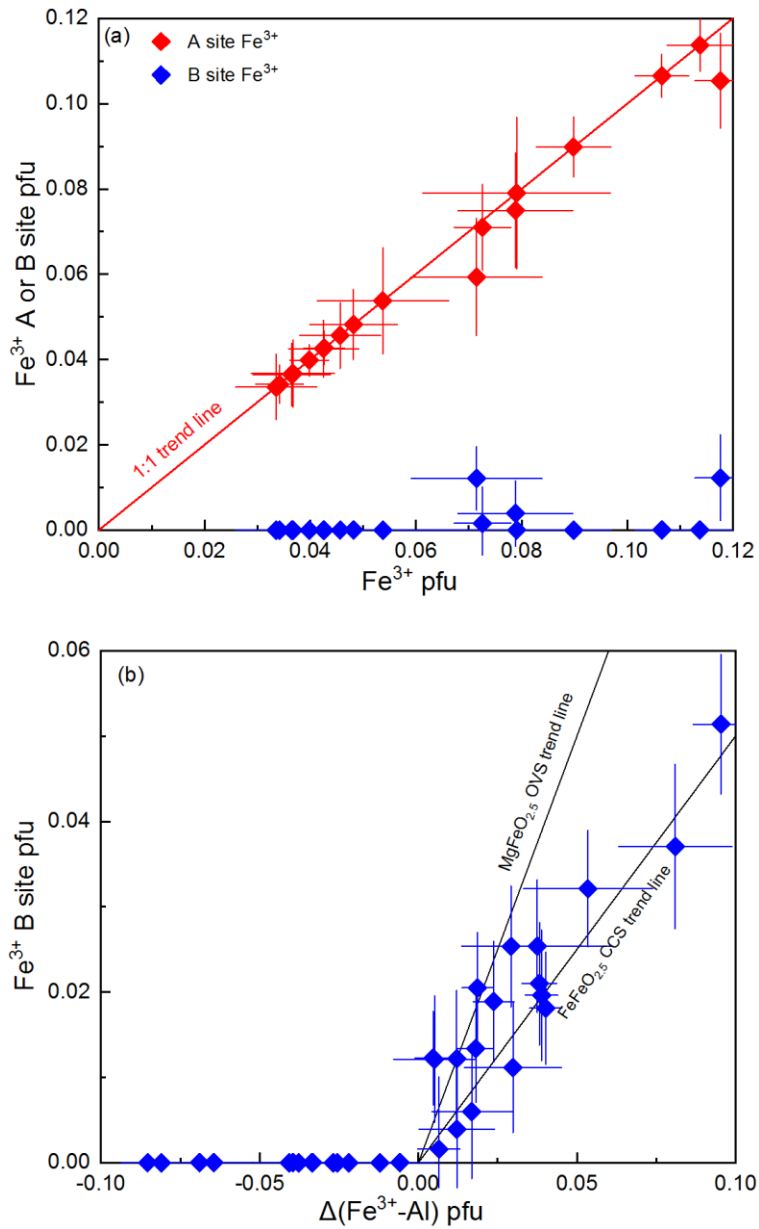
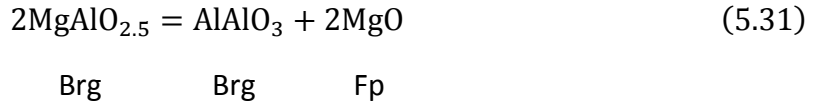
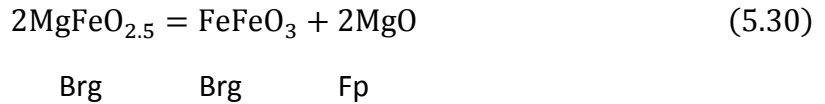


Fig. 5.6 (a) The amount of Fe³⁺ on the A site and B site versus the total Fe³⁺ content in Brg for Al > Fe³⁺. Red diamonds indicate Fe³⁺ on the A site and blue diamonds indicate Fe³⁺ on the B site. The 1:1 trend line representing all Fe³⁺ at the A site is also shown. (b) The amount of Fe³⁺ on the B site versus the difference between Fe³⁺ and Al in Brg. When Δ(Fe³⁺-Al) ≤ 0, no Fe³⁺ is considered present at the B site while when Δ(Fe³⁺-Al) > 0, Fe³⁺ starts to go into the B site. The two solid lines indicate the MgFeO_{2.5} OVS and FeFeO₃ CCS trend line expected.

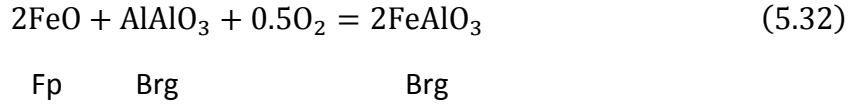
In reality, however the site occupancies are likely to be more complicated than assumed by this simple treatment. In the Fe or Al free systems both 3+ cations are capable of entering both sites and both appear to be capable of entering the B site with charge balance

provided by the OVS mechanism. Although the FeAlO₃ component is likely important, if excesses of Al or Fe³⁺ occur then each cation still has to enter the other site. Furthermore, it is improbable on configurational entropy grounds that Fe³⁺ and Al order fully into the A and B sites respectively, even when they are present in equal proportions.

In order to build a thermodynamic model that correctly describes the effects of Al, total Fe content and f_{O_2} on the Brg Fe³⁺ content a number of components need to be considered in order to allow the site occupancies of 3+ cations to be realistically described. By including a mass balance constraint for the bulk Al content three equilibria are required to describe the 3+ cation site occupancies. For this purpose the following equilibria are used,



And



Expressions for the standard state Gibbs free energies for equilibria (5.30) and (5.31) are given in equations (5.21) and (5.12) and the activities of each component have also been defined. For equilibrium (5.32) we can write,

$$\Delta G_{(5.32)}^0 = -RT \ln \frac{\left(a_{\text{FeAlO}_3}^{\text{Brg}}\right)^2}{\left(a_{\text{FeO}}^{\text{Fp}}\right)^2 a_{\text{AlAlO}_3}^{\text{Brg}} \left(f_{O_2}\right)^{0.5}} \quad (5.33)$$

where $a_{\text{FeAlO}_3}^{\text{Brg}} = x_{\text{Fe}^{3+},\text{A}} x_{\text{Al},\text{B}}$ and $a_{\text{AlAlO}_3}^{\text{Brg}} = x_{\text{Al},\text{A}} x_{\text{Al},\text{B}}$ with the latter also used for equilibrium (5.31) for consistency. Values for $\Delta G_{(5.30)}^0$, $\Delta G_{(5.31)}^0$ and $\Delta G_{(5.32)}^0$ are calculated for each experimental data point by allowing the site occupancies of Fe³⁺ on the A and B sites and Al on the A site to vary in a minimisation routine that finds sets of occupancies where ΔG^0 values for each of the three equilibrium are identical for each data point. The Al

content on the B site and the Fe^{2+} content on the A site are determined from a mass balance using the bulk Al and Fe contents of the experimental samples. The experimental oxygen fugacity is employed and the Mg and Si sites are constrained by summing site occupancies to unity. A range of successful sets of constant ΔG^0 values can be found for the experimental parameters with the overall optimisation then judged by how accurately the total Fe^{3+} content of each experimental is matched. The best fit to the 11 experimental data points employed was found for the values $\Delta G_{(5.30)}^0 = -180.438$ kJ/mol, $\Delta G_{(5.31)}^0 = -32.807$ kJ/mol and $\Delta G_{(5.32)}^0 = 24.605$ kJ/mol. The quality of this fit is shown in Fig. 5.7a where the fit to the Al-free data set is also shown. One data point deviates from the model at Al=0.07, Fe=0.07 atoms pfu at $\sim\Delta IW=2$ because it actually has a lower total Fe content of 0.06 atoms pfu with respect to the other data points. The agreement with the experimental data in both total Fe^{3+} and $\text{Fe}^{3+}/\Sigma\text{Fe}$ is very good considering that the model has only 3 adjustable parameters.

Activity composition models similar to those described for the Fe-Mg-Si-O system were tested but no significant improvement in the data fitting was achieved. It should be noted that this does not necessarily imply that the site mixing is ideal but rather that activity composition relations do not have a sufficient effect over the compositional range examined. Using this model, the ferric Fe content and its distribution over A and B sites in Brg at 25 GPa and 1973 K as well as the composition of coexisting Fp can be obtained at any given oxygen fugacity and Fe and Al content in Brg. The $\text{Fe}^{3+}/\Sigma\text{Fe}$ ratio as a function of Al content in Brg calculated at constant $f_{\text{O}_2}=\text{IW}-0.6$ and Fe=0.11 atoms pfu and $f_{\text{O}_2}=\text{IW}+7.5$ and Fe=0.11 atoms pfu are in good agreement with our experimental data (Fig. 5.1a). The $\text{Fe}^{3+}/\Sigma\text{Fe}$ ratio was also calculated as a function of Fe content in Brg at Al content of 0.07 pfu and oxygen fugacity of IW-1, which also reproduce the experimental trend very well (Fig. 5.1b).

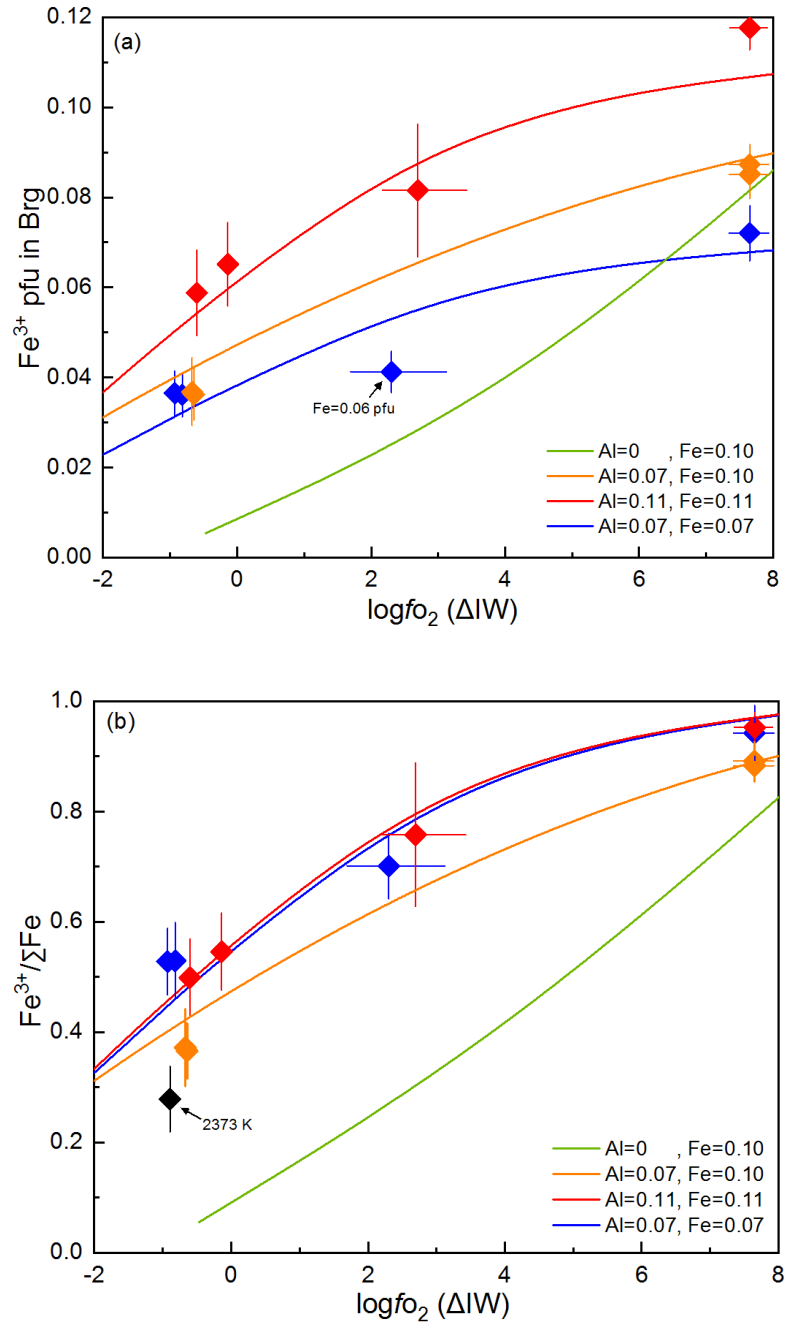


Fig. 5.7 Calculated model curves predicting the (a) Fe³⁺ content and (b) Fe³⁺/ΣFe ratio in Fe, Al-bearing Brg given the oxygen fugacity, the bulk Al and Fe content in Brg at 25 GPa and 1973 K, plotted with the data at similar conditions and compositions from the experiments. The model curve for Al free samples described in section 5.3.2 is also plotted for comparison. The black diamond indicates a Brg sample with Al=0.12 and Fe=0.12 atoms pfu synthesized at higher temperature of 2373 K.

5.4 Composition of bridgmanite and ferropericlase as a function of oxygen fugacity in pyrolite

Using the model described above for the Brg composition in conjunction with the expression for the Fe²⁺-Mg distribution coefficient between Fp and Brg from Nakajima et al. (2012), it is possible to calculate the coexisting compositions for Brg and Fp as a function of f_{O_2} for a given bulk composition. The pyrolite bulk composition employed by Irifune (1994) is used for this purpose. The Fe²⁺-Mg distribution coefficient between Brg and Fp, $K_D = (x_{FeSiO_3}^{Brg}/x_{MgSiO_3}^{Brg})/(x_{FeO}^{Fp}/x_{MgO}^{Fp})$, is described by

$$RT \ln K_D = -\Delta G^o(P, T) - W_{FeMg}^{Brg} (1 - 2x_{FeSiO_3}^{Brg}) + W_{FeMg}^{Fp} (1 - 2x_{FeO}^{Fp}) \quad (5.34)$$

where $\Delta G^o = (22300 + 200P + 4T)$ J/mol, $W_{FeMg}^{Brg} = 4900$ J/mol and $W_{FeMg}^{Fp} = (11000 + 110 \cdot P)$ J/mol and P is pressure in GPa (Nakajima et al., 2012). A mass balance is constructed to determine the mineral compositions and proportions corresponding to this bulk composition with the Fe²⁺ and Fe³⁺ contents for Brg and Fp calculated from the model. The Al content of Brg is refined to agree with the mass balance and a small amount of Al (Table 5.3) is considered in Fp in line with measurements made in this study. For completeness a CaSiO₃ perovskite composition has also been included. The concentrations of Cr, Na and Ti are not considered in the model neither is the Ca content of Brg and the Mg content of CaSiO₃ as these concentrations are all small. The results of such a calculation are shown in Table 5.3 and compared with the results of two experiments performed on this bulk composition by Irifune (1994) and Irifune et al. (2010) at 1873 K and approximately 28 GPa. Note that the model has only been fit to data from 25 GPa and 1973 K, but as these previous studies show, such differences in conditions should lead to relatively modest changes in mineral compositions once pressures above the garnet stability field are reached. In order to achieve a similar distribution of total Fe between Brg and Fp it was necessary to perform the calculation at an oxygen fugacity of $IW + 1.5$, which is a reasonable value for these experiments. As can be seen in Table 5.3 the agreement between the model

Table 5.3 Comparison between experimental and model calculations for lower mantle phase compositions in weight % for a pyrolite bulk composition.

	Fraction	SiO ₂	TiO ₂	Al ₂ O ₃	Cr ₂ O ₃	ΣFeO	FeO	Fe ₂ O ₃	MgO	CaO	NiO	Na ₂ O	Total	K _D (app)
Pyrolite Bulk		45.2	0.3	3.9	0.5	8.1			37.5	3.8	0.3	0.3	99.9	
<i>Model results, 25 GPa, 1973 K, ΔIW=1.5</i>														
Brg	0.785	52.97		5.04		7.09	1.77	5.32	34.9				100	0.79
Fp	0.134			0.36		18.88	18.88		79.55				100	
CaPv	0.079	51.72								48.27			100	
Bulk		45.74		4.01		8.11			38.12	3.84			100	
<i>Irifune et al. (2010)</i>														
<i>M439, 28.7 GPa, 1873 K</i>														
Brg		50.21	0.40	4.58	0.58	6.61			33.42	0.48	0.04	0.07	96.38	0.77(5)
		(72)	(15)	(9)	(20)	(35)			(100)	(45)	(3)	(5)		
Fp		0.81	0.10	0.71	0.71	18.90			73.47	0.11	1.45	0.07	97.31	
		(62)	(10)	(3)	(20)	(3)			(84)	(14)	(27)	(22)		
<i>Irifune (1994)</i>														
<i>E631, 28 GPa, 1873 K</i>														
Brg		53.07	0.31	4.92	0.56	7.04			33.43	0.25	0.15	0.23	99.96	0.75
Fp		1.01		0.97	0.98	20.47			72.56	0.25	1.22	1.22	98.33	

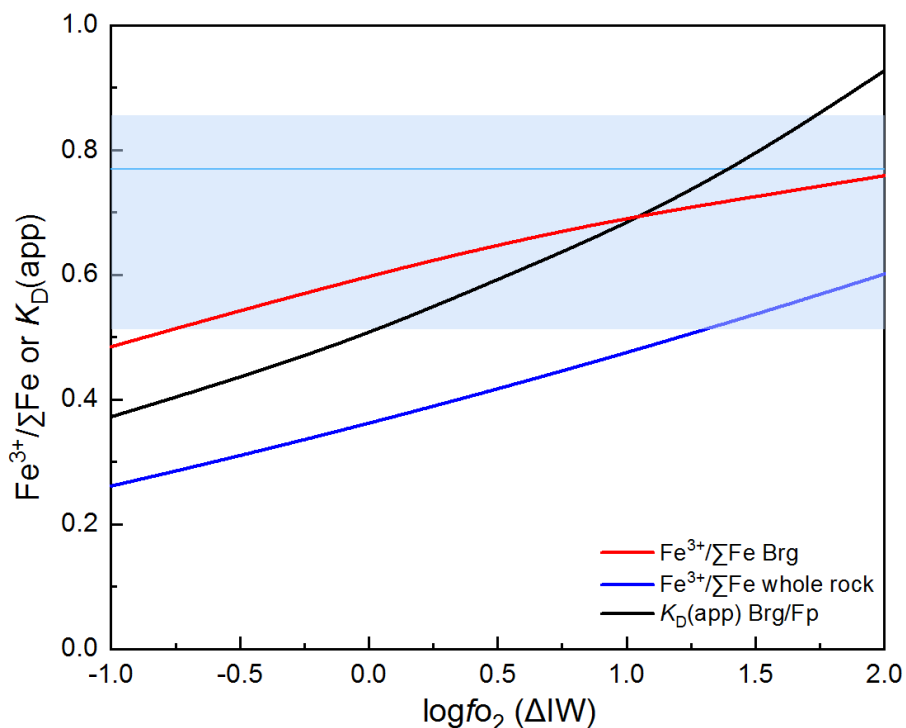


Fig 5.8. Model results for $K_D(app)$ describing the Fe-Mg exchange between Brg and Fp and the $Fe^{3+}/\Sigma Fe$ ratio of both Brg and the whole rock calculated for a pyrolite composition as a function of oxygen fugacity. The calculation is based on the model determined from data at 25 GPa and 1973 K. The blue shaded region shows the range in $K_D(app)$ reported by Irifune et al. (2010) for a pyrolite composition between 28.7 and 47.4 GPa, with the solid horizontal line showing the value at 28.7 GPa. While Irifune et al. (2010) suggest that the changes in $K_D(app)$ may result from an Fe^{2+} spin transition in Fp, the results presented here show that changes in the experimental f_{O_2} between IW and IW +1.5 can also explain the range of $K_D(app)$.

calculation at these conditions and both experiments is very good. Furthermore Irifune et al. (2010) report two estimates of the $Fe^{3+}/\Sigma Fe$ ratios of Brg in the reported experiment of 0.66 (± 0.06) and 0.52 (± 0.1) from electron energy loss and Mössbauer spectroscopy measurements respectively. The $Fe^{3+}/\Sigma Fe$ ratio obtained from the model at $f_{O_2}=IW + 1.5$ is 0.79 and 0.67 at $f_{O_2}=IW + 1$.

Irifune et al. (2010) calculated the apparent Fe-Mg distribution coefficient, $K_D(app)$, between Brg and Fp where all Fe is considered to be Fe^{2+} . Between 28 and 47.4 GPa a decrease in $K_D(app)$ was reported which they attributed to a possible iron spin transition.

For experiment M439 of Irifune et al. (2010) reported in Table 5.3 the calculated $K_D(app)$ is 0.77(5) whereas the model gives a value of 0.79 at f_{O_2} of IW + 1.5. In fact as shown in Fig 5.8 $K_D(app)$ is a strong function of f_{O_2} and the entire range in values reported by Irifune et al. (2010) can be achieved through changes in f_{O_2} between IW and IW + 1.5. Such an oxygen fugacity range would be quite consistent with the use of graphite capsules by Irifune et al. (2010) which would impose only a maximum possible f_{O_2} of approximately 2 log units above IW as discussed in section 6.1. There could of course be other reasons why $K_D(app)$ was observed to change with pressure, including a spin transition, however these results clearly demonstrate that such determinations are unconstrained unless the oxygen fugacity is fixed as a result of the strong variation in the Fe^{3+} content of Brg with f_{O_2} . Variations in f_{O_2} , for example, could easily explain the significant discrepancies in $K_D(app)$ found for deep lower mantle conditions shown in Fig 1.11b

Figure 5.9 shows how the proportions of 3+ cations on each Brg site change with the oxygen fugacity for a pyrolite composition. The proportion of oxygen vacancies (OV) is also shown. The amount of Fe^{3+} on the Brg B site is determined to be less than 0.0001 atoms pfu and is therefore not shown. As the ferric iron content increases Al is pushed out of the A site and into the B site. At the same time the amount of 3+ cations charge balanced in the B site through oxygen vacancies decreases. No direct comparison can be made with the experiments because the Brg formed in the pyrolite composition contains approximately 0.1 total cations of Al and 0.07 cations of iron pfu. However the proportion of oxygen vacancies determined for a bulk composition with Al=0.1 cations and Fe=0.1 cations pfu is shown for comparison and is in reasonable agreement with a general decrease, although the propagated errors are large. It is important to note that at high oxygen fugacity the 3+ cation proportions can be described almost completely with a charge coupled $Fe^{3+}AlO_3$ component, however, at lower oxygen fugacities both the $AlAlO_3$ and $(Mg,Fe)AlO_{2.5}$ components are present, although the latter is also near negligible in proportion. The presence of OV at oxygen fugacities that are more realistic for the bulk of the lower mantle is likely to be important for Brg transport properties.

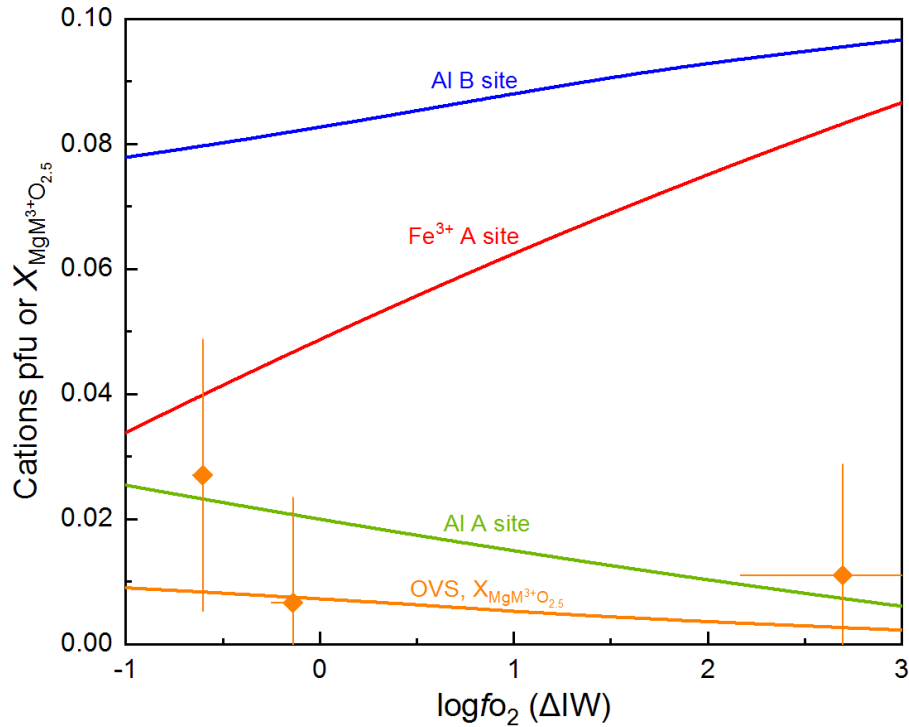


Fig. 5.9 Model results for proportions of trivalent cations and oxygen vacancy substitution fractions in Brg as a function of oxygen fugacity for a pyrolite composition. The calculation is based on data at 25 GPa and 1973 K. Brg formed in a pyrolite composition contains 0.10 pfu Al and 0.07 pfu Fe. The orange diamonds show experimentally determined OVS proportions in Brg with 0.11 pfu Fe and Al.

5.5 Metal saturation determination

As shown in Fig. 5.8 the $\text{Fe}^{3+}/\Sigma\text{Fe}$ ratio of the pyrolite whole rock is a function of the oxygen fugacity and even at oxygen fugacities below IW the ratio remains over 0.2. Upper mantle rocks have low $\text{Fe}^{3+}/\Sigma\text{Fe}$ ratios with values generally not exceeding 0.03 (Canil et al., 1994; Woodland et al., 2006). As pointed out by Frost et al. (2004), this implies that if the mantle has a relatively constant bulk oxygen content then the oxygen fugacity in the lower mantle would be driven to values where iron-nickel alloy or iron-nickel-sulphur rich phases would form. The oxygen released by this reduction satisfies the requirement of Brg for ferric iron at low oxygen fugacities. Ferric iron is therefore produced through the reaction



Although there is no evidence that NiO is present in the 3+ oxidation state in Brg, NiO would start to reduce to form Fe-Ni alloy at a higher oxygen fugacity than that at which reaction (5.35) would occur in the lower mantle and the reduction of NiO would therefore also provide oxygen to form ferric iron in Brg. Using a pyrolite bulk composition with an initially defined bulk $Fe^{3+}/\Sigma Fe$ ratio, the proportion of iron-nickel metal that would precipitate to provide sufficient ferric iron in Brg for the implied oxygen fugacity can be calculated. This calculation uses the model describes in section 5.3.3 combined with a pyrolite composition mass balance and a thermodynamic description for the reduction of NiO to Fe-Ni metal.

In this calculation the oxygen fugacity is fixed by the equilibria



And



where the f_{O_2} for equilibrium (5.36) is determined from

$$\log f_{O_2} = \frac{\Delta G_{(5.36)}^0}{RT \ln(10)} + 2 \log \frac{x_{FeO}^{Fp}}{x_{Fe}^{Alloy}} + 2 \log \frac{\gamma_{FeO}^{Fp}}{\gamma_{Fe}^{Alloy}} \quad (5.38)$$

$\Delta G_{(5.36)}^0$ is the standard state free energy of equilibrium (5.36) at the pressure and temperature of interest and is determined employing the equations of Holland and Powell (2011) but using the data given in Table 5.5. γ_{FeO}^{Fp} , the activity coefficient of FeO in ferropericlasite, is determined using a ternary (MgO-FeO-NiO) symmetric Margules equation with the terms given in Table 5.4. In order to obtain Ni partition coefficients between Fp and Fe-Ni alloy that were in agreement with the existing experimental data (Urakawa, 1991) it was necessary to assume ideal mixing in the Fe-Ni alloy. An identical expression to equation (5.38) can be written for equilibrium (5.37). In the refinement the f_{O_2} is, therefore, constrained by the equilibria (5.36) and (5.37). The alloy composition and the proportion of

NiO in Fp are refined within the constraints of a mass balance such that both equilibria yield the same oxygen fugacity, but with the total amount of alloy produced controlled by the Brg Fe³⁺ content through reaction (5.35). The FeO concentration of Fp is controlled by equilibrium (5.36) and the Brg FeO content is constrained by the conditions of equilibrium for equilibria (5.30), (5.31) and (5.32), which in turn depends on the f_{O_2} and the total Fe and Al in the bulk composition. A non-linear least squares minimization routine is used to vary the proportions and compositions of the four phases, Brg, Fp, CaSiO₃ perovskite and Fe-Ni alloy, while maintaining mass balance and ensuring that the Gibbs free energy of each of the described equilibria is equal to zero. This also requires that the site occupancies of 3+ cations in Brg are also refined simultaneously.

Table 5.4 Margules terms for non-ideal mixing of Fp.

W_{Fe-Mg}	W_{Fe-Ni}	W_{Mg-Ni}
11000+110* P (GPa)	-9500	-14000

Table 5.6 shows the resulting calculated compositions of lower mantle phases for a pyrolite bulk composition with an initial Fe³⁺/ΣFe ratio of 0.03 i.e. similar to the value proposed for the upper mantle. The oxygen fugacity is $1W - 0.8$, which results in the formation of 0.6 wt.% Fe-Ni alloy containing approximately 26 wt.% Ni. The resulting Fe³⁺/ΣFe ratio of Brg is 0.51 and the bulk pyrolite has a ratio of 0.28. Figure 5.10 shows similar calculations performed for both a pyrolite and a harzburgite bulk composition assuming different initial bulk Fe³⁺/ΣFe ratios. The proportion of metal alloy that forms is much smaller for a harzburgite bulk composition because the Al content of the Brg formed is smaller, approximately 0.2 atoms pfu, and the Fe³⁺/ΣFe ratio in equilibrium with metallic alloy is only approximately 0.3.

Table 5.5 Thermodynamic and equation of state data.

	$\Delta_f H^\circ$ (J/mol)	S (J/K/mol)	V (J/bar)	a	b	c	d	α_o ($\times 10^5$) (K ⁻¹)	K_o (kbar)	K'
FeO Fp	-271970	60.6	1.226	44.4	0.00828	-1214200	185.2	3.49	1469	4.00
NiO Fp	-239470	38	1.097	47.7	0.007824	-392500	0	3.30	1900	5.40
Fe Alloy		27.09	0.707	46.2	0.005159	723100	-556.2	3.56	1330	5.00
Ni Alloy		29.87	0.659	49.8	0	585900	-533.9	4.28	1790	4.30
O ₂				48.3	-0.0006913	499230	-420.66			
FeAlO ₃ (Brg)			2.708					1.87	2510	4.14
AlAlO ₃ (Brg)			2.579					1.87	2510	4.14
MgAlO _{2.5} (Brg)			2.664					1.87	2510	4.14
FeFeO ₃ (Brg)			2.947					1.87	2510	4.14
MgFeO _{2.5} (Brg)			2.750					1.87	2510	4.14

Notes: All data from Holland and Powell (2011) except Brg data where the volumes are from this study and equation of state data are assumed to be the same as for MgSiO₃ Brg from Holland and Powell (2011) and data in italics which are from Campbell et al. (2009). a-d are heat capacities terms with $C_p = a + bT + cT^{-2} + dT^{-0.5}$

Table 5.6 Model calculation for the composition and proportions of lower mantle phases as well as the precipitated metal in weight % for a pyrolite bulk composition assuming an initial Fe³⁺/ΣFe ratio of 0.03

	Fraction	SiO ₂	Al ₂ O ₃	ΣFeO	FeO	Fe ₂ O ₃	MgO	CaO	NiO	Ni	Fe	Total
Brg	0.771	54.02	5.08	5.25	2.43	2.82	35.63		0.05			100
Fp	0.143			25.89	25.89		73.36		0.74			100
CaPv	0.080	51.72						48.27				100
Alloy	0.006									26.33	73.66	
Bulk		45.79	3.92	8.20	5.57	2.18	37.96	3.87	0.14	0.16	0.45	100

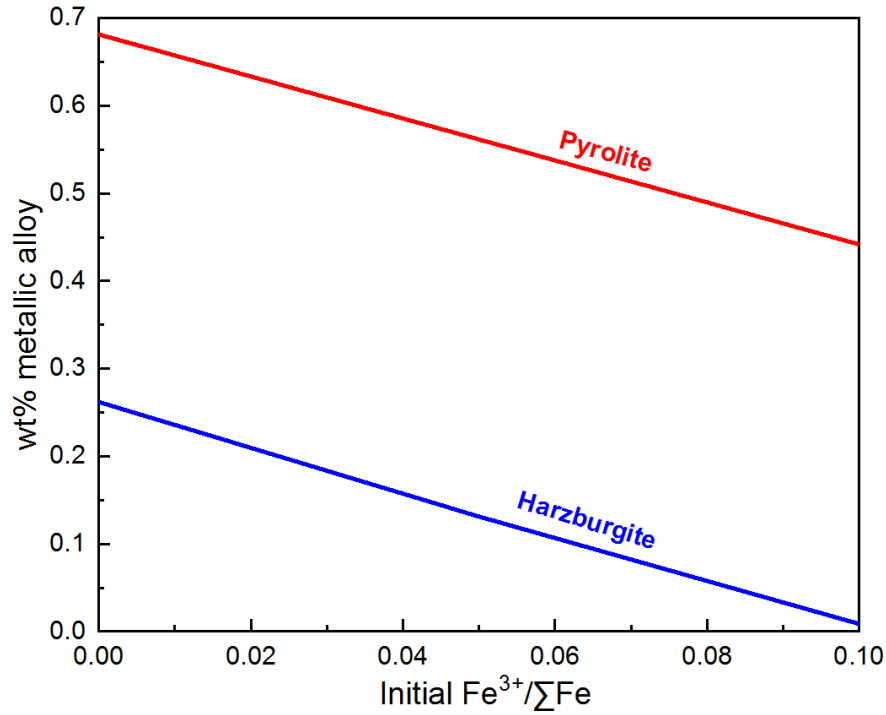


Fig. 5.10 The metallic alloy formed in weight % for pyrolite and harzburgite bulk compositions as a function of the initial $\text{Fe}^{3+}/\Sigma\text{Fe}$ ratio of the whole rock.

5.6 Extrapolation to higher pressures

In the model described in section 5.3.3 the composition of Brg is determined using three equilibria involving different Brg and Fp components, for which standard state Gibbs free energies have been estimated at the pressure and temperature of interest, i.e. 25 GPa and 1973 K. In section 4.2 the volumes of these Brg components have been determined which allows the pressure dependencies of the three equilibria to be estimated. For equilibrium (5.32) for example the pressure dependence can be included using the equation

$$\Delta G_{(5.32)}^0 - \int_0^{25} \Delta V \cdot dp + \int_0^P \Delta V \cdot dp = -RT \ln \frac{(a_{\text{FeAlO}_3}^{\text{Brg}})^2}{(a_{\text{FeO}}^{\text{Fp}})^2 a_{\text{AlAlO}_3}^{\text{Brg}} (f_{\text{O}_2})^{0.5}} \quad (5.39)$$

where the first integral corrects the standard state of $\Delta G_{(5.32)}^0$ to room pressure. Similar equations can then be written for equilibrium (5.30) and (5.31). Volumes and equation of state data used to calculate the integrals are given in Table 5.5. The formalism of Holland and Powell (2011) is employed. Equation of state terms for the Brg components are assumed to be the same as those for MgSiO_3 Brg. Although there may be significant uncertainties in assuming that the compressibilities of the Brg components are identical, this assumption is unlikely to change the direction of the calculated trends with increasing pressure but there are significant uncertainties in the gradients of the calculated trends with pressure. These uncertainties increase with pressure and for this reason the extrapolation is performed over a relatively small pressure range. The model was calculated from 26-40 GPa at two assumed conditions: (1) at a constant oxygen fugacity of IW+1.5; (2) in equilibrium with Fe-Ni metal. Extrapolation to pressures higher than 40 GPa maybe not suitable due to the possible spin transition in ferropicrinite proposed to begin at 40-50 GPa (see Lin et al., 2013 for a review). The predicted $\text{Fe}^{3+}/\Sigma\text{Fe}$ ratio of Brg versus pressure is plotted in Fig. 5.11 in which the results from previous studies are also shown for comparison. Due to the negative volume change of reaction (5.32), the calculated $\text{Fe}^{3+}/\Sigma\text{Fe}$ ratio of Brg increases with pressure. The $\text{Fe}^{3+}/\Sigma\text{Fe}$ ratio of the two multi-anvil studies from Irifune et al. (2010) and Stagno et al. (2011) (open circles in Fig. 5.11) fall well within the range between the two model curves. Although the Al content (0.07 atoms pfu) of Brg in Stagno et al. (2011) is slightly lower than Irifune et al. (2010) and our model (0.10 atoms pfu), it was buffered at an oxygen fugacity of IW+2 that is slightly higher than used in the model calculation. The carbon capsule adopted in Irifune et al. (2010) also implies that the oxygen fugacity in their experiments should not have exceeded approximately IW+2, as discussed in section 6.1. The $\text{Fe}^{3+}/\Sigma\text{Fe}$ ratios of Brg reported from previous laser heated diamond anvil cell experiments have, in general, lower values (Fig. 5.11). For the studies of in Prescher et al. (2014) and Kuppenko et al. (2015) the Al contents of Brg were lower (0.05-0.07 pfu) than our model (0.1 atoms pfu), which as shown in Fig. 5.1a may account for some of the difference in $\text{Fe}^{3+}/\Sigma\text{Fe}$ ratio compared with the model. The Fe content of Brg in in the study of Shim et al. (2017) and Kuppenko et al. (2015) was also much higher (~ 0.2 atoms pfu)

than our model (0.1 atoms pfu) which as shown in Fig. 5.1b would also result in lower $\text{Fe}^{3+}/\Sigma\text{Fe}$ ratios. Shim et al. (2017) performed one of the only studies in DAC where attempts were made to buffer the f_{O_2} with the presence of Fe metal. However, Fp was not present in the experiments, which instead contained an SiO_2 polymorph. As such the results are not applicable to the model determined in this study. Andraut et al. (2018) report that the potential presence of garnet in their experimental results up to 30-35 GPa may explain why the $\text{Fe}^{3+}/\Sigma\text{Fe}$ ratios are low. However if Brg coexisted with garnet at these conditions its Al content would be expected to be very high (Akaogi et al., 2002) and if the bulk Fe contents were comparable, the minimum $\text{Fe}^{3+}/\Sigma\text{Fe}$ ratio should be greater than that determined from the model. The Al and Fe contents of Brg were not reported in the study of Andraut et al. (2018), so it is very hard to make a comparison with these results. One point worth noting is that in most of the DAC experiments, the $\text{Fe}^{3+}/\Sigma\text{Fe}$ ratios measured from the high pressure samples are quite close to those of the starting material, which may indicate a lack of equilibrium. For example, the $\text{Fe}^{3+}/\Sigma\text{Fe}$ ratios of the starting materials are 0.07, 0.35 and 0.42 for Andraut et al. (2018), Kuppenko et al. (2015) and Prescher et al. (2014) respectively and the corresponding $\text{Fe}^{3+}/\Sigma\text{Fe}$ ratio of Brg at 23-27 GPa are 0.12, 0.38 and 0.42 respectively. This comparison serves to underline the fact that control of factors such as f_{O_2} , Brg Al and Fe contents and SiO_2 activity are likely essential if any systematic information is to be gained on the evolution of Brg $\text{Fe}^{3+}/\Sigma\text{Fe}$ ratios with pressure.

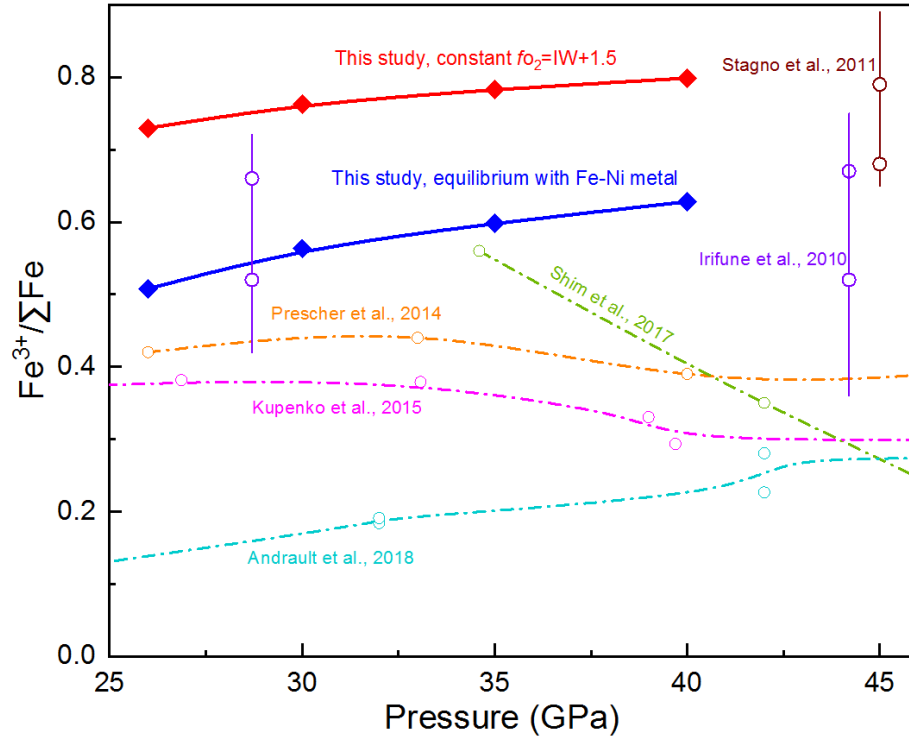


Fig. 5.11 $\text{Fe}^{3+}/\Sigma\text{Fe}$ ratio of aluminous bridgmanite as a function of pressure. The red solid line indicates model results calculated with a constant $f_{\text{O}_2} = \text{IW} + 1.5$ and the blue solid line indicates model results calculated for an assemblage in equilibrium with Fe-Ni metal. Previous diamond anvil cell results from Andrault et al. (2018); Kuppenko et al. (2015); (2014); Shim et al. (2017) and multi-anvil experiment results from Irifune et al. (2010) and Stagno et al. (2011) are also shown for comparison. The upper and lower value from Irifune et al. (2010) are measurements made on the same sample using electron energy loss and Mössbauer spectroscopy respectively.

The apparent K_D for Mg and Fe exchange between Brg and Fp was also calculated as a function of pressure assuming three different scenarios: (1) at a constant oxygen fugacity of IW+1.5; (2) for constant $\text{Fe}^{3+}/\Sigma\text{Fe}$ ratio in Brg equal to 0.69; and (3) for an initial whole rock $\text{Fe}^{3+}/\Sigma\text{Fe}$ ratio of 0.03 which would result in the precipitation of Fe-Ni metal. The results are shown and compared with those of Irifune et al. (2010) in Fig. 5.12. The K_D (app) value assuming constant $f_{\text{O}_2} = \text{IW} + 1.5$ is the largest while that with initial whole rock ferric Fe over total Fe ratio of 0.03 is the smallest. For both conditions, the K_D (app) does not change very much in the pressure range of 26-40 GPa. In contrast, the K_D (app) value for constant $\text{Fe}^{3+}/\Sigma\text{Fe} = 0.69$ in Brg decreases from 0.67 at 26 GPa to 0.48 at 40 GPa. The K_D (app) value of 0.48 at 40 GPa for Brg $\text{Fe}^{3+}/\Sigma\text{Fe}$ ratio of 0.69 is in good agreement with that from Irifune et

al. (2010) which has a $\text{Fe}^{3+}/\Sigma\text{Fe}$ ratio of 0.67 and a K_D (app) of 0.51(7). Therefore for the two data points where $\text{Fe}^{3+}/\Sigma\text{Fe}$ ratios were measured by Irifune et al. (2010) there is reasonable agreement with the model. The K_D (app) decreases because of the effect of pressure on Fe^{2+} -Mg exchange between Brg and Fp. For the other scenarios this is not apparent because the $\text{Fe}^{3+}/\Sigma\text{Fe}$ ratio increases with pressure. In order for the $\text{Fe}^{3+}/\Sigma\text{Fe}$ ratio to remain constant the f_{O_2} would have had to decrease in the experiments from IW+1 to IW. This provides one explanation for the overall decrease in K_D (app) but the sharp drop observed in K_D (app) can only be explained if some further evolution in the f_{O_2} of the experiments occurred. This again serves to underline the fact that experiments on Fe-Mg partitioning in the lower mantle are simply unconstrained unless the f_{O_2} and $\text{Fe}^{3+}/\Sigma\text{Fe}$ ratio of Brg, are constrained.

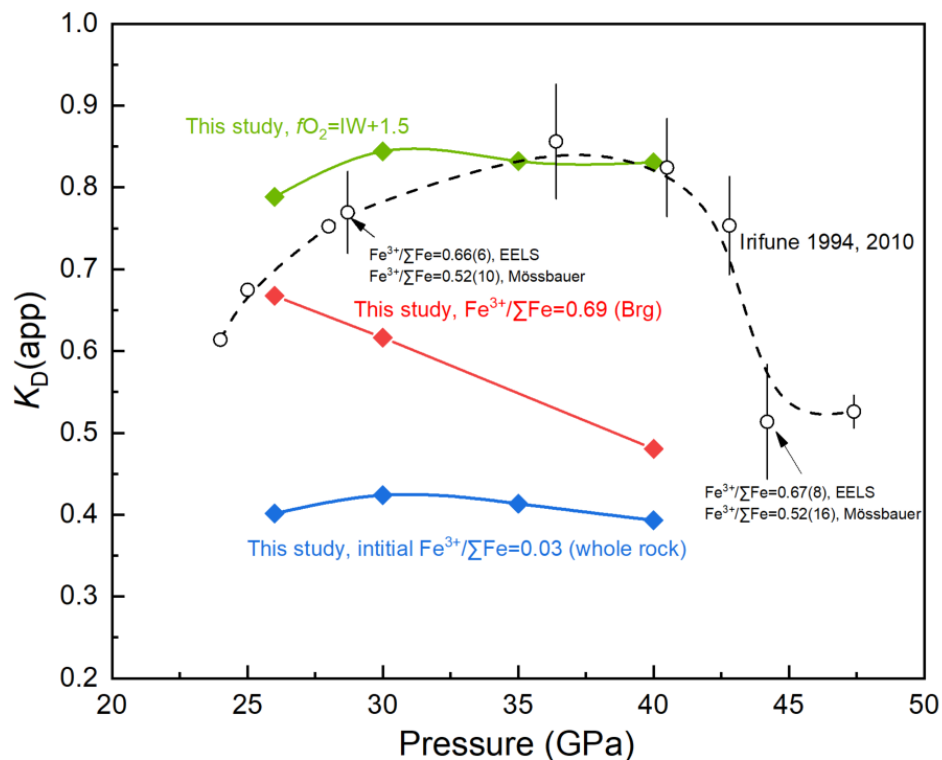


Fig. 5.12 Model curves for Fe-Mg exchange K_D between Brg and Fp plotted against pressure at different assumed conditions. Data from Irifune et al. (2010) also are shown for comparison. The arrows represent the two pressure points where the $\text{Fe}^{3+}/\Sigma\text{Fe}$ in Brg were measured in Irifune et al. (2010) and the values obtained are indicated. The different $\text{Fe}^{3+}/\Sigma\text{Fe}$ value shown from Irifune et al. (2010) are measurements made on the same sample using electron energy loss and Mössbauer spectroscopy respectively.

Oxygen vacancies in Brg have aroused great interest as they have been considered to be possible sites for the substitution of hydrogen and noble gases (Litasov et al., 2003; Shcheka and Keppler, 2012) and may also influence the compressibility and transport properties of Brg. The model predicts that the proportion of oxygen vacancies in Brg decreases with pressure. As shown in Fig. 5.13, calculated at an $f_{O_2}=IW + 1.5$ and for a pyrolite composition, the proportion of oxygen vacancies decreases sharply up to ~32 GPa, reaching practically zero at ~40 GPa. This trend is consistent with previous results in Al-Brg in both experimental and theoretical studies (Brodholt, 2000; Liu et al., 2017). Although the proportion of oxygen vacancies in Brg appears relatively small at 26 GPa, no other mantle mineral contains such a large amount of such vacancies. Since the amount of oxygen vacancies should be positively correlated to the rate of chemical diffusion, at least for oxygen anions, the decrease in Brg oxygen vacancies with pressure in the upper part of the lower mantle may influence transport properties in the upper regions of the lower mantle (Karato and Wu, 1993). It might, for example, provide an explanation for a proposed increase in lower mantle viscosity towards 1000 km depth (Rudolph et al., 2015). This viscosity increase was proposed as a possible physical mechanism to explain why some subducting slabs seem to stagnate towards the mid lower mantle (Fukao and Obayashi, 2013).

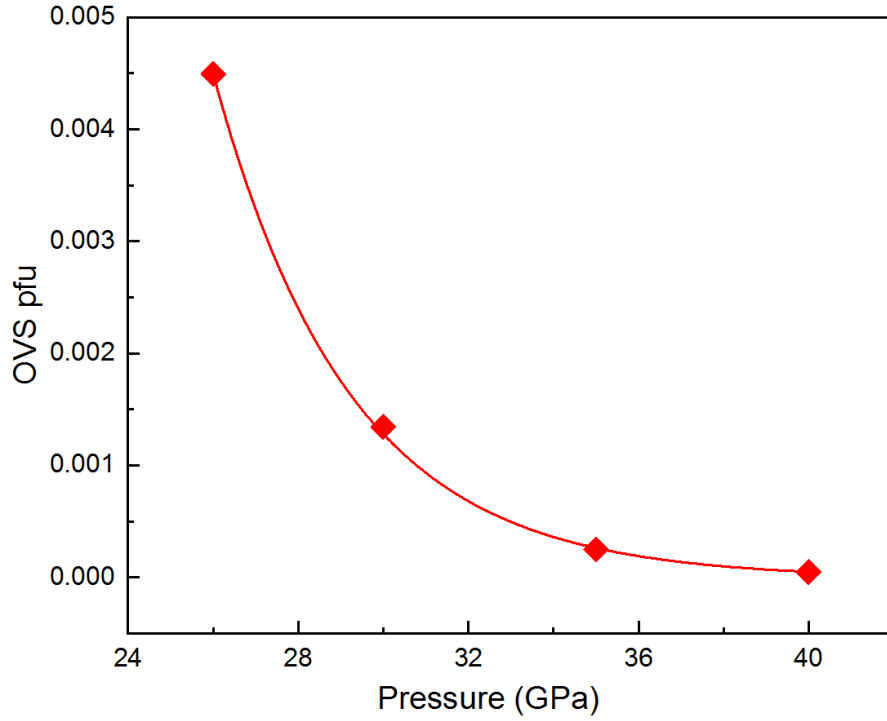


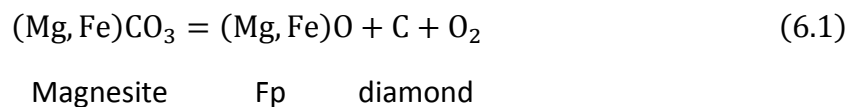
Fig. 5.13 The proportion of oxygen vacancies per formula unit in Brg versus the pressure at a constant oxygen fugacity of IW+1.5 calculated for a pyrolite composition using the thermodynamic model developed in this study. Note that the oxygen vacancy proportion shown here is the absolute number of oxygen vacancies pfu in Brg which is half the value of mole fraction of $\text{MgM}^{3+}\text{O}_{2.5}$ component ($X_{\text{MgM}^{3+}\text{O}_{2.5}}$) as in Fig. 5.9.

6 Other Mg, Fe-bearing phases coexisting with bridgmanite

6.1 Speciation of carbon at different oxygen fugacities

Fig. 6.1 summarizes $\text{Fe}^{3+}/\Sigma\text{Fe}$ ratios measured for Brg as a function of the f_{O_2} of the synthesis experiments (Table 3.2). As discussed in the previous section the Brg $\text{Fe}^{3+}/\Sigma\text{Fe}$ ratios vary at a fixed oxygen fugacity due to the different amounts of Al or bulk Fe present in the samples. As mentioned in section 3.2 small amounts of carbon appear to have also been present in some of the experiments as a contaminant (Table 3.2). As the oxygen fugacities are well constrained in the experiments, information on the speciation of carbon as a function of f_{O_2} can be obtained and, in particular, limits can be placed on the extent of the MgCO_3 stability field with respect to f_{O_2} . This information can be combined with data on the $\text{Fe}^{3+}/\Sigma\text{Fe}$ ratios of proposed Brg inclusions from natural diamonds in order to determine whether it is possible that such diamonds formed through the reduction of carbonates in the mantle.

As indicated in Table 3.2 and shown in Fig 6.1, at oxygen fugacities of $\leq \text{IW}$, carbon is observed to be present in the experiments as carbide or diamond. At oxygen fugacities $> \text{IW}+2.7$ (monitored by Ir as the sliding redox sensor), however, carbon is present as $(\text{Mg,Fe})\text{CO}_3$ carbonate. This means that the equilibrium:



is bracketed by the experiments between oxygen fugacity of IW and $\text{IW} + 2.7$. Stagno et al. (2011) determined the f_{O_2} of this equilibrium at approximately 25 GPa between 1773–1973 K to be at $\text{IW}+2.46$, as shown in Fig 6.1, which is in very good agreement with the current results. However, the Fe-Ir alloy used to determine the f_{O_2} in these experiments has large

associated uncertainties. Using the Holland and Powell (2011) data base the calculated f_{O_2} for this equilibrium is IW+4.0, which is significantly higher than both experimental determinations. This probably arises from uncertainties in the equation of state of $MgCO_3$ and likely means that the derivative of the bulk modulus with respect to pressure, K' , is less than the value of 4 proposed in the database.

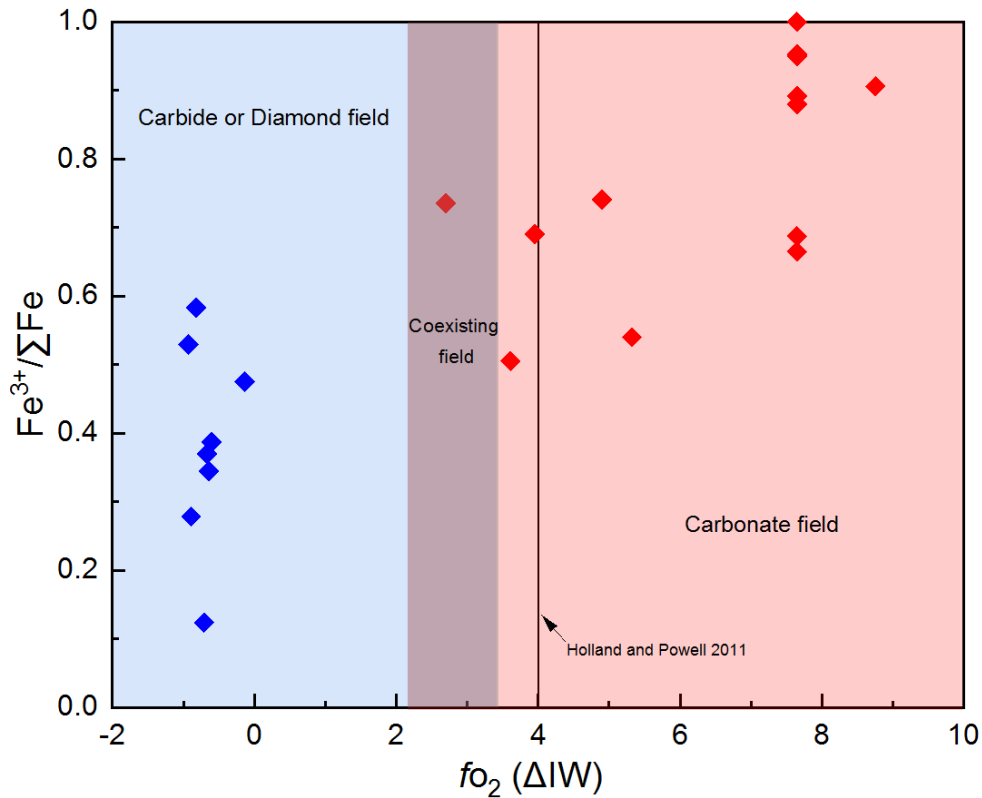


Fig. 6.1 The $Fe^{3+}/\Sigma Fe$ ratio in Brg obtained in this study is shown as a function of oxygen fugacity. The blue and red symbols indicate experiments where carbon exist as carbide/diamond or carbonate, respectively. The grey shaded area shows the oxygen fugacity at which diamond and carbonate coexist in Stagno et al. (2011) at 23-25 GPa and 1773-1973 K. The solid line shows the f_{O_2} of equilibrium determined with the database of Holland and Powell (2011).

If diamonds in the sub lithospheric mantle are produced from carbonates, as often proposed (Brenker et al., 2007), then equilibrium (6.1) defines the f_{O_2} at which this should occur. The results shown in Fig. 6.1 indicate that this cannot happen at typical lower mantle oxygen fugacities, which as demonstrated in section 5.5 must be at approximately IW - 0.8 at the top of the lower mantle, because carbonates are clearly unstable at these conditions.

McCammon et al. (1997) report $\text{Fe}^{3+}/\Sigma\text{Fe}$ ratios for two inclusions in diamonds from the São Luiz River, Brazil, that are proposed to have originally been Brg trapped at conditions of the top of the lower mantle. Using the model proposed in section 5.4 the oxygen fugacities recorded by these inclusions can be determined assuming they formed at conditions compatible with the top of the lower mantle, which has been proposed for at least some of the inclusions (McCammon et al., 2004a). One inclusion (BZ251B) is reported to have an Al_2O_3 content of 1.3 %, a total Fe content of 3.8 % and a $\text{Fe}^{3+}/\Sigma\text{Fe}$ ratio of 0.20(6). Using the model, the minimum f_{O_2} for such a composition, where it coexists with Fe-Ni alloy, is determined to be $\sim \text{IW} - 0.8$ and the minimum $\text{Fe}^{3+}/\Sigma\text{Fe}$ ratio is determined to be 0.32, which is higher than observed but potentially still within the combined uncertainties of the model and measurement. Considering the results of section 5.2 the lower $\text{Fe}^{3+}/\Sigma\text{Fe}$ ratio of the inclusion with respect to the model conditions might also imply that it formed at slightly higher temperatures. Given its f_{O_2} it is unlikely that the diamond itself formed from a carbonate bearing assemblage. A second inclusion (BZ210B) is reported to contain 10 wt.% Al_2O_3 and 5.56 % total iron and has an $\text{Fe}^{3+}/\Sigma\text{Fe}$ ratio of 0.75(3). The f_{O_2} calculated for this inclusion is $\text{IW} + 0.7$ which falls between the conditions bracketed in Fig. 6.1 for the carbonate-diamond stability fields but is most likely too low in f_{O_2} to imply formation from carbonate. One further inclusion (KK-16 b; McCammon et al., 2004a; Stachel et al., 2000) in a deep mantle diamond reported from Kankan, Guinea, has an Al_2O_3 content of 0.55 wt.%. This Al_2O_3 content is too low to be interpreted using the Al-bearing model reported in section 5.3.3 but can be examined using the Al-free model from section 5.3.2. The resulting f_{O_2} for this inclusion, which contains 3.34 wt.% total iron and has a $\text{Fe}^{3+}/\Sigma\text{Fe}$ ratio of 0.09 (25), is $\text{IW} - 0.5$, which is very close to equilibrium with Fe-Ni metal. A value of $\text{IW} + 3.0$ is obtained, however, for the upper uncertainty boundary, which would be consistent with formation from carbonate. Interestingly the diamond in which this inclusion is found also contains FeCO_3 siderite, however, the Brg inclusion is unlikely to have been in equilibrium with such a carbonate because as shown in section 3.2 equilibrium carbonates should have $\text{Fe}/(\text{Fe}+\text{Mg})$ ratios of approximately 0.01-0.03.

In summary, the Al and Al-free models developed in the previous section can be used to interpret the oxygen fugacities at which Brg inclusions in diamonds were formed. By comparison with phase equilibrium data on the f_{O_2} stability of carbonate these data can then be used to determine if the diamonds themselves were likely to have been formed by the reduction of carbonate, which would imply a likely origin from subducted material. Two inclusions from São Luiz River, Brazil reveal oxygen fugacities that are clearly below the carbonate stability field and therefore are unlikely to have been produced from pure carbonate phases. The uncertainty in the $Fe^{3+}/\Sigma Fe$ ratio from one inclusion from Kankan, Guinea, on the other hand, translates to an f_{O_2} range that potentially overlaps with the pure carbonate stability field.

6.2 Fe partitioning between bridgmanite and melt and density of the melt

6.2.1 Chemical compositions of coexisting Brg and melt

Water was added to a number of experiments conducted at 25 GPa between 1873-1973 K (Table 2.2) with the initial aim of encouraging the growth of larger Brg single crystals. Phase assemblages from these experiments, that all contained hydrous melt, are reported in Table 3.1. All recovered samples contained bridgmanite and ferropericlase coexisting with quenched microcrystals from the melt. These experiments allow the systematics of melt compositions at these pressures to be examined as a function of temperature and in particular the iron partitioning between minerals and melts can be determined, which is a very important aspect when determining melt densities in the lower mantle.

Backscattered electron (BSE) images of typical liquidus assemblages are shown in Fig. 6.2. In the central part of the capsule (i.e. the highest temperature region), Brg coexists with quenched melt, while at the end side of the capsule (i.e. lower temperatures), Fp coexists with Brg. The composition of the Brg throughout the whole capsule is quite homogeneous and within 0.01 atoms pfu when normalized to 2 cations. In Fig. 6.3a, the $Fe/(Mg+Fe)$ ratio

is plotted against the (Mg+Fe)/Si ratio of the quenched melt; previous studies in both hydrous (Nakajima et al., 2019) and anhydrous systems (Hirose and Fei, 2002; Kuwahara et al., 2018; Liebske et al., 2005; Ohtani and Sawamoto, 1987; Trønnnes, 2000; Trønnnes and Frost, 2002) where Brg and Fp coexist with melt are also shown for comparison. The Fe/(Mg+Fe) ratios of the hydrous melts analyzed in this study are significantly higher (0.32-0.38) than those reported recently by Nakajima et al. (2019) (0.10-0.12). The two points with the highest Fe/(Mg+Fe) ratio of 0.59 from Liebske et al. (2005) and 0.48 from Trønnnes (2000) are due to the high FeO content (34.8-35.2 wt.%) in the CI chondrite analogue starting material (Fig. 6.3a). The other points in previous studies all used peridotitic starting materials with a lower FeO content (~ 8 wt.%). All experiments were conducted at 23.5-27 GPa but the temperatures range from 1573-1873 K for the hydrous experiments of Nakajima et al. (2019), to 1873-1973 K for this study, and to 2293-2723 K for the anhydrous studies. The (Mg+Fe)/Si ratio of the melt can be seen to increase with decreasing temperature (Fig. 6.3b), consistent with previous experimental observations made at lower pressures (Kawamoto, 2004). The Fe/(Mg+Fe) ratio in the melt does not appear to have a simple dependence on either temperature or (Mg+Fe)/Si ratio (Fig. 6.3c).

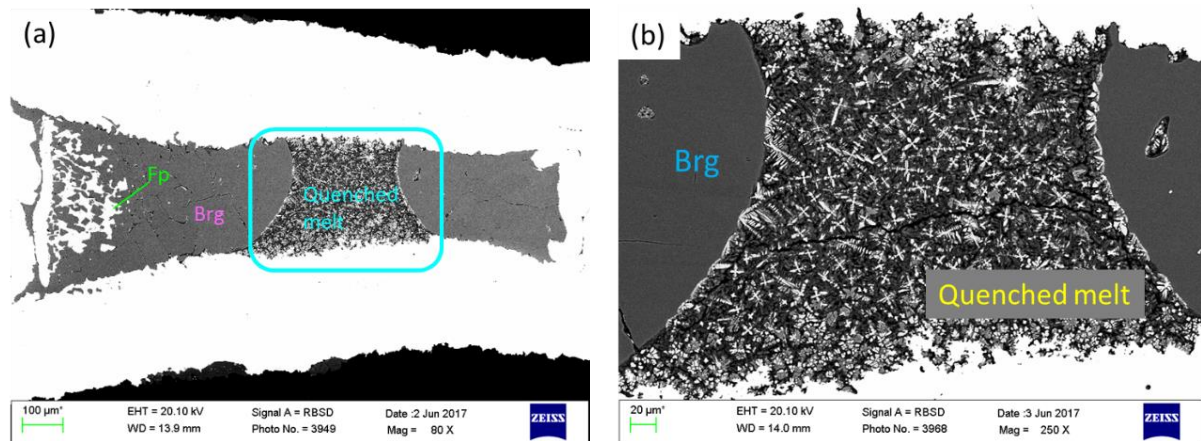
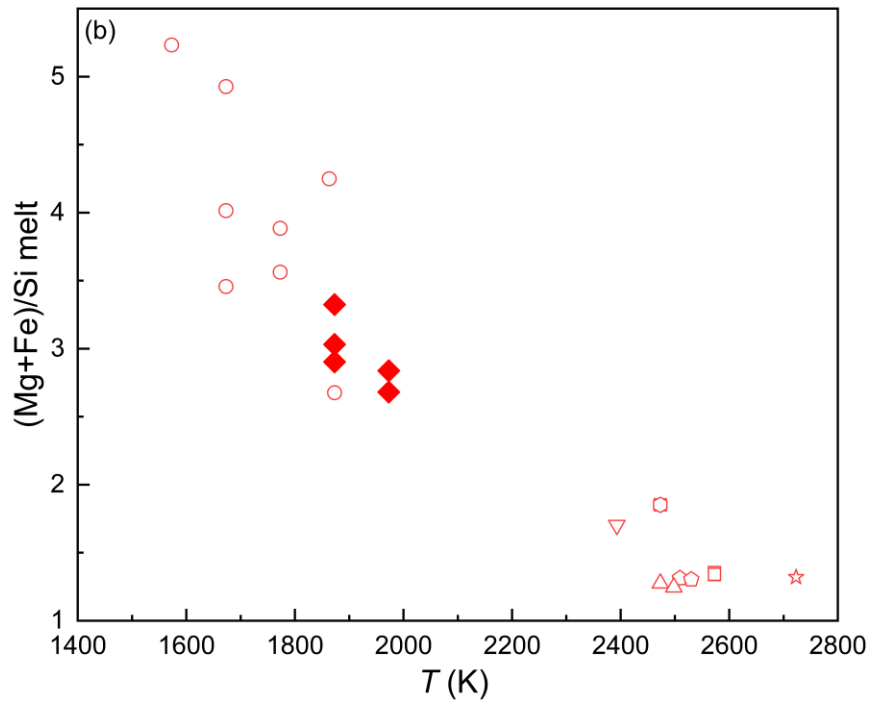
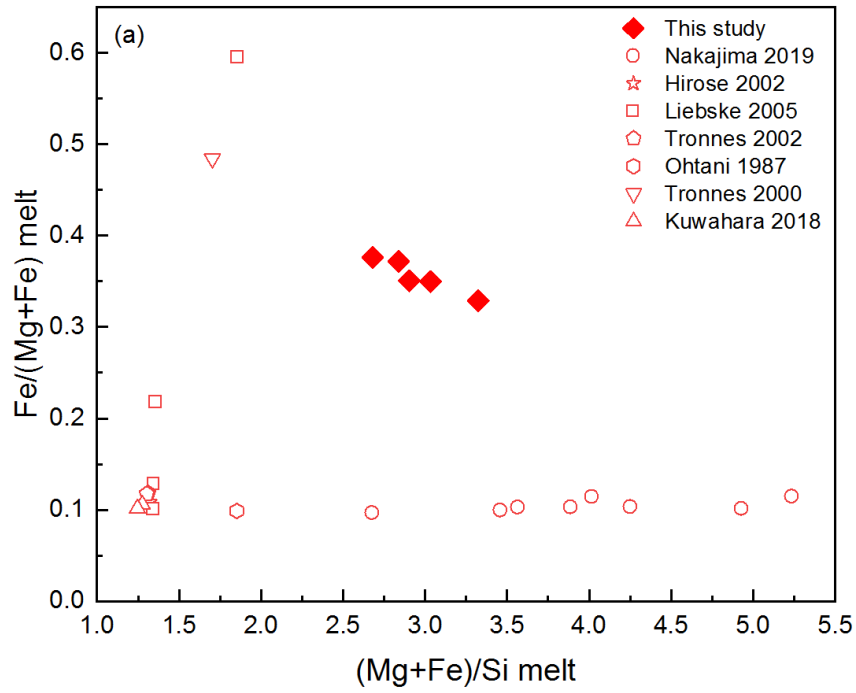


Figure 6.2 (a) Back-scattered electron (BSE) image of Run S6843 recovered from 25 GPa and 1873 K. The hydrous quenched melt concentrates in the central part of the capsule, most likely where the hottest part of the capsule was. Bridgmanite (Brg) coexists with hydrous melt in the middle part of the capsule but melt also appears on grain boundaries in regions towards the end of the capsule where bridgmanite coexists with ferropericlasite (Fp). (b) An enlargement of the blue area in (a), showing melt coexisting with Brg.



$$\Delta G_0 = -RT \ln K_D - W_{\text{MgFe}}^{\text{Brg}} (1 - 2x_{\text{FeSiO}_3}^{\text{Brg}}) + W_{\text{MgFe}}^{\text{melt}} (1 - 2x_{\text{FeO}}^{\text{melt}}) \quad (6.4)$$

assuming symmetrical Fe-Mg mixing models for Brg and melt where $W_{\text{MgFe}}^{\text{Brg}}$ and $W_{\text{MgFe}}^{\text{melt}}$ are the Margules interaction parameters describing the interaction energy between Fe and Mg in Brg solid solution and melt respectively. Compositions of Brg and melt in anhydrous systems from Hirose and Fei (2002); Liebske et al. (2005); Trønnnes (2000); Trønnnes and Frost (2002) and Ohtani and Sawamoto (1987) were used to fit equation (6.4) using a non-linear least squares algorithm to determine ΔG_0 at ~ 25 GPa and 2573 K and the two interaction parameters $W_{\text{MgFe}}^{\text{Brg}}$ and $W_{\text{MgFe}}^{\text{melt}}$. Because these two interaction parameters are highly correlated, $W_{\text{MgFe}}^{\text{Brg}} = 0$ KJ/mol at 25 GPa taken from Nakajima et al. (2012) was fixed and the value of $W_{\text{MgFe}}^{\text{melt}}$ and ΔG_0 was allowed to be refined. The least-square fitting gave $W_{\text{MgFe}}^{\text{melt}} = 15.0$ KJ/mol and $\Delta G_0 = 29.6 \pm 2$ KJ/mol at 25 GPa and 2573 K. If the same $W_{\text{MgFe}}^{\text{melt}}$ is assumed for the lower temperatures of the current study 1873-1973 K, then ΔG_0 is calculated to be 22.3 (7) KJ/mol. Values of $K_D^{\text{Brg-melt}}$ determined from the current and previous studies are plotted against the $x_{\text{FeSiO}_3}^{\text{Brg}}$ of Brg in Fig. 6.4 along with the results of the fitting procedure performed at 1973 K and 2673 K. Values of K_D determined from the results of Nakajima et al. (2019) are much higher than those calculated for either the hydrous experiments from this study or previous anhydrous experiments (Fig. 6.4). Even though the experimental conditions in the study of Nakajima et al. (2019) overlap with those from the current study they contain much less iron in the melts for a given Brg iron content. This discrepancy most likely has one major cause, in that the starting material employed by Nakajima et al. (2019) only contained ferric iron. The oxygen fugacity in the experiments was, therefore, very high and due to the presence of H₂O and potential loss of H₂ from the capsule it is most likely that all iron remained in the ferric state. As the K_D for these experiments is close to unity it can be concluded that ferric iron partitions evenly between Brg and melt at these high f_{O_2} conditions. However, in the current study the starting materials contained metallic iron and although this iron oxidized due to reaction with H₂O, Mössbauer measurements show that the Fe³⁺/ΣFe ratio of Brg in one of the

samples is 0.54 (7). Given that the starting materials and K_D values are all similar, it is likely that the $\text{Fe}^{3+}/\Sigma\text{Fe}$ ratios are all in this range. However, as we expect silicate melts to contain more ferric and ferrous iron than the mineral phases the K_D is driven to lower values that are likely more compatible with those in the mantle. In fact in three samples (S6833, S6843, S6848) the presence of Ir metal allowed the f_{O_2} to be estimated by Eq. (5.2) using the composition of coexisting Fp and Fe-Ir alloy which gave a consistent oxygen fugacity of IW + 2. Using the model determined in section 5.3.3 the $\text{Fe}^{3+}/\Sigma\text{Fe}$ ratio expected for Brg with such a composition and at this f_{O_2} is 0.47, which is just inside the analysis uncertainties.

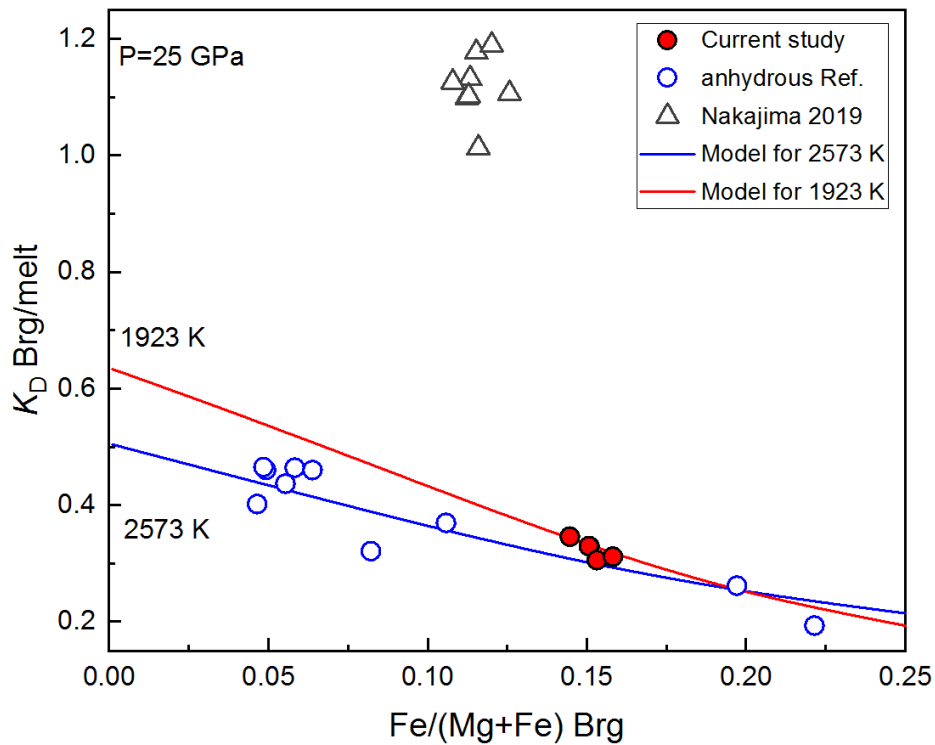


Fig. 6.4 Experimental results of Fe-Mg partitioning between Brg and melt plotted as K_D against $x_{\text{FeSiO}_3}^{\text{Brg}}$ in Brg. Results from the previous studies of Hirose and Fei (2002); Kuwahara et al. (2018); Liebske et al. (2005); Ohtani and Sawamoto (1987); Trønnnes (2000); Trønnnes and Frost (2002) and Nakajima et al. (2019) are also shown. The blue and red line show isothermal K_D values at 2573 K and 1923 K respectively, obtained by fitting equation (6.4) to the data.

In summary, it would appear that the Fe-Mg K_D between silicate melt and Brg is strongly affected by the oxygen fugacity whereas the effects of temperature and other melt components, such as H_2O , are apparently much smaller. The release of H_2O from a

subducting slab into the mantle may well cause oxidation through the generation and release of H₂. The effect causes oxidation in the high-pressure multi-anvil experiments because the H₂ produced then diffuses through the metal capsule and leaves the system. Loss of H₂ in this way can lead to almost complete oxidation of minerals in an experiment (McCammon et al., 2004a). The extent of oxidation that may take place due to H₂O in the mantle, however, is hard to assess because it depends on what happens to the H₂ and on the equilibrium relationship between the amount of H₂ formed and the oxygen fugacity. As the oxygen fugacity increases the amount of H₂ produced would decrease and the mantle may reach a limiting amount of H₂O oxidation. The recent observation of a very water rich ringwoodite inclusion within a diamond (Pearson et al., 2014) is at least one indication that the extent of mantle oxidation by H₂O may be limited as the f_{O_2} must have at least remained in the diamond stability field. In the following we assume an oxidation state similar to the experiments, i.e. IW + 2. Higher oxidation states, however, would lead to more ferric iron in the system but proportionately lower iron contents in the melts, which would obviously cause melts to have lower densities.

6.2.3 Composition of hydrous melt at the uppermost lower mantle

Using partition and exchange coefficients between Brg, Fp and melt a model can be developed to determine the composition of a hydrous melt at the top of the lower mantle. This composition can then be used to estimate melt densities. Assuming a pyrolite type bulk silicate earth composition (McDonough and Sun, 1995) in a simple MgO-SiO₂-FeO-Al₂O₃-CaO system and that partial melting occurs with melt coexisting with Brg and Fp, the composition and proportion of each phase can be calculated based on a mass balance for various melt fractions (0.1 wt.%, 0.5 wt.%, and 1 wt.%) and melt water contents (15-30 wt.%) at 25 GPa and 1923 K. The water concentration of the melt is poorly constrained. Nakajima et al. (2019) assume an H₂O content at 1673-1773 K of 29.9 wt.% based on the deficit in the energy dispersive X-ray spectrometry totals but a simple melting point depression calculation implies that the H₂O contents must be at least 15 wt.% and for this reason a range up to 30 wt.% is examined (Novella et al., 2017). The following further constraints are

used in the calculation: (1) The Mg-Fe partition coefficient between Brg and Fp (K_D) describing only ferrous iron (Fe^{2+}) exchange was taken from Nakajima et al. (2012) and the $\text{Fe}^{3+}/\Sigma\text{Fe}$ ratio in Brg was assumed to be 0.5 as in the experiments and corresponding to $\Delta\text{IW} + 2$; (2) the Mg-Fe partition coefficient (K_D) between Brg and melt obtained from the current study described in chapter 6.2.2 was used; (3) The (Mg+Fe)/Si ratio in the melt and the partition coefficient of Al between Brg and melt ($D_{\text{Al}}^{\text{Brg-melt}} = x_{\text{Al}}^{\text{Brg}}/x_{\text{Al}}^{\text{melt}}$) were fixed to be equal to the values found in this study. In the experiments equilibrated at 25 GPa and 1923 ± 50 K, the partition coefficient of Al between Brg and melt ($D_{\text{Al}}^{\text{Brg-melt}} = x_{\text{Al}}^{\text{Brg}}/x_{\text{Al}}^{\text{melt}}$) is 3.19 and the (Mg+Fe)/Si ratio of the melt is 2.96. Moreover, the CaO content of the melt was set to be 9 wt.% according to the average values in hydrous melt from Nakajima et al. (2019). Assuming 15 wt.% water in the melt, the calculated FeO content in the melt would decrease from 16.25 wt.% with a 0.1 wt.% melt fraction to 16.1 wt.% with 1 wt.% melt fraction. Assuming 30 wt.% water in the melt, the calculated FeO content in the melt would decrease from 13.02 wt.% with 0.1 wt.% melt fraction to 12.89 wt.% with 1 wt.% melt fraction.

6.2.4 Density of the melt

Based on the calculated melt composition, melt densities were determined using the second-order Birch-Murnaghan equation of state with the thermal pressure term proposed by Wakabayashi and Funamori (2013):

$$P = \frac{2}{3}K_{0,T_0} \left(\left(\frac{V_{0,T_0}}{V_{P,T}} \right)^{\frac{7}{3}} - \left(\frac{V_{0,T_0}}{V_{P,T}} \right)^{\frac{5}{3}} \right) + \alpha_{0,T_0} K_{0,T_0} (T - T_0) \quad (6.5)$$

where P , T , K , V , α are pressure, temperature, bulk modulus, molar volume and thermal expansion coefficient respectively. The first and second subscripts denote the pressure and temperature respectively. T_0 is the reference temperature of 2500 K. Parameters for the equation of state of silicate melt were provided as $V_{0,T_1,i}$, $\alpha_{0,T_1,i}$ and $K_{0,T_1,i}$ for each melt

component SiO₂, Al₂O₃, FeO, MgO, and CaO (Wakabayashi and Funamori, 2013). Using $V_{0,T_1,i}$, the zero-pressure molar volume of silicate melts at T_1 could be expressed as:

$$V_{0,T_1} = \sum_i x_i V_{0,T_1,i} \quad (6.6)$$

where x_i is the molar fraction of component i and T_1 is the reference temperature of 1773 K. Differentiating equation (6.6) with respect to temperature yields

$$\alpha_{0,T_1} V_{0,T_1} = \sum_i x_i \alpha_{0,T_1,i} V_{0,T_1,i} \quad (6.7)$$

and then the zero-pressure thermal expansion coefficient of silicate melt at T_1 is calculated from,

$$\alpha_{0,T_1} = \frac{\sum_i x_i \alpha_{0,T_1,i} V_{0,T_1,i}}{V_{0,T_1}} \quad (6.8)$$

The zero-pressure thermal expansion coefficient at the temperature of interest is,

$$\alpha_{0,T} = \frac{\alpha_{0,T_1} \left(1 - \frac{10}{\sqrt{T}}\right)}{1 - \frac{10}{\sqrt{T_1}}} \quad (6.9)$$

The zero-pressure molar volume at T_0 is calculated from the values of the molar volume and zero-pressure thermal expansion coefficient at T_1 according to

$$V_{0,T_0} = V_{0,T_1} \exp\left(\int_{T_1}^{T_0} \alpha_{0,T} dT\right) \quad (6.10)$$

Differentiating equation (6.5) with respect to pressure yields

$$\frac{V_{0,T_0}}{K_{0,T_0}} = \sum_i x_i \frac{V_{0,T_0,i}}{K_{0,T_0,i}} \quad (6.11)$$

so the zero-pressure bulk modulus at T_0 can be calculated by

$$K_{0,T_0} = \frac{V_{0,T_0}}{\sum_i x_i \frac{V_{0,T_0,i}}{K_{0,T_0,i}}} \quad (6.12)$$

To this end, we have all the parameters (K_{0,T_0} , V_{0,T_0} , and α_{0,T_0}) of equation (6.5) and the molar volume of silicate melt at any pressure and temperature of interest could be calculated accordingly. The average molecular weight can be calculated from the molecular weight of each component by

$$M = \sum_i x_i M_i \quad (6.13)$$

and the density of the silicate melt at any pressure and temperature of interest is then calculated from

$$\rho = \frac{M}{V_{P,T}} \quad (6.14)$$

Parameters used in this study are listed in Table 6.1 (Wakabayashi and Funamori, 2013). In Fig. 6.5 densities of silicate melts estimated using equation (6.5) and the parameters in Table 6.1 are compared with high-pressure experimental results obtained using the sink-float technique with both olivine and diamond (Agee and Walker, 1993; Ohtani et al., 1997; Suzuki and Ohtani, 2003; Suzuki et al., 1995, 1998). There is very good agreement for the different melt compositions.

Table 6.1 Parameters for silicate melt density calculation used in this study from Wakabayashi and Funamori (2013).

	$M_i(\text{g/mol})$	$V_{0,T_1,i} (\text{cm}^3/\text{mol})$ ($T_1=1,773 \text{ K}$)	$\alpha_{0,T_1,i} (10^{-5}/\text{K})$ ($T_1=1,773 \text{ K}$)	$K_{0,T_0,i} (\text{GPa})$ ($T_0=2,500 \text{ K}$)
SiO ₂	60.1	23.1	2	41
Al ₂ O ₃	102	27.1	10	98
FeO	71.8	13.97	20.9	82
MgO	40.3	11.73	22.3	82
CaO	56.1	16.85	17.3	82

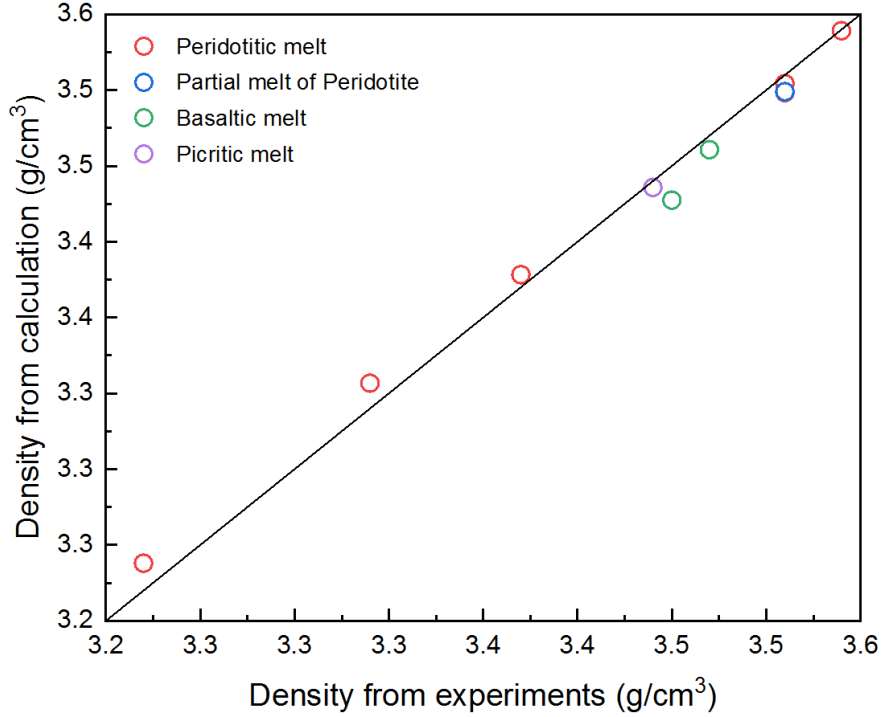


Fig. 6.5 Comparison of silicate melt densities calculated from the equation of state of Wakabayashi and Funamori (2013) with high-pressure experimental results. The calculation was performed under the same conditions (i.e. pressure, temperature and composition) as reported in the experiments. The solid line indicates the 1: 1 correspondence. The experimental data on peridotitic melt are from Agee and Walker (1993); Ohtani et al. (1997); Suzuki and Ohtani (2003); Suzuki et al. (1995, 1998). The experimental data on partial melt of peridotite which is melt formed by partial melting of PHN1611 peridotite at 20 GPa is taken from Ohtani et al. (1997). The experimental data on Basaltic and Picritic melt are from Ohtani and Maeda (2001).

Because the melt contains some amount of water, the effect of H₂O on the density of silicate melt needs to be considered. The partial molar volume of H₂O at the pressure and temperature of interest is calculated using the Vinet equation of state (Sakamaki, 2017):

$$P = 3K_T \left[1 - \left(\frac{\bar{V}_{H_2O}}{\bar{V}_{H_2O,0}} \right)^{\frac{1}{3}} \right] \left(\frac{\bar{V}_{H_2O}}{\bar{V}_{H_2O,0}} \right)^{\frac{2}{3}} \exp \left\{ \frac{3}{2} (K' - 1) \left[1 - \left(\frac{\bar{V}_{H_2O}}{\bar{V}_{H_2O,0}} \right)^{\frac{1}{3}} \right] \right\} \quad (6.15)$$

where \bar{V}_{H_2O} is the high-pressure partial molar volume of H₂O, $\bar{V}_{H_2O,0}$ is the zero-pressure partial molar volume taken from Bouhifd et al. (2015) at a reference temperature of 1273 K

and K_T is the isothermal bulk modulus. The zero-pressure partial molar volume of water at the temperature of interest is calculated from

$$\bar{V}_{\text{H}_2\text{O},0,T} = \bar{V}_{\text{H}_2\text{O},0,1273\text{ K}} + \left(\frac{\partial \bar{V}_{\text{H}_2\text{O},0}}{\partial T} \right)_P \quad (6.16)$$

The parameter of $\frac{\partial \bar{V}_{\text{H}_2\text{O},0}}{\partial T}$ as well as $\bar{V}_{\text{H}_2\text{O},0}$, K_T and K' were taken from Sakamaki (2017) and are shown in Table 6.2 where the temperature effects on K_T and K' have been neglected. The density of the hydrous melt is calculated at the pressure and temperature of interest from

$$\rho = \frac{(1 - x_{\text{H}_2\text{O}})M_{\text{melt}} + x_{\text{H}_2\text{O}}M_{\text{H}_2\text{O}}}{(1 - x_{\text{H}_2\text{O}})V_{\text{melt},P,T} + x_{\text{H}_2\text{O}}\bar{V}_{\text{H}_2\text{O},P,T}} \quad (6.17)$$

where $x_{\text{H}_2\text{O}}$ is the molar fraction of H_2O in the melt, M_{melt} is the average molecular weight of the melt without H_2O calculated from equation (6.13), $M_{\text{H}_2\text{O}}$ is the molecular weight of water, $V_{\text{melt},P,T}$ is the partial molar volume at high pressure and temperature from equation (6.5) and $\bar{V}_{\text{H}_2\text{O},P,T}$ is the high-pressure and high temperature partial molar volume of H_2O obtained from equation (6.15).

Table 6.2 Parameters used in this study for the equation of state for the partial molar volume of H_2O in magma from Sakamaki (2017).

	Parameters at 1273 K
$\bar{V}_{\text{H}_2\text{O},0}$ (cm ³ /mol)	23.8
$(\partial \bar{V}_{\text{H}_2\text{O},0} / \partial T)_P$ (cm ³ /(mol · K))	15.9×10^{-3}
K_T (GPa)	1.29
K'	6.38

The obtained densities for hydrous melts at 25 GPa and 1923 K are plotted against the melt water contents for different partial melt fractions in Figure 6.6. The hydrous silicate melts range in density between 3.95 and 3.98 g/cm³ over the range of parameters examined and decrease with the water content. The uncertainties in the melt H_2O composition, therefore, have very little effect on the determined densities at these conditions.

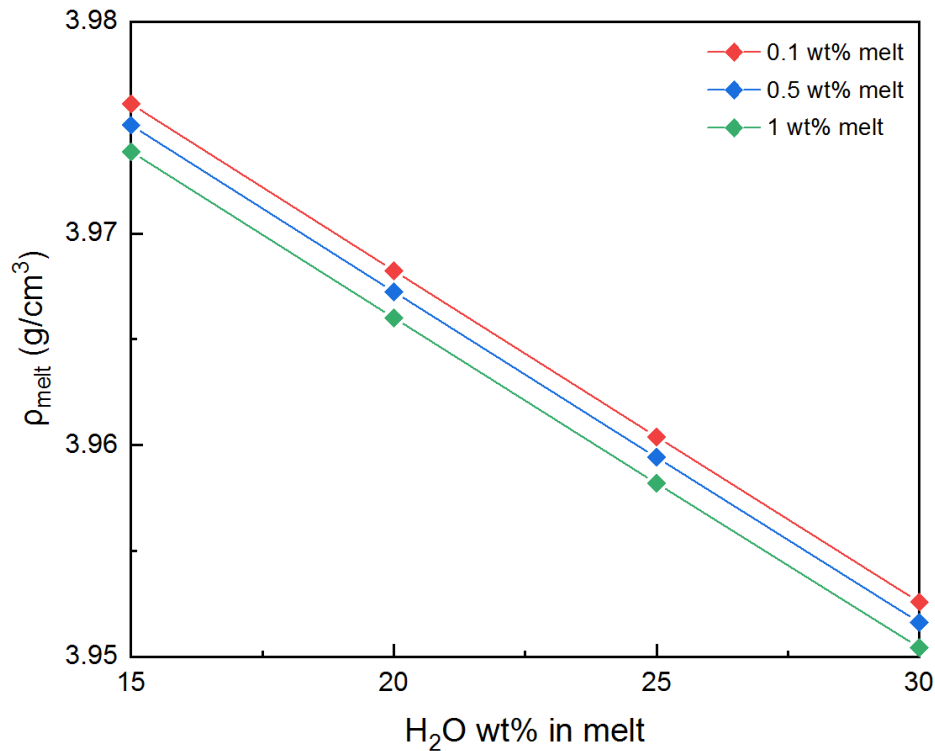


Figure 6.6 The density of the hydrous melt versus the water content of the melt calculated with different melt fractions at 25 GPa and 1923 K.

The low solubility of H₂O in Brg and Fp raises the possibility that water could be released by subducting material as it enters the lower mantle (Bolfan-Casanova et al., 2003). Released H₂O would then cause partial melting. The density of the hydrous partial melts then formed is important for determining whether they are likely to rise out of the lower mantle and potentially rehydrate the transition zone or whether they could form neutrally buoyant melt layers that could potentially lead to seismically observable decreases in shear wave velocities (Schmandt et al., 2014). Nakajima et al. (2019) attempted this calculation based on the chemical compositions of experimental melts produced in equilibrium with Brg and Fp and found melts to have a lower density than the lower mantle. However, as described in section 6.2.2 the iron contents of these melts were likely lower than plausible for the lower mantle as a result of the use of a highly oxidized starting material and the strong effect of redox state on the Fe-Mg partitioning between Brg and melt. Nakajima et al. (2019) also made no consideration for the degree of melting and simply used melt compositions found in their experiments. In the mantle the proportion of H₂O present will control the

melt fraction, which in turn will control the amount of iron in the melt. Although no analysis exists that is specific for the lower mantle, a comparison with a study made for the 410 km discontinuity (Hier-Majumder and Courtier, 2011) implies that observable decreases in shear wave velocity in the lower mantle could result from partial melt fractions that lie in the range of 0.005 to 0.01 (Schmandt et al., 2014).

In Figure 6.7 the densities of hydrous peridotite partial melts with compositions calculated in this study are determined along a mantle geotherm (Brown and Shankland, 1981) using the equations of state (6.5) and (6.15). For comparison, the PREM model for the density of the mantle (Dziewonski and Anderson, 1981) is also shown. The red and blue solid lines show the result for hydrous melts containing 15 wt.% H₂O and 30 wt.% H₂O produced by 1 wt.% melting of the mantle respectively. The hydrous melt density obtained for 0.1 and 0.5 wt.% partial melting is nearly identical to 1 wt.% melting with a difference of only $\sim 0.002 \text{ g/cm}^3$, and is therefore not shown. Because the density of water in silicate melt intersects with that of silicate melt at $\sim 25.3 \text{ GPa}$, the water content has a negligible effect on the melt density between 25-26 GPa (Sakamaki, 2017). Below 25 GPa, the difference of the two compositions increases with decreasing pressure due to the high compressibility of H₂O and the effect of H₂O content on the density becomes more significant with decreasing pressure (Fig. 6.7). Extrapolations to higher and lower pressures are isochemical, however, whereas in reality the melt composition will change gradually with pressure to make the prediction increasingly inaccurate. The density of partial melts generated from peridotite under hydrous conditions (Kawamoto, 2004; Nakajima et al., 2019) at $\sim 25 \text{ GPa}$ and $\sim 1673 \text{ K}$ and dry conditions (Ito and Takahashi, 1987; Kuwahara et al., 2018; Trønnnes and Frost, 2002; Wang and Takahashi, 2000) at $\sim 25 \text{ GPa}$ and $2473\text{-}2773 \text{ K}$ are also calculated and shown for comparison (Fig. 6.7). The density profile of hydrous melts (Kawamoto, 2004; Nakajima et al., 2019) were calculated along the current mantle geotherm (Brown and Shankland, 1981). The water content in the melt was assumed to be 30 wt.% by Nakajima et al. (2019) from the deficit in the EDS analysis totals. For Kawamoto (2004) the same technique using the electron microprobe analysis totals leads to a 40 wt.% melt water content. It can be seen that the hydrous melt in our study is denser than both those of Nakajima et al. (2019) and

Kawamoto (2004) (Fig. 6.7). As this is the case when both melt H₂O contents are identical, the higher density in our study can be wholly attributed to the higher Fe content of the melt, as discussed in section 6.2.2. The density of dry melt generated by peridotite was calculated along the mantle geotherm as well as the peridotite solidus (Herzberg et al., 2000). The composition of the dry melt was taken from the average value from Ito and Takahashi (1987); Kuwahara et al. (2018); Trønnes and Frost (2002); Wang and Takahashi (2000). As can be seen in Fig. 6.7, the density of dry melt along the peridotite solidus is much lower than the hydrous melt in our study and Nakajima et al. (2019) at 22-28 GPa. Compared with the dry melt density calculation along the mantle geotherm (purple line in Fig. 6.7), the smaller density of dry melt is not only caused by the higher temperature but also the smaller Fe content in the melt. At higher temperatures in anhydrous melting experiments, the Fe content in both melt and coexisting Brg decreases, mainly due to the higher melt fractions encountered. Kuwahara et al. (2018), for example, estimated that melts containing 7-8 wt.% FeO account for 81-99 wt.% based on mass balance calculations.

Schmandt et al. (2014) reported a region of low shear wave velocities below the 660 km discontinuity under the south western USA, which from the lateral extent might be interpreted as a region containing neutrally buoyant partial melt. In Fig. 6.7, however, it is clear that the density of such a 1 wt.% hydrous partial melt would be much lower than the density of the lower mantle at this depth, as constrained by the PREM model (Dziewonski and Anderson, 1981). Such a melt composition, however, should also be close to equilibrium with an assemblage compatible with the base of the transition zone, as the solid phases must also be in equilibrium with such an assemblage at slightly lower pressures. This raises the possibility, therefore, that hydrous melts might rise out of the lower mantle but may tend to pond at the base of the transition zone on top of the 660 km discontinuity or that they may freeze due to the increase in H₂O solubility of the mantle minerals. The region examined by Schmandt et al. (2014) appears to be down welling, however, with a rate of up to 2 cm/year. It may be that hydrous mantle is continuously dragged down from the transition zone into the lower mantle and that the low velocities arise due to melts forming in this downwelling material and rising back up again in a continuous cycle.

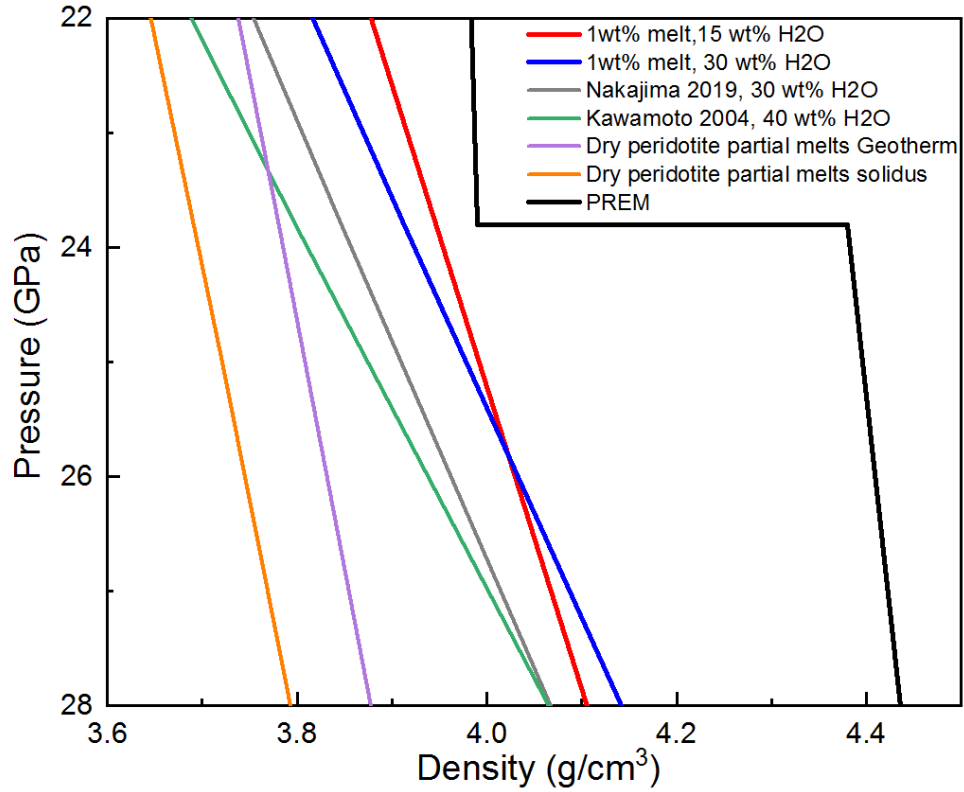


Figure 6.7 Calculated densities of the partial melts of anhydrous and hydrous peridotite from the current study and previous studies along the mantle geotherm (Brown and Shankland, 1981). The preliminary reference earth model (PREM) is also plotted (Dziewonski and Anderson, 1981) as a solid black line. The red and blue lines are compositions calculated from the current study for 1 % partial melt containing 15 wt.% and 30 wt.% water respectively. Melt densities based on the results of previous hydrous and anhydrous melting studies are shown for comparison.

7 Major conclusions

This thesis focused on investigating the substitution mechanisms in bridgmanite (Brg), the speciation of Al and Fe³⁺ as a function of oxygen fugacity and composition, the influence of Fe and Al substitution on the crystal structure of Brg as well as the composition, mainly the Fe content, of hydrous melts coexisting with Brg. The main conclusions can be summarized as follows:

(1) In Fp saturated systems, at low M³⁺ (M³⁺=Fe³⁺+Al³⁺) concentrations (<0.15 atoms pfu in Al bearing system, <0.03 atoms pfu in Fe bearing system and <0.10 atoms pfu in Fe, Al-bearing system), both charge-coupled substitution (CCS) and oxygen vacancy substitution (OVS) mechanisms are important in Brg. At higher trivalent cation concentrations, the charge coupled substitution predominates. The maximum amount of OVS in the current study is 0.04 pfu. This maximum OVS component value was achieved in the sample where the Al content (0.23 atoms pfu) is significantly higher than the Fe³⁺ content (0.11 atoms pfu) in Brg (S7214). The oxygen vacancy proportion shown in Fig. 5.13 is the absolute number of oxygen vacancies pfu in Brg which is half the value of that expressed in mole fraction of MgM³⁺O_{2.5} component ($x_{\text{MgM}^{3+}\text{O}_{2.5}}$).

(2) When both Fe³⁺ and Al are present, Al prefers to occupy the B site and Fe³⁺ prefers to go onto the A site, which is confirmed by single crystal X-ray diffraction through refinement of the mean atomic numbers at the A and B sites. FeAlO₃ charge coupled substitution is the major substitution mechanism for trivalent cations when the amount of Fe³⁺ and Al in Brg are similar. When there is additional Al or Fe³⁺, MgAlO_{2.5}, MgFe³⁺O_{2.5} OVS and AlAlO₃ or Fe³⁺Fe³⁺O₃ CCS are also present. For the samples analyzed in this study it appears that Fe³⁺ enters the B site only when the amount of Fe³⁺ is larger than Al.

(3) The molar volume of Brg increases with increasing Fe and Al substitution. The molar volume of pure MgSiO₃ end-member is 24.447(5) cm³/mol. If a linear volume relation is assumed, the molar volumes of the Brg end-members FeSiO₃, FeAlO₃, MgAlO_{2.5}, MgFeO_{2.5} and FeFeO₃ are determined to be 25.339 cm³/mol, 27.081 cm³/mol, 26.565 cm³/mol, 27.5

cm³/mol and 29.494 cm³/mol, respectively. The volumes of these components are essential for any thermodynamic calculation of Brg chemistry at pressures within the lower mantle.

(4) All lattice parameters of Brg increase with increasing M³⁺M³⁺O₃ and MgM³⁺O_{2.5} substitution, with the largest increase being that of the *c*-axis and the smallest being that of the *a*-axis. This can, in part, be attributed to changes in the corresponding individual B-O and A-O bond distances. The Fe²⁺SiO₃ has only a minor effect on *b*- and *c*- axes but results in increases in the *a*-axis.

(5) All B-O bond distances in Brg increase with increasing M³⁺M³⁺O₃ and MgM³⁺O_{2.5} substitution, with the B-O1 individual length which lies mainly along the *c*-axis increasing more rapidly than the intermediate B-O2 distances which are mainly in the *a-b* plane. This gives rise to an elongation of the B site octahedron along the *c*-axis due to the M³⁺ cation substituting Si at this site. Fe²⁺SiO₃ substitution has no obvious effect on the B-O bond distances.

(6) The shortest four A-O bond distances in Brg decrease while the other longer distances increase with increasing M³⁺M³⁺O₃ and MgM³⁺O_{2.5} substitution, leading to a larger distortion of the A-site coordination polyhedral. Fe²⁺SiO₃ substitution, on the contrary, decreases the distortion of the A site.

(7) The orthorhombic distortion of Brg has been described using the irreducible representations (Irreps) describing the displacive modes of the A cation and oxygens from the atomic positions of the cubic perovskite aristotype structure. Five mode displacements are allowed for the orthorhombic Brg structure: R_4^+ and M_3^+ , which describe the out-of-phase tilting along the [110] direction and the in-phase octahedral tilting along [001] respectively, are the two primary distortion modes in Brg. The secondary modes include X_5^+ , which describes the displacement of O and of Mg from the center of the aristotype unit cell and the R_5^+ mode, which describes the displacement of the Mg atoms along the orthorhombic *a*-axis. Although these modes are only secondary (i.e. do not drive the cubic to orthorhombic phase transformation) they have a no negligible amplitude which increase with increasing M³⁺M³⁺O₃ and MgM³⁺O_{2.5} substitutions. In contrast, the Fe²⁺SiO₃

substitution decreases the R_4^+ tilting and the X_5^+ and R_5^+ displacements of the A cations and therefore its distortion in agreement with the variation observed for the A-O individual bond distances.

(8) The spontaneous strain e_4 and e_{tx} in Brg increases with $M^{3+}M^{3+}O_3$ and $MgM^{3+}O_{2.5}$ substitution and decreases with $Fe^{2+}SiO_3$ substitution. The coupling coefficient between the order parameters (describing the octahedral tilting driving the cubic to orthorhombic phase transition) and the spontaneous strain is strongly dependent on composition.

(9) At constant pressure and temperature, the $Fe^{3+}/\Sigma Fe$ ratio in Brg is found to be a function of oxygen fugacity (f_{O_2}) as well as the Al and Fe content. At a fixed oxygen fugacity and Fe content, the $Fe^{3+}/\Sigma Fe$ ratio in Brg increases with Al content, whereas this dependency decreases at higher oxygen fugacities. This is simply because the $Fe^{3+}/\Sigma Fe$ ratio approaches unity at high f_{O_2} regardless of the Al content. At a fixed Al and Fe content, the $Fe^{3+}/\Sigma Fe$ ratio in Brg increases with oxygen fugacity and the dependency is smaller at higher Al content. At fixed Al content and oxygen fugacity, the $Fe^{3+}/\Sigma Fe$ ratio in Brg decreases slightly with increasing Fe content. In addition, the $Fe^{3+}/\Sigma Fe$ ratio in Brg seems to decrease with increasing temperature if all other parameters remain constant.

(10) Previous studies (Liu et al., 2017, 2019a, 2019b) indicate that for Fe-free Al-bearing Brg, the $AlAlO_3$ CCS increases monotonically with Al content while the $MgAlO_{2.5}$ component first increases with Al content, reaching a maximum at $Al=0.1$ pfu and then decreases with Al content. This behavior can be described by a thermodynamic model with $W_{MgAl,A}^{Brg} = 152.6$ kJ/mol and $\Delta G_{(5.12)}^0 = -85(4)$ kJ/mol for the equilibrium $2MgAlO_{2.5} = AlAlO_3 + 2MgO$ (5.12) at 27 GPa and 2000 K. The large interaction parameter is necessary because a significant change in the speciation occurs over a relatively narrow Brg Al content.

(11) A similar thermodynamic model can be constructed using the equilibrium $2MgFeO_{2.5} = FeFeO_3 + 2MgO$ (5.21) in Al-free, Fe-bearing Brg with an additional equilibrium used to determine the oxygen fugacity dependence i.e. $2FeO + 0.5O_2 = FeFeO_3$ (5.27) at 25 GPa and 1973 K. The best solution was achieved with $\Delta G_{(5.21)}^0 = -27.886$ kJ/mol and $\Delta G_{(5.27)}^0 =$

172.236 kJ/mol. Using activity-composition models does not improve the fitting even with Margules parameters in the order of MJ/mol. Therefore, the resulting model which has only two fitting parameters is considered to provide the best fit within experimental uncertainties.

(12) In order to develop a thermodynamic model to describe the Fe³⁺ and Al speciation in Brg it is necessary to consider mixing of the 3+ cations on both cation sites and to constrain this inter-site mixing using the equilibria: $2\text{MgFeO}_{2.5} = \text{FeFeO}_3 + 2\text{MgO}$ (5.30) and $2\text{MgAlO}_{2.5} = \text{AlAlO}_3 + 2\text{MgO}$ (5.31). One further equilibrium is then used to impose the control of f_{O_2} i.e. $2\text{FeO} + \text{AlAlO}_3 + 0.5\text{O}_2 = 2\text{FeAlO}_3$ (5.32). The experimental data were then fitted by allowing the site occupancies of 3+ cations for each experimental composition to vary under the constraints of mass balance and finding the sets of site occupancies that allow three constant values of ΔG^0 values to be determined for all the experiments. Using 11 experimental analyses of coexisting Brg and Fp samples with varying concentrations of total Fe, Al and at different oxygen fugacities the following best fit standard state Gibbs free energies were obtained at 25 GPa and 1973 K: $\Delta G_{(5.31)}^0 = -180.438$ kJ/mol, $\Delta G_{(5.32)}^0 = -32.807$ kJ/mol and $\Delta G_{(5.33)}^0 = 24.605$ kJ/mol. Brg total Fe³⁺ and Fe³⁺/ΣFe ratio calculated using the model are in good agreement with the experimental data even though the model has only three adjustable parameters. Several activity-composition models were tested but were found not to significantly improve the fitting. This does not imply that the mixing is ideal but that the activity-composition relations do not have a significant effect in the compositional range examined. Using this model, the ferric Fe content of Brg and its distribution over the A and B sites can be determined at 25 GPa and 1973 K as a function of f_{O_2} for any given bulk Fe and Al content of Brg.

(13) Using this model combined with a mass balance calculation, the composition and proportion of coexisting Brg and Fp were calculated for a pyrolite bulk composition at different oxygen fugacities. The results were compared with the experimental results of Irifune (1994) and Irifune et al. (2010) at ~28 GPa that employed the same composition. The model can reproduce the apparent K_D (i.e. the Mg-Fe exchange coefficient between Brg

and Fp that assumes all iron is Fe²⁺) and the Fe³⁺/ΣFe ratio in Brg from these experiments if an oxygen fugacity of IW + 1.5 is assumed. This is a quite reasonable assumption for these experiments that employed carbon capsules.

(14) The model shows that K_D (app) is a strong function of oxygen fugacity due to the variation of the Brg Fe³⁺ content with f_{O_2} . The changes in K_D (app) observed between 28 and 47.4 GPa by Irifune et al. (2010) can be achieved through changes in f_{O_2} between IW and IW +1.5. While Irifune et al. (2010) attributed changes in K_D (app) to an Fe²⁺ spin transition in Fp, the results of this study shown that changes in experimental f_{O_2} provide at least as good an explanation. The absence of f_{O_2} measurements in almost all previous experimental determinations of K_D (app) for Brg-Fp at deep lower mantle conditions almost certainly explains the large variations observed between studies.

(15) The calculated models for a pyrolite composition show that ferric Fe on Brg A site increases with oxygen fugacity causing Al to be pushed from A site to B site. Moreover, the oxygen vacancy component in Brg decreases with increasing oxygen fugacity. At low oxygen fugacities, which are more realistic for the bulk of the lower mantle, both AlAlO₃ and (Mg,Fe)AlO_{2.5} components are present, which may be important for Brg transport properties and lower mantle transport properties in general.

(16) If the mantle has a relatively constant bulk oxygen content, the oxygen fugacity in the lower mantle would be driven to values where iron-nickel alloy or iron-nickel-sulphur-rich phases would form to fulfill the requirement of Brg for high Fe³⁺ concentrations. Ferric iron would be formed through disproportionation of Fe²⁺ as well as reduction of NiO. Our calculations show that for a pyrolite bulk composition with an initial Fe³⁺/ΣFe ratio of 0.03, the oxygen fugacity at the top of the lower mantle would be IW – 0.8, which results in the formation of 0.6 wt.% Fe-Ni alloy containing approximately 26 wt.% Ni. The resulting Fe³⁺/ΣFe ratio of Brg is 0.51 and the bulk pyrolite has a ratio of 0.28. The proportion of metal alloy that forms is much smaller for a harzburgite bulk composition because the Al content of the Brg formed is smaller.

(17) Using the partial molar volumes determined for the different Brg 3+ cation components the thermodynamic model describing the mineral compositions in a pyrolite bulk composition can be extrapolated to high pressures. This extrapolation was made assuming both a constant oxygen fugacity (IW+1.5) and assuming an initial bulk $\text{Fe}^{3+}/\Sigma\text{Fe}$ ratio of 0.03, where Fe-Ni metal is formed. In both cases the $\text{Fe}^{3+}/\Sigma\text{Fe}$ ratio of Brg increases with pressure between 26-40 GPa, which is in contrast to the results of a number of laser heated diamond anvil cell experiments. This comparison underlines the fact that it is very important to control the f_{O_2} in such experiments if any meaningful conclusions are to be made.

(18) Model pyrolite calculations indicate that K_{D} (app), determined either at a constant f_{O_2} of IW+1.5 or at equilibrium with Fe-Ni metal, does not change significantly over the pressure range of 26-40 GPa. In contrast, K_{D} (app) calculated for a constant Brg $\text{Fe}^{3+}/\Sigma\text{Fe}$ ratio of 0.69, i.e. similar to the value reported from the multianvil experiments of Irifune et al. (2010), decreases from 0.67 at 26 GPa to 0.48 at 40 GPa. This decrease is in very good agreement with the results of Irifune et al. (2010) i.e. the model reproduces both the experimental K_{D} (app) and the Brg $\text{Fe}^{3+}/\Sigma\text{Fe}$ ratio.

(19) The proportion of oxygen vacancies in Brg determined using the model extrapolation for a pyrolite composition at $f_{\text{O}_2}=\text{IW}+1.5$, decreases continuously from 25 to 40 GPa, reaching almost zero at ~ 40 GPa. This decrease in oxygen vacancies with pressure in the upper part of the lower mantle may provide an explanation for a proposed increase in mantle viscosity between 660 and 1000 km depth.

(20) In the experiments performed to determine Brg and Fp compositions at 25 GPa and 1973 K, carbon occurs as either diamond or carbide at oxygen fugacities $\leq \text{IW}$ and as carbonate at oxygen fugacities $>\text{IW}+2.7$. These observations bracket the f_{O_2} of the $(\text{Mg,Fe})\text{CO}_3 = (\text{Mg,Fe})\text{O} + \text{C} + \text{O}_2$ equilibrium. This indicates that sub-lithospheric diamonds cannot be formed from carbonate at typical uppermost lower mantle oxygen fugacities, which are likely to be $\sim \text{IW} - 0.8$ if the upper mantle has the same bulk oxygen concentration as the lower mantle.

(21) For three diamond inclusions, which were proposed to have originally been Brg trapped at conditions of the top of the lower mantle (McCammon et al., 1997; McCammon et al., 2004c; Stachel et al., 2000), the oxygen fugacities can be calculated, using the model derived in the current study, based on measurements of the inclusion $\text{Fe}^{3+}/\Sigma\text{Fe}$ ratios and assuming that they originally formed as Brg at the top of the lower mantle. The results show a minimum f_{O_2} of IW-0.8 for one inclusion and IW+0.7 and -0.5 for the other two inclusions. This implies that these diamonds were unlikely to have been formed by the reduction of pure carbonate, which would imply a likely origin from subducted material.

(22) From water bearing experiments where hydrous melts were formed it was possible to calculate values of $K_D^{\text{Brg-Melt}}_{\text{Fe-Mg}}$ describing the Mg-Fe exchange between Brg and melt. The values determined for this K_D were lower than those reported in the recent study of Nakajima et al. (2019) that imply a much higher Fe content in the melt for a given Brg iron content. This discrepancy can be attributed to the very oxidized conditions employed in the experiments of Nakajima et al. (2019) and compared to the more realistic reducing conditions used in the current study.

(23) A model was developed to describe the Mg-Fe partitioning between Brg and melt, based on the ion-exchange equilibrium. Using this model and mass balance constraints, the compositions of Brg and hydrous melt for a pyrolite composition at the top of the lower mantle were calculated for various melt fractions (0.1 wt.%, 0.5 wt.%, and 1 wt.%) and melt water contents (15-30 wt.%) for which some uncertainty exists. The model shows the melt iron content to be higher than previous experimental studies not just due to the difference in assumed f_{O_2} but also due to the examination of smaller, more realistic melt fractions that do not significantly deplete the solid residue in iron.

(24) Based on the calculated melt composition, melt densities were determined using a second-order Birch-Murnaghan equation of state along a mantle geotherm from 22-28 GPa. In this pressure range, the hydrous melt formed in the current study is determined to be denser than those encountered by Nakajima et al. (2019) and Kawamoto (2004) and also much higher than the density of dry melt generated near the dry peridotite solidus. This

raised density is mainly due to the higher proportion of Fe partitioning into the melt. The density of a 1 wt.% hydrous partial melt would be significantly lower than the density of the lower mantle at this depth but would be close to neutral buoyancy at the base of the transition zone. This raises the possibility, that hydrous melts might rise out of the lower mantle but pond or freeze on entering the transition zone. If such a process occurs in regions of down-welling then melt bearing regions may be continuously dragged into the lower mantle before grain scale migration allows them to flow upwards, potentially creating long term low velocity layers (Nakajima et al., 2019).

References

- Agee, C.B., Walker, D., 1993. Olivine flotation in mantle melt. *Earth and Planetary Science Letters* 114, 315-324.
- Akaogi, M., 2007. Phase transitions of minerals in the transition zone and upper part of the lower mantle, in: Ohtani, E. (Ed.), *Advances in High-pressure Mineralogy*. Geological Society of America Special Paper 421, pp. 1-13.
- Akaogi, M., Tanaka, A., Ito, E., 2002. Garnet–ilmenite–perovskite transitions in the system $\text{Mg}_4\text{Si}_4\text{O}_{12}$ – $\text{Mg}_3\text{Al}_2\text{Si}_3\text{O}_{12}$ at high pressures and high temperatures: phase equilibria, calorimetry and implications for mantle structure. *Physics of the Earth and Planetary Interiors* 132, 303-324.
- Albarède, F., van der Hilst, R.D., 2002. Zoned mantle convection. *Philosophical Transactions of the Royal Society of London. Series A: Mathematical, Physical and Engineering Sciences* 360, 2569-2592.
- Allègre, C.J., Poirier, J.-P., Humler, E., Hofmann, A.W., 1995. The chemical composition of the Earth. *Earth and Planetary Science Letters* 134, 515-526.
- Allen, F., Kennard, O., Watson, D., Brammer, L., Orpen, A., Taylor, R., 1992. *International Tables for Crystallography, Vol. C*, edited by AJC Wilson. Dordrecht: Kluwer Academic Publishers.
- Amthauer, G., Grodzicki, M., Lottermoser, W., Redhammer, G., Beran, A., Libowitzky, E., 2004. Mössbauer spectroscopy: Basic principles. *Spectroscopic Methods in Mineralogy* 6, 345-367.
- Anderson, D.L., 1989. Composition of the Earth. *Science* 243, 367-370.
- Andrault, D., Bolfan-Casanova, N., Guignot, N., 2001. Equation of state of lower mantle (Al,Fe)- MgSiO_3 perovskite. *Earth and Planetary Science Letters* 193, 501-508.
- Andrault, D., Muñoz, M., Pesce, G., Cerantola, V., Chumakov, A., Kantor, I., Pascarelli, S., Rüffer, R., Hennet, L., 2018. Large oxygen excess in the primitive mantle could be the source of the Great Oxygenation Event. *Geochemical Perspectives Letters*, 5-10.
- Andrault, D., Neuville, D., Flank, A.-M., Wang, Y., 1998. Cation sites in Al-rich MgSiO_3 perovskites. *American Mineralogist* 83, 1045-1053.
- Andrews, J., Deuss, A., 2008. Detailed nature of the 660 km region of the mantle from global receiver function data. *Journal of Geophysical Research: Solid Earth* 113, B06304.
- Angel, R., Downs, R., Finger, L., 2000. High-temperature–high-pressure diffractometry. *Reviews in mineralogy and geochemistry* 41, 559-597.
- Angel, R., Finger, L., 2011. SINGLE: a program to control single-crystal diffractometers. *Journal of Applied Crystallography* 44, 247-251.

- Angel, R.J., Zhao, J., Ross, N.L., 2005. General rules for predicting phase transitions in perovskites due to octahedral tilting. *Physical Review Letters* 95, 025503.
- Arevalo, R., McDonough, W.F., 2010. Chemical variations and regional diversity observed in MORB. *Chemical Geology* 271, 70-85.
- Armstrong, K., 2018. Redox Evolution of the Early Earth's Mantle, Doctoral thesis, Bayreuther Graduiertenschule für Mathematik und Naturwissenschaften - BayNAT. Universität Bayreuth.
- Ballmer, M.D., Houser, C., Hernlund, J.W., Wentzcovitch, R.M., Hirose, K., 2017. Persistence of strong silica-enriched domains in the Earth's lower mantle. *Nature Geoscience* 10, 236-240.
- Becerro, A., McCammon, C., Langenhorst, F., Seifert, F., Angel, R., 1999. Oxygen vacancy ordering in $\text{CaTiO}_3\text{-CaFeO}_{2.5}$ perovskites: from isolated defects to infinite sheets. *Phase Transitions: A Multinational Journal* 69, 133-146.
- Benz, H., Vidale, J., 1993. Sharpness of upper-mantle discontinuities determined from high-frequency reflections. *Nature* 365, 147-150.
- Bercovici, D., Karato, S.-i., 2003. Whole-mantle convection and the transition-zone water filter. *Nature* 425, 39-44.
- Bina, C.R., 2003. Seismological constraints upon mantle composition, in: Carlson, R.W. (Ed.), *The Mantle and Core: Treatise on Geochemistry*, Vol. 2. Elsevier-Pergamon, Oxford, pp. 39-59.
- Bina, C.R., Helffrich, G., 2014. Geophysical Constraints on Mantle Composition, in: Carlson, R.W. (Ed.), *The Mantle and Core: Treatise on Geochemistry*, Vol. 3. Elsevier-Pergamon, Oxford, pp. 41-65.
- Boffa Ballaran, T., Frost, D.J., Miyajima, N., Heidelbach, F., 2010. The structure of a super-aluminous version of the dense hydrous-magnesium silicate phase D. *American Mineralogist* 95, 1113-1116.
- Boffa Ballaran, T., Kurnosov, A., Glazyrin, K., Frost, D.J., Merlini, M., Hanfland, M., Caracas, R., 2012. Effect of chemistry on the compressibility of silicate perovskite in the lower mantle. *Earth and Planetary Science Letters* 333-334, 181-190.
- Bolfan-Casanova, N., Keppler, H., Rubie, D.C., 2003. Water partitioning at 660 km depth and evidence for very low water solubility in magnesium silicate perovskite. *Geophysical Research Letters* 30, 1905.
- Bostock, M., 1996. A seismic image of the upper mantle beneath the North American craton. *Geophysical Research Letters* 23, 1593-1596.
- Bouhifd, M.A., Whittington, A., Richet, P., 2015. Densities and volumes of hydrous silicate melts: new measurements and predictions. *Chemical Geology* 418, 40-50.

- Boujibar, A., Bolfan-Casanova, N., Andrault, D., Bouhifd, M.A., Trcera, N., 2016. Incorporation of Fe²⁺ and Fe³⁺ in bridgmanite during magma ocean crystallization. *American Mineralogist* 101, 1560-1570.
- Brenker, F.E., Vollmer, C., Vincze, L., Vekemans, B., Szymanski, A., Janssens, K., Szaloki, I., Nasdala, L., Joswig, W., Kaminsky, F., 2007. Carbonates from the lower part of transition zone or even the lower mantle. *Earth and Planetary Science Letters* 260, 1-9.
- Brese, N., O'keeffe, M., 1991. Bond-valence parameters for solids. *Acta Crystallographica Section B: Structural Science* 47, 192-197.
- Brodholt, J.P., 2000. Pressure-induced changes in the compression mechanism of aluminous perovskite in the Earth's mantle. *Nature* 407, 620-622.
- Brown, I., Altermatt, D., 1985. Bond-valence parameters obtained from a systematic analysis of the inorganic crystal structure database. *Acta Crystallographica Section B: Structural Science* 41, 244-247.
- Brown, J., Shankland, T., 1981. Thermodynamic parameters in the Earth as determined from seismic profiles. *Geophysical Journal International* 66, 579-596.
- Cammarano, F., Deuss, A., Goes, S., Giardini, D., 2005. One-dimensional physical reference models for the upper mantle and transition zone: Combining seismic and mineral physics constraints. *Journal of Geophysical Research: Solid Earth* 110, B01306.
- Campbell, A.J., Danielson, L., Richter, K., Seagle, C.T., Wang, Y., Prakapenka, V.B., 2009. High pressure effects on the iron-iron oxide and nickel-nickel oxide oxygen fugacity buffers. *Earth and Planetary Science Letters* 286, 556-564.
- Campbell, A.J., Danielson, L., Richter, K., Wang, Y., Davidson, G., Wang, Y., 2006a. Oxygen fugacity at high pressure: Equations of state of metal-oxide pairs.
- Campbell, B.J., Stokes, H.T., Tanner, D.E., Hatch, D.M., 2006b. ISODISPLACE: a web-based tool for exploring structural distortions. *Journal of Applied Crystallography* 39, 607-614.
- Canil, D., O'Neill, H.S.C., 1996. Distribution of ferric iron in some upper-mantle assemblages. *Journal of Petrology* 37, 609-635.
- Canil, D., O'Neill, H.S.C., Pearson, D., Rudnick, R.L., McDonough, W.F., Carswell, D., 1994. Ferric iron in peridotites and mantle oxidation states. *Earth and Planetary Science Letters* 123, 205-220.
- Carpenter, M.A., Becerro, A.I., Seifert, F., 2001. Strain analysis of phase transitions in (Ca,Sr)TiO₃ perovskites. *American Mineralogist* 86, 348-363.
- Carpenter, M.A., Howard, C., Knight, K., Zhang, Z., 2006. Structural relationships and a phase diagram for (Ca,Sr)TiO₃ perovskites. *Journal of Physics: Condensed Matter* 18, 10725.
- Catalli, K., Shim, S.-H., Dera, P., Prakapenka, V.B., Zhao, J., Sturhahn, W., Chow, P., Xiao, Y., Cynn, H., Evans, W.J., 2011. Effects of the Fe³⁺ spin transition on the properties of aluminous perovskite—New insights for lower-mantle seismic heterogeneities. *Earth and Planetary Science Letters* 310, 293-302.

- Catalli, K., Shim, S.-H., Prakapenka, V.B., Zhao, J., Sturhahn, W., Chow, P., Xiao, Y., Liu, H., Cynn, H., Evans, W.J., 2010. Spin state of ferric iron in MgSiO₃ perovskite and its effect on elastic properties. *Earth and Planetary Science Letters* 289, 68-75.
- Chantel, J., Frost, D.J., McCammon, C.A., Jing, Z., Wang, Y., 2012. Acoustic velocities of pure and iron-bearing magnesium silicate perovskite measured to 25 GPa and 1200 K. *Geophysical Research Letters* 39, L19307.
- Cottaar, S., Heister, T., Rose, I., Unterborn, C., 2014. BurnMan: A lower mantle mineral physics toolkit. *Geochemistry, Geophysics, Geosystems* 15, 1164-1179.
- Day, E.A., Deuss, A., 2013. Reconciling PP and P' P' precursor observations of a complex 660 km seismic discontinuity. *Geophysical Journal International* 194, 834-838.
- Deuss, A., 2009. Global observations of mantle discontinuities using SS and PP precursors. *Surveys in Geophysics* 30, 301-326.
- Dyar, M.D., Agresti, D.G., Schaefer, M.W., Grant, C.A., Sklute, E.C., 2006. Mössbauer spectroscopy of earth and planetary materials. *Annual Review of Earth and Planetary Sciences* 34, 83-125.
- Dziewonski, A.M., Anderson, D.L., 1981. Preliminary reference Earth model. *Physics of the Earth and Planetary Interiors* 25, 297-356.
- Eugster, H., 1957. Heterogeneous reactions involving oxidation and reduction at high pressures and temperatures. *The Journal of Chemical Physics* 26, 1760-1761.
- Fan, D., Fu, S., Yang, J., Tkachev, S.N., Prakapenka, V.B., Lin, J.-F., 2019. Elasticity of single-crystal periclase at high pressure and temperature: The effect of iron on the elasticity and seismic parameters of ferropericlase in the lower mantle. *American Mineralogist: Journal of Earth and Planetary Materials* 104, 262-275.
- Farrugia, L.J., 1999. WinGX suite for small-molecule single-crystal crystallography. *Journal of Applied Crystallography* 32, 837-838.
- Fei, Y., Virgo, D., Mysen, B., Wang, Y., Mao, H., 1994. Temperature-dependent electron delocalization in (Mg, Fe)SiO₃ perovskite. *American Mineralogist* 79, 826-837.
- Fiquet, G., Dewaele, A., Andrault, D., Kunz, M., Le Bihan, T., 2000. Thermoelastic properties and crystal structure of MgSiO₃ perovskite at lower mantle pressure and temperature conditions. *Geophysical Research Letters* 27, 21-24.
- Fitoussi, C., Bourdon, B., Wang, X., 2016. The building blocks of Earth and Mars: A close genetic link. *Earth and Planetary Science Letters* 434, 151-160.
- Flanagan, M.P., Shearer, P.M., 1998. Global mapping of topography on transition zone velocity discontinuities by stacking SS precursors. *Journal of Geophysical Research: Solid Earth* 103, 2673-2692.
- Frost, B.R., 1991. Introduction to oxygen fugacity and its petrologic importance. *Reviews in Mineralogy and Geochemistry* 25, 1-9.

- Frost, D.J., 1999. The stability of dense hydrous magnesium silicates in Earth's transition zone and lower mantle. *Mantle petrology: field observations and high pressure experimentation: a tribute to Francis R.(Joe) Boyd*, 283-296.
- Frost, D.J., 2003. Fe²⁺-Mg partitioning between garnet, magnesiowüstite, and (Mg,Fe)₂SiO₄ phases of the transition zone. *American Mineralogist* 88, 387-397.
- Frost, D.J., 2008. The Upper Mantle and Transition Zone. *Elements* 4, 171-176.
- Frost, D.J., Fei, Y., 1998. Stability of phase D at high pressure and high temperature. *Journal of Geophysical Research: Solid Earth* 103, 7463-7474.
- Frost, D.J., Langenhorst, F., 2002. The effect of Al₂O₃ on Fe–Mg partitioning between magnesiowüstite and magnesium silicate perovskite. *Earth and Planetary Science Letters* 199, 227-241.
- Frost, D.J., Liebske, C., Langenhorst, F., McCammon, C.A., Trønnnes, R.G., Rubie, D.C., 2004. Experimental evidence for the existence of iron-rich metal in the Earth's lower mantle. *Nature* 428, 409-412.
- Frost, D.J., McCammon, C.A., 2008. The redox state of Earth's mantle. *Annual Review of Earth and Planetary Sciences* 36, 389-420.
- Fujii, T., Scarfe, C.M., 1985. Composition of liquids coexisting with spinel lherzolite at 10 kbar and the genesis of MORBs. *Contributions to Mineralogy and Petrology* 90, 18-28.
- Fujino, K., Nishio-Hamane, D., Seto, Y., Sata, N., Nagai, T., Shinmei, T., Irifune, T., Ishii, H., Hiraoka, N., Cai, Y.Q., Tsuei, K.-D., 2012. Spin transition of ferric iron in Al-bearing Mg–perovskite up to 200GPa and its implication for the lower mantle. *Earth and Planetary Science Letters* 317-318, 407-412.
- Fukao, Y., Obayashi, M., 2013. Subducted slabs stagnant above, penetrating through, and trapped below the 660 km discontinuity. *Journal of Geophysical Research: Solid Earth* 118, 5920-5938.
- Fukao, Y., Obayashi, M., Inoue, H., Nenbai, M., 1992. Subducting slabs stagnant in the mantle transition zone. *Journal of Geophysical Research: Solid Earth* 97, 4809-4822.
- Fukao, Y., Widiyantoro, S., Obayashi, M., 2001. Stagnant slabs in the upper and lower mantle transition region. *Reviews of Geophysics* 39, 291-323.
- Garvie, L.A., Craven, A.J., 1994. Use of electron-energy loss near-edge fine structure in the study of minerals. *American Mineralogist* 79, 411-425.
- Gasparik, T., 1993. The role of volatiles in the transition zone. *Journal of Geophysical Research: Solid Earth* 98, 4287-4299.
- Ghosh, S., Schmidt, M.W., 2014. Melting of phase D in the lower mantle and implications for recycling and storage of H₂O in the deep mantle. *Geochimica et Cosmochimica Acta* 145, 72-88.
- Glazer, A., 1972. The classification of tilted octahedra in perovskites. *Acta Crystallographica Section B: Structural Crystallography and Crystal Chemistry* 28, 3384-3392.

- Glazyrin, K., Boffa Ballaran, T., Frost, D.J., McCammon, C.A., Kantor, A., Merlini, M., Hanfland, M., Dubrovinsky, L., 2014. Magnesium silicate perovskite and effect of iron oxidation state on its bulk sound velocity at the conditions of the lower mantle. *Earth and Planetary Science Letters* 393, 182-186.
- Green, D., 1979. Petrogenesis of mid ocean ridge basalts. *The Earth: its origin, structure and evolution*, 200-299.
- Gu, Y.J., Dziewoński, A.M., Ekström, G., 2003. Simultaneous inversion for mantle shear velocity and topography of transition zone discontinuities. *Geophysical Journal International* 154, 559-583.
- Gu, Y.J., Okeler, A., Schultz, R., 2012. Tracking slabs beneath northwestern Pacific subduction zones. *Earth and Planetary Science Letters* 331, 269-280.
- Gudmundsson, G., Wood, B., 1995. Experimental tests of garnet peridotite oxygen barometry. *Contributions to Mineralogy and Petrology* 119, 56-67.
- Gütlich, P., Link, R., Trautwein, A.X., 1978. Mössbauer spectroscopy and transition metal chemistry. Springer, Berlin.
- Hart, S.R., Zindler, A., 1986. In search of a bulk-Earth composition. *Chemical Geology* 57, 247-267.
- Heinrich, K.F., Newbury, D., 2013. Electron probe quantitation. Springer Science & Business Media.
- Heit, B., Yuan, X., Bianchi, M., Kind, R., Gossler, J., 2010. Study of the lithospheric and upper-mantle discontinuities beneath eastern Asia by SS precursors. *Geophysical Journal International* 183, 252-266.
- Helfrich, G., Bina, C.R., 1994. Frequency dependence of the visibility and depths of mantle seismic discontinuities. *Geophysical Research Letters* 21, 2613-2616.
- Herzberg, C., Raterron, P., Zhang, J., 2000. New experimental observations on the anhydrous solidus for peridotite KLB-1. *Geochemistry, Geophysics, Geosystems* 1, paper no. 2000GC000089.
- Herzberg, C., Zhang, J., 1996. Melting experiments on anhydrous peridotite KLB-1: Compositions of magmas in the upper mantle and transition zone. *Journal of Geophysical Research: Solid Earth* 101, 8271-8295.
- Hier-Majumder, S., Courtier, A., 2011. Seismic signature of small melt fraction atop the transition zone. *Earth and Planetary Science Letters* 308, 334-342.
- Hirose, K., 1997. Melting experiments on Iherzolite KLB-1 under hydrous conditions and generation of high-magnesian andesitic melts. *Geology* 25, 42-44.
- Hirose, K., 2002. Phase transitions in pyrolitic mantle around 670-km depth: Implications for upwelling of plumes from the lower mantle. *Journal of Geophysical Research: Solid Earth* 107, 2078.

- Hirose, K., Fei, Y., 2002. Subsolidus and melting phase relations of basaltic composition in the uppermost lower mantle. *Geochimica et Cosmochimica Acta* 66, 2099-2108.
- Hirose, K., Fei, Y., Ma, Y., Mao, H.-K., 1999. The fate of subducted basaltic crust in the Earth's lower mantle. *Nature* 397, 53-56.
- Hirose, K., Kawamoto, T., 1995. Hydrous partial melting of lherzolite at 1 GPa: the effect of H₂O on the genesis of basaltic magmas. *Earth and Planetary Science Letters* 133, 463-473.
- Hirose, K., Kushiro, I., 1993. Partial melting of dry peridotites at high pressures: determination of compositions of melts segregated from peridotite using aggregates of diamond. *Earth and Planetary Science Letters* 114, 477-489.
- Hirose, K., Sinmyo, R., Hernlund, J., 2017. Perovskite in Earth's deep interior. *Science* 358, 734-738.
- Hirose, K., Takafuji, N., Sata, N., Ohishi, Y., 2005. Phase transition and density of subducted MORB crust in the lower mantle. *Earth and Planetary Science Letters* 237, 239-251.
- Hofmann, A.W., 1997. Mantle geochemistry: the message from oceanic volcanism. *Nature* 385, 219-229.
- Holland, T.J.B., Hudson, N.F., Powell, R., Harte, B., 2013. New thermodynamic models and calculated phase equilibria in NCFMAS for basic and ultrabasic compositions through the transition zone into the uppermost lower mantle. *Journal of Petrology* 54, 1901-1920.
- Holland, T.J.B., Powell, R., 2011. An improved and extended internally consistent thermodynamic dataset for phases of petrological interest, involving a new equation of state for solids. *Journal of Metamorphic Geology* 29, 333-383.
- Holzappel, C., Rubie, D.C., Frost, D.J., Langenhorst, F., 2005. Fe-Mg interdiffusion in (Mg,Fe)SiO₃ perovskite and lower mantle reequilibration. *Science* 309, 1707-1710.
- Horiuchi, H., Ito, E., Weidner, D.J., 1987. Perovskite-type MgSiO₃: single-crystal X-ray diffraction study. *American Mineralogist* 72, 357-360.
- Howard, C.J., Stokes, H.T., 1998. Group-theoretical analysis of octahedral tilting in perovskites. *Acta Crystallographica Section B: Structural Science* 54, 782-789.
- Howard, C.J., Stokes, H.T., 2005. Structures and phase transitions in perovskites—a group-theoretical approach. *Acta Crystallographica Section A: Foundations of Crystallography* 61, 93-111.
- Hsu, H., Blaha, P., Cococcioni, M., Wentzcovitch, R.M., 2011. Spin-state crossover and hyperfine interactions of ferric iron in MgSiO₃ perovskite. *Physical Review Letters* 106, 118501.
- Hsu, H., Umemoto, K., Blaha, P., Wentzcovitch, R.M., 2010. Spin states and hyperfine interactions of iron in (Mg,Fe)SiO₃ perovskite under pressure. *Earth and Planetary Science Letters* 294, 19-26.

- Hu, J., Yang, H., Li, G., Wen, L., 2013. Seismic signature of the mantle transition zone beneath eastern Tibet and Sichuan Basin. *Journal of Asian Earth Sciences* 62, 606-615.
- Hummer, D.R., Fei, Y., 2012. Synthesis and crystal chemistry of Fe³⁺-bearing (Mg,Fe³⁺)(Si,Fe³⁺)O₃ perovskite. *American Mineralogist* 97, 1915-1921.
- Humphreys, E.D., Dueker, K.G., Schutt, D.L., Smith, R.B., 2000. Beneath Yellowstone: Evaluating plume and nonplume models using teleseismic images of the upper mantle. *GSA Today* 10, 1-7.
- Hunter, L., Gordon, J., Peck, S., Ang, D., Lin, J.-F., 2013. Using the Earth as a polarized electron source to search for long-range spin-spin interactions. *Science* 339, 928-932.
- Irifune, T., 1994. Absence of an aluminous phase in the upper part of the Earth's lower mantle. *Nature* 370, 131-133.
- Irifune, T., 1998. The Postspinel Phase Boundary in Mg₂SiO₄ Determined by in Situ X-ray Diffraction. *Science* 279, 1698-1700.
- Irifune, T., Ringwood, A.E., 1987a. Phase transformations in a harzburgite composition to 26 GPa: implications for dynamical behaviour of the subducting slab. *Earth and Planetary Science Letters* 86, 365-376.
- Irifune, T., Ringwood, A.E., 1987b. Phase transformations in primitive MORB and pyrolite compositions to 25 GPa and some geophysical implications. *High-Pressure Research in Mineral Physics: A Volume in Honor of Syun-iti Akimoto*, 231-242.
- Irifune, T., Ringwood, A.E., 1993. Phase transformations in subducted oceanic crust and buoyancy relationships at depths of 600-800 km in the mantle. *Earth and Planetary Science Letters* 117, 101-110.
- Irifune, T., Shinmei, T., McCammon, C.A., Miyajima, N., Rubie, D.C., Frost, D.J., 2010. Iron partitioning and density changes of pyrolite in Earth's lower mantle. *Science* 327, 193-195.
- Irifune, T., Tsuchiya, T., 2015. Phase transitions and mineralogy of the lower mantle, in: Price, G., Schubert, G. (Eds.), *Mineral Physics: Treatise on geophysics*, Vol. 2. Elsevier, Amsterdam, pp. 33-60.
- Ito, E., Takahashi, E., 1987. Melting of peridotite at uppermost lower-mantle conditions. *Nature* 328, 514-517.
- Ito, E., Takahashi, E., 1989. Postspinel transformations in the system Mg₂SiO₄-Fe₂SiO₄ and some geophysical implications. *Journal of Geophysical Research: Solid Earth* 94, 10637-10646.
- Jackson, I., 1983. Some geophysical constraints on the chemical composition of the Earth's lower mantle. *Earth and Planetary Science Letters* 62, 91-103.
- Jackson, J.M., Sturhahn, W., Shen, G., Zhao, J., Hu, M.Y., Errandonea, D., Bass, J.D., Fei, Y., 2005. A synchrotron Mössbauer spectroscopy study of (Mg,Fe)SiO₃ perovskite up to 120 GPa. *American Mineralogist* 90, 199-205.

- Jagoutz, E., Palme, H., Baddenhausen, H., Blum, K., Cendales, M., Dreibus, G., Spettel, B., Lorenz, V., Wänke, H., 1979. The abundances of major, minor and trace elements in the Earth's mantle as derived from primitive ultramafic nodules, Lunar and Planetary Science Conference Proceedings, pp. 2031-2050.
- Javoy, M., 1995. The integral enstatite chondrite model of the Earth. *Geophysical Research Letters* 22, 2219-2222.
- Javoy, M., Kaminski, E., Guyot, F., Andrault, D., Sanloup, C., Moreira, M., Labrosse, S., Jambon, A., Agrinier, P., Davaille, A., 2010. The chemical composition of the Earth: Enstatite chondrite models. *Earth and Planetary Science Letters* 293, 259-268.
- Jephcoat, A., Hriljac, J., McCammon, C.A., O'Neill, H.S.C., Rubie, D.C., Finger, L., 1999. High-resolution synchrotron X-ray powder diffraction and Rietveld structure refinement of two $(\text{Mg}_{0.95}\text{Fe}_{0.05})\text{SiO}_3$ perovskite samples synthesized under different oxygen fugacity conditions. *American Mineralogist* 84, 214-220.
- Jochum, K., Hofmann, A., Ito, E., Seufert, H.M., White, W., 1983. K, U and Th in mid-ocean ridge basalt glasses and heat production, K/U and K/Rb in the mantle. *Nature* 306, 431-436.
- Kakizawa, S., Inoue, T., Nakano, H., Kuroda, M., Sakamoto, N., Yurimoto, H., 2018. Stability of Al-bearing superhydrous phase B at the mantle transition zone and the uppermost lower mantle. *American Mineralogist: Journal of Earth and Planetary Materials* 103, 1221-1227.
- Kaminsky, F.V., Ryabchikov, I.D., McCammon, C.A., Longo, M., Abakumov, A.M., Turner, S., Heidari, H., 2015. Oxidation potential in the Earth's lower mantle as recorded by ferropericlasite inclusions in diamond. *Earth and Planetary Science Letters* 417, 49-56.
- Kaneshima, S., Helffrich, G., 1999. Dipping low-velocity layer in the mid-lower mantle: evidence for geochemical heterogeneity. *Science* 283, 1888-1892.
- Kaneshima, S., Helffrich, G., 2003. Subparallel dipping heterogeneities in the mid-lower mantle. *Journal of Geophysical Research: Solid Earth* 108, 2272.
- Karato, S.-i., Wu, P., 1993. Rheology of the upper mantle: A synthesis. *Science* 260, 771-778.
- Katsura, T., Yamada, H., Nishikawa, O., Song, M., Kubo, A., Shinmei, T., Yokoshi, S., Aizawa, Y., Yoshino, T., Walter, M.J., 2004. Olivine - wadsleyite transition in the system $(\text{Mg,Fe})_2\text{SiO}_4$. *Journal of Geophysical Research: Solid Earth* 109, B02209.
- Katsura, T., Yamada, H., Shinmei, T., Kubo, A., Ono, S., Kanzaki, M., Yoneda, A., Walter, M.J., Ito, E., Urakawa, S., 2003. Post-spinel transition in Mg_2SiO_4 determined by high P - T in situ X-ray diffractometry. *Physics of the Earth and Planetary Interiors* 136, 11-24.
- Katzman, R., Zhao, L., Jordan, T.H., 1998. High-resolution, two-dimensional vertical tomography of the central Pacific mantle using ScS reverberations and frequency-dependent travel times. *Journal of Geophysical Research: Solid Earth* 103, 17933-17971.

- Kawai, N., Endho, S., Itho, K., 1970. Split sphere high pressure vessel and phase equilibrium relation in the system Mg_2SiO_4 - Fe_2SiO_4 . *Physics of the Earth and Planetary Interiors* 3, 182-185.
- Kawamoto, T., 2004. Hydrous phase stability and partial melt chemistry in H_2O -saturated KLB-1 peridotite up to the uppermost lower mantle conditions. *Physics of the Earth and Planetary Interiors* 143, 387-395.
- Kellogg, L.H., Hager, B.H., Van Der Hilst, R.D., 1999. Compositional stratification in the deep mantle. *Science* 283, 1881-1884.
- Kennedy, B.J., Howard, C.J., Chakoumakos, B.C., 1999. Phase transitions in perovskite at elevated temperatures—a powder neutron diffraction study. *Journal of Physics: Condensed Matter* 11, 1479-1488.
- Kennett, B.L., Engdahl, E., 1991. Traveltimes for global earthquake location and phase identification. *Geophysical Journal International* 105, 429-465.
- Kennett, B.L., Engdahl, E., Buland, R., 1995. Constraints on seismic velocities in the Earth from traveltimes. *Geophysical Journal International* 122, 108-124.
- Keppler, H., Dubrovinsky, L.S., Narygina, O., Kantor, I., 2008. Optical absorption and radiative thermal conductivity of silicate perovskite to 125 gigapascals. *Science* 322, 1529-1532.
- Keppler, H., Frost, D.J., 2005. Introduction to minerals under extreme conditions, in: Miletich, R. (Ed.), *Mineral Behaviour at Extreme Conditions*, European Mineralogical Union Lecture Notes in Mineralogy, vol. 7. Eötvös University Press, Budapest, pp. 1-30.
- Kessel, R., Beckett, J.R., Stolper, E.M., 2001. Thermodynamic properties of the Pt-Fe system. *American Mineralogist* 86, 1003-1014.
- Kind, R., Li, X., 2015. Deep earth structure-transition zone and mantle discontinuities, in: G. Schubert, B. Romanowicz, Dziewonski, A. (Eds.), *Deep Earth Seismology: Treatise on Geophysics*, Vol. 1. Elsevier, Amsterdam, pp. 655-682.
- King, H., Finger, L., 1979. Diffracted beam crystal centering and its application to high-pressure crystallography. *Journal of Applied Crystallography* 12, 374-378.
- Kirby, S.H., Stein, S., Okal, E.A., Rubie, D.C., 1996. Metastable mantle phase transformations and deep earthquakes in subducting oceanic lithosphere. *Reviews of Geophysics* 34, 261-306.
- Kojitani, H., Katsura, T., Akaogi, M., 2007. Aluminum substitution mechanisms in perovskite-type $MgSiO_3$: an investigation by Rietveld analysis. *Physics and Chemistry of Minerals* 34, 257-267.
- Krot, A., Keil, K., Scott, E., Goodrich, C., Weisberg, M., 2014. Classification of meteorites and their genetic relationships. *Meteorites and Cosmochemical Processes*, 1-63.
- Kupenko, I., McCammon, C.A., Sinmyo, R., Cerantola, V., Potapkin, V., Chumakov, A., Kantor, A., Rüffer, R., Dubrovinsky, L., 2015. Oxidation state of the lower mantle: In situ

- observations of the iron electronic configuration in bridgmanite at extreme conditions. *Earth and Planetary Science Letters* 423, 78-86.
- Kupenko, I., McCammon, C.A., Sinmyo, R., Prescher, C., Chumakov, A., Kantor, A., Ruffer, R., Dubrovinsky, L., 2014. Electronic spin state of Fe, Al-containing MgSiO₃ perovskite at lower mantle conditions. *Lithos* 189, 167-172.
- Kurnosov, A., Marquardt, H., Frost, D.J., Ballaran, T.B., Ziberna, L., 2017. Evidence for a Fe³⁺-rich pyrolitic lower mantle from (Al,Fe)-bearing bridgmanite elasticity data. *Nature* 543, 543-546.
- Kuwahara, H., Nomura, R., Nakada, R., Irifune, T., 2018. Simultaneous determination of melting phase relations of mantle peridotite and mid-ocean ridge basalt at the uppermost lower mantle conditions. *Physics of the Earth and Planetary Interiors* 284, 36-50.
- Lauterbach, S., McCammon, C., Van Aken, P., Langenhorst, F., Seifert, F., 2000. Mössbauer and ELNES spectroscopy of (Mg,Fe)(Si,Al)O₃ perovskite: a highly oxidised component of the lower mantle. *Contributions to Mineralogy and Petrology* 138, 17-26.
- Li, J., Fei, Y., 2014. Experimental constraints on core composition, in: Carlson, R. (Ed.), *The Mantle and Core: Treatise on geochemistry*, Vol. 3. Elsevier-Pergamon, Oxford, pp. 527-557.
- Li, J., Sturhahn, W., Jackson, J., Struzhkin, V., Lin, J., Zhao, J., Mao, H., Shen, G., 2006. Pressure effect on the electronic structure of iron in (Mg,Fe)(Si,Al)O₃ perovskite: a combined synchrotron Mössbauer and X-ray emission spectroscopy study up to 100 GPa. *Physics and Chemistry of Minerals* 33, 575-585.
- Liebske, C., Corgne, A., Frost, D.J., Rubie, D.C., Wood, B.J., 2005. Compositional effects on element partitioning between Mg-silicate perovskite and silicate melts. *Contributions to Mineralogy and Petrology* 149, 113-128.
- Lin, J.-F., Alp, E.E., Mao, Z., Inoue, T., McCammon, C.A., Xiao, Y., Chow, P., Zhao, J., 2012. Electronic spin states of ferric and ferrous iron in the lower-mantle silicate perovskite. *American Mineralogist* 97, 592-597.
- Lin, J.-F., Speziale, S., Mao, Z., Marquardt, H., 2013. Effects of the Electronic Spin Transitions of Iron in Lower Mantle Minerals: Implications for Deep Mantle Geophysics and Geochemistry. *Reviews of Geophysics* 51, 244-275.
- Litasov, K., Ohtani, E., Langenhorst, F., Yurimoto, H., Kubo, T., Kondo, T., 2003. Water solubility in Mg-perovskites and water storage capacity in the lower mantle. *Earth and Planetary Science Letters* 211, 189-203.
- Liu, J., Dorfman, S.M., Zhu, F., Li, J., Wang, Y., Zhang, D., Xiao, Y., Bi, W., Alp, E.E., 2018a. Valence and spin states of iron are invisible in Earth's lower mantle. *Nature Communications* 9, 1284.
- Liu, L.-g., 1982. Speculations on the composition and origin of the Earth. *Geochemical Journal* 16, 287-310.

- Liu, Z., Akaogi, M., Katsura, T., 2019a. Increase of the oxygen vacancy component in bridgmanite with temperature. *Earth and Planetary Science Letters* 505, 141-151.
- Liu, Z., Ballaran, T.B., Huang, R., Frost, D.J., Katsura, T., 2019b. Strong correlation of oxygen vacancies in bridgmanite with Mg/Si ratio. *Earth and Planetary Science Letters* 523, 115697.
- Liu, Z., Ishii, T., Katsura, T., 2017. Rapid decrease of $\text{MgAlO}_{2.5}$ component in bridgmanite with pressure. *Geochemical Perspectives Letters*, 12-18.
- Liu, Z., Park, J., Karato, S.-i., 2016. Seismological detection of low-velocity anomalies surrounding the mantle transition zone in Japan subduction zone. *Geophysical Research Letters* 43, 2480-2487.
- Liu, Z., Park, J., Karato, S.-i., 2018b. Seismic evidence for water transport out of the mantle transition zone beneath the European Alps. *Earth and Planetary Science Letters* 482, 93-104.
- Lodders, K., 2003. Solar system abundances and condensation temperatures of the elements. *The Astrophysical Journal* 591, 1220-1247.
- Lundin, S., Catalli, K., Santillán, J., Shim, S.H., Prakapenka, V.B., Kunz, M., Meng, Y., 2008. Effect of Fe on the equation of state of mantle silicate perovskite over 1 Mbar. *Physics of the Earth and Planetary Interiors* 168, 97-102.
- Luth, R.W., Virgo, D., Boyd, F.R., Wood, B.J., 1990. Ferric iron in mantle-derived garnets. *Contributions to Mineralogy and Petrology* 104, 56-72.
- Manthilake, G.M., de Koker, N., Frost, D.J., McCammon, C.A., 2011. Lattice thermal conductivity of lower mantle minerals and heat flux from Earth's core. *Proceedings of the National Academy of Sciences* 108, 17901-17904.
- Mao, H.-K., Hemley, R.J., Fei, Y., Shu, J.F., Chen, L.C., Jephcoat, A.P., Wu, Y., Bassett, W.A., 1991. Effect of pressure, temperature, and composition on lattice parameters and density of (Fe,Mg)SiO₃-perovskites to 30 GPa. *Journal of Geophysical Research* 96, 8069-8079.
- Mao, Z., Lin, J.F., Liu, J., Prakapenka, V.B., 2011. Thermal equation of state of lower-mantle ferropericlase across the spin crossover. *Geophysical Research Letters* 38, L23308.
- Mao, Z., Lin, J.F., Yang, J., Inoue, T., Prakapenka, V.B., 2015. Effects of the Fe³⁺ spin transition on the equation of state of bridgmanite. *Geophysical Research Letters* 42, 4335-4342.
- Mao, Z., Wang, F., Lin, J.-F., Fu, S., Yang, J., Wu, X., Okuchi, T., Tomioka, N., Prakapenka, V.B., Xiao, Y., Chow, P., 2017. Equation of state and hyperfine parameters of high-spin bridgmanite in the Earth's lower mantle by synchrotron X-ray diffraction and Mössbauer spectroscopy. *American Mineralogist* 102, 357-368.
- Marquardt, H., Miyagi, L., 2015. Slab stagnation in the shallow lower mantle linked to an increase in mantle viscosity. *Nature Geoscience* 8, 311-314.

- Martin, C.D., Crichton, W.A., Liu, H., Prakapenka, V., Chen, J., Parise, J.B., 2006. Phase transitions and compressibility of NaMgF₃ (Neighborhoodite) in perovskite- and post-perovskite-related structures. *Geophysical Research Letters* 33, L11305.
- Martin, C.D., Parise, J.B., 2008. Structure constraints and instability leading to the post-perovskite phase transition of MgSiO₃. *Earth and Planetary Science Letters* 265, 630-640.
- Mattern, E., Matas, J., Ricard, Y., Bass, J., 2005. Lower mantle composition and temperature from mineral physics and thermodynamic modelling. *Geophysical Journal International* 160, 973-990.
- McCammon, C.A., 1997. Perovskite as a possible sink for ferric iron in the lower mantle. *Nature* 387, 694-696.
- McCammon, C.A., 1998. The crystal chemistry of ferric iron in Fe_{0.05}Mg_{0.95}SiO₃ perovskite as determined by Mössbauer spectroscopy in the temperature range 80–293 K. *Physics and Chemistry of Minerals* 25, 292-300.
- McCammon, C.A., 2004. Mössbauer spectroscopy: applications. *Spectroscopic Methods in Mineralogy* 6, 369-398.
- McCammon, C.A., 2005. Mantle oxidation state and oxygen fugacity: Constraints on mantle chemistry, structure, and dynamics. Washington DC American Geophysical Union Geophysical Monograph Series 160, 219-240.
- McCammon, C.A., 2006. Microscopic properties to macroscopic behaviour: The influence of iron electronic state. *Journal of Mineralogical and Petrological Sciences* 101, 130-144.
- McCammon, C.A., Dubrovinsky, L., Narygina, O., Kantor, I., Wu, X., Glazyrin, K., Sergueev, I., Chumakov, A., 2010. Low-spin Fe²⁺ in silicate perovskite and a possible layer at the base of the lower mantle. *Physics of the Earth and Planetary Interiors* 180, 215-221.
- McCammon, C.A., Frost, D., Smyth, J., Laustsen, H., Kawamoto, T., Ross, N., Van Aken, P., 2004a. Oxidation state of iron in hydrous mantle phases: implications for subduction and mantle oxygen fugacity. *Physics of the Earth and Planetary Interiors* 143, 157-169.
- McCammon, C.A., Glazyrin, K., Kantor, A., Kantor, I., Kuppenko, I., Narygina, O., Potapkin, V., Prescher, C., Sinmyo, R., Chumakov, A., Rüffer, R., Sergueev, I., Smirnov, G., Dubrovinsky, L., 2013. Iron spin state in silicate perovskite at conditions of the Earth's deep interior. *High Pressure Research* 33, 663-672.
- McCammon, C.A., Griffin, W.L., Shee, S., O'Neill, H.S.C., 2001. Oxidation during metasomatism in ultramafic xenoliths from the Wesselton kimberlite, South Africa: implications for the survival of diamond. *Contributions to Mineralogy and Petrology* 141, 287-296.
- McCammon, C.A., Hutchison, M., Harris, J., 1997. Ferric iron content of mineral inclusions in diamonds from Sao Luiz: a view into the lower mantle. *Science* 278, 434-436.

- McCammon, C.A., Kantor, I., Narygina, O., Rouquette, J., Ponkratz, U., Sergueev, I., Mezouar, M., Prakapenka, V., Dubrovinsky, L., 2008. Stable intermediate-spin ferrous iron in lower-mantle perovskite. *Nature Geoscience* 1, 684-687.
- McCammon, C.A., Lauterbach, S., Seifert, F., Langenhorst, F., Van Aken, P., 2004b. Iron oxidation state in lower mantle mineral assemblages: I. Empirical relations derived from high-pressure experiments. *Earth and Planetary Science Letters* 222, 435-449.
- McCammon, C.A., Peyronneau, J., Poirier, J.P., 1998. Low ferric iron content of (Mg,Fe)O at high pressures and temperatures. *Geophysical Research Letters* 25, 1589-1592.
- McCammon, C.A., Rubie, D., Ross, C., Seifert, F., O'Neill, H.S.C., 1992. Mössbauer spectra of $^{57}\text{Fe}_{0.05}\text{Mg}_{0.95}\text{SiO}_3$ perovskite at 80 and 298 K. *American Mineralogist* 77, 894-897.
- McCammon, C.A., Stachel, T., Harris, J., 2004c. Iron oxidation state in lower mantle mineral assemblages: II. Inclusions in diamonds from Kankan, Guinea. *Earth and Planetary Science Letters* 222, 423-434.
- McDonough, W.F., Rudnick, R.L., 1998. Mineralogy and composition of the upper mantle. *Reviews in Mineralogy* 37, 139-164.
- McDonough, W.F., Sun, S.-S., 1995. The composition of the Earth. *Chemical Geology* 120, 223-253.
- Michael, P.J., Bonatti, E., 1985. Peridotite composition from the North Atlantic: regional and tectonic variations and implications for partial melting. *Earth and Planetary Science Letters* 73, 91-104.
- Miletich, R., Hejny, C., Krauss, G., Ullrich, A., 2005. Diffraction techniques: Shedding light on structural changes at extreme conditions. *Mineral behaviour at extreme conditions. European Mineralogical Union Notes in Mineralogy* 7, 281-338.
- Miller, S.C., Love, W.F., 1967. Tables of irreducible representations of space groups and co-representations of magnetic space groups. Pruet Press.
- Momma, K., Izumi, F., 2011. VESTA 3 for three-dimensional visualization of crystal, volumetric and morphology data. *Journal of Applied Crystallography* 44, 1272-1276.
- Murakami, M., Hirose, K., Kawamura, K., Sata, N., Ohishi, Y., 2004. Post-perovskite phase transition in MgSiO_3 . *Science* 304, 855-858.
- Murakami, M., Hirose, K., Ono, S., Ohishi, Y., 2003. Stability of CaCl_2 -type and α - PbO_2 -type SiO_2 at high pressure and temperature determined by in-situ X-ray measurements. *Geophysical Research Letters* 30, 1207.
- Murakami, M., Hirose, K., Yurimoto, H., Nakashima, S., Takafuji, N., 2002. Water in Earth's lower mantle. *Science* 295, 1885-1887.
- Murakami, M., Ohishi, Y., Hirao, N., Hirose, K., 2012. A perovskitic lower mantle inferred from high-pressure, high-temperature sound velocity data. *Nature* 485, 90-94.

- Myhill, R., Ojwang, D.O., Ziberna, L., Frost, D.J., Boffa Ballaran, T., Miyajima, N., 2016. On the P - T - fO_2 stability of Fe_4O_5 , Fe_5O_6 and Fe_4O_5 -rich solid solutions. *Contributions to Mineralogy and Petrology* 171, 51.
- Nakajima, A., Sakamaki, T., Kawazoe, T., Suzuki, A., 2019. Hydrous magnesium-rich magma genesis at the top of the lower mantle. *Scientific Reports* 9, 7420.
- Nakajima, Y., Frost, D.J., Rubie, D.C., 2012. Ferrous iron partitioning between magnesium silicate perovskite and ferropervicite and the composition of perovskite in the Earth's lower mantle. *Journal of Geophysical Research: Solid Earth* 117, B08201.
- Narygina, O.V., Kantor, I.Y., McCammon, C.A., Dubrovinsky, L., 2010. Electronic state of Fe^{2+} in $(Mg,Fe)(Si,Al)O_3$ perovskite and $(Mg,Fe)SiO_3$ majorite at pressures up to 81 GPa and temperatures up to 800 K. *Physics and Chemistry of Minerals* 37, 407-415.
- Navrotsky, A., 1999. A lesson from ceramics. *Science* 284, 1788-1789.
- Navrotsky, A., Schoenitz, M., Kojitani, H., Xu, H., Zhang, J., Weidner, D.J., Jeanloz, R., 2003. Aluminum in magnesium silicate perovskite: Formation, structure, and energetics of magnesium-rich defect solid solutions. *Journal of Geophysical Research: Solid Earth* 108, 2330.
- Nishio-Hamane, D., Nagai, T., Fujino, K., Seto, Y., Takafuji, N., 2005. Fe^{3+} and Al solubilities in $MgSiO_3$ perovskite: implication of the $Fe^{3+}AlO_3$ substitution in $MgSiO_3$ perovskite at the lower mantle condition. *Geophysical Research Letters* 32, L16306.
- Nishio-Hamane, D., Seto, Y., Fujino, K., Nagai, T., 2008. Effect of $FeAlO_3$ incorporation into $MgSiO_3$ on the bulk modulus of perovskite. *Physics of the Earth and Planetary Interiors* 166, 219-225.
- Novella, D., Dolejš, D., Myhill, R., Pamato, M.G., Manthilake, G., Frost, D.J., 2017. Melting phase relations in the systems Mg_2SiO_4 - H_2O and $MgSiO_3$ - H_2O and the formation of hydrous melts in the upper mantle. *Geochimica et Cosmochimica Acta* 204, 68-82.
- O'Neill, H.S.C., 1987. Quartz-fayalite-iron and quartz-fayalite-magnetite equilibria and the free energy of formation of fayalite (Fe_2SiO_4) and magnetite (Fe_3O_4). *American Mineralogist* 72, 67-75.
- O'Neill, H.S.C., McCammon, C., Canil, D., Rubie, D., Ross, C., Seifert, F., 1993a. Mössbauer spectroscopy of mantle transition zone phases and determination of minimum Fe^{3+} content. *American Mineralogist* 78, 456-460.
- O'Neill, H.S.C., Nell, J., 1997. Gibbs free energies of formation of RuO_2 , IrO_2 , and OsO_2 : A high-temperature electrochemical and calorimetric study. *Geochimica et Cosmochimica Acta* 61, 5279-5293.
- O'Neill, H.S.C., Rubie, D., Canil, D., Geiger, C., Ross, C., Seifert, F., Woodland, A., Takahashi, E., Jeanloz, R., 1993b. Ferric iron in the upper mantle and in transition zone assemblages: implications for relative oxygen fugacities in the mantle, in: Takahashi, E., Jeanloz, R., Rubie, D. (Eds.), *Evolution of the Earth and planets: Geophysical Monograph*

74. international Union of Geodesy and Geophysics and the American Geophysical Union, Washington, DC, pp. 73-88.
- O'Neill, H.S.C., Wall, V., 1987. The Olivine—Orthopyroxene—Spinel oxygen geobarometer, the nickel precipitation curve, and the oxygen fugacity of the Earth's Upper Mantle. *Journal of Petrology* 28, 1169-1191.
- Ohta, K., Yagi, T., Hirose, K., 2014. Thermal diffusivities of MgSiO_3 and Al-bearing MgSiO_3 perovskites. *American Mineralogist* 99, 94-97.
- Ohtani, E., Maeda, M., 2001. Density of basaltic melt at high pressure and stability of the melt at the base of the lower mantle. *Earth and Planetary Science Letters* 193, 69-75.
- Ohtani, E., Mizobata, H., Yurimoto, H., 2000. Stability of dense hydrous magnesium silicate phases in the systems $\text{Mg}_2\text{SiO}_4\text{-H}_2\text{O}$ and $\text{MgSiO}_3\text{-H}_2\text{O}$ at pressures up to 27 GPa. *Physics and Chemistry of Minerals* 27, 533-544.
- Ohtani, E., Sawamoto, H., 1987. Melting experiment on a model chondritic mantle composition at 25 GPa. *Geophysical Research Letters* 14, 733-736.
- Ohtani, E., Suzuki, A., Kato, T., 1997. Flotation of olivine and diamond in mantle melt at high pressure: Implications for fractionation in the deep mantle and ultradeep origin of diamond, *Properties of Earth and Planetary Materials at High Pressure and Temperature: Geophysical Monograph* 101. American Geophysical Union, Washington pp. 227-239.
- Ohtani, E., Toma, M., Kubo, T., Kondo, T., Kikegawa, T., 2003. In situ X-ray observation of decomposition of superhydrous phase B at high pressure and temperature. *Geophysical Research Letters* 30, 1029.
- Ohtani, E., Toma, M., Litasov, K., Kubo, T., Suzuki, A., 2001. Stability of dense hydrous magnesium silicate phases and water storage capacity in the transition zone and lower mantle. *Physics of the Earth and Planetary Interiors* 124, 105-117.
- Okino, K., Ando, M., Kaneshima, S., Hirahara, K., 1989. The horizontally lying slab. *Geophysical Research Letters* 16, 1059-1062.
- Okuda, Y., Ohta, K., Sinmyo, R., Hirose, K., Yagi, T., Ohishi, Y., 2019. Effect of spin transition of iron on the thermal conductivity of (Fe,Al)-bearing bridgmanite. *Earth and Planetary Science Letters* 520, 188-198.
- Ono, S., Hirose, K., Murakami, M., Isshiki, M., 2002. Post-stishovite phase boundary in SiO_2 determined by in situ X-ray observations. *Earth and Planetary Science Letters* 197, 187-192.
- Ono, S., Ito, E., Katsura, T., 2001. Mineralogy of subducted basaltic crust (MORB) from 25 to 37 GPa, and chemical heterogeneity of the lower mantle. *Earth and Planetary Science Letters* 190, 57-63.
- Pacalo, R.E., Parise, J.B., 1992. Crystal structure of superhydrous B, a hydrous magnesium silicate synthesized at 1400 °C and 20 GPa. *American Mineralogist* 77, 681-684.

- Palme, H., Nickel, K., 1985. Ca/Al ratio and composition of the Earth's upper mantle. *Geochimica et Cosmochimica Acta* 49, 2123-2132.
- Palme, H., O'Neill, H.S.C., 2014. Cosmochemical estimates of mantle composition, in: Carlson, R. (Ed.), *The Mantle and Core: Treatise on Geochemistry*, Vol. 3. Elsevier-Pergamon, Oxford, pp. 1-40.
- Panero, W.R., Akber-Knutson, S., Stixrude, L., 2006. Al₂O₃ incorporation in MgSiO₃ perovskite and ilmenite. *Earth and Planetary Science Letters* 252, 152-161.
- Parise, J., Wang, Y., Yeganeh-Haeri, A., Cox, D., Fei, Y., 1990. Crystal structure and thermal expansion of (Mg,Fe)SiO₃ perovskite. *Geophysical Research Letters* 17, 2089-2092.
- Pearson, D.G., Brenker, F.E., Nestola, F., McNeill, J., Nasdala, L., Hutchison, M.T., Matveev, S., Mather, K., Silversmit, G., Schmitz, S., Vekemans, B., Vincze, L., 2014. Hydrous mantle transition zone indicated by ringwoodite included within diamond. *Nature* 507, 221-224.
- Perez-Mato, J., Orobengoa, D., Aroyo, M., 2010. Mode crystallography of distorted structures. *Acta Crystallographica Section A: Foundations of Crystallography* 66, 558-590.
- Petersen, N., Vinnik, L., Kosarev, G., Kind, R., Oreshin, S., Stammer, K., 1993. Sharpness of the mantle discontinuities. *Geophysical Research Letters* 20, 859-862.
- Piet, H., Badro, J., Nabiei, F., Dennenwaldt, T., Shim, S.-H., Cantoni, M., Hébert, C., Gillet, P., 2016. Spin and valence dependence of iron partitioning in Earth's deep mantle. *Proceedings of the National Academy of Sciences* 113, 11127-11130.
- Potapkin, V., McCammon, C.A., Glazyrin, K., Kantor, A., Kuppenko, I., Prescher, C., Sinmyo, R., Smirnov, G., Chumakov, A.I., Rüffer, R., 2013. Effect of iron oxidation state on the electrical conductivity of the Earth's lower mantle. *Nature Communications* 4, 1-6.
- Pownceby, M.I., O'Neill, H.S.C., 1994. Thermodynamic data from redox reactions at high temperatures. IV. Calibration of the Re-ReO₂ oxygen buffer from EMF and NiO + Ni-Pd redox sensor measurements. *Contributions to Mineralogy and Petrology* 118, 130-137.
- Prescher, C., Langenhorst, F., Dubrovinsky, L.S., Prakapenka, V.B., Miyajima, N., 2014. The effect of Fe spin crossovers on its partitioning behavior and oxidation state in a pyrolytic Earth's lower mantle system. *Earth and Planetary Science Letters* 399, 86-91.
- Prescher, C., McCammon, C.A., Dubrovinsky, L., 2012. MossA: a program for analyzing energy-domain Mössbauer spectra from conventional and synchrotron sources. *Journal of Applied Crystallography* 45, 329-331.
- Priestley, K., Cipar, J., Egorkin, A., Pavlenkova, N., 1994. Upper-mantle velocity structure beneath the Siberian platform. *Geophysical Journal International* 118, 369-378.
- Ramesh, D., Kawakatsu, H., Watada, S., Yuan, X., 2005. Receiver function images of the central Chugoku region in the Japanese islands using Hi-net data. *Earth, Planets and Space* 57, 271-280.

- Reed, S.J.B., 2005. Electron microprobe analysis and scanning electron microscopy in geology. Cambridge University Press.
- Reichmann, H., Jacobsen, S., Mackwell, S., McCammon, C., 2000. Sound wave velocities and elastic constants for magnesiowüstite using gigahertz interferometry. *Geophysical Research Letters* 27, 799-802.
- Ringwood, A.E., 1962. Mineralogical constitution of the deep mantle. *Journal of Geophysical Research* 67, 4005-4010.
- Ringwood, A.E., 1975. *Composition and Petrology of the Earth's Mantle*. MacGraw-Hill, New York.
- Ringwood, A.E., 1979. *Origin of the Earth and Moon*. Springer-Verlag, New York.
- Ringwood, A.E., 1991. Phase transformations and their bearing on the constitution and dynamics of the mantle. *Geochimica et Cosmochimica Acta* 55, 2083-2110.
- Rohrbach, A., Schmidt, M.W., 2011. Redox freezing and melting in the Earth's deep mantle resulting from carbon-iron redox coupling. *Nature* 472, 209-212.
- Ross, N.L., Hazen, R.M., 1990. High-pressure crystal chemistry of MgSiO₃ perovskite. *Physics and Chemistry of Minerals* 17, 228-237.
- Rudolph, M.L., Lekić, V., Lithgow-Bertelloni, C., 2015. Viscosity jump in Earth's mid-mantle. *Science* 350, 1349-1352.
- Saikia, A., Ballaran, T.B., Frost, D.J., 2009. The effect of Fe and Al substitution on the compressibility of MgSiO₃-perovskite determined through single-crystal X-ray diffraction. *Physics of the Earth and Planetary Interiors* 173, 153-161.
- Sakamaki, T., 2017. Density of hydrous magma. *Chemical Geology* 475, 135-139.
- Schmandt, B., Jacobsen, S.D., Becker, T.W., Liu, Z., Dueker, K.G., 2014. Dehydration melting at the top of the lower mantle. *Science* 344, 1265-1268.
- Shannon, R.D., 1976. Revised effective ionic radii and systematic studies of interatomic distances in halides and chalcogenides. *Acta crystallographica section A: crystal physics, diffraction, theoretical and general crystallography* 32, 751-767.
- Shcheka, S.S., Keppler, H., 2012. The origin of the terrestrial noble-gas signature. *Nature* 490, 531-534.
- Shearer, P.M., 1991. Constraints on upper mantle discontinuities from observations of long-period reflected and converted phases. *Journal of Geophysical Research: Solid Earth* 96, 18147-18182.
- Shearer, P.M., 1993. Global mapping of upper mantle reflectors from long-period SS precursors. *Geophysical Journal International* 115, 878-904.
- Shearer, P.M., 2000. Upper mantle seismic discontinuities, Earth's Deep Interior: Mineral Physics and Tomography From the Atomic to the Global Scale: *Geophysical Monograph* 117. American Geophysical Union, Washington, DC, pp. 115-132.

- Sheldrick, G.M., 2008. A short history of SHELX. *Acta Crystallographica Section A: Foundations of Crystallography* 64, 112-122.
- Shim, S.-H., Grocholski, B., Ye, Y., Alp, E.E., Xu, S., Morgan, D., Meng, Y., Prakapenka, V.B., 2017. Stability of ferrous-iron-rich bridgmanite under reducing midmantle conditions. *Proceedings of the National Academy of Sciences* 114, 6468-6473.
- Sinmyo, R., Hirose, K., Muto, S., Ohishi, Y., Yasuhara, A., 2011. The valence state and partitioning of iron in the Earth's lowermost mantle. *Journal of Geophysical Research* 116, B07205.
- Sinmyo, R., Ozawa, H., Hirose, K., Yasuhara, A., Endo, N., Sata, N., Ohishi, Y., 2008. Ferric iron content in (Mg,Fe)SiO₃ perovskite and post-perovskite at deep lower mantle conditions. *American Mineralogist* 93, 1899-1902.
- Stachel, T., Harris, J.W., Brey, G.P., Joswig, W., 2000. Kankan diamonds (Guinea) II: lower mantle inclusion parageneses. *Contributions to Mineralogy and Petrology* 140, 16-27.
- Stagno, V., Frost, D.J., 2010. Carbon speciation in the asthenosphere: Experimental measurements of the redox conditions at which carbonate-bearing melts coexist with graphite or diamond in peridotite assemblages. *Earth and Planetary Science Letters* 300, 72-84.
- Stagno, V., Ojwang, D.O., McCammon, C.A., Frost, D.J., 2013. The oxidation state of the mantle and the extraction of carbon from Earth's interior. *Nature* 493, 84-88.
- Stagno, V., Tange, Y., Miyajima, N., McCammon, C., Irifune, T., Frost, D., 2011. The stability of magnesite in the transition zone and the lower mantle as function of oxygen fugacity. *Geophysical Research Letters* 38, L19309.
- Stixrude, L., Jeanloz, R., 2007. Constraints on seismic models from other disciplines—constraints from mineral physics on seismological models, in: Dziewonski, A., Romanowicz, B. (Eds.), *Seismology and Structure of the Earth*. Elsevier, Amsterdam, pp. 775–803.
- Stixrude, L., Lithgow-Bertelloni, C., 2005. Thermodynamics of mantle minerals—I. Physical properties. *Geophysical Journal International* 162, 610-632.
- Stixrude, L., Lithgow-Bertelloni, C., 2011. Thermodynamics of mantle minerals - II. Phase equilibria. *Geophysical Journal International* 184, 1180-1213.
- Stokes, H.T., Hatch, D.M., 1988. *Isotropy subgroups of the 230 crystallographic space groups*. World Scientific.
- Sun, S.-S., 1982. Chemical composition and origin of the Earth's primitive mantle. *Geochimica et Cosmochimica Acta* 46, 179-192.
- Suzuki, A., Ohtani, E., 2003. Density of peridotite melts at high pressure. *Physics and Chemistry of Minerals* 30, 449-456.
- Suzuki, A., Ohtani, E., Kato, T., 1995. Flotation of diamond in mantle melt at high pressure. *Science* 269, 216-218.

- Suzuki, A., Ohtani, E., Kato, T., 1998. Density and thermal expansion of a peridotite melt at high pressure. *Physics of the Earth and Planetary Interiors* 107, 53-61.
- Tange, Y., Takahashi, E., Nishihara, Y., Funakoshi, K.-i., Sata, N., 2009. Phase relations in the system MgO-FeO-SiO₂ to 50 GPa and 2000 °C: An application of experimental techniques using multianvil apparatus with sintered diamond anvils. *Journal of Geophysical Research* 114, B02214.
- Tateno, S., Hirose, K., Sata, N., Ohishi, Y., 2010. Structural distortion of CaSnO₃ perovskite under pressure and the quenchable post-perovskite phase as a low-pressure analogue to MgSiO₃. *Physics of the Earth and Planetary Interiors* 181, 54-59.
- Tibi, R., Wiens, D.A., 2005. Detailed structure and sharpness of upper mantle discontinuities in the Tonga subduction zone from regional broadband arrays. *Journal of Geophysical Research: Solid Earth* 110, B06313.
- Tonegawa, T., Hirahara, K., Shibutani, T., 2005. Detailed structure of the upper mantle discontinuities around the Japan subduction zone imaged by receiver function analyses. *Earth, Planets and Space* 57, 5-14.
- Tonegawa, T., Hirahara, K., Shibutani, T., Shiomi, K., 2006. Upper mantle imaging beneath the Japan Islands by Hi-net tiltmeter recordings. *Earth, Planets and Space* 58, 1007-1012.
- Tono, Y., Kunugi, T., Fukao, Y., Tsuboi, S., Kanjo, K., Kasahara, K., 2005. Mapping of the 410- and 660-km discontinuities beneath the Japanese islands. *Journal of Geophysical Research: Solid Earth* 110, B03307.
- Trønnes, R.G., 2000. Melting relations and major element partitioning in an oxidized bulk Earth model composition at 15–26 GPa. *Lithos* 53, 233-245.
- Trønnes, R.G., 2010. Structure, mineralogy and dynamics of the lowermost mantle. *Mineralogy and Petrology* 99, 243-261.
- Trønnes, R.G., Canil, D., Wei, K., 1992. Element partitioning between silicate minerals and coexisting melts at pressures of 1–27 GPa, and implications for mantle evolution. *Earth and Planetary Science Letters* 111, 241-255.
- Trønnes, R.G., Frost, D.J., 2002. Peridotite melting and mineral–melt partitioning of major and minor elements at 22–24.5 GPa. *Earth and Planetary Science Letters* 197, 117-131.
- Tsujino, N., Nishihara, Y., Nakajima, Y., Takahashi, E., Funakoshi, K.-i., Higo, Y., 2013. Equation of state of γ -Fe: Reference density for planetary cores. *Earth and Planetary Science Letters* 375, 244-253.
- Urakawa, S., 1991. Partitioning of Ni between magnesiowüstite and metal at high pressure: implications for core-mantle equilibrium. *Earth and Planetary Science Letters* 105, 293-313.

- Van Aken, P., Liebscher, B., 2002. Quantification of ferrous/ferric ratios in minerals: new evaluation schemes of Fe L_{23} electron energy-loss near-edge spectra. *Physics and Chemistry of Minerals* 29, 188-200.
- Van der Hilst, R.D., Engdahl, R., Spakman, W., Nolet, G., 1991. Tomographic imaging of subducted lithosphere below northwest Pacific island arcs. *Nature* 353, 37-43.
- Van der Hilst, R.D., Seno, T., 1993. Effects of relative plate motion on the deep structure and penetration depth of slabs below the Izu-Bonin and Mariana island arcs. *Earth and Planetary Science Letters* 120, 395-407.
- Van der Hilst, R.D., Widiyantoro, S., Engdahl, E., 1997. Evidence for deep mantle circulation from global tomography. *Nature* 386, 578-584.
- Vanpeteghem, C.B., Angel, R.J., Ross, N.L., Jacobsen, S.D., Dobson, D.P., Litasov, K.D., Ohtani, E., 2006. Al, Fe substitution in the $MgSiO_3$ perovskite structure: A single-crystal X-ray diffraction study. *Physics of the Earth and Planetary Interiors* 155, 96-103.
- Vinnik, L., Kato, M., Kawakatsu, H., 2001. Search for seismic discontinuities in the lower mantle. *Geophysical Journal International* 147, 41-56.
- Wakabayashi, D., Funamori, N., 2013. Equation of state of silicate melts with densified intermediate-range order at the pressure condition of the Earth's deep upper mantle. *Physics and Chemistry of Minerals* 40, 299-307.
- Walter, M., Kohn, S., Araujo, D., Bulanova, G., Smith, C., Gaillou, E., Wang, J., Steele, A., Shirey, S., 2011. Deep mantle cycling of oceanic crust: evidence from diamonds and their mineral inclusions. *Science* 334, 54-57.
- Wang, D., Angel, R.J., 2011. Octahedral tilts, symmetry-adapted displacive modes and polyhedral volume ratios in perovskite structures. *Acta Crystallographica Section B: Structural Science* 67, 302-314.
- Wang, W., Takahashi, E., 2000. Subsolidus and melting experiments of K-doped peridotite KLB-1 to 27 GPa: Its geophysical and geochemical implications. *Journal of Geophysical Research: Solid Earth* 105, 2855-2868.
- Wänke, H., Dreibus, G., Jagoutz, E., 1984. Mantle chemistry and accretion history of the Earth, *Archaean Geochemistry*. Springer, pp. 1-24.
- Wasson, J.T., Kallemeyn, G.W., 1988. Compositions of chondrites. *Philosophical Transactions of the Royal Society of London. Series A, Mathematical and Physical Sciences* 325, 535-544.
- Wilson, A.J.C., Prince, E., 1992. *International tables for crystallography*. Kluwer Dordrecht.
- Wood, B.J., Bryndzia, L.T., Johnson, K.E., 1990. Mantle oxidation state and its relationship to tectonic environment and fluid speciation. *Science* 248, 337-345.
- Wood, B.J., Fraser, D., 1977. *Elementary Thermodynamics for Geologists*. Oxford University Press, Oxford, United Kingdom.

- Woodland, A., Koch, M., 2003. Variation in oxygen fugacity with depth in the upper mantle beneath the Kaapvaal craton, Southern Africa. *Earth and Planetary Science Letters* 214, 295-310.
- Woodland, A., Kornprobst, J., Tabit, A., 2006. Ferric iron in orogenic lherzolite massifs and controls of oxygen fugacity in the upper mantle. *Lithos* 89, 222-241.
- Xu, F., Vidale, J.E., Earle, P.S., 2003. Survey of precursors to $P'P'$: Fine structure of mantle discontinuities. *Journal of Geophysical Research: Solid Earth* 108, 2024.
- Xu, W., Lithgow-Bertelloni, C., Stixrude, L., Ritsema, J., 2008. The effect of bulk composition and temperature on mantle seismic structure. *Earth and Planetary Science Letters* 275, 70-79.
- Xu, Y., McCammon, C.A., Poe, B.T., 1998. The effect of alumina on the electrical conductivity of silicate perovskite. *Science* 282, 922-924.
- Yamazaki, A., Hirahara, K., 1994. The thickness of upper mantle discontinuities, as inferred from short-period J-array data. *Geophysical Research Letters* 21, 1811-1814.
- Zhang, J., Herzberg, C., 1994. Melting experiments on anhydrous peridotite KLB-1 from 5.0 to 22.5 GPa. *Journal of Geophysical Research: Solid Earth* 99, 17729-17742.
- Zhao, J., Ross, N., Angel, R., 2004. New view of the high-pressure behaviour of $GdFeO_3$ -type perovskites. *Acta Crystallographica Section B: Structural Science* 60, 263-271.
- Zhao, Y., Weidner, D.J., Parise, J.B., Cox, D.E., 1993a. Critical phenomena and phase transition of perovskite—data for $NaMgF_3$ perovskite. Part II. *Physics of the Earth and Planetary Interiors* 76, 17-34.
- Zhao, Y., Weidner, D.J., Parise, J.B., Cox, D.E., 1993b. Thermal expansion and structural distortion of perovskite—data for $NaMgF_3$ perovskite. Part I. *Physics of the Earth and Planetary Interiors* 76, 1-16.

Acknowledgements

First and foremost, I would like to sincerely thank my supervisors Dan Frost and Tiziana Boffa Ballaran who brought me to the wonderful world of Earth's deep interior. They are always patient and support me a lot during my PhD study. I'm inspired by their brilliant ideas and seriousness on science.

Many thanks to Catherine McCammon for assisting and instructing me with Mössbauer spectroscopy and for valuable suggestions. I also thank Nobuyoshi Miyajima for helping me with EELS measurement and discussions.

I'm also grateful to Raphael Njul and Alexander Rother for the excellent sample preparation, to Heinz Fischer and Stefan Übelhack for the high-quality high-pressure assemblies and cubes, to Detlef Krause and Anke Potzel for assistance with the electron microprobe, to Ulrike Trenz and Doro Wiesner for aid with the chemical laboratory and SEM, and to Sven Lindhardt who helped me to solve electrical problems. I gratefully acknowledge Petra Buchert, Janina Potzel, Lydia Kison-Herzig and Anna Dinius for their administrative helps who make my life easier in Germany.

I am in debt to Dr. Florian Heidelberg for the translation of my thesis abstract into German. I would like to thank all my friends and colleagues in BGI. I offer my special thanks to all my Chinese friends, either moved on or still in BGI, for their help and company both in study and in daily life. Without them, I could not live such a happy life.

Last but not least, I would like to thank my parents who always give me unconditional support and encouragement.

(Eidesstattliche) Versicherungen und Erklärungen

(§ 9 Satz 2 Nr. 3 PromO BayNAT)

Hiermit versichere ich eidesstattlich, dass ich die Arbeit selbstständig verfasst und keine anderen als die von mir angegebenen Quellen und Hilfsmittel benutzt habe (vgl. Art. 64 Abs. 1 Satz 6 BayHSchG).

(§ 9 Satz 2 Nr. 3 PromO BayNAT)

Hiermit erkläre ich, dass ich die Dissertation nicht bereits zur Erlangung eines akademischen Grades eingereicht habe und dass ich nicht bereits diese oder eine gleichartige Doktorprüfung endgültig nicht bestanden habe.

(§ 9 Satz 2 Nr. 4 PromO BayNAT)

Hiermit erkläre ich, dass ich Hilfe von gewerblichen Promotionsberatern bzw. -vermittlern oder ähnlichen Dienstleistern weder bisher in Anspruch genommen habe noch künftig in Anspruch nehmen werde.

(§ 9 Satz 2 Nr. 7 PromO BayNAT)

Hiermit erkläre ich mein Einverständnis, dass die elektronische Fassung meiner Dissertation unter Wahrung meiner Urheberrechte und des Datenschutzes einer gesonderten Überprüfung unterzogen werden kann.

(§ 9 Satz 2 Nr. 8 PromO BayNAT)

Hiermit erkläre ich mein Einverständnis, dass bei Verdacht wissenschaftlichen Fehlverhaltens Ermittlungen durch universitätsinterne Organe der wissenschaftlichen Selbstkontrolle stattfinden können.

.....
Ort, Datum, Unterschrift